NASA Contractor Report 187177

Numerical Prediction of Turbulent Oscillating Flow and Associated Heat Transfer

W.J. Koehler, S.V. Patankar, and W.E. Ibele
University of Minnesota
Minneapolis, Minnesota

August 1991

Prepared for
Lewis Research Center
Under Grant NAG3-1024

National Aeronautics and
Space Administration

TABLE OF CONTENTS

LIST OF FIGURES

LIST OF TABLES

NOMENCLATURE

Principal Symbols

a	coefficient for numerical scheme
α	generalized coefficient for numerical scheme
A_e	control volume interface area
A_R	amplitude ratio, eq. (2.28)
β	isobaric coefficient of expansion, eq. (2.14)
c_μ, c_1, c_2	constants in the k-ε turbulence model
c_p, c_v	specific heat capacities at constant pressure and volume, respectively
D	diameter of tube
d_e	quantity for numerical scheme, eq. (4.42)
ε	turbulent dissipation rate
Ec	Eckert number, eq.(2.24)
F	total integrated mass flux across a control volume interface
Φ	viscous dissipation function
ϕ	scalar transport variable
f_1, f_2, f_3	time integration factors (Chapter 4 only)
f_μ, f_1, f_2	functions in the k-ε turbulence model
$\vec{f}$	body force vector in the momentum equations
Γ	generalized diffusion coefficient
G	rate of generation of turbulent kinetic energy
γ	specific heat ratio c_p/c_v
h	enthalpy
J	total integrated flux of ϕ across a control volume interface
φ	azimuthal direction
k	turbulent kinetic energy or thermal conductivity according to context

κ	von Karmann constant
K_a	acceleration parameter, eq. (3.38) and (6.21)
L	length
l_m	mixing length
M	molecular weight
μ	dynamic viscosity
ν	kinematic viscosity
P	modified pressure or main grid point, according to context
p	thermodynamic pressure
Pr	Prandtl number, eq.(2.23)
ρ	density
r	radial coordinate
Re	Reynolds number, eq. (2.21)
R_t	turbulent Re number, eq. (3.20)
R_y	turbulent Re number, eq. (3.21)
$\overline{R_u}$	universal gas constant
S	source term
$\dot{S}'''_{gen}$	volumetric entropy generation rate
s	entropy
$\sigma_{k,\varepsilon,T}$	trubulent Prandtl number for k, ε and T
σ_{max}	residual of solution of continuity equation
Str	Strouhal number, eq. (2.25)
T	temperature
τ	stress tensor
t	time
t	time
Tl	turbulence intensity at the inflow cross section
u	axial component of velocity vector
u^+	dimensionless velocity

u_τ	friction velocity
$\vec{u}$	velocity vector
V	volume
v	radial component of velocity vector
Va	Valensi number, eq. (2.22)
ω	angular fraquency
w	azimuthal velocity
x	axial coordinate
y	wall distance
y^+	dimensionless wall coordinate
z	dummy quantity for averaging
$\vec{q}$	heat flux vector

Subscripts and Superscripts

'	randomly time-fluctuating quantity
–	phase-averaged quantity
i, j, 1, 2	indices for tensor notation
m	mean
t	turbulent
o	moleclar reference
ref	reference value
∞	value of the ambient

Operators

def	deformation tensor (strain tensor)
div	divergence
grad, grad(...)^T	gradient and transpose of the gradient
∂	differential operator
D/Dt	substantial derivative

PART I: STATEMENT OF THE PROBLEM AND SOLUTION TECHNIQUE

1. INTRODUCTION

1.1. Background

The distinct feature of a Stirling engine as compared to most other power producing devices is its ability to be driven by virtually any heat source such as solar energy or combustable refuse, among others. This leads to a number of promising applications: The Stirling engine as a prospective power source for future space missions or as the rice husk driven motor for agricultural machinery. In addition, a Stirling engine is silent, has low emission levels if powered by a combustion process and is energy efficient.

A crucial point for further development of Stirling engines is the optimization of its heat exchangers which operate under oscillatory flow conditions. Heat exchanger optimization depends on the ability to accurately simulate the fluid flow and heat transfer behavior. It has been found that the most important thermodynamic uncertainties in the Stirling engine designs for space power are in the heat transfer between gas and metal in all engine components and in the pressure drop across the heat exchanger components. So far, performance codes cannot predict the power output of a Stirling engine reasonably enough if used for a wide variety of engines. Thus, there is a strong need for better performance codes. However, a performance code is usually not concerned with the details of the flow. This information must be provided externally. While for laminar oscillating flow analytical relationships exist, there has been hardly any information about transitional and turbulent oscillating flow which could be introduced into the performance codes.

In 1986 a survey by Seume and Simon (1986a) revealed that most Stirling engine heat exchangers operate in the transitional and turbulent regime. Consequently, research has since focussed on the unresolved issue of transitional and turbulent oscillating flow and heat transfer. Since 1988, the University of Minnesota oscillating flow test facility has obtained experimental data about transitional and turbulent oscillating flow. However, since the experiments in this field are extremely difficult, lengthy and expensive, it will be advantageous to numerically simulate the flow and heat transfer accurately from first principles. With a simulation program, one can enhance the understanding of the oscillating flow phenomena in general. Also, a simulation program is useful in guiding the experiment in some areas. Once tested for its validity, many more operating points can be "probed" with such a simulation program than with any experimental set-up. Finally, this program can generate the input data needed for a performance code, as mentioned above.

It is the purpose of this research to contribute to the development of a realistic simulation program, thereby adding to the basic knowledge and understanding of turbulent oscillating flow and heat transfer and to the further the development of Stirling engines.

1.2. Literature Survey of Oscillating Flow Research

1.2.1. Scope and limitations of this Survey

The objective of this survey is to answer the following questions:

On oscillatory pipe flow, ...

a) ... what experimental data is available?

b) ... what numerical results are reported and how do they compare with experiments and theory?

c) ... what are the open questions for numerical analysis in this field?

Currently there is no consensus in the literature about the nomenclature of periodic unsteady flows. Expressions like pulsating, pulsatile, oscillating or oscillatory are used synonymously. In this work, we are primarily concerned with information about periodically reversing flow with zero mean velocity. In the following, we shall denote this situation by "oscillatory" or "oscillating" flow only. The expressions "pulsatile" or "pulsating" flow will be used for flow situations with a net mean velocity.

Fully developed laminar pulsatile flow can be expected to be a superposition of a steady mean flow and an oscillatory flow, since the equation of motion is linear in that special case. For an entry length situation and/or transitional or turbulent flow, this is no longer true and oscillatory flow has to be treated separately from pulsatile flow. Moreover, some analytical solutions for pulsatile flow have singularities for zero mean velocity. Yet, results for pulsatile flow can possibly be taken as qualitatively representative for oscillatory flow. For instance the question whether the turbulence structure in an unsteady flow is different from that in steady flow can be discussed with knowledge about pulsatile flow. The majority of publications deal with pulsatile flow, and these results are included in this survey, but listed and described distinct from those for oscillatory flow. Similarly, although our focus is on internal pipe flow, other geometries investigated could be a valuable qualitative source of information and are therefore included. From a numerical point of view, turbulence models for general unsteady situations may be of great importance and are therefore included, too.

This literature survey extends and updates the excellent review of *Seume and Simon (1986a)* for the fluid flow problem. Since it is assumed that fluid flow is the underlying problem, this review does not include information about heat transfer. Once the fluid flow is understood, the heat transfer can be inferred.

1.2.2. Laminar Flow

1.2.2.1. Fully Developed Flow

From the literature surveyed it is clear that fully developed oscillatory and pulsatile laminar flow are well understood. Since the Navier-Stokes equations for this special case are linear, a pulsating velocity can be split into a steady mean component and an oscillating component. However, a distinction between oscillatory and pulsatile flow is necessary in the case of an entry length problem.

Straight Geometries

The oscillating flow effect was experimentally discovered for laminar oscillating flow conditions by *Richardson and Tyler (1929)*, when they found the velocity distribution near the mouth of a pipe different than the steady state profile, i.e. the maximum velocity was located near the pipe walls and not in the center. *Sexl (1930)* was able to predict this behavior for sinusoidal motion in a pipe. Following are a number of analyses and experiments performed to study the flow pattern, pressure drop and friction factor for different geometries as well as for bent circular pipes:

Analyses. *Wommersley (1955)* and *Uchida (1956)* calculated the velocities of laminar pulsatile flow in a straight pipe for non-sinusoidal motions of the fluid. The Uchida analysis is still the most prominent analysis for laminar flow. *Drake (1965)* and *Gedeon (1986)* analyzed the flow pattern of oscillating flows in rectangular channels of finite and infinite width. Drake also derived a solution for the skin friction. *Vosse (1986)* treated oscillatory flow in a flat plate channel numerically with a finite element method. Employing a one-dimensional analysis and the well-known steady state friction factor, *Jones (1985)* gave an analytical solution for the instantaneous pressure drop in oscillatory flow. For pulsatile flow, *Trikha (1975)* obtained the time dependent friction factor by a Laplace transform solution. *Ohmi et al. (1981b,c)* gave instantaneous and time averaged values for

friction factor and pressure drop in a pipe and found behavior qualitatively similar to turbulent flow. *Chen and Griffin (1983)* stated that the pressure loss in oscillatory flow is considerably larger than in steady flow. For general unsteady motion, *Chambre and Schrock (1978)* derived an analytical solution for fully developed laminar pipe flow. *Iguchi et al. (1985a)* obtained a time dependent representation of the wall shear stress from the integral momentum and energy equations. Unsteady boundary layers were treated in detail e.g. by *Telionis (1975)*. *Cebeci (1986)* describes an intelligent numerical scheme for unsteady boundary layers with large flow reversals.

Experiments. Studies of oscillatory flow in a straight pipe are reported by *Shizgal et al. (1965)*, while *Edwards and Wilkinson (1971)* did the pulsatile flow case. Their results show good agreement with the Uchida analysis. *Valensi (1947)* performed experiments of a liquid in a U-shaped tube with free oscillations, while forced oscillations were investigated by *Chan and Baird (1974)*. Oscillatory flow in tapered channels was studied experimentally and analytically by *Gaver (1986)*, who found that the results differed substantially from those in a straight channel. Similar results were presented by *Ikeo and Uzawa (1986)*, who investigated the oscillatory flow pattern in an convergent tube numerically and experimentally. *Duck (1985)* solved the flow pattern of a pulsatile flow in a nonuniform channel numerically and found that above a critical amplitude of oscillation, a failure of the boundary layer equations ocured.

Flow in Curved Ducts

The flow pattern of laminar pulsatile flow in bent circular pipes of various cross sections was studied experimentally by *Chandran et al. (1974)*. That of oscillating flow was investigated numerically and experimentally by *Sudou et al. (1985)*. *Chandran et al.(1974)* found that the maximum velocity was shifted towards the center of curvature compared to steady flow. *Sudou et al. (1985)* found good agreement of experiment and prediction. A study by *Sumida and Sudou (1986b)* for pulsatile flow used laser-doppler anemometry to measure the axial velocity in a curved pipe. They reported good agreement

with their numerical predictions. *Telionis (1981)* gave similarity parameters for nondimensional treatment of pulsatile flow in curved pipes. *Takami (1984)* determined the pressure drop in pulsatile curved-pipe flow by a time-dependent numerical analysis and by an approximation method and found good agreement. The wall shear stress in oscillating flow as a function of radius of curvature was calculated by *Sumida and Sudou (1985)*. *Yamane et al. (1985)* found an increase of wall shear stress compared to a straight pipe under identical conditions. Finally, *Sumida and Sudou (1986a)* determined the pressure drop of an oscillating fluid in a curved pipe by experiment and analysis.

1.2.2.2. Entry Length Conditions

Oscillatory Flow in Straight Geometries

The first investigation of this kind was reported by *Disselhorst and Wijngaarden (1980)*, who studied separation near the entrance of a tube under acoustic resonance. Thereafter separation only occurs for small and moderate Strouhal numbers. *Peacock and Stairman (1983)* predicted the entry length shorter than in steady state conditions. However, *Seume and Simon (1986a)* argued that experiments do not support this hypothesis. *Chayrreyon (1984)* proposed a time dependent entry length. *Ohmi (1986a)* measured the velocity distribution and the entry length. Apparently the only experimental investigation into pressure drop behavior of oscillatory flow in a straight pipe was reported by *Taylor and Aghili (1984)*, who gave values for pressure drop which were consistently higher than steady state values. Their results implicitly included entry length effects. It is not clear how much of the reported losses were due to the oscillating flow effect alone.

Pulsatile Flow

Using a Laplace transform, the straight co-axial annulus was analytically solved by *Atabek (1961)*, where the limiting cases (circular pipe and parallel-plate channel) received special consideration.

1.2.3. Turbulent Flow

1.2.3.1. Oscillating Flow

The concept of turbulence in oscillating flow is inseparable from the problem of transition. We will, however, distinguish between research which is primarily focussed on the turbulent flow structure itself, and research whose focus is the transition. The above mentioned experiments by *Taylor and Aghili (1983)* also covered the range of turbulent flow. *Hino et al. (1983)* investigated turbulent flow in a rectangular duct experimentally in great detail. For Re_{max}=22500 and Va=309, they found that the turbulence structure of the oscillating flow was substantially different from steady flow, and that the accelerating and decelerating phases themselves had different turbulence structures. While in the accelerating phase turbulence was triggered near the wall but suppressed, the turbulent kinetic energy would be generated explosively near the wall in the decelerating phase. They also observed that "during the whole cycle, a layer that obeys the semilogarithmic law exists above a sublayer similar to the viscous sublayer"[1]. While in the accelerating phase, this layer was very thin, its thickness increased in the deceleration phase. *Hino et al.* also stressed the point that while the statistics of oscillating flow turbulence are quite different from steady flow, "the elementary process which maintains the turbulent production is almost the same as in the steady wall turbulent flow"[2]. In a paper in Japanese, *Yoshiki et al. (1986)* studied the velocity distributions in air between two pistons of arbitrary phase difference including 180°. The Re number and Va number range was 1.32×10^4 to 5.94×10^4 and 119 to 353, respectively. Their results indicated that the turbulence appeared "in velocity waves for all conditions independently of the piston phase difference. The instantaneous velocity distribution became almost uniform in the center region and looked like those for steady

---

[1]M. Hino, M. Kashiwayanagi, Nakayama, A and T. Hara in J. Fluid Mechanics, vol. 131, p 370, 1983.
[2]M. Hino, M. Kashiwayanagi, Nakayama, A and T. Hara in J. Fluid Mechanics, vol. 131, p 398, 1983.

turbulent flows, regardless of the phase difference"[1]. As in laminar flow, the near wall fluid reacted faster according to acceleration and deceleration.

1.2.3.2. Pulsatile Flow

Experiments in Straight Pipes

Mizushina et al. (1973) measured velocity profiles and turbulence intensities and found that there are two distinct classes of flows according to the pulsation frequency: For lower pulsation frequencies, the velocities behave quasi-steady and the turbulence intensity does not pulsate. For higher pulsation frequencies the velocity profile is quite different from the steady state form and the turbulence intensity fluctuation pulsates oppositely to the velocity. *Cousteix (1979)* found, that pulsations do not significantly influence the boundary layer and the turbulence structure. He therefore applied a steady state turbulence model to simulate the boundary layer numerically. However, only a single frequency was investigated. *Kirmse (1979)* compared his own experimental data with the computations of *Vasilev and Kvon (1971)* finding poor agreement.

Ohmi et al. (1980a,b,c; 1981a,d) derived 4 characteristic parameters to describe the flow pattern, but without physical interpretation. They examined the influence of the pulsation frequency on flow pattern and turbulent friction losses. Three flow regimes (quasi-steady, intermediate and inertia dominant) are reported as a function of frequency. It is stated that the instantaneous friction factor was either equal, greater than or less than the steady state friction factor, but the time averaged friction factor was always greater than the one for steady state. *Ohmi et al. (1983)* investigated the eddy viscosity distribution as a function of pulsating frequency with a X-wire probe. The distribution was found different from the one in steady flow. *Tu and Ramaprian (1983)* studied instantaneous velocity and wall shear stress when the mean flow was well in the turbulent range ($Re_m = 5 \cdot 10^4$). The frequency was varied over a wide range. Their results showed that the time mean flow was

[1] H. Yoshiki, S. Tsumura, T. Endoh and N. Takama in Nihon Kikaigakkai rombunshu, vol. 52, p. 3650, Nov. 1986

affected by pulsations when the oscillation frequency approached the characteristic frequency of turbulence. According to their results, neither the time mean nor the ensemble-averaged velocity followed the universal log-law. The unsteadiness affected the turbulence intensity and the Reynolds-stress significantly. They noted that quasi-steady turbulence models neglect this effect of unsteadiness on the time mean flow. *Iguchi et al. (1985b)* studied the structure of turbulence as a function of time averaged Reynolds number, frequency and amplitude ratio. They presented a turbulence model including a lag in response time and compared it with their experimental results. *Ohmi et al. (1986b)* measured the turbulent slug and the velocity field in the inlet region of a pipe. *Mao and Hanratty (1985;1986)* measured the time variations of the wall shear stress for small velocity amplitude ratios and high frequencies. Their results indicate that the wall shear stress varies sharply over a narrow frequency range. *Iguchi et al. (1986b)* observed two types of turbulent-slug behavior, according to whether the pulsation frequency was low or high. In both cases the occurrence of the turbulent slug was periodic, in contrast to the randomness that is characteristic in steady flows. On the basis of his experiments *Bulatowa et al. (1986)* concluded that the turbulent fluctuations are not altered by frequency or channel length. He also found that a peak in the mean velocity coincided with a minimum in the turbulent fluctuations.

Numerical Analyses of Straight Pipes

Only fully developed situations have been investigated so far. *Vasilev and Kvon (1971)* used a steady state turbulence model for pulsatile flow. Their results were not confirmed by *Kirmse (1979)*. *Thomas (1974)* used a turbulence model which utilized the mean residence time of a fluid particle at the wall and predicted cross-section averaged values of the shear stress for low frequencies. *Younis (1978)* used the low-Re number k-ε turbulence model to predict the data of *Lu et al. (1973)*. *Kita et al. (1980)* proposed a fluctuating (five-layer) eddy viscosity model to calculate the velocity distribution and the friction factor. Their results are confirmed by experiment. *Blondeaux and Colombini (1985)*, using the steady state turbulence model of Saffman, predicted the failure of the log-law. The application of

this turbulence model was suggested for low frequencies only, and no conclusions about the general validity of the model were drawn. *Kebede et al. (1985)* used an alternative to the widely used concept of eddy viscosity. They replaced the Bousinesq stress-strain law by a set of differential rate equations for turbulence stresses. Surprisingly, this low-Re number differential stress model gave superior predictions than a one-equation turbulence model, but worse results than the low Re number k-ε model. *Reddy et al. (1985)* applied a pseudospectral method to investigate the viscous wall region. The amplitude of the pulsations was large. The pulsation frequency was large and characteristic of the wall region eddies in steady turbulent flow. "The mean profiles of axial velocity, fluctuation intensity and turbulent production rate were essentially the same as in steady flow"[1]. The instantaneous turbulence production rate was largest at large adverse pressure gradients, which agrees with the findings of *Hino et al. (1983)* for oscillating flow.

Other Geometries

Flows over a flat plate were experimentally studied by *Cousteix (1982; 1985)* and *Cook et al. (1985)*, who also did a numerical analysis. For the flat plate, *Cousteix (1982)* obtained similar findings as for the pipe *(Cousteix,1979)*, where the turbulence structure near the wall was not much altered by the pulsations. *Cook (1985)* used an unsteady boundary layer code together with a steady state turbulence model. A comparison with his experiments showed fair results. Experiments of *Binder (1982)* for large amplitude pulsations in a parallel- plate channel showed that the mean velocity and the streamwise turbulent intensity of the flow were unaffected by the large amplitude pulsations. The wall shear stress lead the free stream and its amplitude was less than predicted by theory.

1.2.3.3. Generally Unsteady Turbulent Flows

Gosman (1980) discussed turbulence models for the near wall region of unsteady flows. Given the uncertainty of whether the law of the wall holds generally, he suggested a

[1]U. Reddy, J. B. McLaughlin, R. J. Nunge in Fluid Eng. Trans. ASME, vol. 107, n.2, p.205, June 1985

systematic investigation in turbulent oscillating flow in a simple geometry. He mentioned numerical computations by *Younis* for fully developed oscillating flow, using the low Reynolds number turbulence model of *Jones and Launder (1973)*. The results of those computations suggested that the law of the wall does not hold for Reynolds numbers and frequencies typical for automobile engines. *Iguchi and Ohmi (1983a)* studied the influence of acceleration and deceleration on velocity, shear stress, friction factor and eddy viscosity experimentally. On that basis they stated a limit for the applicability of the quasi-steady state to an unsteady condition. In *Iguchi and Ohmi (1983b)* the authors expand the former paper to frictional losses in a pipe.

1.2.4. Transitional Flows

1.2.4.1. Transition in Oscillating Flow

Flow in a Pipe

The description of transition depends strongly on the criterion used to define transition. This criterion is not necessarily consistent in all publications, nor is it always stated. *Sergeev (1966)* used flow vizualization to describe transition in oscillating flow and was the first to give an equation relating the critical Re number to the Va number. *Merkli and Thomann (1975)* observed transition in a resonance tube at very high frequencies. For these conditions they reported a weak vortex street outside the boundary layer. A similar observation was made for channel flow by *Sobey (1985)*. He also predicted these vortices numerically through stability considerations. *Hino et al. (1976)* took hot wire measurements of transition. Their signals showed a laminar-like phase during the acceleration and a turbulent-like phase during deceleration. *Grassmann and Tuma (1979)* visualized transition by means of an electrolytic technique and reported an equation for the critical Re number. *Ohmi et al. (1982)* found a large parameter range between laminar and turbulent regime and quantified their findings in a transition equation. *Dijkstra (1984)* observed transition, but did not state a criterion. Numerical studies were done by *Cayzac et*

al. (1985). They were able to predict the lower bound of stability qualitatively, but not quantitatively. In his experimental work, *Seume (1988)* defined as criterion for transition a rapid increase in the measured rms velocity fluctuations. The parameter range covered in his experiments was representative for Stirling engines heaters and coolers. Aside from the always-laminar region and the transitional region he identified also an always turbulent region at very high Reynolds and Valensi numbers. He verified that the critical Re number in oscillating flow depends on the Valensi number and described two mechanisms to trigger turbulence: externally caused transition due to incoming fluid, and internal transition due to the usual boundary layer instability at higher Re numbers. All researchers agree that transition to turbulence can be described by a relation of the form

$$Re_{m,max} = \text{const.} \cdot Va^{0.5}$$

where the constant is some number around 1000.

Other Geometries

Park and Baird (1970) reported transition during free oscillations of a liquid in an U-tube. *Von Kerczek and Davis (1972)* predicted the lower bound of stability of Stokes layers on a flat plate. They, like *Caycac et al. (1985)*, could predict transition only qualitatively, but not quantitatively. *Iguchi et al. (1982)* studied free oscillations in an U-tube and defined transition as the moment, when the velocity profile deviated from the Uchida-type laminar profile. *Akao et al. (1986)* studied transitional oscillatory flows in a rectangular duct. In agreement with *Hino (1976)* they found that the flow had two different phases: a quasi-laminar one and a turbulent one. However, the flow in the laminar-like phase was quite different from temporary fully developed laminar flow.

1.2.4.2. Transition in Pulsatile Flow

Gerrard (1971) probed a pulsatile flow with a mean Re-number of 3770. He found that closer to the wall, in the turbulent phase the velocity profile can be represented by a power

law according to $(y/R)^{1/n}$. *Sumida et al. (1984)* measured pressure drop losses in transitional flow in curved pipes as mean-time values. Good agreement with an approximation is reported. *Iguchi et al (1986a)* studied the relaminarization of turbulent slugs in a rectangular duct at four different aspect ratios. At low accelerations the behavior is quasi-steady. At high accelerations they observed the disappearance and reappearance of turbulent slugs at fixed phases in a cycle, which cannot be inferred from steady state behavior. *Shemer et al. (1985a,b)* found for pipe flow that the mean properties of the flow was not influenced by the moderate pulsations in both laminar and turbulent flow regimes. They presented the oscillating part of the flow parameters as a function of amplitude and phase at exitation frequency. In particular, they explained the phase lag between the mean flow and the Reynolds stresses by the relaxation time of turbulence relative to the instantaneous mean shear. To capture this feature of turbulence, they proposed a complex-valued turbulence viscosity. *Stettler and Hussain (1986)* observed transition in a pipe flow using laser-doppler anemometry (LDA) measurement and defined the stability-transition boundary as functions of $Re_{u,mean}$, $Re_{frequency}$ and the frequency itself. They report phase-locked turbulent slugs, like *Iguchi et al. (1986a)*. *Tozzi and von Kerczek (1986)* examined the linear stability theory for sinusoidally pulsating pipe flow and found that the relevant axisymmetric disturbances are more stable in pulsatile flow than those of the mean flow alone.

1.2.4.3. Transition in Generally Unsteady Flows

Davis (1976) gave an extensive review for theoretical approaches to stability, which could be applied to oscillatory flows. *Lefebre and White (1987)* investigated transition to turbulence in a constant-acceleration pipe flow started from rest. It was reported that the time of transition was constant throughout the pipe, and that the critical Re number varied from 2×10^5 to 5×10^5 depending on the acceleration. Two characteristic parameters were derived to characterize the onset of transition: an acceleration parameter and a local boundary-layer thickness Re number.

1.2.5. Conclusions

1.) Laminar oscillating flow is well understood. Analytical and numerical analyses agree well with experiments.

2.) There are numerous investigations on turbulent pulsatile flow, but no agreement exists on whether pulsations significantly disturb the steady flow pattern. *Mizushina et al (1973), Ohmi et al. (1983)* and *Tu and Ramaprian (1983)* reported differences compared to the quasi-steady pattern, while *Binder (1982)* and *Cousteix (1979, 1982, 1985)* found no significant differences. It is believed that much of this confusion can be attributed to a reluctance by the various researchers to use consistent dimensionless similarity parameters to classify their investigations. However, the collective findings seem to indicate that the mean and instantaneous flow parameters are significantly affected by moderate to large amplitudes at high but not too high frequencies of pulsation.

3.) For transitional and turbulent oscillatory flow, especially the works of *Hino et al. (1983)* and *Seume (1988)* provide a pool of useful experimental data. Additional qualitative information can be found foremost in the papers on pulsatile flow by *Tu and Ramaprian (1983)* and *Shemer (1985)*. So far, no numerical investigation of transitional and turbulent oscillatory flow in a pipe of finite length has been made. Even for the fully developed situation, only one investigation was mentioned (*Gosman, 1980*).

4.) A turbulence model which is well suited for unsteady situations has not been identified yet. However, it was mentioned by several authors that the turbulence model sought should provide a means for the relaxation time of turbulence [*Shemer et al. (1985), Kebebe et al. (1985), Iguchi et al.(1985b)*].

1.3. Objectives

1.) Develop a numerical algorithm suitable for solving the governing equations in an exact and efficient manner.

2.) Identify a turbulence model which has the capabilities to predict unsteady turbulent flow.

3.) Evaluate the performance of the turbulence model chosen for its capability to predict transition.

4.) If necessary, modify or optimize the chosen turbulence model.

5.) Compute the fluid flow and heat transfer of a number of data points representative for Stirling engine heaters and coolers and compare the predictions with experimental results if available.

6.) Answer the following questions:

- Are steady state correlations appropriate representations for the friction coefficient and Nusselt number of the fully developed turbulent flow?
- Do entrance length effects play a role?
- Is heat transfer or fluid flow the major contributor to irreversibilities in the cases considered?

1.4. Outline of This Work

To start with, the problem will be described in a general mathematical way. In order to estimate the limitations of the approach chosen it is important to state and introduce the assumptions made, which is done next. Then, the choice of the turbulence model is laid out and the model and some alternatives are discussed. At this point, the complete system of equations is established, whose solution should lead to the desired results. This brings us

to the numerical method for solving this system of equations, which is presented and discussed next. Following this, the computational results are given: First, we will test the numerical model and the turbulence model with known steady state cases. Then, the performance of the turbulence model for transition predictions is shown. Finally, the results of the oscillating flow computations are given in the order fluid flow, heat transfer and irreversibility.

2. PHYSICAL SITUATION AND ITS MATHEMATICAL DESCRIPTION

2.1. Differential Equations

The governing differential equations express the conservation of mass, momentum and energy for a continuum and are given in the following for an infinitesimal control volume.

Conservation of mass:

$$\frac{\partial \rho}{\partial t} + \mathrm{div}(\rho \vec{u}) = 0 \tag{2.1}$$

Conservation of momentum:

$$\rho \frac{\partial \vec{u}}{\partial t} + \rho \vec{u} \bullet \mathrm{grad}(\vec{u}) = - \mathrm{grad}(p) + \mathrm{div}(\tau) + \vec{f} \tag{2.2}$$

Conservation of energy as enthalpy equation (neglecting radiation):

$$\rho \frac{\partial h}{\partial t} + \rho \vec{u} \bullet \mathrm{grad}(h) = - \mathrm{div}(\vec{q}) + \frac{\partial p}{\partial t} + \vec{u} \bullet \mathrm{grad}(p) + \mu \Phi \tag{2.3}$$

where $\vec{u}$ is the velocity vector, ρ is the density, p the thermodynamic pressure and μ is the dynamic viscosity. τ denotes the stress tensor and $\vec{f}$ stands for any additional body forces. h is the specific enthalpy of the fluid and $\vec{q}$ represents the heat flux vector. Φ denotes the viscous dissipation function and is defined as

$$\mu \Phi \equiv \tau \bullet \mathrm{grad}(\vec{u}) \tag{2.4}$$

It may be pointed out here that this set of differential equations together with the boundary conditions of Chapter 2.4 specify the problem completely, even in the case of turbulent flow. However, a practical solution of these differential equations involves some averaging (e.g. ensemble averaging) over time and/or space. It is this process of averaging, during which the new unknown terms are created, for which a turbulence model needs to be employed later on.

2.2. Basic Assumptions

The heat transfer and fluid flow problem in Stirling engine heat exchangers combines several different problems, some of which are not of primary importance of this research. For instance, a Stirling engine heater usually consists of a bundle of bent circular tubes. The fact that the tubes are bent further complicates the underlying situation but is not essential in order to reach the goal of this research. Therefore, the physical domain in this research shall be a *straight tube*. Also, we will assume that no changes happen in the azimuthal direction and that the velocity in this direction is zero,

$$w = 0 \qquad \frac{\partial}{\partial \varphi} = 0 \tag{2.5}$$

Throughout this work the fluid will be treated as a *Newtonian continuum*. Together with the *Stokes hypothesis*, we can express the divergence of the stress tensor of eq. (2.2) as

$$\mathrm{div}(\tau) = 2\,\mathrm{div}(\mu\,\mathrm{def}(\vec{u})) - \frac{2}{3}\,\mathrm{grad}(\mu\,\mathrm{div}(\vec{u})) \tag{2.6}$$

where $\mathrm{def}(\vec{u})$ denotes the deformation tensor and is defined as

$$\mathrm{def}(\vec{u}) = \frac{1}{2}\left[\mathrm{grad}(\vec{u}) + [\mathrm{grad}(\vec{u})]^{T}\right] \tag{2.7}$$

Here the superscript "T" denotes the transpose of the tensor. With this input and the assumption of *no body forces*, the conservation equation for momentum becomes the Navier-Stokes equations:

$$\rho \frac{\partial \vec{u}}{\partial t} + \rho \vec{u} \bullet \text{grad}(\vec{u}) = -\text{grad}(p) - \text{div}(\mu\, \text{grad}(\vec{u})) + \text{div}\left[\mu\, [\text{grad}(\vec{u})]^T\right] - \frac{2}{3}\, \text{grad}(\mu\, \text{div}(\vec{u})) \qquad (2.8)$$

Defining the pressure as

$$\boxed{P = p + \frac{2}{3}\mu\, \text{div}(\vec{u})} \qquad (2.9)$$

equation (2.7) can be rewritten in the form

$$\boxed{\rho \frac{\partial \vec{u}}{\partial t} + \rho \vec{u} \bullet \text{grad}(\vec{u}) = -\text{grad}(P) + \text{div}(\mu\, \text{grad}(\vec{u})) + \text{div}\left[\mu\, [\text{grad}(\vec{u})]^T\right]} \qquad (2.10)$$

It may be noted here that, for the laminar case, a more convenient form of P could have been defined as

$$P = p - \frac{1}{3}\mu\, \text{div}(\vec{u}) \qquad (2.11)$$

It can be shown that, for the case of constant dynamic viscosity, with this formulation the momentum equations can be expressed like eq. (2.10) but without the last term. Often, in laminar flow problems, the viscosity can be treated as constant. However, in case of turbulent flow, the effect of turbulent mixing is frequently expressed by the concept of a turbulent viscosity which is not a fluid property but depends on the flow conditions and is therefore not a constant. In this case, the definition of P as in eq. (2.9) is preferred and eq.

(2.10) is applicable as written. The formulation of eq. (2.10) in axisymmetrical coordinates is given in the appendix.

Generally, the physical properties of the working fluid should be temperature dependent. Since we are concerned with turbulent oscillatory flows, turbulent diffusion will be the dominant effect, and a variation in the molecular diffusion coefficient due to temperature effects may be secondary. For now we will restrict the computations to *constant properties*. Once the basic problems in turbulent oscillatory flow are understood, variable properties may be introduced. The numerical program is perfectly capable of handling variable properties. As a consequence of the assumptions of constant properties the convective heat transfer problem is decoupled from the fluid flow problem and the latter can be solved first.

In the energy equation (2.3), the first term on the left hand side may be simplified using *Fourier's law*,

$$\vec{q} = -k \, \mathrm{grad}(T) \tag{2.12}$$

To transform h to T as the variable on the left hand side of eq. (2.3), we use the thermodynamic identity

$$\frac{Dh}{Dt} = c_p \frac{DT}{Dt} + \frac{1}{\rho}(1-\beta T)\frac{Dp}{Dt} \tag{2.13}$$

where D/Dt represents the substantial derivative and β denotes the isobaric coefficient of compressibility

$$\beta \equiv \rho \left(\frac{\partial(1/\rho)}{\partial T} \right)_p \tag{2.14}$$

which is zero in case of an incompressible liquid and 1/T for an ideal gas. Using the vector identiy

$$\frac{1}{c_p}\,\mathrm{div}[k\,\mathrm{grad}(T)] = \mathrm{div}[\frac{k}{c_p}\,\mathrm{grad}\,(T)] + k\,\frac{\mathrm{grad}(c_p)}{c_p^2}\,\mathrm{grad}(T) \tag{2.15}$$

the energy equation takes the form

$$\rho\frac{\partial T}{\partial t} + \rho\vec{u}\bullet\mathrm{grad}(T) = \mathrm{div}[\frac{k}{c_p}\,\mathrm{grad}(T)] + \frac{\beta T}{c_p}\,\{\frac{\partial p}{\partial t} + \vec{u}\bullet\mathrm{grad}(p)\} + \frac{\mu}{c_p}\Phi$$

$$+ k\,\frac{\mathrm{grad}(c_p)}{c_p^2}\bullet\mathrm{grad}(T) \tag{2.16}$$

The viscous dissipation function Φ for a Newtonian fluid in axisymmetric coordinates is given in the appendix. Assuming *constant properties*, the last term of eq.(2.16) is zero. For an *ideal gas*, this equation then becomes

$$\boxed{\rho\frac{\partial T}{\partial t} + \rho\vec{u}\bullet\mathrm{grad}(T) = \mathrm{div}[\frac{k}{c_p}\,\mathrm{grad}(T)] + \frac{1}{c_p}\,\{\frac{\partial p}{\partial t} + \vec{u}\bullet\mathrm{grad}(p)\} + \frac{\mu}{c_p}\Phi} \tag{2.17}$$

Equations (2.1), (2.10) and (2.17) provide four equations for the four independent variables are u, v, T and P. They are the complete set of equations necessary to describe the fluid flow and heat transfer in oscillating flow conditions. For irreversibility considerations entropy comes into play but no additional differential equation needs to be solved. For a single phase single substance our thermodynamic system has two degrees of freedom. We have already specified p and T. Thus s = s(P,T), and we can solve locally for s. The information content of the second law of thermodynamics is implicitly contained in the momentum and energy equations by virtue of the definition of the stress tensor and by

Fourier's law, both of which specify directions of processes. However, the differential equation for the entropy is useful to determine the amount of entropy generated in a given control volume. But since the generated entropy is a deduced quantity based upon the solution of the equations above, its derivation will be deferred to chapter 11.

Summarizing, the most important basic assumptions are listed in the following table:

Table 2.1: Basic Assumptions

- axisymmetric situation
- constant properties
- continuum
- Newtonian fluid
- Stokes hypothesis
- no body forces
- Fourier's law
- No radiation heat transfer

2.3. Dimensional Analysis

Two different physical situations are physically equivalent if the dimensionless parameters characteristical for the situation are the same. In order to obtain meaningful dimensionless parameters, proper scales for length, time, velocity, pressure and temperature have to be defined. Seume and Simon (1986a) have identified the following scales for the oscillatory flow problem:

length scale	$x_{scale} = R = D/2$	pipe radius
time scale	$t_{scale} = 1/\omega$	time for one oscillation
velocity scale	$u_{scale} = u_{m,max}$	amplitude of the mean velocity

pressure scale $\quad p_{scale} = \rho\, u_{m,max}^2$

temperature scale $\quad t_{scale} = (\Delta T)_{ref}$

Since for now we are concerned with relative temperatures and pressures only, we will subtract a reference value (T_o, p_o) from T and p. For a situation where there is a significant variation in the thermodynamic pressure as in real Stirling engines, it may be advantageous to scale the pressure with some reference pressure and not with the velocity scale (Recktenwald, 1989). The precise nature of the temperature scale $(\Delta T)_{ref}$ is yet to be determined. For the University of Minnesota oscillatory flow experiment, a suitable definition would be $(\Delta T)_{ref} = T_{wall} - T_{in}$. Using these scales and suitable reference values for the thermophysical properties, the dimensionless quantities are :

$$x = \frac{x}{R} \qquad r = \frac{r}{R} \qquad t = \omega t$$

$$u = \frac{u}{u_{m_{max}}} \qquad v = \frac{v}{u_{m_{max}}}$$

$$\Phi = \frac{R^2}{u_{m_{max}}^2}\Phi \qquad grad = R\ \mathrm{grad} \qquad div = R\ \mathrm{div}$$

$$p = \frac{p - p_o}{\rho\, u_{m_{max}}^2} \qquad P = p + \frac{2}{3}\mu\, div(\vec{u}) \qquad T = \frac{T - T_o}{(\Delta T)_{ref}}$$

$$\rho = \frac{\rho}{\rho_{ref}} \qquad \mu = \frac{\mu}{\mu_{ref}} \qquad c_p = \frac{c_p}{c_{p_{ref}}} \qquad k = \frac{k}{k_{ref}}$$

With these definitions the conservation equations of chapter 2.2 can be written in the following way.

Mass conservation:

$$Va\frac{\partial \rho}{\partial t}+\frac{1}{2}Re_{max}\,div(\rho\vec{u})=0 \tag{2.18}$$

Conservation of momentum:

$$Va\,\rho\frac{\partial \vec{u}}{\partial t}+\frac{1}{2}Re_{max}\,\rho\vec{u}\bullet grad(\vec{u})=-\frac{Re_{max}}{2}grad(P)+div[\mu\,grad(\vec{u})]+div[\mu\,grad(\vec{u})^T] \tag{2.19}$$

Energy equation:

$$Va\,\rho\frac{\partial T}{\partial t}+\frac{1}{2}Re_{max}\,\rho\vec{u}\bullet grad(T)=\frac{1}{Pr}div[\frac{k}{c_p}grad(T)]$$

$$+Va\,Ec\frac{\partial p}{\partial t}+\frac{1}{2}Re_{max}\,Ec\,\vec{u}\bullet grad(p)+Ec\Phi \tag{2.20}$$

where the dimensionless parameters are defined as:

$$Re=\frac{\rho_{ref}\,u_{m_{max}}\,D}{\mu_{ref}} \tag{2.21}$$

$$Va=\frac{\rho_{ref}\,\omega\,D^2}{4\,\mu_{ref}} \tag{2.22}$$

$$Pr=\frac{\mu_{ref}\,c_{p_{ref}}}{k_{ref}} \tag{2.23}$$

$$Ec=\frac{u_{m_{max}}{}^2}{c_{p_{ref}}\,(\Delta T)_{ref}} \tag{2.24}$$

Other, related dimensional parameters could have been be used instead, like

$$Sr = \frac{\omega D}{u_{m,max}} = 4 \frac{Va}{Re_{max}} \tag{2.25}$$

$$Ma = \frac{u_{m_{max}}}{\sqrt{\gamma \bar{R}_u/M \, T_o}} = \sqrt{\frac{1}{\gamma - 1} \frac{(\Delta T)_{ref}}{T_o} Ec} \qquad \text{(ideal gas)} \tag{2.26}$$

where $$\gamma = \frac{c_{p_{ref}}}{c_{v_{ref}}} \tag{2.27}$$

Geometric similarity is maintained if L/D is identical. For sinusoidal flow, the relative amplitude ratio, A_R, is a related and dependent similarity parameter:

$$A_R = \frac{2 \, u_{m_{max}}}{\omega \, L} = \text{... sinusoidal flow ...} = \frac{1}{2} \frac{D}{L} \frac{Re_{max}}{Va} \tag{2.28}$$

2.4. Boundary Conditions

The boundary conditions for these equations are:

	u	v	p	T
wall:	$u_{wall} = 0$	$v_{wall} = 0$	$\frac{\partial p}{\partial r} = 0$	$T_{wall} = \text{const.}$
centerline	$\frac{\partial u}{\partial r} = 0$	$v_{centerline} = 0$	$\frac{\partial p}{\partial r} = 0$	$\frac{\partial T}{\partial r} = 0$
inflow	$u_{in} = u_m$	$v_{in} = 0$	$\frac{\partial p}{\partial x} = 0$	$T_{in} = \text{const.}$
outflow	$\frac{\partial u}{\partial x} = 0$	$v_{out} = 0$	$\frac{\partial p}{\partial x} = 0$	$\frac{\partial T}{\partial x} = 0$

2.5. Operating Range of Experiment and Points of Investigation

Seume and Simon (1986a) have compiled the similarity parameters for a great number of Stirling engines. Based on this information, the test rig of the University of Minnesota was designed to cover the parameter range of most of the Sirling engines compiled. Figure 2.1 shows the operating range of the experiment . The two offset regions correspond to two different pipe diameters. Within this operating range, the points chosen for numerical investigation are marked, maintaining the lettering from the experiments of Seume (1988).

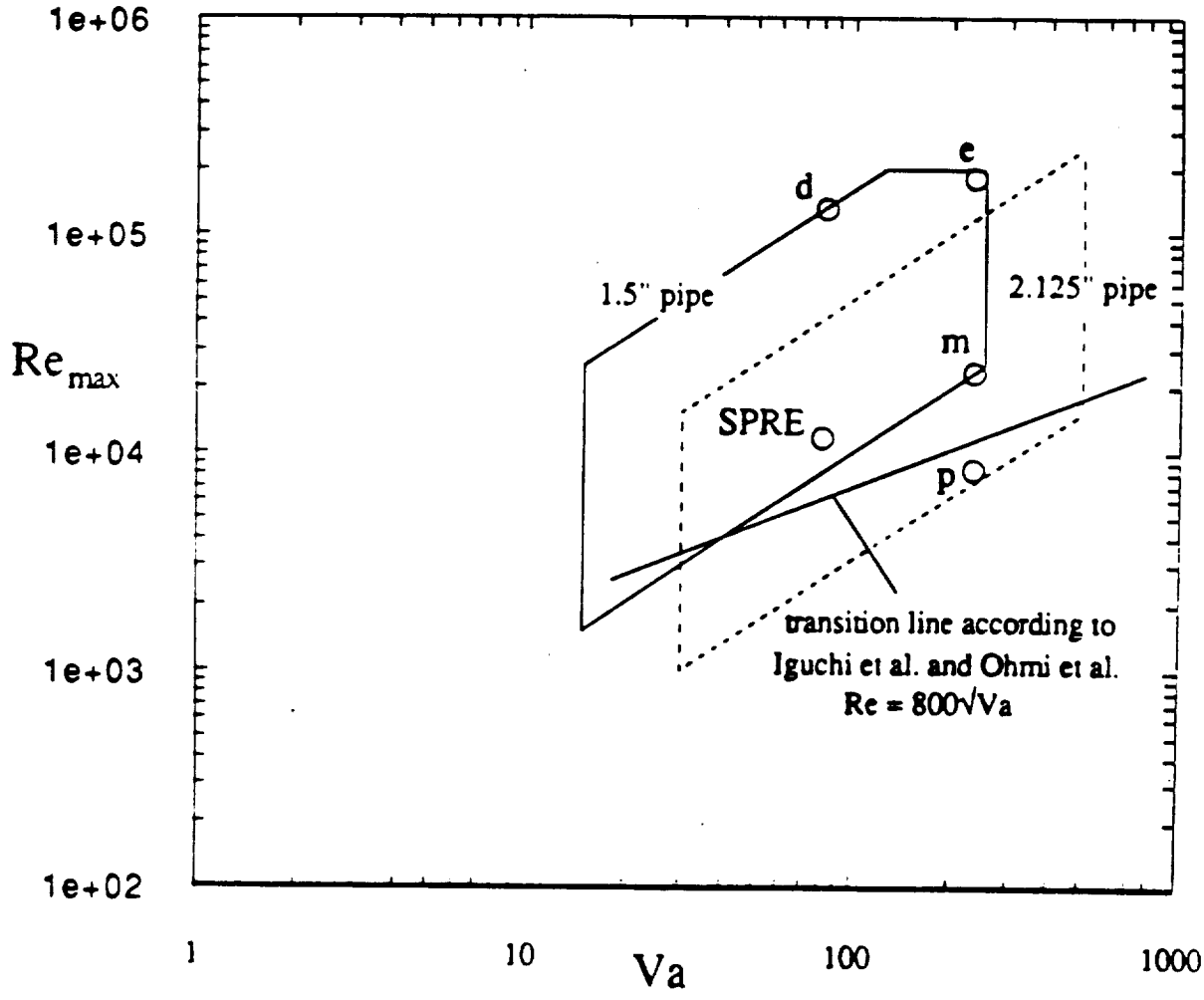

Fig. 2.1: Data points investigated

3. TURBULENCE MODELING OF OSCILLATORY FLOW

The purpose of this chapter is to document the choice of a turbulence model for further investigation and to discuss some of its already known deficiencies with respect to their impact on oscillating flow modeling.

For now, we will restrict our attention to constant density flows. Since the Cartesian tensor notation dominates the turbulence literature, it shall be adopted here.

3.1. Background

As pointed out in Chapter 2, the basic equations to describe the fluid flow and heat transfer problem are valid also in the case of turbulence. However, it can be shown that in order to solve a problem with the mathematical model of Chapter 2, $Re^{9/4}$ grid points in 3 dimensions and $Re^{3/4}$ time steps are necessary. An example of the required effort to fully simulate steady turbulent channel flow (without any turbulence model) at a Re number of 10 000 is given by Ragallo and Moin (1984): If the smallest eddies were resolved with four grid points in each direction, a total of 5×10^{10} grid points and 2000 time steps would be necessary to get to the statistical steady state. For an oscillating flow situation, a large number of cycles would have to be computed to filter out the periodic steady state. It would be impractical and excessively expensive to solve such a huge system of equations and to perform so many time steps. Even if a "direct" solution of the turbulence problem was achieved, the vast amount of generated data would have to be treated statistically, i.e. averaged, in order to provide manageable and meaningful information.

Averaging the nonlinear constituent equations instead of the results eliminates some of the mathematical problems associated with a "direct" solution, but introduces new, unknown terms for which a closure has to be found by either experiment or theory. There are several ways by which the constituent equations can be averaged. If we are interested in

the coarse structure of turbulence, a *subgrid model* is appropriate. Here, the governing equations are averaged over some small volume and time interval. The flow can be calculated on a grid greater than this small volume and time interval. It is the effect of the turbulence directly in this small volume during this time interval on the flow "seen" by the grid which has to be provided by the subgrid model. If we are interested only in time-mean values, one can average the governing equations over a long time and compute the time-averages of the flow quantities. This is usually called *Reynolds averaging*. With Reynolds averaging, the details of the turbulence structure are lost; only the effect of the turbulence on the mean flow is described. Another technique for averaging is the *renormalization group* (RNG) approach. In the RNG theory, the velocity field is first transformed into a wave-number space by a Fourier transform. The short wave-length modes from a narrow wave-vector band are then averaged and their effect on the long wave-vector modes (in which one is usually interested) is described by a renormalized viscosity. This process is repeated until all scales below a certain level of wave-lengths are eliminated. RNG theory can generate subgrid models or Reynolds averaged models, depending on what the lowest allowable level of wave-lengths should be. Details of this approach can be found in Yakhot and Orszag (1986).

Since the scope of this work is to give insights about practically useful quantities like friction coefficient and Nusselt number, the details of the turbulence structure need not be resolved. Consequently, a subgrid model was not considered in this research.

Once a decision has been made which form of averaging should be used for a given problem, there are a number of closure options for the new terms created in the averaging process. The remainder of this chapter deals with the consequences of the closure assumptions made in the chosen model.

3.2. Phase Averaged Governing Equations

The concept of time-averaging becomes more cumbersome in unsteady flows. According to Reynolds and Hussain (1972), the time independent mean flow is found by time-averaging the flow over some long time. If we are dealing with cycles (e.g. pulsatile flow), this long time must be an integer multiple of a cycle time. A time-periodic cyclic quantity is obtained by "phase" averaging, i.e. ensemble averaging at fixed times of a cycle. For completely unsteady flows, the only way an average can be obtained is ensemble averaging the results of many experiments at fixed times measured from the start of the experiment and having identical initial conditions. Since our attention is oscillatory flow, the time-mean of this flow is known to be zero, and long-time averaging is obsolete. The periodic steady state--which is the focus of this work--can be extracted from the full equations by phase-averaging.

The process of phase-averaging the equations consists of three steps: (1) decompose any transport quantity into a periodic and a randomly fluctuating part $z = \bar{z} + z'$; (2) insert the decomposed quantities into the governing equations; and (3) phase-average the equations. In the following, an apostrophe will denote a fluctuating part of a quantity, an overbar will indicate the phase average over this quantity.

With this technique one is not limited to the condition that the characteristic time of the flow must be much larger than the Kolmogorov time scale, $(\nu/\varepsilon)^{1/2}$. The emphasis is on the condition that the time behavior of the flow must have a nonrandom structure which can be recovered by proper averaging. Since this is the case even for high frequency oscillatory flows, a turbulence model may successfully be applied to this situation.

Continuity Equations:

$$\frac{\partial u_j}{\partial x_j} = 0 \qquad \frac{\partial \overline{u}_j}{\partial x_j} = 0 \qquad \frac{\partial u'_j}{\partial x_j} = 0 \tag{3.1a,b,c}$$

The phase averaged and the fluctuating velocity fields both satisfy the continuity equation independently. Since the continuity equation is linear, averaging causes no new terms in equation (3.1b). Note that new quantities would be introduced if density fluctuations were to play a role here.

Navier-Stokes Equations:

$$\rho \frac{\partial \overline{u}_i}{\partial t} + \rho \overline{u}_j \frac{\partial \overline{u}_i}{\partial x_j} + \rho \overline{u'_j \frac{\partial u'_i}{\partial x_j}} = \frac{\partial \overline{P}}{\partial x_i} + \frac{\partial}{\partial x_j}\left(\mu \frac{\partial \overline{u}_i}{\partial x_j}\right) \tag{3.2}$$

where:

Rate of change of the mean velocity

Change of mean momentum due to convective transport in *mean* velocity field

Change of mean momentum due to convective transport in *fluctuating* velocity field

Mean driving force

Diffusion of mean momentum

As can be seen from equation (3.2), the phase averaged transport equations for the mean momentum contain a term involving the unknown fluctuating velocity. If no transport

equation is solved for the momentum transport of the fluctuating momentum field, this term must be modeled with a turbulence model. However, even if transport equations are solved for these terms, these transport equations will contain other, higher order terms which originate during the averaging of those equations and which must be modeled. The point is that any type of averaging of a non-linear transport equation like the Navier-Stokes equations will lead to additional unknown terms (well-known closure problem).

Energy Equation:

$$\rho \frac{\partial \bar{T}}{\partial t} + \rho \bar{u}_j \frac{\partial \bar{T}}{\partial x_j} + \rho \overline{u'_j \frac{\partial T'}{\partial x_j}} = \frac{\partial}{\partial x_j}\left(\frac{k}{c_p} \frac{\partial \bar{T}}{\partial x_j} \right) + \frac{1}{c_p} \left(\frac{\partial \bar{p}}{\partial t} + \bar{u}_j \frac{\partial \bar{p}}{\partial x_j} + \overline{u'_j \frac{\partial p'}{\partial x_j}} \right) + \frac{\mu}{c_p} \bar{\Phi} + \rho \varepsilon \tag{3.3}$$

where ε denotes the turbulent dissipation rate defined later. Here, the third term on the LHS of equation (3.3) must be modeled as well as the pressure-diffusion term $\overline{u'_j \, \partial p'/\partial x_j}$. However, according to Mansour (1989), this term is negligible.

3.3. Turbulence Models for the Phase-Averaged Equations

It should be emphasized here that the turbulence model to predict oscillating flow should give correct answers for engineering applications. It should be as simple as possible and may very well be "custom made" for oscillating flow in a pipe and not be applicable to other situations. It is <u>not</u> the purpose of this research to find a generally valid turbulence model for any unsteady flow situation.

The turbulence models in question can be divided into two groups, i.e. those models which use the eddy viscosity concept and those which directly solve an equation for the term $\{\rho \overline{u'_j \partial u'_i/\partial x_j}\}$. The latter models are called stress models. In a differential stress model, a differential equation is derived for each component of the turbulent shear stress tensor, $\rho \overline{u_i' u_j'}$. The algebraic stress model simplifies those differential equations

sufficiently that an algebraic relation can be extracted. Among the models which use the eddy viscosity concept are the mixing length model, the k-ε model and the stream function-vorticity model.

3.3.1. Eddy Viscosity Concept

The third term on the left hand side of equation (3.2) is frequently called "Reynolds stresses" or "turbulent stresses" because it is responsible for the enhanced turbulent cross stream transport of streamwise momentum and therefore works just like the diffusion of momentum which stems from the viscous stresses. This similarity between the laminar diffusion and the turbulent diffusion-like convection is the basis of a simple, old, yet very successful turbulence concept, the eddy viscosity concept (EVC). Noting that for now $\partial\overline{u_j}/\partial x_j = 0$, we can transform this term as

$$\rho\,\overline{u'_j\frac{\partial u'_i}{\partial x_j}} = \frac{\partial}{\partial x_j}\left(\rho\overline{u'_i u'_j}\right) = -\frac{\partial}{\partial x_j}(\tau'_{ij}) \tag{3.4}$$

According to Boussinesq (1877), the Reynolds stresses can be expressed just like viscous stresses, but with a different diffusivity, called the eddy viscosity μ_t:

$$-\rho\overline{u'_i u'_j} = \mu_t\left(\frac{\partial\overline{u_i}}{\partial x_j} + \frac{\partial\overline{u_j}}{\partial x_i}\right) - \frac{2}{3}\rho\,k\,\delta_{ij} \qquad \text{EVC} \tag{3.5}$$

This equation represents the eddy-viscosity concept, in which k stands for the turbulent kinetic energy, defined as

$$k \equiv \frac{1}{2}\left(\overline{u'^2} + \overline{v'^2} + \overline{w'^2}\right) \tag{3.6}$$

and δ_{ij} is the Kronecker delta in tensor form. The last term in eq. (3.5) can be absorbed in the pressure term without loss of generality[1]. For an arbitrary scalar transport variable ϕ, the EVC can be written as

$$-\rho\overline{u'_j\phi'} = \frac{\mu_t}{\sigma_\phi}\frac{\partial\bar{\phi}}{\partial x_j} \tag{3.7}$$

where σ_ϕ is the appropriate turbulent Prandtl number.

Following the analogy used here, the turbulent motion is analogous to the molecular, the "turbulent eddy " is the analogy for the molecule and, after Prandtl, the analogy to the mean free path is the so-called mixing length. From kinetic theory it is known that the dynamic viscosity is proportional to the mean speed of a molecule times the mean free path. Consequently, the turbulent viscosity can be expressed as

$$\nu_t \sim \hat{U}_{scale} \cdot \hat{L}_{scale} \tag{3.8}$$

The problem is now reduced to finding appropriate velocity and length scales and a proportionality constant in order to determine μ_t. Once μ_t is known, the Reynolds stresses can be evaluated with (3.5) and the Navier-Stokes equations can be solved. Some consequences of the EVC are discussed in section 3.3.6..

3.3.2. Mixing Length Model

The mixing length model, introduced by Prandtl in 1925, is still widely used today in industry and shall therefore be reviewed for its applicability in oscillating pipe flow. It uses the eddy viscosity concept of equation (3.5) and can be summarized as follows:

- length scale = mixing length l_m ; needs to be specified from empirical information

---

[1] Then, the modified pressure of equ. (2.9) becomes $P \equiv p + 2/3\,[\mu\,\mathrm{div}(\vec{u}) + \rho k]$

- velocity scale $= l_m \left(\left(\frac{\partial \overline{u_i}}{\partial x_j} + \frac{\partial \overline{u_j}}{\partial x_i} \right) \frac{\partial \overline{u_i}}{\partial x_j} \right)^{1/2}$ (3.9)

- Proportionality constant = 1.0

For a 2-dimensional boundary layer type situation, the Reynolds stresses then become:

$$- \overline{u'_i u'_j} = l_m^2 \left| \frac{\partial \overline{u_1}}{\partial x_2} \right| \frac{\partial \overline{u_1}}{\partial x_2} \qquad (3.10)$$

The main features of this model are:

+ good results for simple flows
+ simple to implement
+ economical
- for complex flows, it is difficult to specify l_m
- does not take transport of turbulence into account
- not suitable for rapidly developing flows and recirculating flows

Because of the shortcomings outlined above, the mixing length model cannot be used in this study.

3.3.3. Comparative Computational Tests of Various Turbulence Models

Presently, there are many versions of k-ε models and stress models available, and it is not obvious which model is best suited for the given task. However, most recently, a number of researchers conducted exhaustive tests of various turbulence models for the Reynolds-averaged Navier-Stokes equations.

Patel, Rodi and Scheurer (1985) examined and tested 8 turbulence models for turbulent flow past a flat plate with and without pressure gradient. The models investigated were the k-ε models of Chien (1982), Dutoga and Michard (1981), Hassid and Poreh (1978), Hoffmann (1975), Lam and Bremhorst (1981), Launder and Sharma (1974), Reynolds (1976) and the k-ω model of Wilcox and Rubesin (1980). All those models are based on the eddy-viscosity concept. Patel et. al. found that the models of Chien, Lam and Bremhorst, Launder and Sharma and Wilcox and Rubesin gave comparable results and were decidedly better than the others. For turbulence model modifications it seems desirable that a model bears an immediate relationship with physically measurable quantities. This, however, is not the case for the Wilcox and Rubesin model.

Henkes and Hoogedoorn (1989) did a similar performance evaluation of turbulence models for natural convection flows along a vertical flat plate. They investigated the k-ε models of Chien (1982), Hassid and Poreh (1978), Hoffman (1975), Jones and Launder (1972), Lam and Bremhorst (1981), Reynolds (1976) and To and Humphrey (1975) as well as the high-Reynolds number k-ε model. Additionally, they investigated the algebraic stress model of Cebeci and Smith (1974). Their findings were similar to those of Patel et. al. (1985): Overall, the models of Chien (1982), Jones and Launder (1972) and Lam and Bremhorst (1981) showed the best results. It is remarkable that the algebraic stress model by Cebeci and Smith gave significantly worse predictions than the k-ε model above.

Martinuzzi and Pollard (1989) compared turbulence models for steady turbulent fully developed pipe flow at Re numbers of 10000, 38000, 90000 and 380000. They compared the high-Reynolds number k-ε model, the Lam-Bremhorst low-Re number model and four variants of an algebraic stress model (the ones of Launder et. al. (1975) and Naot et. al. (1970), both for with and without wall functions). They showed that the low-Re number k-ε model gave the best results and claimed that the use of algebraic stress models should be confined to high Re numbers or regions where there is only moderate shear.

In a 1985 paper, Kebede, Launder and Younis investigated whether a differential stress model applied to pulsatile flow yielded better results than the conventional EVC. They conclude that the EVC with k-ε model has the best performance near the wall. A one-equation EVC model lead to rather large phase *leads* of $\overline{u'v'}$ as compared to the experiment, while the differential stress model produced a too large phase *lag*.

Conclusions. On the basis of these tests, stress models did not yield superior results to models using the eddy viscosity concept. Moreover, since stress models are also more complicated to implement and more expensive to run, a stress model shall not be used in this work. The models of Jones and Launder (1972) (or the updated version by Launder and Sharma, 1974), Chien (1982) and Lam and Bremhorst (1981) seem to be the most versatile and reliable. Of those, the Lam-Bremhorst model is the only one which uses the true isotropic turbulent dissipation rate itself and is the easiest to implement computationally. Therefore we have chosen the Lam-Bremhorst model for further investigation.

3.3.4. The Lam-Bremhorst Form of the k-ε Model

The k-ε model uses the eddy viscosity concept , but different scales than the mixing length model. Whereas it has long been agreed on that $\sqrt{k}$ represents a well chosen velocity scale for the large scale motion[1], many attempts have been made to conveniently specify a length scale. Mainly because of simple boundary conditions the use of ε as a quasi-length scale[2] became very common. Even though the turbulent dissipation occurs at the smallest scales, ε is a quasi-length scale for the large scale motion. It is defined as:

---

[1] It is known that the turbulent kinetic energy is contained mainly in the large scale eddies. Therefore $\sqrt{k}$ is a velocity scale for the large scale turbulent motion.

[2] $$\varepsilon \sim \frac{\text{kinetic energy}}{\text{charact. time}} = \frac{k}{\sqrt{k}/L} = \frac{k}{\sqrt{k}\,L} = \frac{k^{\frac{3}{2}}}{L} \quad \Rightarrow \quad \varepsilon \sim L^{-1}$$

$$\varepsilon = \nu \overline{\left(\frac{\partial u'_i}{\partial x_j} + \frac{\partial u'_j}{\partial x_i} \right) \frac{\partial u'_i}{\partial x_j}} \qquad (3.11)$$

From here on, we will only be concerned with the isotropic part of ε:

$$\varepsilon = \nu \overline{\frac{\partial u'_i}{\partial x_j} \frac{\partial u'_i}{\partial x_j}} \qquad (3.12)$$

In the k-ε model, two additional partial differential equations for the turbulent kinetic energy and the turbulent dissipation rate are derived by manipulating the full, time-dependent Navier-Stokes equations. The resulting equations for k and ε contain some terms which must be modeled. The hypotheses and assumptions going into this closure were examined most recently by Mansour (1989) and shall not be discussed here. It may, however, be pointed out here that if a far reaching modification of the k-ε model proves to be necessary for oscillatory flows, the closure assumptions themselves will be up for discussion. In his paper, Mansour pointed out that the existing models for the ε equation should be improved near the wall.

Harlow and Nakayama (1967) were the first to introduce a k-ε model, but their model did not predict turbulent pipe flow well. Jones and Launder (1972, 1973) proposed a different k-ε model which gave good results for a great number of flows. Based on the model of Jones and Launder, a number of modified low-Re number forms have been proposed by various researchers. All of these different forms use the same, generally agreed on closure assumptions for the exact equations for k and ε. The difference between them is how the boundary conditions are introduced and how the wall functions are formulated. The particular formulation of Lam and Bremhorst (1981) offers the advantage that no additional terms are added to the k or ε equation in case of low turbulence levels. As mentioned above, this version will be adopted here for further work and is shown in Table

3.1. For a more thorough discussion of the differences between the Jones/Launder and the Lam/Bremhorst models, the reader is referred to the work of Schmidt and Patankar (1987).

The so-called high-Reynolds number model (HRN) is a special case where the functions f_μ, f_1 and f_2 are set to 1. However, in case of fully turbulent flow where the turbulence Reynolds numbers R_k and R_t are high, those functions asymptotically approach unity. The real difference between the HRN and the low-Reynolds number model (LRN) is due to the boundary conditions.

Boundary Conditions for the HRN Model.

centerline	Neumann boundary condition	$\partial k/\partial r = 0$	$\partial \varepsilon/\partial r = 0$
inflow	Dirichlet boundary condition		
outflow	Neumann boundary condition	$\partial k/\partial x = 0$	$\partial \varepsilon/\partial x = 0$
wall	take guidance from the law of the wall and set the near wall viscosity to $\mu_t = \mu y^+/u^+$ where $u_\tau = c_\mu^{0.25}\, k^{0.5}$		
	Neumann boundary condition for k	$\partial k/\partial r = 0$	
	Dirichlet Boundary condition for ε	$\varepsilon = u_\tau^3/\kappa y$	

Boundary Conditions for the LRN Model.

Same as above for centerline, inflow and outflow.

wall	Dirichlet and Neumann boundary condition for k		$k=0$, $\partial k/\partial r = 0$
	Neumann boundary condition for ε	$\partial \varepsilon/\partial r = 0$	

Table 3.1: The Lam-Bremhorst Form of the k-ε Turbulence Model

EVC	$\nu_t = \text{const.} \cdot \hat{U}_{scale} \cdot \hat{L}_{scale}$
Prandtl Kolmogorov Expression	$\nu_t = c_\mu f_\mu \quad k^{1/2} \quad \frac{k^{3/2}}{\varepsilon} = c_\mu f_\mu \frac{k^2}{\varepsilon}$ (3.13)

Rate of Change	Convection	Diffusion	Generation	Destruction
$\rho \frac{\partial k}{\partial t}$	$+ \rho \overline{u}_j \frac{\partial k}{\partial x_j}$	$= \frac{\partial}{\partial x_j}\left(\frac{\mu_t}{\sigma_k}\frac{\partial k}{\partial x_j}\right)$	$+ \rho G$	$- \rho \varepsilon$ (3.14)
$\rho \frac{\partial \varepsilon}{\partial t}$	$+ \rho \overline{u}_j \frac{\partial \varepsilon}{\partial x_j}$	$= \frac{\partial}{\partial x_j}\left(\frac{\mu_t}{\sigma_\varepsilon}\frac{\partial \varepsilon}{\partial x_j}\right)$	$+ c_1 f_1 \rho G \frac{\varepsilon}{k}$	$- c_2 f_2 \rho \frac{\varepsilon^2}{k}$ (3.15)

Constant	c_μ	c_1	c_2	σ_k	σ_ε
Value	0.09	1.92	1.44	1.0	1.3

$$G \equiv -\overline{u'_i u'_j}\frac{\partial \overline{u}_i}{\partial x_j} = \nu_t\left(\frac{\partial \overline{u}_i}{\partial x_j} + \frac{\partial \overline{u}_j}{\partial x_i}\right)\frac{\partial \overline{u}_i}{\partial x_j} \quad (3.16a,b)$$

HRN model: $f_\mu = f_1 = f_2 = 1.0$

LRN model:

$$f_\mu = \left(1 - \exp(-0.0163\, R_y)\right)^2 \left(1 + \frac{20}{R_t}\right) \quad (3.17)$$

$$f_1 = 1 + \left(\frac{0.055}{f_\mu}\right)^3 \quad (3.18)$$

$$f_2 = 1 - \exp(-R_t^2) \quad (3.19)$$

$$R_t = \frac{k^2}{\nu \varepsilon} \quad (3.20)$$

$$R_y = \frac{\sqrt{k}\, y}{\nu} \quad (3.21)$$

3.3.5. Evaluation of the Constants in the k-ε Model

There are 5 empirical constants for the model, c_μ, c_1, c_2, σ_k, σ_ε. In order to judge whether the customarily used values of those constants are applicable also for oscillatory flows, it is useful to examine how these constants were determined for fully turbulent flow ($f_\mu = f_1 = f_2 = 1$).

$\boxed{c_\mu}$. The closure for G, Eq. (3.16b), applied to thin shear layers, yields

$$\frac{\partial \overline{u_i}}{\partial x_j} = - \frac{\overline{u'_i u'_j}}{\nu_t} \tag{3.22}$$

Substitution of (3.22) into the definition of G, Eq.(3.16a), leads to

$$G = \frac{\overline{u'_i u'_j}^2}{\nu_t} = \frac{\overline{u'_i u'_j}^2}{c_\mu \frac{k^2}{\varepsilon}} \tag{3.23}$$

For local equilibrium layers the generation and destruction of turbulent kinetic energy are in balance:

$$G = \varepsilon \tag{3.24}$$

Thus ε cancels and

$$c_\mu = \left(\frac{\overline{u'_i u'_j}}{k} \right)^2 \tag{3.25}$$

The square root of the quantity of the right hand side was measured by Champagne, Harris and Corrsin (1970) to be approximately 0.3. Hence $c_\mu = 0.09$.

c_2. Batchelor and Townsend (1948) found that for grid generated turbulence at high Re numbers, k is inversely proportional to the distance to the grid,

$$k \sim 1/x_1 \qquad \text{or} \qquad k = \gamma\, 1/x_1 \qquad \gamma = \text{const.} \tag{3.26}$$

The transport equation for steady flow past a turbulence grid is

$$\overline{u_1}\,\frac{\partial k}{\partial x_1} = -\varepsilon \tag{3.27}$$

Together with Eq. (3.26) this becomes

$$\varepsilon = \gamma\,\overline{u_1}\,x_1^{-2} \tag{3.28}$$

The transport equation for ε behind the grid is

$$\overline{u_1}\,\frac{\partial \varepsilon}{\partial x_1} = -c_2\,\frac{\varepsilon^2}{k} \tag{3.29}$$

Inserting Eq.(3.28) into (3.29) shows that $c_2 = 2$. Later on, c_2 is adjusted to 1.92.

c_1. Near the wall Eq. (3.24) holds approximately and the universal law of the wall may be assumed:

$$u^+ = \frac{\ln(9y^+)}{\kappa} \tag{3.30}$$

$$u^+ = \frac{\overline{u_1}}{u_\tau} \qquad y^+ = \frac{u_\tau\, y}{\nu} \qquad u_\tau = \sqrt{\frac{\tau_w}{\rho}} \tag{3.31a,b,c}$$

where u^+ is the normalized velocity and y^+ is the dimensionless wall distance and u_τ is the friction velocity.

Neglecting the convective terms, using Eq. (3.24), and substituting ν_t from (3.13), the transport equation for ε becomes

$$\frac{\partial}{\partial x_2}\left(\frac{c_\mu k^2}{\sigma_\varepsilon \varepsilon}\frac{\partial \varepsilon}{\partial x_2}\right) + (c_1 - c_2)\frac{\varepsilon^2}{k} = 0 \tag{3.32}$$

Equation (3.24) alone, combined with the definition for G, Eq. (3.16), yields another equation for ε. Assuming that near the wall the shear stress is approximately equal to the wall shear stress and using the definition for u_τ from (3.31a), we can write

$$\varepsilon = u_\tau^2 \frac{\partial \overline{u_1}}{\partial x_2} \tag{3.33}$$

With this, (3.32) becomes:

$$\frac{\partial}{\partial x_2}\left(\frac{c_\mu k^2}{\sigma_\varepsilon}\frac{\partial^2 \overline{u_1}/\partial x_2^2}{\partial \overline{u_1}/\partial x_2}\right) + (c_1 - c_2)\frac{u_\tau^4 \left(\partial \overline{u_1}/\partial x_2\right)^2}{k} = 0 \tag{3.34}$$

Using the law of the wall (3.30), the velocity gradients are evaluated as

$$\frac{\partial \overline{u_1}}{\partial x_2} = \frac{u_\tau}{\kappa x_2} \qquad \frac{\partial^2 \overline{u_1}}{\partial x_2^2} = -\frac{u_\tau}{\kappa x_2^2}$$

From experimental data (e.g. Laufer 1954) it is known that $k = 3.5\, u_\tau^2$. Then Eq. (3.34) can be solved for c_1:

$$c_1 = c_2 - \frac{\kappa^2 c_\mu 3.5^3}{\sigma_\varepsilon} \tag{3.35}$$

For $c_2 = 1.92$, $\kappa = 0.4$ and $\sigma_\varepsilon = 1.3$, c_1 is determined as 1.44.

Alternatively, from Eq. (3.25), is is known that $k = u_\tau^2 c_\mu^{-0.5}$. Then, Eq. (3.35) can be rewritten as

$$c_1 = c_2 - \frac{\kappa^2}{\sigma_\varepsilon \sqrt{c_\mu}} \tag{3.36}$$

Rodi and Scheurer (1986) argue that the assumption about the wall shear stress leading to Eq. (3.33) is not realistic for adverse pressure gradient flows.

σ_k and σ_ε. The two Prandtl numbers were first assumed to be close to unity[1]. Then "... *many calculations were performed in which the constants were systematically varied. The values chosen are those which we believed gave the best overall agreement for the flows considered* "[2]. However, the flows considered were all steady flows. It seems likely that a tuning of the turbulent Prandtl numbers to unsteady flows might yield different results. But in turbulent pipe flows, the most dominant terms in the k and ε equation are the production and destruction terms. Therefore it seems unlikely that a moderate change in σ_k and σ_ε has a significant effect on the overall results.

Conclusions. The constants are determined for fully turbulent flow in the near wall region for simplified equilibrium situations. Even though c_1 is not specifically derived for steady flows, based on the observations of Rodi and Scheurer (1986), it appears likely that this constant is affected by the unsteadiness of the flow. The values for σ_k and σ_ε are tied to steady flow experiments, but it is believed that the impact of a variation of their values is small.

---

[1] W. Rodi (1984) in **Turbulence Models and Their Application in Hydraulics: a State of the Art Review**, 2nd ed., Int. Assoc. for Hydr. Res., Delft, p.28

[2] K. Hanjalic and B.E. Launder (1972) in J. Fluid Mech, v.52, part.4, p.619

3.3.6. Discussion of Some Obvious Shortcomings of the Turbulence Model Chosen

Even though the eddy viscosity concept contains many crucial assumptions, the measurements of Seume (1988) clearly indicate that the turbulent transport is proportional to the level of fluctuations and suggest that some kind of EVC seems to be appropriate for oscillating flows.

A troublesome assumption of the EVC underlying the k-ε model is the stress-strain response time. Commonly, turbulence is seen as a cascade process in which energy is transferred from the mean flow field to ever smaller eddies. At the end of this cascade process dissipation of this energy into molecular motion takes place. The amount of energy dissipated depends on the large scale motion, whereas the scale at which this dissipation occurs depends on the molecular viscosity. Clearly, this cascade process takes time in reality. However, the eddy viscosity concept as used here disregards this fact. With the EVC, a change in the large scale mean flow causes an immediate response in the turbulent stresses which are due to the action of the smaller scale motion. For strongly unsteady flows it seems to be absolutely necessary to modify the EVC in order to incorporate a relaxation time. Such proposals have been made in the literature. Shemer et al. (1985) proposed that the eddy viscosity should be a complex number and mentioned earlier successful computations with such a model. Iguchi et al. (1985b) proposed a model for the axial component of the fluctuating velocity u'_{rms} which took the phase lag between u_m and u'_{rms} into account. However, this model required the experimental measurement of the phase lag which is impractical.

The eddy viscosity concept hinges on the assumption of local isotropy of turbulence, i.e. that the turbulence structure is locally independent of direction. It is known that this condition is frequently not satisfied. Especially in low Re number flows, where the large scale and the small scale are not far apart, the assumption of local isotropy seems physically questionable. Despite that, turbulence models using the eddy viscosity concept have proven

to be highly successful in recent years. One reason for this could be that strongly anisotropic turbulent eddies have little influence on the main velocity field, a theory which is supported by Yakhot and Orszag (1986). Moreover, as Yakhot and Orszag (1986) argue, the effects of anisotropy might be asymptotically small and may be neglected. Rodi (1984) asserted that "*in recirculating flows where the normal stress and shear-stress terms in the momentum equations are of the same order, both terms are often small compared with the inertial and pressure-gradient terms so that isotropy of the turbulence model is of little importance*"[1].

Rodi and Scheurer (1986) have found that the predictions with the k-ε model become rather poor for a flat plate boundary layer for the case of a strong adverse pressure gradient and suggest a modification to the model to overcome this difficulty. They showed that the problem of the LRN model to predict strongly adverse-pressure-gradient flat plat boundary layers satisfactorily stemmed from the near wall region. The problem was traced to a too small generation rate of ε in the near wall region which leads to an oversized length scale and too high turbulent viscosities. However, the results of this study indicated that a modification of the k-ε model as proposed by Hanjalic and Launder (1980) worked well for adverse pressure gradient situations on a flat plate.

Even though Rodi and Scheurer's findings uncover a serious problem in the k-ε model, they cannot be used directly for oscillatory pipe flow. First, the convective deceleration over a flat plate does *not* translate easily into the local deceleration experienced in pipe flow. In their study, the flow over the flat plate was steady at a fixed point in space. Here, the cascade process is statistically steady. Viewing the flow from a Lagrangian point of view, the decelerated fluid particle travels through regions of steady cascade processes for which the EVC applies fairly well. On the contrary, during a local deceleration of the flow, the shortcoming of the EVC will affect the predictions directly. Second, the extension of the Hanjalic and Launder proposal rests on the condition that the irrotational contribution

---

[1] W. Rodi (1984) in **Turbulence Models and Their Application in Hydraulics: a State of the Art Review**, 2nd ed., Int. Assoc. for Hydr. Res., Delft, p. 30

$\partial u_m/\partial x$ of the generation term G in the ε equation is (i) retained[1] and (ii) multiplied by a higher constant than the rotational part. In our computational scheme, the irrotational contribution is always retained and the presence of a $\partial u_m/dx$ quantity does *not* give the desired response to a local deceleration $\partial u_m/\partial t$. Nor do we have the freedom to just replace $\partial u_m/dx$ by $1/u_m\ \partial u_m/\partial t$.

However, following the general ideas of Rodi and Scheurer (1986), a plausible modification of the k-ε model would be the addition of an deceleration or acceleration term to the generation term of the ε equation. One definition of such a term is

$$G_{\varepsilon,accel} \equiv \varepsilon\, K_a \tag{3.37}$$

where K_a is a dimensionless acceleration parameter defined as[2]

$$K_a = \frac{\mu}{\rho u_m(t)^3} \frac{du_m(t)}{dt} \tag{3.38}$$

Then, equation (3.15) becomes

$$\rho \frac{D\varepsilon}{Dt} = \frac{\partial}{\partial x_j}\left[\frac{\mu_t}{\sigma_\varepsilon}\frac{\partial \varepsilon}{\partial x_j}\right] + c_1 f_1 \rho \frac{\varepsilon}{k}[G + c_3 K_a \varepsilon] - \rho\varepsilon \tag{3.39}$$

where D/Dt is the substantial derivative and c_3 is a new constant which has to be scaled against experimental data.

---

[1] Hanjalic and Launder (1980) as well as Rodi and Scheurer (1986) used boundary layer codes which usually negelct terms like $\partial u_m/dx$.

[2] Iguchi et al. (1986a) defined another acceleration parameter as $K^* = \frac{0.545\,\mu}{\rho U(t)^3}\left(\frac{du_m(t)}{dt} + \frac{\lambda_{qs}}{2D} u_m^2\right)$ where λ_{qs} is the time dependent quasi-steady friction factor. It remains to be seen whether the use of this parameter would yield better results.

Before any modification is recommended, the results of the unmodified chosen model must carefully be analyzed. Only if a clear need for a modification is indicated, should it be pursued.

3.4. Summary

The k-ε model discussed here is based on the eddy viscosity concept and uses two additional transport equations for the velocity scale and the turbulent length scale. It is given in the form of general unsteady transport equations. In its derivation, no specific assumptions about steady flow have been made. It accounts for the convective transport of turbulence. While the HRN version relies on the validity of the universal law of the wall, the LRN does not. Both the HRN and the LRN models are thoroughly tested and have shown, especially the LRN version, good results for a great many flow situations. In the derivation of the model, no specific assumptions have been made about the steadiness of the flow. Therefore this model is, in principle, applicable for unsteady situations and is used for further investigation.

4. NUMERICAL METHOD FOR THE SOLUTION OF THE GOVERNING EQUATIONS

The elliptic partial differential equations together with the boundary conditions and the assumptions given in Chapter 2 give a complete mathematical description of the problem. However, since this set of coupled differential equations cannot be solved analytically, numerical methods are needed. Any numerical method has two basic steps: First, the differential equations must be transformed to a set of algebraic equations by discretizing them. Second, this set of algebraic equations has to be solved. In this chapter, those two steps will be outlined.

The aim of this chapter is (i) to document the discretization method used here, in particular the time discretization developed in this study, (ii) to describe the solution techniques investigated and (iii) to discuss criteria for convergence.

4.1. Discretization Method

4.3.1. General Discretization

Many methods to discretize differential equations have been proposed. Among the most prominent discretization methods are the finite difference method, the finite element method and collocation method. For a more detailed overview the reader is referred to Shadid (1989), who gives an excellent classification of the individual methods. According to Patankar (1988), so far no method can be claimed to be superior. The method employed in this work is the finite volume method which is closely related to finite difference method. Here, the governing equations are integrated over a small control volume. For completeness the standard features of this technique will be outlined. A thorough treatment of the finite volume discretization technique can be found in Patankar (1980). However, the

validity of the method shown there is extended here to variable-density time-dependent convective-diffusive situations. This extension will be shown in detail.

The first important step for an efficient treatment of a set of partial differential equation is to cast all differential equations into one general form. Then, only one algorithm is needed for virtually all dependent variables. For any scalar transport variable, the rate of change in a control volume must equal the net inflow into the control volume plus the rate of generation of this scalar within the control volume. The net inflow is the sum of the convective and the diffusive inflow. Then,we can write for the generalized scalar ϕ in an infinitesimal control volume[1]:

$$\frac{\partial(\rho\phi)}{\partial t} + \mathrm{div}(\rho\vec{u}\,\phi - \Gamma_\phi \,\mathrm{grad}\,\phi) = S \qquad (4.1)$$

Here, the second term on the left hand side is the sum of the convective and diffusive transport transport *out of* the control volume. Γ is the general diffusion coefficient for the variable ϕ and S denotes a source term which stands originally for the rate of generation of the scalar ϕ. However, without loss of generality we will take the freedom to cast everything which does not fit on the left hand side of the equation into this source term. Equations (2.1), (2.9) and (2.13) can be recovered from equation (4.1) by choosing the appropriate quantities for ϕ, Γ and S which are given in Table 4.1.

[1] In this chapter, we will drop the overbar for the phase averaged quantities. Unless otherwise specified, reference to a quantity will then be to the phase averaged quantity.

Table 4.1: Interpretations of ϕ, Γ and S for the governing equations

Name	Equation	ϕ	Γ	S
Continuity	2.1	1	0	0
x-Momentum	2.10	u	μ_{eff}	$-\frac{\partial P}{\partial x} + \text{div}(\mu_{eff}\,[\text{grad}(u)]^T)$
r-Momentum	2.10	v	μ_{eff}	$-\frac{\partial P}{\partial r} + \text{div}(\mu_{eff}\,[\text{grad}(v)]^T)$
Energy	2.17	T	$\frac{k}{c_p} + \frac{\mu_t}{\sigma_T}$	$\frac{\partial p}{\partial t} + \vec{u}\,\text{grad}(p) + \mu\phi + \rho\varepsilon$
Turb. Kin. Energy	3.14	k	$\frac{\mu_t}{\sigma_k}$	$\rho G - \rho\varepsilon$
Turb. Diss. Rate	3.15	ε	$\frac{\mu_t}{\sigma_\varepsilon}$	$c_1 f_1 \rho G \frac{\varepsilon}{k} - c_2 f_2 \rho \frac{\varepsilon^2}{k}$

Now, the calculation domain Ω is divided into a number of finite control volumes which constitute the computational grid. This grid may be different for each dependent variable. As shown by Patankar (1980) it is advantageous to use a "staggered grid" for each velocity component and a "main grid" for all other variables. The values of the dependent variables will be evaluated at the center of their respective control volumes. Figure 4.1. shows a typical grid and a typical control volume cluster and gives the nomenclature for the following derivations. Denoting the flux vector of the variable ϕ for an infinitesimal control volume interface as $\vec{J}$, equation (4.1) may be rewritten as

$$\frac{\partial(\rho\phi)}{\partial t} + \text{div}(\vec{J}) = S \tag{4.2}$$

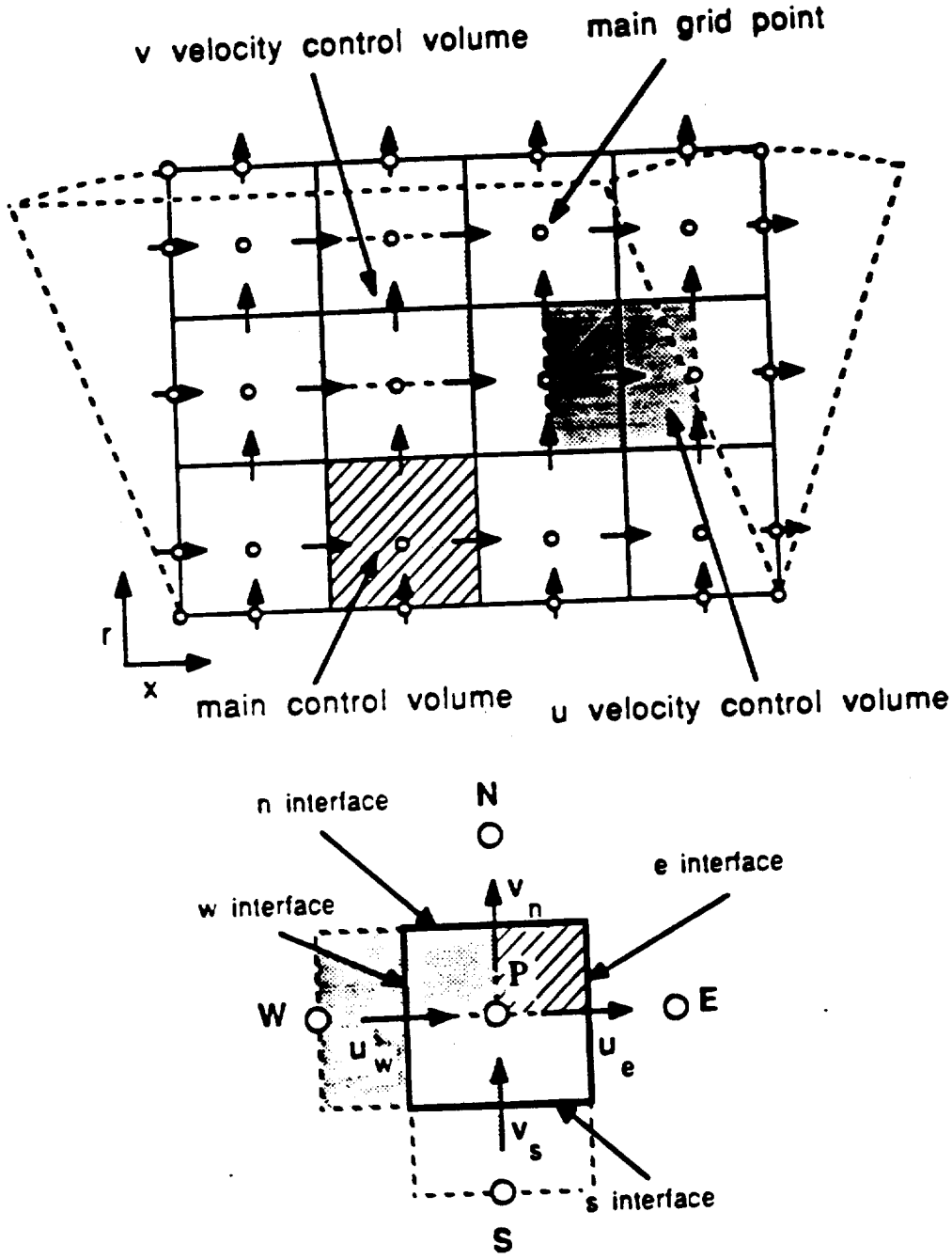

Figure 4.1: The staggered grid and details of the typical control volumes

This equation may be integrated in space over the finite control volume[1] and in time as

$$\int_s^n \int_w^e \int_t^{t+\Delta t} \frac{\partial(\rho\phi)}{\partial t}\, dt'\, dx'\, rdr' + \int_t^{t+\Delta t} \int_s^n \int_w^e \mathrm{div}(\vec{J})\, dx'\, rdr'\, dt' = \int_t^{t+\Delta t} \int_s^n \int_w^e S\, dx'\, rdr'\, dt' \tag{4.3}$$

Now we express the time integral over any quantity z as the product of the mean value of z during the time step times the length of the time step Δt,

$$\int_t^{t+\Delta t} z(t)\, dt' \equiv \bar{z}\, \Delta t \tag{4.4}$$

To evaluate the individual terms in equation (4.3) a number of profile assumptions must be made with respect to the variation of the variables to be integrated. First, we assume that the mean value $\bar{z}$ is some "mix" of the old time value and the new time value,

$$\bar{z} \equiv f\, z_{t+\Delta t} + (1-f)\, z_t \tag{4.5}$$

Here, f is a "time integration factor" which may be different for each dependent variable and for each control volume. For now we will assume that f is a constant for each dependent variable. Later we will present a scheme which uses locally variable time integration factors.

Second, for the first term on the left hand side and for the right hand side of equation (4.3) we suppose that the quantities $\rho\phi$ and S are constant over the control volume. Then, the integrated form of equation (4.3) can be written as

[1] Note that the third dimension of the control volume is set to unity in the 2-D formulation. Therefore, $dV = dA\, dx$ where $dA = rdr$.

$$\frac{\rho_P\phi_P - \rho_P^\circ\phi_P^\circ}{\Delta t}\Delta V + f_1\,\Sigma J + (1-f_1)\,\Sigma J^\circ = f_1 S + (1-f_1)\,S^\circ \qquad (4.6)$$

where f_1 is the time integration factor for the ϕ equation and S denotes the volume integrated source term. The superscript $^\circ$ denotes the known values at time t, whereas the absence of a superscript indicates the new time level $t+\Delta t$. The term ΣJ is defined as

$$\Sigma J \equiv J_e - J_w + J_n - J_s \qquad (4.7)$$

ΣJ° is defined similarly and indicates the net outflow of the integrated fluxes of the variable ϕ at time t.

In the same manner, the continuity equation may be integrated with another, still arbitrary time integration factor f_2:

$$\frac{\rho_P - \rho_P^\circ}{\Delta t}\Delta V + f_2\,\Sigma F + (1-f_2)\,\Sigma F^\circ = 0 \qquad (4.8)$$

where

$$\Sigma F \equiv F_e - F_w + F_n - F_s \qquad (4.9)$$

Here, ΣF and ΣF° stand for the sum of the integrated mass fluxes at the time levels $t+\Delta t$ and t, respectively.

According to Patankar (1980) we define:

$$J_e - F_e\,\phi_P = a_E\,(\phi_P - \phi_E) \qquad (4.10)$$

$$a_E = D_e\,A(|Pe_e|) + \max[-F_e, 0] \qquad (4.11)$$

$$J_e^\circ - F_e^\circ \phi_P^\circ = a_E^\circ (\phi_P^\circ - \phi_E^\circ) \tag{4.12}$$

$$a_E^\circ = D_e^\circ A(|Pe_e^\circ|) + \max[-F_e^\circ, 0] \tag{4.13}$$

$$J_w - F_w \phi_P = - a_W (\phi_P - \phi_W) \tag{4.14}$$

$$a_W = D_w A(|Pe_w|) + \max[-F_w, 0] \tag{4.15}$$

$$J_w^\circ - F_w^\circ \phi_P^\circ = - a_W^\circ (\phi_P^\circ - \phi_W^\circ) \tag{4.16}$$

$$a_W^\circ = D_w^\circ A(|Pe_w^\circ|) + \max[-F_w^\circ, 0] \tag{4.17}$$

$$Pe_i = \frac{F_i}{D_i} \quad , i = e, w, n, s \tag{4.18}$$

$$A(|Pe_i|) = \max\left[0, (1-0.1|Pe_i|)^5\right] \quad , i = e, w, n, s \tag{4.19}$$

where D is the integrated diffusion flux across a control volume interface and Pe is the Peclet number associated with this interface.

The definitions for a_N , a_N°, a_S and a_S° are analogous. Furthermore it is

$$a_i = \frac{\rho_P \Delta V}{\Delta t} \tag{4.20}$$

$$a_i^\circ = \frac{\rho_P^\circ \Delta V}{\Delta t} \tag{4.21}$$

$$S = S_c \Delta V + S_p \phi_p \Delta V \tag{4.22}$$

For simplicity, we write

$$\Sigma a_{NB} = a_E + a_S + a_N + a_S \tag{4.23}$$

In order to transform equation (4.6) into an equation for the dependent variable ϕ, equation (4.8) is formally multiplied by some "mix" of the dependent variable ϕ

$$f_3 \phi_p + (1-f_3) \phi_p^\circ \tag{4.24}$$

and then subtracted from equation (4.6). Then, after some algebra, the discretization equation for ϕ for the control volume around P becomes

$$\left[a_t + f_1 \left\{ \Sigma a_{NB} + \Sigma F - S_p \Delta V \right\}\right] \phi_p =$$

$$f_1 \Sigma (a_{NB} \phi_{NB}) + \left[a_t^\circ - (1-f_1) \left\{ \Sigma a_{NB}^\circ + \Sigma F^\circ - S_p^\circ \Delta V \right\}\right] \phi_p^\circ +$$

$$f_1 S_c \Delta V + (1-f_1) \left[S_c^\circ \Delta V + \Sigma (a_{NB}^\circ \phi_{NB}^\circ)\right] \tag{4.25}$$

Note that equation (4.25) does neither depend on f_2 nor on f_3, and that no assumptions were made about the values of the f's. A value of 0 corresponds to a fully explicit time marching procedure (FE), a value of 1 to a fully implicit scheme (FI) and a value of 0.5 to the well-known Crank-Nicholson scheme (CN). Since equation (4.23) is independent of f_2, we can set f_2 in equation (4.8) to unity without loss of generality and substitute for $\Sigma F = a_t^\circ - a_t$. For the fully implicit scheme we define

$$a_{P,FI} = \Sigma a_{NB} + a_t^\circ - S_p \Delta V \tag{4.26}$$

$$b_{FI} = S_c \Delta V + a_t^\circ \phi_P^\circ \tag{4.27}$$

Then equation (4.23) can be transformed to

$$[f_1 a_{P,FI} + (1-f_1) a_t] \phi_P = f_1 [\Sigma (a_{NB} \phi_{NB}) + b_{FI}] +$$

$$(1-f_1) [\Sigma (a_{NB}^\circ (\phi_{NB}^\circ - \phi_P^\circ)) + (S_c^\circ + S_P^\circ \phi_P^\circ) \Delta V + (a_t^\circ - \Sigma F^\circ) \phi_P^\circ] \tag{4.28}$$

From this is can be seen that any non-fully implicit formulation can be interpreted as a deviation from the fully implicit case.

The choice of the value of f_1 is dictated by accuracy and stability considerations. While the Crank-Nicholson scheme is the most accurate, the fully implicit scheme is the most stable. The Crank-Nicholson scheme is mathematically unconditionally stable but can lead to physically unrealistic oscillations. Therefore, our goal is to develop a scheme which is as close as possible to a Crank-Nicholson scheme, but also gives always physically realistic results. To get the limit of stability for the Crank-Nicholson scheme, an analytical perturbation analysis can only be performed for the simplified case of constant coefficients. In such a situation for two dimensions and an equidistant Cartesian grid, it can be shown (Roache, 1968) that the physical limit of stability is given by the von Neuman analysis as

$$\frac{\alpha \Delta t}{\Delta x^2} + \frac{\alpha \Delta t}{\Delta y^2} < \frac{1}{2} \tag{4.29}$$

$$\frac{u \Delta t}{\Delta x} + \frac{v \Delta t}{\Delta y} < 1 \tag{4.30}$$

$$\frac{u \Delta x}{\alpha} + \frac{v \Delta y}{\alpha} < 4 \tag{4.31}$$

where $\alpha = \Gamma/(\rho c_p)$. It is evident that for an ever finer grid condition (4.29) is the most stringent condition, since the the time step must be reduced proportional to Δx^2 and Δy^2. Computing a situation with wall turbulence requires an extremely fine grid near the wall so properly resolve the steep gradients there. In such a situation it is therefore practically impossible to apply any scheme other than the fully implicit one if a vast number of time steps is to be avoided. For a situation with varying coefficients and a nonuniform grid, another way to treat stability is the rule[1], that all coefficients in equation (4.25) are to be positive. If this condition is violated, physically unrealistic solutions may arise. It can be shown that the term in the wavy brackets on the left hand side of equation (4.25) is always positive, regardless of the value of f_1. However, it is also evident that the coefficient before ϕ_P^o may very well become negative for small values of f_1. A remedy for this situation can be formulated and is shown next.

4.3.2. Adaptive Time Integration Scheme

As pointed out above, the task is to have a time integration scheme which at each grid location is as close to a Crank-Nicholson scheme as numerical stability considerations will allow. The condition for stability is that the coefficient in front of ϕ_P^o is nonnegative. Due to the convective-diffusive formulation of the coefficients of the neighboring points which we have adopted here, it is made sure that they are always nonnegative. It can be shown that the coefficient in front of ϕ_P is always nonnegative provided S_P is formulated properly. The situation is more complicated for ϕ_P^o.

An equation equivalent to (4.25) can be derived in the same manner as shown above if one individual time integration factor is introduced *for each control volume center* and one *for each interface* (see Figure 4.2).

---

[1] S. V. Patankar in "Numerical Heat Transfer and Fluid Flow", Hemisphere Publ. Co., Washington, 1980, p. 37

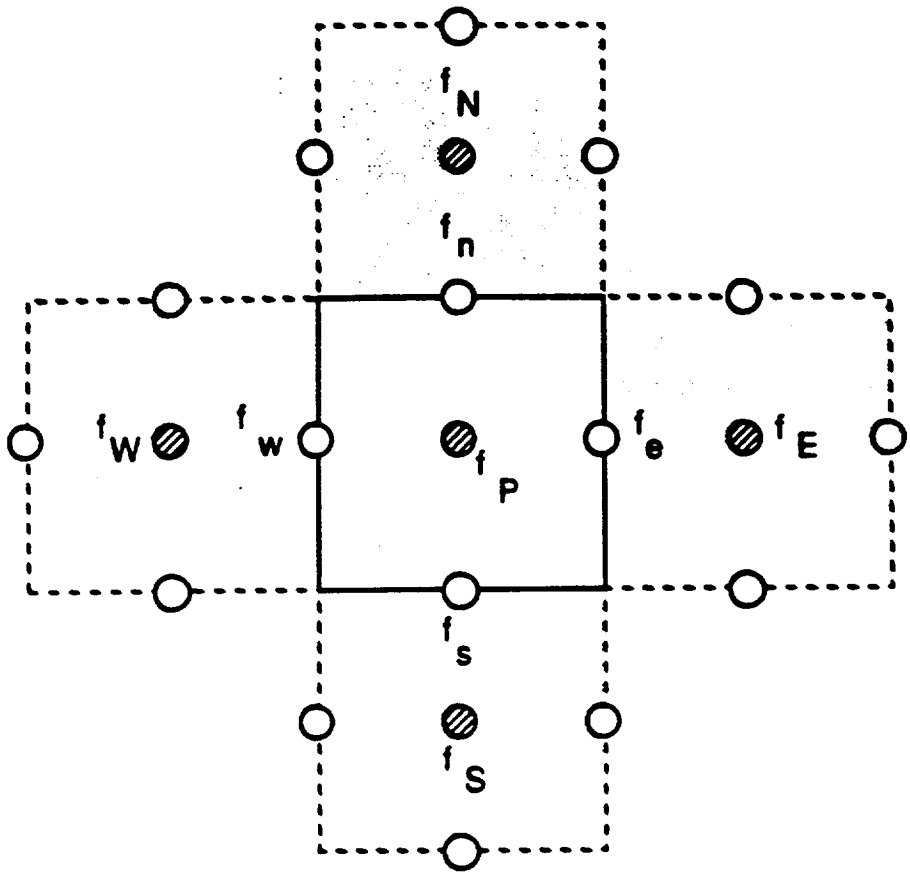

Figure 4.2: Placement of time integration factors for adaptive time integration scheme

For brevity, we will drop the index 1 in the following and define the subscript nb for the control volume interfaces e, w, n, s. Then equation (4.25) takes the form

$$\left[a_1 + \left\{\Sigma f_{nb} a_{NB} + \Sigma f_{nb} F - f_P S_P \Delta V\right\}\right] \phi_P =$$

$$\Sigma (f_{nb}\, a_{NB} \phi_{NB}) + \left[a_1^\circ - \left\{\Sigma (1-f_{nb}) a_{NB}^\circ + \Sigma (1-f_{nb}) F^\circ - (1-f_P) S_P^\circ \Delta V\right\}\right] \phi_P^\circ +$$

$$f_P S_c \Delta V + (1-f_P) S_c^\circ \Delta V + \Sigma (1-f_{nb})\, (a_{NB}^\circ \phi_{NB}^\circ) \qquad (4.32)$$

It may be pointed out here that in order to maintain interface-flux consistency, the interface time integration factors are essential. This may be demonstrated in the following example:

Consider two adjacent control volumes around the points W and P as shown below.

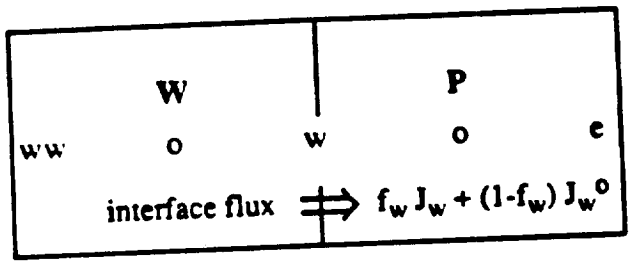

The integrated flux across the w-interface is $f_w J_w + (1-f_w) J_w^o$, regardless whether it is evaluated from the W or the P control volume. If, instead, only f_W and f_P were employed, the flux at w evaluated from control volume W would be equal to $f_W J_w + (1-f_W) J_w^o$ while the flux evaluated from P would be $f_P J_w + (1-f_P) J_w^o$. This inconsistency could lead to physically unrealistic solutions.

The next task is to optimize the individual time integration factors f_P and f_{nb}. We define the coefficient in front of ϕ^o, a_ϕ^o, as

$$a_{\phi}^{o} = a_{i}^{o} - \sum(1-f_{nb})a_{NB}^{o} + \sum(1-f_{nb})F^{o} - (1-f_P)S_P^{o}\Delta V \qquad (4.33)$$

where f_{nb} and f_P are given an initial value of 0.5 corresponding to the Crank-Nicholson scheme. Subsequently, for each control volume, a_ϕ^o is evaluated and f_{nb} and f_P will be corrected if a_ϕ^o is negative. The correction sought is

$$\Delta a_{\phi}^{o} = \sum \Delta f_{nb} a_{NB}^{o} + \sum \Delta f_{nb} F_{nb}^{o} - \Delta f_P S_P^{o} \Delta V = \max[0, -a_{\phi, \text{initial evaluation}}^{o}] \qquad (4.34)$$

so that when a_ϕ° is negative upon its first evaluation, it will be set to zero, and f_P and f_{nb} will be adjusted correspondingly. When a_ϕ° is positive, no action is taken. To evaluate the corrections of the time integration factors, we will assume that the *correction* applied will be the same for all time integration factors associated with one control volume, $\Delta f_{nb} = \Delta f_P$. Then, we can solve equation (4.34) for Δf as

$$\Delta f_P = \Delta f_{nb} = \frac{\max[0,\ -a^\circ_{\phi,\ \text{initial evaluation}}]}{\Sigma a_{NB} + \Sigma F - S_P^\circ \Delta V} \tag{4.35}$$

The Δf's are evaluated for all control volume centers and interfaces in Ω. This will usually lead to a multiple evaluation of the interface time integration factors. For the actual correction of the time integration factors, which is of the form $f_{new} = f_{initial} + \Delta f$, the *largest* correction will be taken. This will ensure that in no control volume the stability criterion is violated. Based on our experience, the CPU time increase due to this scheme is insignificant.

It has been argued that the interface time integration factors can be replaced by the control volume center factors. Using

$$\Sigma f_{nb} a_{NB} = f_P \Sigma a_{NB} + \Sigma (f_{nb} - f_P) a_{NB}$$

and

$$\Sigma f_{nb} F = f_P \Sigma F + \Sigma (f_{nb} - f_P) F$$

one can asses the qualitative impact of such a measure by transforming equation (4.32) to

$$\gamma[\, a_i + f_p\{\Sigma a_{NB} + \Sigma F - S_p\Delta V\}]\,\phi_p + \underline{[\Sigma(f_{nb} - f_p)\, a_{NB} + \Sigma(f_{nb} - f_p)\, F]\,\phi_p} =$$

$$f_p\Sigma a_{NB}\phi_{NB} + [a_i^\circ - (a-f_p)\{\Sigma a_{NB}^\circ + \Sigma F - S_p^\circ\Delta V\}]\,\phi_p^\circ +$$

$$f_p S_c\Delta V + (1-f_p)S_c^\circ\Delta V + (1-f_p)\Sigma a_{NB}^\circ\phi_{NB}^\circ + \underline{\Sigma(f_{nb} - f_p)(a_{NB}\phi_{NB} - a_{NB}^\circ\phi_{NB}^\circ)}$$

$$\underline{[\Sigma(f_{nb} - f_p)\, a_{NB}^\circ + \Sigma(f_{nb} - f_p)\, F^\circ]\,\phi_p^\circ} \qquad (4.36)$$

It can be seen that the underlined terms containing the interface time integration factors become negligible for $\phi_P = \phi_P^\circ$, $\phi_{NB} = \phi_{NB}^\circ$, $a_{NB} = a_{NB}^\circ$ and $F_i = F_i^\circ$. This is generally given for very small time steps, but for larger time steps the omission of those terms introduces a considerable numerical error whose consequences are not known.

Arguing that in an unsteady situation with sufficient time steps the coefficients will vary little, equation (4.32) could be simplified if the old time coefficients a_{NB}° were replaced by the new time coefficients. While this measure seems advantageous from an economic point of view, this would introduce another numerical error into the discretized equations. It may be pointed out that the old time coefficients are readily available at the end of each time step calculation. Since the time integration factors also depend only on knowledge of the old time step, the entire term a_ϕ° can be efficiently evaluated at the end of each time step. Therefore, it is neither necessary nor desirable to employ this simplification.

4.3.3. The Pressure Equation

For incompressible situations, the continuity equation does not contain the the density. The equation of state for an incompressible fluid only gives a relationship between pressure and temperature. Thus, an explicit equation for the pressure is still missing. In what follows, we derive auxiliary equations for pressure. Furthermore, a so-called pressure

correction equation is derived to correct the velocity field such that it satisfies the continuity equation exactly. Both derivations are tied to the solution algorithm for pressure-velocity coupling. The solution algorithm employed here is based on a proposal by Patankar and Spalding (1972) and is of the SIMPLE type. The name "pressure correction equation" can be understood from the development of the original SIMPLE algorithm. In the context of the newer SIMPLER algorithm used here, this name is misleading since pressure is *not corrected* with this equation. For a review of other methods than the one used here, the interested reader should turn to Patankar (1988).

It was shown above that the time integration scheme for the continuity equation does not influence the final discretization equation for ϕ. Therefore it may be postulated here that the latest velocity field shall always satisfy the continuity equation (i.e. f_2=1). The discretized continuity equation is then

$$a_i - a_i^o + (\rho u A)_e - (\rho u A)_w + (\rho v A)_n - (\rho v A)_s = 0 \tag{4.37}$$

This equation will now be transformed to yield an equation for pressure. Independent of equation (4.25), (4.28) or (4.32), the discretization equation for the dependent variable at one point in space can be written as

$$\alpha_P \phi_P = \alpha_E \phi_E + \alpha_W \phi_W + \alpha_N \phi_N + \alpha_S \phi_S + \beta \tag{4.38}$$

where the α's and β are obtained by comparison with one of the above mentioned equations. On this basis the u-velocity equation can be written at point e as[1]:

$$\alpha_e u_e = \sum \alpha_{nb} u_{nb} + \beta + f_1 A_e (P_P - P_E) + (1-f_1) A_e (P_P^o - P_E^o) \tag{4.39}$$

---

[1]Note that the the coefficient α_e represents the *under-relaxed* coefficient if under-relaxation was done to the u_e equation before the pressure equation is entered. The same applies to β and d.

Here the pressure[1] has been taken out of the source term β and treated in the same fashion as all other terms contained in S_c[2]. From this, an explicit equation for the velocity at e can be obtained

$$u_e = \hat{u}_e + f_1 d_e (P_P - P_E) + (1-f_1)\, d_e (P_P^o - P_E^o) \tag{4.40}$$

with the definitions for the pseudo-velocity $\hat{u}$

$$\hat{u}_e = \frac{\sum \alpha_{nb} u_{nb} + \beta}{\alpha_e} \tag{4.41}$$

and the quantity

$$d_e = \frac{A_e}{\alpha_e} \tag{4.42}$$

Equation (4.40) can be used to eliminate u_e and to introduce P in equation (4.37). The same can be done for the other velocities in equation (4.37). The resulting equation is the *pressure equation* :

$$\alpha_P P_P = \sum (\alpha_{NB}\, P_{NB}) + \beta \tag{4.43}$$

where

$$\alpha_{NB} = f_1 (\rho A)_{nb}\, d_{nb} \tag{4.44}$$

---

[1]Note the double meaning of "P" here: the subscript P stands for the grid point, whereas otherwise P denotes the appropriate pressure term (cf. Chapter 2).

[2]From here on we will restrict discussion to a spatially uniform time discretization scheme and return to the subscript "1". A derivation for an adaptive time integration scheme is straight forward but not needed as shown later.

$$\alpha_P = \sum \alpha_{NB} \tag{4.45}$$

$$\beta = a_l^o - a_l - \sum \hat{F} + (1-f_1)\,\alpha_{NB}(P^o_{NB}-P^o_P) \tag{4.46}$$

and $\Sigma\hat{F}$ is defined equivalently to equation (4.9).

4.3.4. The Pressure Correction Equation

After the velocity field is computed, it will satisfy the momentum equations, but not necessarily the continuity equation. Thus a correction to the velocity field shall be derived which ensures that it satisfies the mass balance exactly. Define a correction to pressure P and velocity u as

$$P = P^* + P' \tag{4.47}$$

$$u = u^* + u' \tag{4.48}$$

and equivalently for v. The starred quantity denotes the quantity after solution of its transport equation, u' denotes the velocity correction sought and P' stands for the corresponding pressure correction. Equation (4.39) can also be written for the starred velocity u*. Subtraction of this equation from equation (4.39) yields an equation for u' as

$$\alpha_e u'_e = \sum \alpha_{nb} u'_{nb} + f_1 A_e(P'_P - P'_E) + (1-f_1)\,A_e(P'^o_P - P'^o_E) \tag{4.49}$$

However, the old pressure field is presumed to be the known and exact; hence there is no correction for it. For simplicity, the first term on the right hand side is omitted. Now an equation for u'_e can be formulated:

$$u_e' = f_1 d_e (P_P' - P_E') \tag{4.50}$$

Similarly, for v_n'

$$v_n' = f_1 d_n (P_P' - P_N') \tag{4.51}$$

With equations (4.50) and (4.51), u' and v' can be eliminated from equation (4.48) and its equivalent for v, and the resulting expressions for the velocities can be substituted into the continuity equation (4.37). This yields an equation for the pressure correction P'

$$\alpha_P P_P' = \sum \alpha_{NB} P_{NB}' + \beta \tag{4.52}$$

where

$$\beta = a_1^o - a_1 - \sum F^* \tag{4.53}$$

and α_{NB} is defined as in equation (4.43). The sum ΣF^* is defined analogously to equation (4.9) where the individual flows are evaluated with the starred velocities. Note that the right hand side of equation (4.53) is the continuity equation. In case of convergence, β will tend to zero and is therefore a measure of convergence as will be pointed out later.

4.3.5. The Velocity Correction Equations

Based on equations (4.48) and (4.50) and knowing the pressure corrections, the velocity filed can be corrected according to

$$u_e = u_e^* + f_1 d_e (P_P' - P_E') \tag{4.54}$$

and $$v_n = v_n^* + f_1 d_n (P'_P - P'_N) \qquad (4.55)$$

4.3.6. On the Correct Choice of the Time Integration Factor for the Auxiliary Equations

So far the pressure and pressure correction equations have been treated entirely equivalent to the general ϕ equation. This treatment lead to the factor f_1 in the definition equations (4.44) of the neighbor point coefficients and in equations (4.54) and (4.55) for the velocity corrections. A consequent treatment of S in the equations for u and v introduces f_1 in equations (4.39) and (4.49). It seems natural that the same values for f_1 should be used with the pressure and the pressure correction equations as with the general ϕ equation. While implementing this scheme and testing it for laminar oscillating flow, this was indeed done initially. However, a thorough inspection of the predicted pressure showed large disagreement with the analytical pressure prediction for fully developed laminar oscillating flow, even though the computed velocities were very close to the analytical ones. The disagreement turned out to be an oscillation around the sinusoidally varying axial pressure distribution. A number of tests have been carried out to examine the influence of f_1 on the pressure prediction. It turns out that the best predictions are obtained when (i) both, the pressure and the pressure correction equation are treated as fully implicit, (ii) the velocity corrections are done fully implicit and (iii) the pressure source term in the momentum equations is treated as fully implicit (see also Fig. 4.4). This constitutes essentially a "staggered grid in time". As in the space grid, the velocity "time grid" differs from the pressure "time grid" unless a fully implicit scheme is used throughout. The code was implemented according to these findings. Since the auxiliary equations will finally be treated as fully implicit, the discussion above was formally carried out for locally uniform time integration factors only.

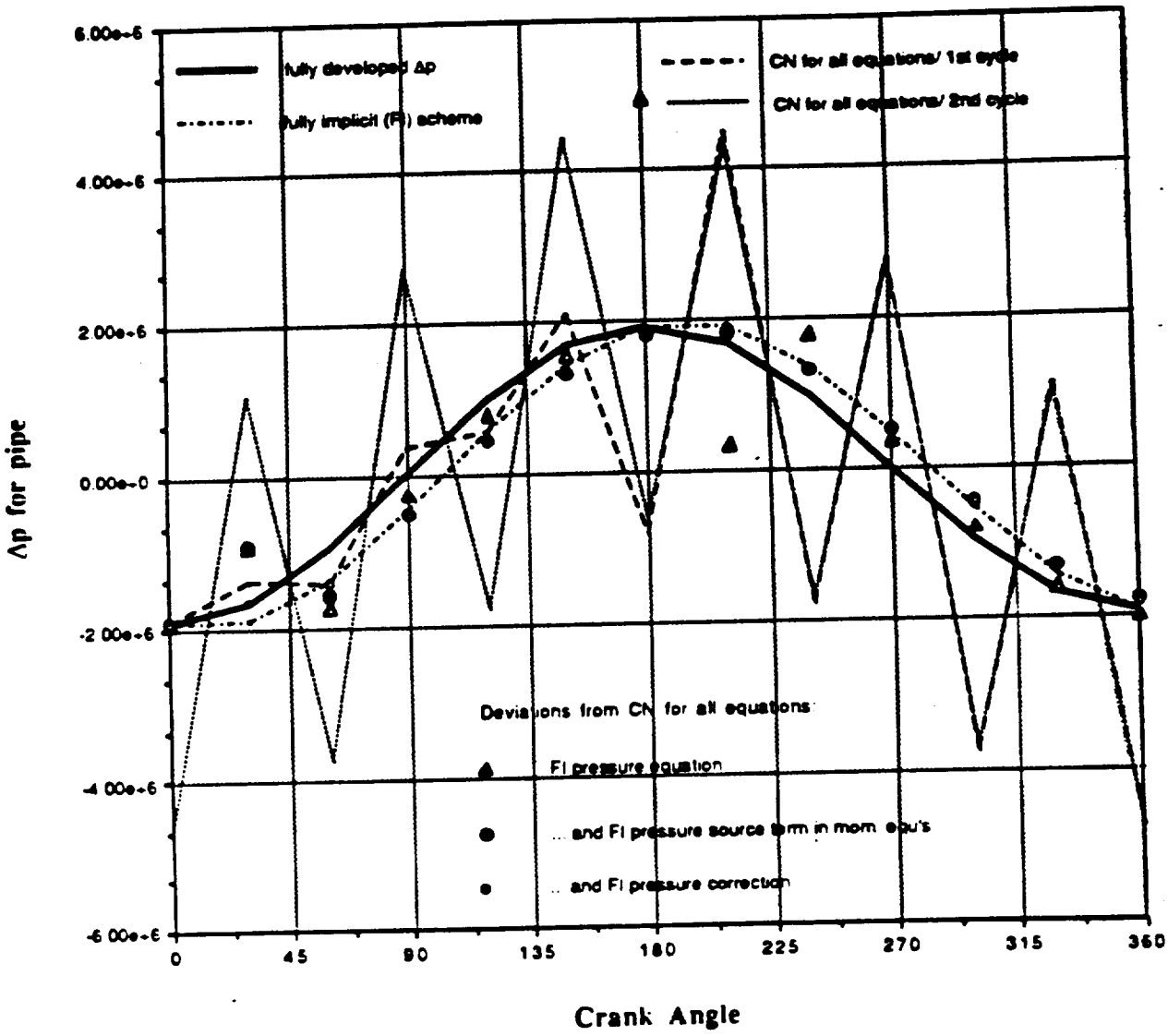

Figure 4.3: Choice of f_1 for pressure and pressure correction equation and for pressure source term treatment in u and v equations

4.2. Solution Method

The set of algebraic discretization equations can be constituted one large matrix which could be solved by a direct solver. For instance Kelkar (1988) used the Yale Sparse Matrix Package to solve the flow and heat transfer around a square cylinder. While this has advantages for the coupling of the equations, this technique would be inefficient since for large matrices it is generally more economical to employ iterative techniques. Furthermore, the equations are, in general, nonlinear. Even if a direct solver was used for the entire set of equations, the coefficient matrix would have to be updated after each solution and solved again, until convergence was achieved. The intermediate solutions during this convergence are exact solutions only to a preliminary coefficient matrix, which is an unnecessary effort. Also, an iterative technique offers more freedom to treat the source terms in the equations. Solving turbulent flow with a k-ε model involves the solution of two equations for always positive variables. In the course of the solution for those variables it is very important that their intermediate values never become negative. Intermediate negative values for k and ε would render their solution meaningless. A technique to prevent this is outlined by Patankar (1980) and requires the freedom to formulate the source terms with flexibility. This flexibility is not given in a direct solution scheme. Therefore it is clear that iterative techniques are more suitable.

An iterative solution method may be divided in two parts: First, the treatment of the nonlinearity and the coupling technique between the individual physical equations, and second, the solution technique used to solve a set of linearized algebraic discretization equations. For the former, the SIMPLER algorithm (Patankar, 1980) was used with an enhancement proposed by Recktenwald (1989). For the latter, a technique was used which proved to be robust and most economical. A discussion of these features follows.

4.2.1. Solution of the Nonlinear Equations

For the solution of the nonlinear equations, the SIMPLER algorithm (Patankar, 1980) was used. In this algorithm, the discretized differential equations are solved sequentially. With the latest velocity, density and viscosity fields, the coefficient matrix of the pressure equation is determined and solved. With the new pressure field, the new velocity field is computed. Next, the pressure correction equation is solved, and, with its help, the velocities are corrected such that the corrected velocity field satisfies exactly the continuity equation. Finally, the equations for the remaining dependent variables are solved. When this is completed, the process is repeated a sufficient number of iterations until an overall convergence is reached. These iterations will be termed "nonlinear" iterations in what follows.

Since the differential equations to be solved are in general nonlinear and coupled, it may be necessary to under-relax their solution in order to achieve convergence. Examples of under-relaxation techniques can be found in Patankar (1980), Kelkar (1988) and Recktenwald (1989). Generally, the stronger two equations are coupled, the more they must be under-relaxed. The degree of under-relaxation determines the speed of convergence of a solution. For the SIMPLER algorithm it is advantageous to have a similar convergence speed for each equation solved. An example of two strongly coupled equations are the equations for the turbulent kinetic energy and the turbulent dissipation rate in the case of turbulent flow. Recktenwald (1989) observed in his calculations that when the solution of the pressure-velocity coupling occurred much more rapidly than the solution of the k-ε coupling, the scheme diverged. It is the *difference* in under-relaxation factors for the velocity and pressure equations on the one hand, and for the k and ε equation on the other, not their absolute level, which is responsible for this divergence. Even seemingly small differences in the values of the under-relaxation factors may effectively constitute large differences. One remedy to this problem would be to set the relaxation factors of all dependent variables at the lowest necessary value. This, however, would be very

wasteful. Alternatively, Recktenwald (1989) proposed an additional level of iterations in which the strongly coupled equations (e.g. k and ε) are solved repeatedly one after the other, each time with updated coefficients. After a sufficient number of such extra iterations, the SIMPLER algorithm is continued. This technique was originally introduced especially for unsteady flow problems; it was tested during this research for steady turbulent pipe flow and found that in steady pipe flow this enhancement also speeds up the nonlinear convergence considerably. A "sufficient number" of these iterations was found to be typically between 1 and 5; 1 at the beginning of the computation and 5 near convergence.

4.2.2. Solution of the Linearized Algebraic Equations

For each grid point and dependent variable ϕ an equation may be written in the linearized form

$$\alpha_P \phi_P = \alpha_E \phi_E + \alpha_W \phi_W + \alpha_N \phi_N + \alpha_S \phi_S + \beta \tag{4.56}$$

The coefficients α and β can be determined by comparison with equation (4.32). For a fully implicit steady-flow scheme, the coefficients are identical to the ones given in Patankar (1980). The coefficients of the equations for all grid points for one dependent variable ϕ constitute a matrix A, so that the problem can be written as

$$A \vec{x} = \vec{b} \tag{4.57}$$

Many techniques for an iterative solution of this equation are available. Some have been tested during this work for their effectiveness. Special care was taken to ensure that the codes used could be fully vectorized. The codes tested were[1]

a) an unvectorized tri-diagonal matrix algorithm (TDMA) applied line by line

[1]For a general description of the line by line method, see e.g. Patankar (1980).

b) a vectorized, inverted TDMA applied line by line

c) a vectorized, inverted red-black TDMA applied line by line

d) a vectorized TDMA line by line method using a Cray-SCILIB subroutine to evaluate dot products of vectors.

e) a vectorized SSOR algorithm

The test problem was a steady turbulent pipe flow on a 23 by 23 grid. The vectorized SSOR algorithm proved to be extremely sensitive to the correct choice of the over-relaxation factor. For an over-relaxation factor greater than 1.2, the solution diverged independently of how accurately the equations were solved. The other four methods gave the following performance in CPU time based on the first method:

a) 100% b) 45.5% c) 66.7% d) 81.2%

The difference between b), c) and d) can be explained by the varying influence of the relative short vector lengths (21 elements). Method b) and c) should break even when the vector length is greater than 128, given the present vector length of 64 words on the Cray 2 computer. Similarly, the use of the SCILIB subroutine pays only for very large vectors. The accuracy[1] of the solution achieved after a fixed sweep through the domain was highest for method a) and about the same for b), c) and d). Due to the coupling and nonlinearity of the physical equations, only a limited accuracy is needed for an intermediate solution. With this in mind, method b) was used for further work.

Other, more sophisticated methods like preconditioned conjugate gradient methods might lead to increased efficiency and accuracy. However, the optimization of the solution algorithm was not the subject of this research.

How accurately shall the linearized equations be determined? When can the overall solution process be terminated? These questions will be discussed next.

---

[1] measured in terms of the residual σ_{max} which is defined below

4.2.3. Linear, Nonlinear Residuals and Convergence

The residual of the linearized discretization equation (4.56) can be expressed as

$$\tilde{r}_P^{kl} = \sum \alpha_{NB}^k \phi_{NB}^l + \beta^k - \alpha_P^k \phi_P^l \tag{4.58}$$

where α_{NB}^k, α_P^k, and β^k are the coefficients af the linearized equations at a *nonlinear iteration k*, ϕ_{NB}^l, ϕ_P^l are the values for the *linear iteration l* within the solution algorithm. $\tilde{r}_P^{kl}$ is the residual corresponding to k nonlinear and l linear iterations. However, the absolute value of $\tilde{r}_P^{kl}$ does not give a sure determination of whether the residual of an equation is small. We require that the value of $\tilde{r}_P^{kl}$ be small compared with $\alpha_p^k \phi_p^l$ (frequently the largest contributor in the sum on the right hand side of equation (4.58)). Therefore we scale each residual to determine its relative importance and define

$$r_p^{kl} \equiv \frac{\tilde{r}_p^{kl}}{\alpha_p^l \phi_p^l} \tag{4.59}$$

This scaling normalizes the coefficient matrix with respect to their diagonal elements. This scaling form offers the advantage, other than described in Recktenwald (1989), that the values at a particular point in the domain can be prescribed without rendering the residuals meaningless. The prescription is typically done by assigning a huge number to coefficient α_p and assigning this huge number times the desired value to coefficient β.

Since there is *one* r_P^{kl} for each nodal point in Ω and dependent variable ϕ, we define a residual vector $\vec{R}_{P\phi}^{kl}$ which contains the individual residuals as coordinates. The Euclidian norm $R_{P\phi}^{kl}$ of the vector is a measure of the overall error of the computed solution of ϕ in Ω,

$$R_{P\phi}^{kl} \equiv \| \vec{R}_{P\phi}^{kl} \| = \sqrt{\sum_{\text{all grid points}} (r_P^{kl})^2} \tag{4.60}$$

During consecutive linear iterations within the solution algorithm, the coefficients remain constant and, in the limit, $R_{P\phi}^{kl}$ will approach zero. However, it is uneconomical to drive the residual to zero at this point because the equation solved is only the linearized form of the actual, nonlinear equation. A perfect solution for the linearized equations may still be far away from the solution of the nonlinear equations. The criterion to determine whether $R_{P\phi}^{kl}$ is small enough to terminate the linear iterations was

$$\frac{R_{P\phi}^{kl}}{R_{P\phi}^{k0}} \leq \delta_{\phi} \tag{4.61}$$

where $R_{P\phi}^{k0}$ is the so-called nonlinear residual, and δ_{ϕ} is some, user specified, small number. Recktenwald (1989) and Van Doormaal and Raithby (1984) have discussed the choice of δ_{ϕ} in detail. Here, δ_{ϕ} was chosen between 0.1 and 0.3.

After completion of the linear solution of one dependent variable, this process is repeated for the other dependent variables.

Table 4.2: Typical Values of δ_{ϕ} in the computations

ϕ	u	v	pc	p	k	ε
δ_{ϕ}	0.3	0.3	0.15	0.15	0.2	0.2

The nonlinear residual $R_{P\phi}^{k0}$ is obtained by evaluating equation (4.39) upon entering the solution algorithm with the latest set of coefficients. The series of the nonlinear residuals, $R_{P\phi}^{k0}$, from one nonlinear iteration to the next is an excellent measure of the overall, nonlinear convergence of a variable ϕ. If this number becomes small enough (e.g. 10^{-6}) for

all dependent variables, then a solution at this time step is obtained and one can proceed with the next time step.

Another measure of nonlinear convergence is the maximum scaled error of the continuity equation, σ_{max}, at any point in Ω:

$$\sigma_{max} = \frac{\max\left[\text{abs}\left[a_t - a_t^0 + \Sigma F^* \right]\right]}{\text{maximum flow rate across any control volume interface in } \Omega} \qquad (4.62)$$

When σ_{max} reaches a value of less than 10^{-4}, reasonable nonlinear convergence is generally obtained. In fact, σ_{max} is probably the single best overall measure of convergence. The nonlinear residual for the u-equation and smax are strongly correlated so that usually it suffices to monitor only σ_{max}. However, it proved useful to monitor the nonlinear residuals for the k and ε equations, because it is possible to reach an intermediate solution for which the continuity equation and the momentum equations are rather well satisfied but for which the k and ε equations have not yet reached convergence.

4.3. Summary

In this chapter, the general discretization equations were developed. A locally adaptive time integration scheme was developed which will be especially helpful in situations with wall turbulence where highly non-uniform grids are usually used. While it is more elaborate to implement this scheme than a fully implicit scheme, the additional CPU time cost is marginal. An enhanced SIMPLER algorithm for the treatment of strongly coupled equations was outlined. A vectorized line-by-line method was found to be a robust and efficient solver for the linearized equations. Criteria for the linear and nonlinear convergence are established and discussed.

PART II: ANALYSIS AND RESULTS OF THE FLUID MECHANICS PROBLEM

5. PREDICTIONS OF FULLY DEVELOPED TURBULENT PIPE FLOW UNDER STEADY CONDITIONS

In order to verify both the turbulence model itself as well as its programming, a series of computational tests were made to compare the predictions for fully developed pipe flow at two different Re numbers. One of the benchmark papers on turbulent pipe flow is that of Laufer (1954), where the detailed characteristics of the flow at Re numbers of 50,000 and 500,000 are investigated. Both, the turbulence model of Jones and Launder (1972) and the model of Lam and Bremhorst (1981) were tuned to match the set of data provided in this paper. To verify our solution at high Re numbers, predictions at Re = 50,000 are compared with the data of Laufer (1954). The paper by Kudva et al. (1972) provides data on pipe flow at Re = 6000, which will be the second Re number for our test.

5.1. Predictions of the High-Reynolds Number k-ε Model

The high-Reynolds number model (HRN) computations were done with a 23 by 23 grid with a finer mesh near the wall. The L/D ratio was 150 for all computations. Figure 5.1 shows the predictions for Re = 50 000. It can be seen that the predicted normalized velocity is consistently too high. But since rather few grid points were used here, this effect may be due in part to the grid size. From Fig. 5.7 it is clear that the use of the HRN turbulence model for a Re number as low as 6000 is inappropriate.

5.2. Predictions of the Low-Reynolds Number k-ε Model

The low-Reynolds number model (LRN) computations were made with a 33 by 51 grid with densely spaced grid points near the wall. For a Re number of 50 000, ca. 7 grid points were placed within the viscous sublayer ($y^+ \leq 11$). For Re = 6000, this number was 17. The L/D ratio was 150 for Re = 50 000 and 250 for Re = 6000. Figure 5.1 shows that the computed data generally follows the law of the wall, but underpredicts u^+ slightly. This is due to a slightly too high u_τ which in turn may be attributed to the relatively small number of grid points in the viscous sublayer. Figure 5.2 compares the computed local friction coefficient $c_{f,x}$ for Re = 5.0×10^4, and a TI (turbulence intensity at the inflow) of 10%, with the experimental value for fully developed flow. Thereafter, the incoming slug flow develops swiftly as the rapidly decreasing c_f indicates. The minimum at about x/D=10 corresponds to the beginning of the development of the turbulent flow structure. The fully developed value is slightly higher than the experimental value. Figures 5.3 and 5.4 show fairly close agreement of the measured and predicted turbulent kinetic energy. Figures 5.5 and 5.6 show the comparison for the turbulent dissipation rate. In Fig. 5.6, the predictions are compared with Laufer's data as shown in the paper by Lam and Bremhorst (1981) as well as with Laufer's data as taken from the the original paper by the present author. There is no explanation for the disagreement of the two sources. However, the predicted data is in satisfactory agreement with Laufer's data. Fig. 5.7 compares the predictions with the data of Kudva (1972) and the law of the wall. As can be seen , the experimental data at Re = 6000 does not follow the logarithmic law of the wall. The measured data lie consistently above the log law. The predictions correctly reflect this trend. As in the case for Re = 50 000, the predictions slightly underestimate the normalized velocity. Finally, Fig. 5.8 compares the predictions for the turbulent kinetic energy. Since Kudva et al. (1972) only report data for u'^2, k can only be estimated from it. Fig. 5.8 shows one such estimate using the same ratio of u'^2/k at each radial location as in Laufer's data. For completeness, also Laufer's data are shown. The prediction are in between the experimental curves.

Fig. 5.1: Predictions of fully developed turbulent pipe flow at Re = 50 000.

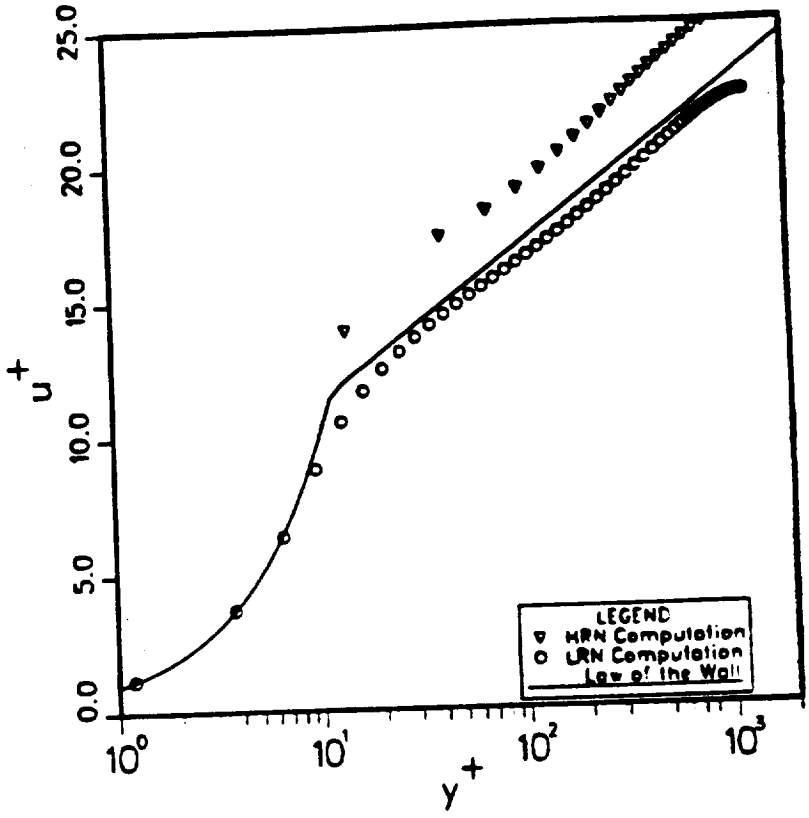

Fig. 5.2: Computed local friction coefficient and steady state correlation for fully developed flow at Re=50000.

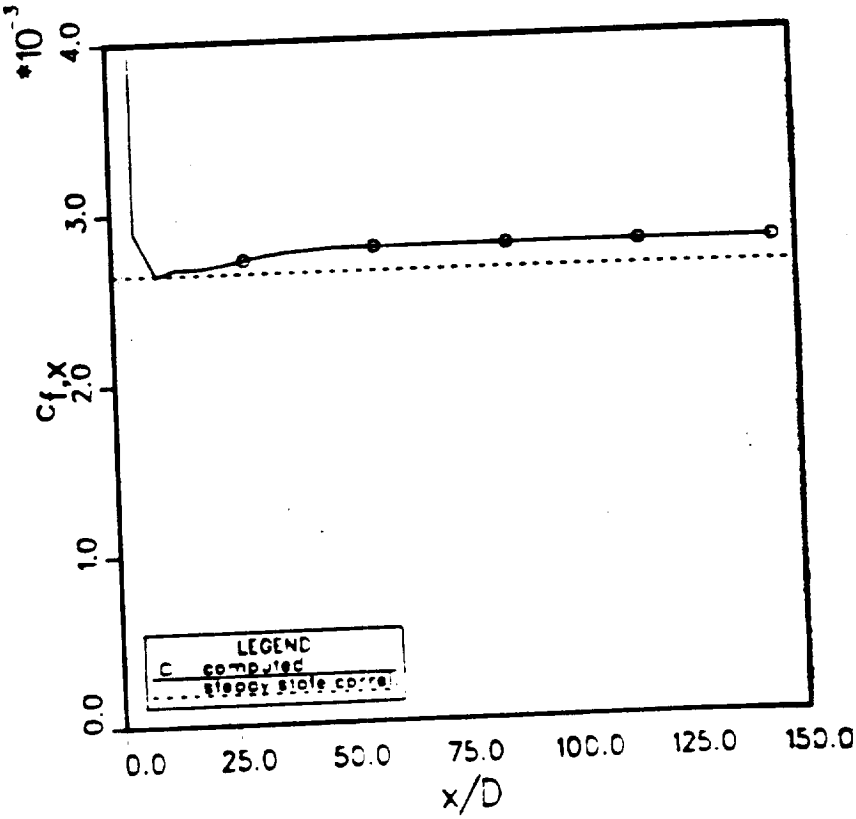

Fig. 5.3: Turbulent kinetic energy for fully developed turbulent pipe flow at Re = 50000.

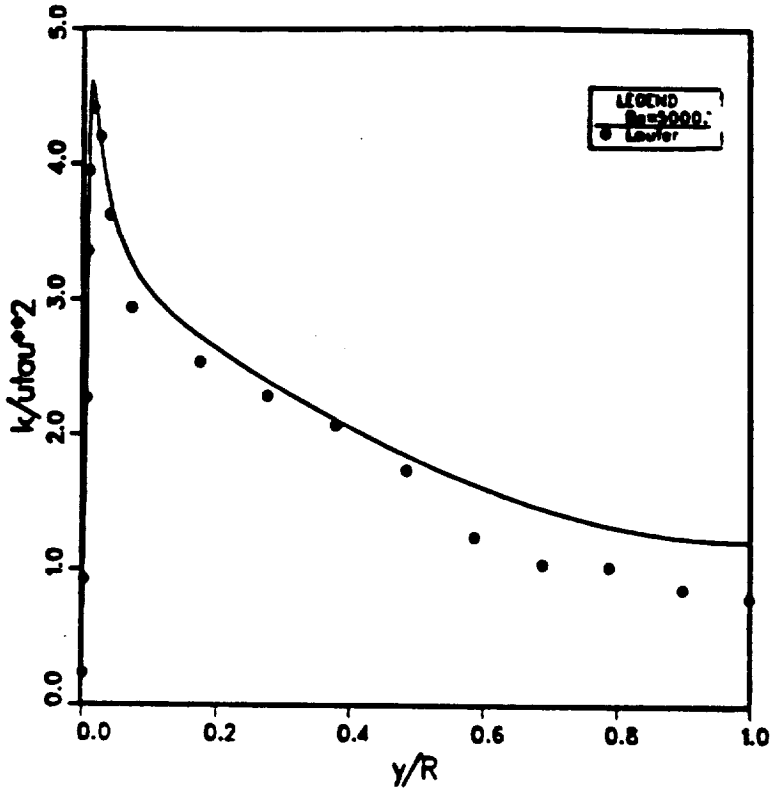

Fig. 5.4: Turbulent kinetic energy for fully developed turbulent pipe flow at Re = 50000 near the wall.

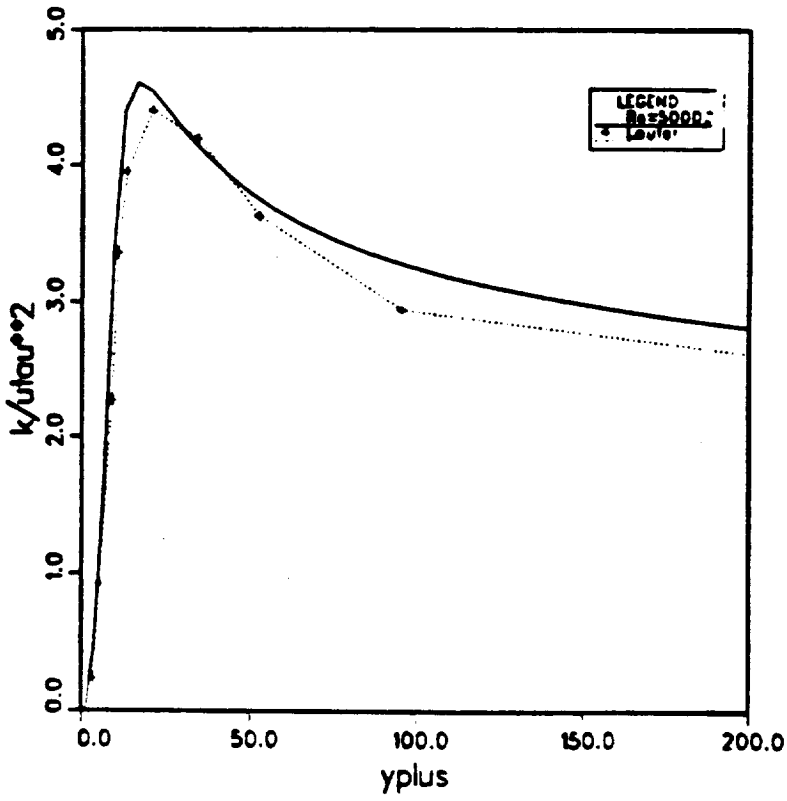

Fig. 5.5: Turbulent dissipation rate for fully developed turbulent pipe flow at Re = 50000.

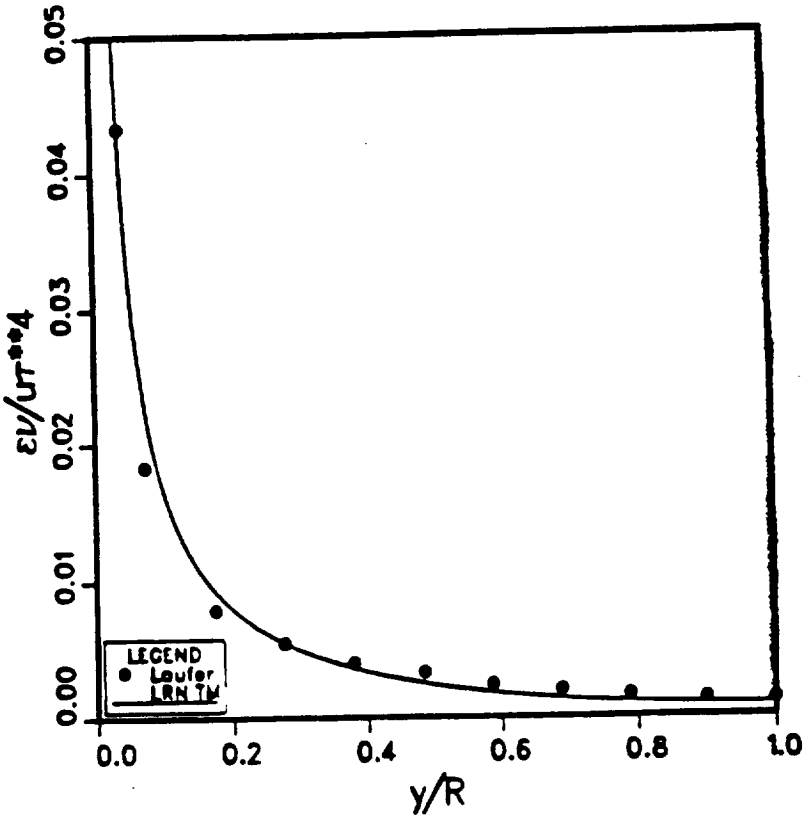

Fig. 5.6: Turbulent dissipation rate for fully developed turbulent pipe flow at Re = 50000 near the wall.

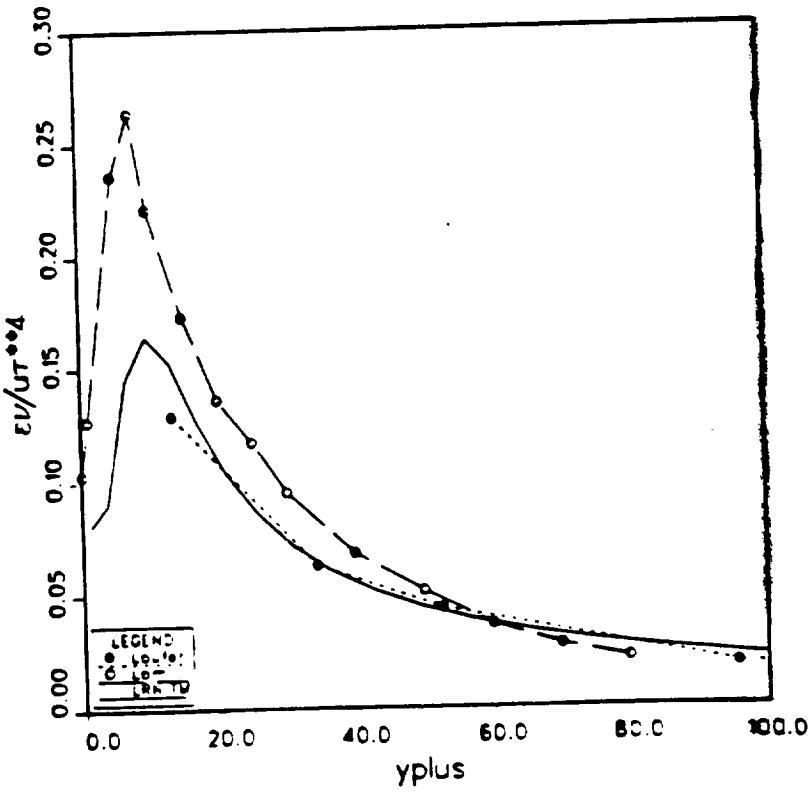

Fig. 5.7: Normalized velocity predictions for fully developed turbulent pipe flow at Re = 6000.

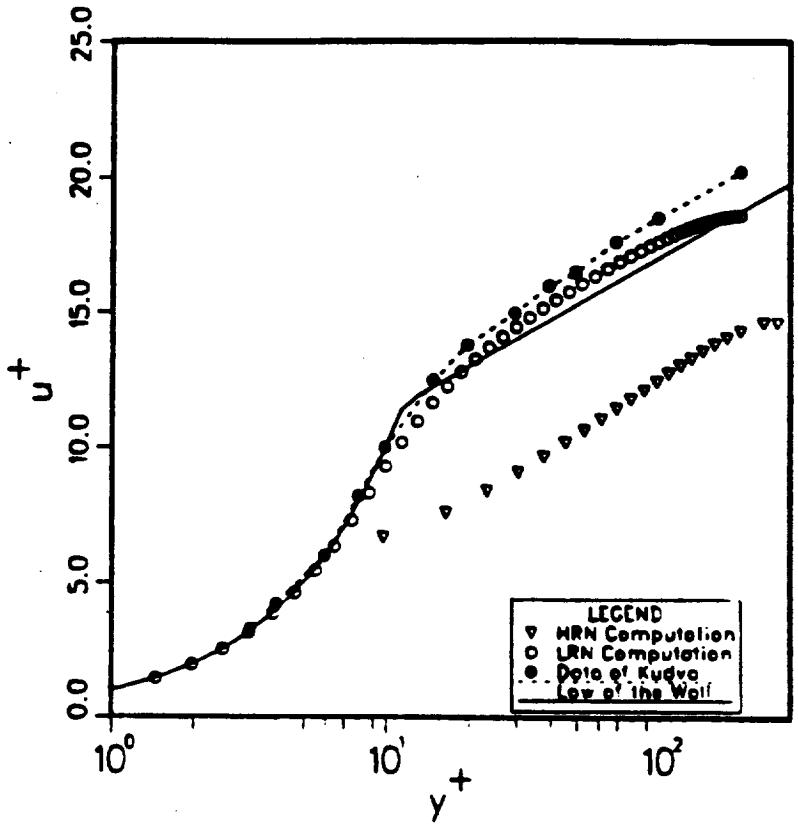

Fig. 5.8: Turbulent kinetic energy for fully developed turbulent pipe flow at Re = 6000.

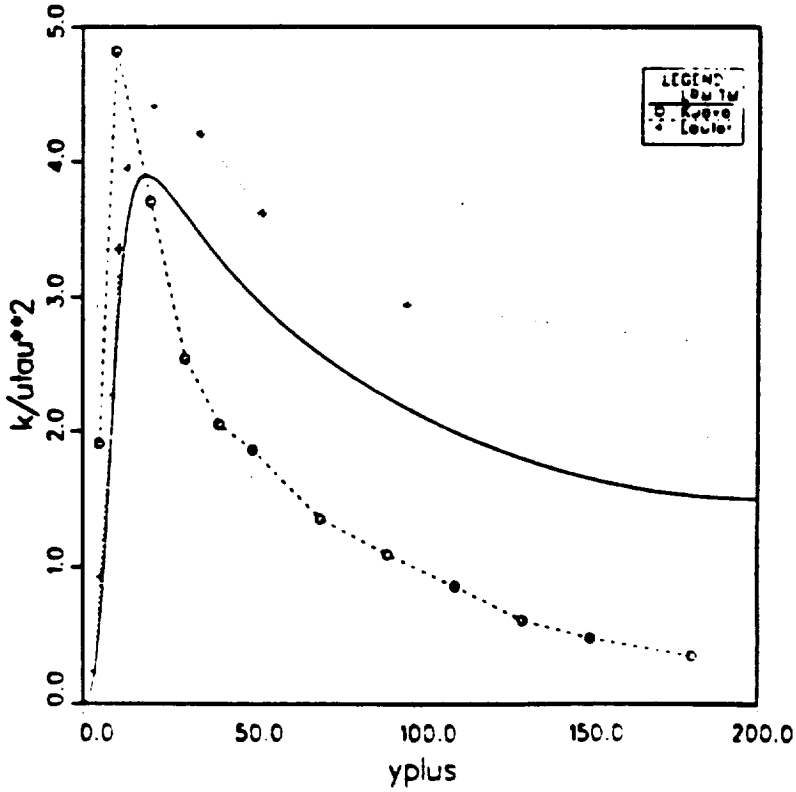

6. TRANSITION PREDICTIONS

In oscillatory flows at sufficiently high Re_{max} numbers, the flow repeatedly undergoes transition from laminar to turbulent and vice versa. The actual Reynolds number at which transition occurs under those conditions is surely influenced by acceleration or deceleration effects and is most likely not the same as the critical Reynolds number for steady flow in smooth pipes, 2300. Even though our goal is to predict turbulent *oscillatory* flows, it is clear that a turbulence model which cannot predict transition for the much simpler case of steady flow has no promise of predicting transition in oscillatory flows.

The objective of this chapter is to investigate the proposed turbulence model for its ability to predict transition in steady and in accelerated pipe flow. This chapter presents the results of a series of computations which examine primarily the following four questions:

1) At what Re number is transition predicted for fully developed steady flow?
2) What is the influence of the inflow boundary conditions for k and ε on the prediction of this transition?
3) What is the entrance region prediction for moderate Reynolds numbers (<10000) ?
4) How do the predictions compare with experiments?
5) How does acceleration affect the predictions?

6.1. Experimental Observations of the Entrance Region

It is well known that the hydrodynamical entrance length in laminar pipe flow is

$$x/D = 0.05\ Re$$

However, there is not a consensus on the entrance length in turbulent flows. Commonly, we speak of entrance length as that distance from the entry along the flow

direction where the velocity profile changes. Wang and Tullis (1974) distinguish 3 different lengths:

1) The length at which the wall shear stress becomes fully developed.

2) The length at which the boundary layer reaches the centerline.

3) The length at which the centerline velocity becomes fully developed.

According to Nikuradse (1932), the entry length is nearly independent of the Reynolds number and is 40 to 50 diameters. This is in good agreement with the findings of Wang and Tullis (1974) who measured an x/D of 49.5. Deissler (1950) reports that the flow at the centerline was still developing at x/D=100 for a rounded entrance. He also found that the flow close to the wall developed to its final form over a shorter distance from the entrance than required by flow in the center. In a later paper (1955) he quantifies this finding stating that the friction (factor) is approximately fully developed after 10 diameters. Bowlus and Brighton (1968) verify this and in addition give an analytically derived relation for the velocity entrance length as

$$x/D = 14.25 \log_{10}(Re) - 46.0$$

In one of the benchmark papers about turbulent pipe flow Laufer (1955) measured fully developed flow in a round pipe at a location of circa 50 diameters. And, based on his review of literature, Truckenbrodt (1980) states the following average relationship

$$x/D = 0.6\, Re^{0.25}\,.$$

This overview clearly shows that the "length of the entrance region" in fully turbulent pipe flow is debated in literature [1]. It is not surprising that for transitional pipe flow even less is known about the entrance length of the flow. A detailed comparison of the entry length computations with experiments was therefore not attempted.

[1] One reason may be that different researchers had different boundary conditions for k and ε, which are not normally reported or even measured.

The computational domain was chosen to be a straight tube with L/D ≤ 500. In view of the discussion above, this was considered to be long enough to ensure that fully developed conditions always exist at the end of the tube. Even if the model were to predict *laminar* flow for a high Reynolds number, the flow would be fully developed at the end of the pipe for Reynolds numbers up to 10000.

6.2. Boundary Conditions at the Inflow

For isotropic turbulence, the turbulence intensity at the inflow can be defined as

$$Tl \equiv \frac{\sqrt{\frac{2}{3}k}}{u_{mean}} \tag{6.1}$$

The specification of a turbulence intensity at the inflow boundary poses no problem. However, the specification of the incoming turbulent dissipation rate ε is a problem. Generally, data about k and ε at inflow are not reported by experimenters[1]. Therefore, assumptions have to be made and their impact on the predictions should be assessed. One option of specifying ε_{in} is

$$\varepsilon_{in} = \zeta \rho \frac{k^2}{\mu} \tag{6.2}$$

where ζ is some function to be determined. It is evident that ζ is like an inverse turbulence Reynolds number Re_t

$$Re_t = \rho \frac{k^2}{\mu \varepsilon} \tag{6.3}$$

---

[1] See e.g. Laufer (1955), Nikuradse (1933), Deissler (1950)

From the definition of the isotropic turbulent viscosity we know that

$$\varepsilon = \frac{c_\mu \rho k^2}{\mu_t} \tag{6.4}$$

It is clear that with increasing Re also μ_t will increase. Therefore we use

$$\varepsilon_{in} = \zeta(Re)\, \rho \frac{k^2}{\mu} \tag{6.5}$$

and we define $\zeta(Re)$ as $1/\sqrt{Re}$. This will give a turbulent viscosity at inflow of

$$\mu_t = \sqrt{Re}\; c_\mu \mu \tag{6.6}$$

At a Re number of 10^6, this will lead to a turbulent viscosity of 90 times the laminar viscosity, whereas for a Re of 10 000, this value is 9. Around the critical Re number of 2300 the inflow turbulent viscosity will be of the same order of magnitude as the laminar viscosity. If Re is further decreased, the numerical turbulent viscosity at the inflow will become less and less important compared to the laminar viscosity. This, of course, is what we require from physical intuition.

Another option in specifying ε_{in} is to assume that at inflow, the rate of production of turbulent kinetic energy is in equilibrium with its dissipation rate,

$$G = \varepsilon \tag{6.7}$$

The production rate is defined as

$$G \equiv -\overline{u_i u_j} \frac{\partial \overline{u}_i}{\partial x_j} = \frac{\tau}{\rho} \frac{\partial \overline{u}_i}{\partial x_j} \tag{6.8}$$

A simple closure for τ is

$$\tau = \mu_t \left(\frac{\partial \overline{u_i}}{\partial x_j} + \frac{\partial \overline{u_j}}{\partial x_i} \right) \tag{6.9}$$

Near the wall

$$\tau = \tau_0 = \mu_t \frac{\partial \overline{u_i}}{\partial x_j} \tag{6.10}$$

Defining the friction velocity as

$$u_\tau^2 = \tau_0 / \rho \tag{6.11}$$

we get

$$G = u_\tau^2 \frac{\partial \overline{u_i}}{\partial x_j} \tag{6.12}$$

The model for the isotropic turbulent viscosity is

$$\mu_t = c_\mu \rho \frac{k^2}{\varepsilon} \tag{6.13}$$

With this, equation (6.10) becomes

$$\tau_0 = c_\mu \rho \frac{k^2}{\varepsilon} \frac{\partial \overline{u_i}}{\partial x_j} \tag{6.14}$$

Eliminating ε with (6.7) and (6.11) yields

$$u_\tau = c_\mu^{0.25}\, k^{0.5} \tag{6.15}$$

Combining (6.4) with (6.10) and (6.14) yields

$$\varepsilon = c_\mu \frac{k^2}{u_\tau^2} \frac{\partial \overline{u_i}}{\partial x_j} \tag{6.15}$$

Using the universal law of the wall, we get

$$\varepsilon = \frac{c_\mu^{0.75}\, k^{1.5}}{\kappa\, y_{in}} \tag{6.16}$$

The choice for y_{in} is either one representative length scale for the inflow (e.g. the radius of the tube) or the distance to the wall. This, however, will lead to a singularity of ε at the wall and a rather low value at the centerline. As a consequence, the turbulent viscosity at inflow will peak sharply in the center and be very low near the wall.

A third way to specify ε is to infer the nature of μ_t from experimental data for fully developed pipe flow. Thereafter, the friction velocity can be expressed as

$$u_\tau = \frac{\nu_0}{D} \begin{cases} 0.197\, Re^{0.875} & Re \le 4 \cdot 10^4 \\ 0.151\, Re^{0.9} & Re > 4 \cdot 10^4 \end{cases} \tag{6.17}$$

From Schlichting (1980), $\nu_{t,max}/(u_\tau R) = 0.09 = c_\mu$.

With (6.17) this can be rewritten as

$$\mu_t = c_\mu\, \mu \begin{cases} 0.1\, Re^{0.875} & Re \le 4 \cdot 10^4 \\ 0.076\, Re^{0.9} & Re > 4 \cdot 10^4 \end{cases} \tag{6.18}$$

In order to have μ_t as a function of the turbulence intensity at the inflow, we define

$$\mu_t = c_\mu \mu \, Tl \, Re^{0.875} \tag{6.19}$$

which gives a function ζ when put into (6.2) of

$$\zeta(Re) = \frac{1}{Tl \, Re^{0.875}} \tag{6.20}$$

It is this formulation that we have adopted for the LRN computations.

6.3. Transition Predictions of Quasi-Steady Flow

The high Reynolds number version of the k-ε model cannot account for any transitional effects. It incorporates only the turbulent viscosity and neglects the influence of the laminar viscosity entirely. This is the major reason why a high-Reynolds number turbulence model is not used in this study.

Contrary to the high-Reynolds number turbulence model, the LRN version can potentially predict transition to turbulence and relaminarization since it takes the effect of the molecular viscosity into account where necessary. It has been shown (Jones and Launder (1972), Launder and Spalding (1974), Schmidt and Patankar (1987)) that low Reynolds number models *are* capable of predicting transition, at least qualitatively. Schmidt and Patankar (1987) investigated the prediction performance of the models of Jones and Launder and of Lam and Bremhorst in steady flow over a flat plate. They found that the starting location of transition was predicted too early and that the length over which transition occurred was underpredicted. Jones and Launder (1972) report the performance of their turbulence model for fully developed pipe flow. It can be seen that their model predicts transition at a too low Reynolds number of 1600 as well as a too narrow range of Re over which the transitional state of the flow prevails (Figure 6.1).

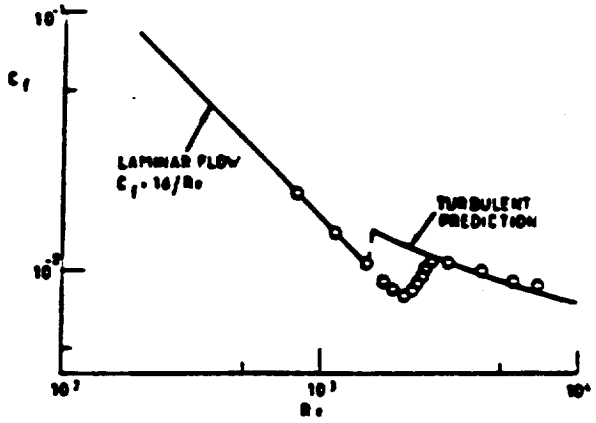

Fig. 6.1: Transition prediction for fully developed pipe flow with the model of Jones and Launder (1972).

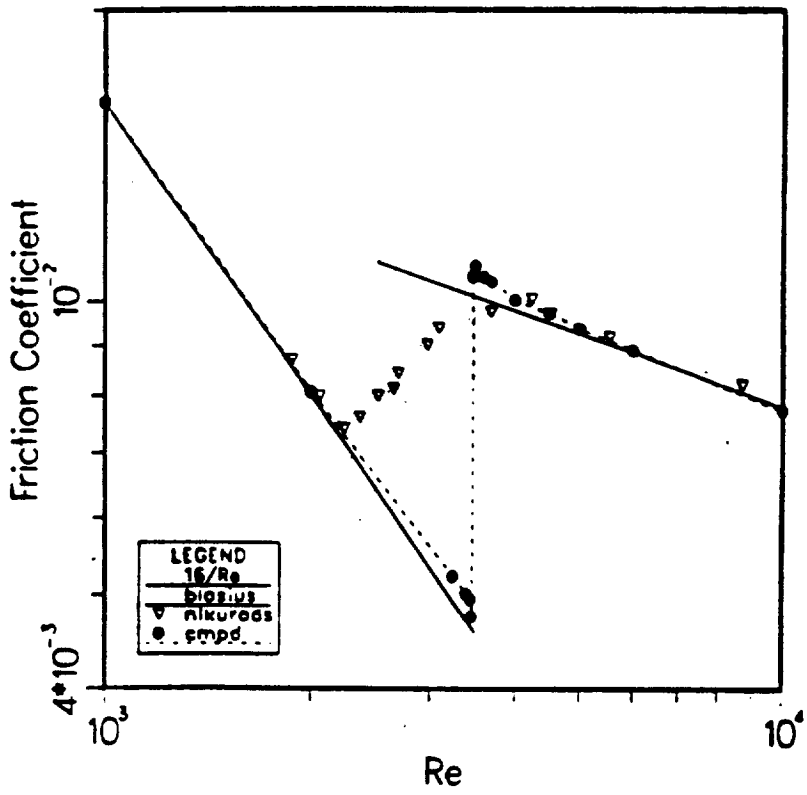

Fig. 6.2: Transition prediction in fully developed pipe flow with the model of Lam and Bremhorst (1981).

In this study, two series of transition tests were performed, one for 10% turbulence intensity, another one for 0.5%. Most of the tests were performed with a grid of 33*51 grid points, where the axial grid lines were equally spaced and the radial grid lines were densely spaced near the wall. This grid was sufficient for the moderate Reynolds numbers under investigation and still provided reasonable convergence rates (as compared to larger grids).

In the following, we define transition of the fully developed flow as the point when the computed friction coefficient at the downstream end of the pipe starts to deviate from the corresponding laminar value. According to this definition, both tests give the same result independent of the turbulence intensity at the inflow and are in line with the findings of Schmidt and Patankar (1987) for transition predictions for flow over a flat plate and Jones and Launder (1972) for fully developed pipe flows. Figure 6.2 shows the results of the friction coefficient computations as well as the measurements of Nukuradse (1932). As can be seen, transition is predicted at a Re number of 3450 which corresponds to the upper end of the Re-number transition range shown by Nikuradse.

The Re number range over which transition is predicted is much smaller than measured for example by Nikuradse (1932, ca. 2 Re_{cr}). At one point in the sequence of computations, the predicted cf values jump suddenly from the laminar values of 16/Re to a turbulent value when the Re number is increased slightly. This does not properly reflect the real intermittent transition process which occurs over a rather broad band of Re numbers.

One must bear in mind that the results shown in Fig. 6.2 are obtained for L/D ratios of up to 500. In a Stirling engine heat exchanger, and in the experimental test rig for oscillating flow research at the University of Minnesota, the L/D ratio is much less. It is therefore of great practical interest to examine the predictions of the model with regard to the *developing* flow. For low turbulence intensity levels at the inflow, the usual laminar flow behavior with laminar entrance length and parabolic fully developed profile is predicted up to a Reynolds number of 3450. At high Re, the flow will first develop as in a

laminar flow. At some point downstream, the flow will become unstable and undergo transition from laminar to turbulent. Since this transition takes place over a very small axial distance, we will speak of a *transition front*. One example of such a transition front is shown in Fig. 6.3. Further, it is interesting to note that the predicted transition occurs simultaneously over the cross section. The location of this transition front depends largely on two factors: (i) the level of turbulence intensity at the inflow (TI) and (ii) the Reynolds number.

Turbulence intensity dependence. As the turbulence intensity is decreased, the transition front moves downstream . In the limit of a very low turbulence intensity the transition front approaches a maximum downstream location and does not move any further (see Fig. 6.4). This can be explained from a physical or numerical point of view: In addition to the imposed turbulence intensity at the entrance of the tube, in real pipe flow there are always disturbances downstream. If the Re number is sufficiently high, these disturbances will cause the flow to become unstable even if extreme caution is exercised to have a very low level of turbulence intensity at the inflow. Numerical approximations also act like physical disturbances. Even if we turn off the imposed turbulence intensity, there will be a residual level of "numerical disturbances" in the domain which will cause transition. A lower turbulence intensity also makes the transition front steeper, more abrupt.

As mentioned above, the results for the fully developed flow are independent of the turbulence intensity at the inflow. However, in the developing region in the transitional Re number range the turbulence intensity level has a decided effect on the flow for most of the length. At Re = 3450, the flow well downstream will be predicted ultimately to be laminar. For a TI of 0.5%, the flow follows a normal laminar behavior throughout. Increasing the TI at this Re number creates a region where the flow looks very much like a turbulent flow over much of the tube length. For example, a TI of 10% will lead to a seemingly fully developed turbulent profile at an x/D beyond 100, but at x/D = 250, the flow suddenly relaminarizes (Fig. 6.5 and Fig. 6.6). This implies that, contrary to the fully developed

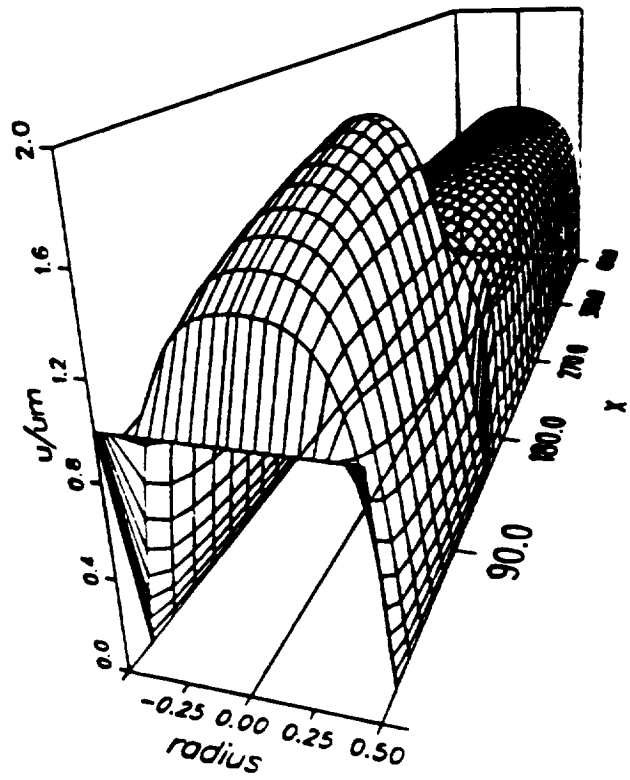

Fig. 6.3: Transition front example for a Re number of 6000 and a turbulence intensity at inflow of 0.5%.

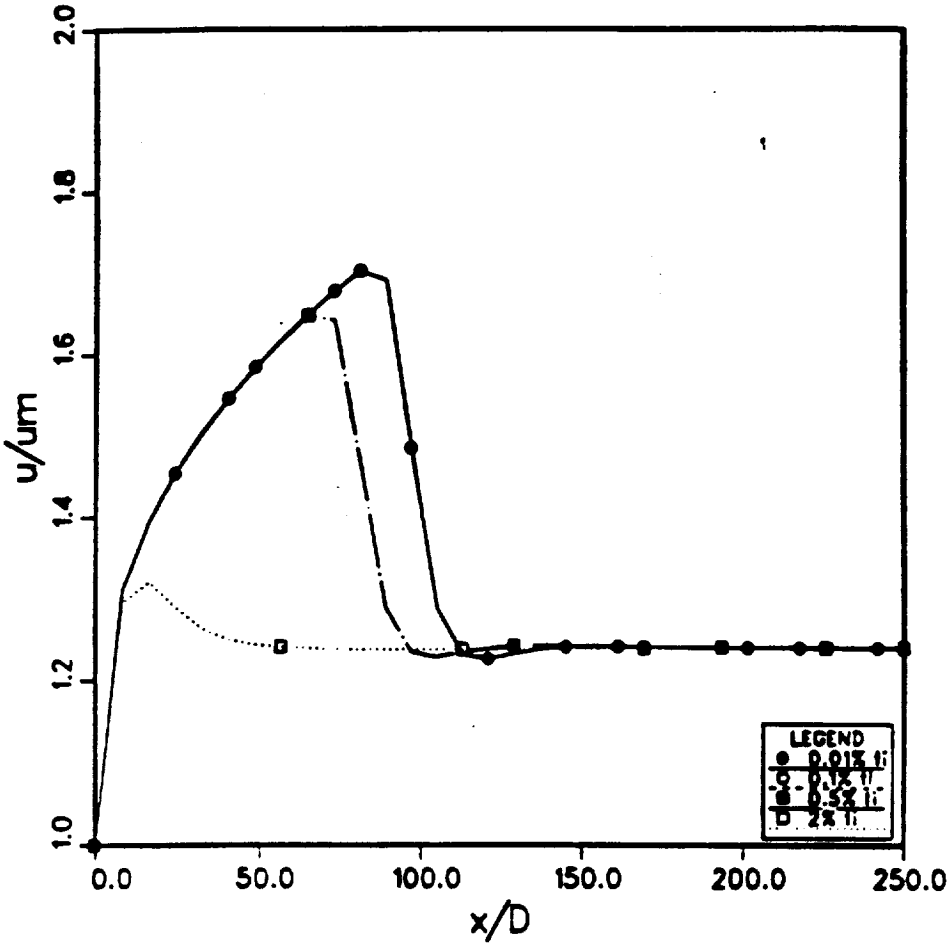

Fig. 6.4: Influence of the turbulence intensity at inflow on the location of the transition front at Re = 6000: normalized centerline velocity vs. axial distance.

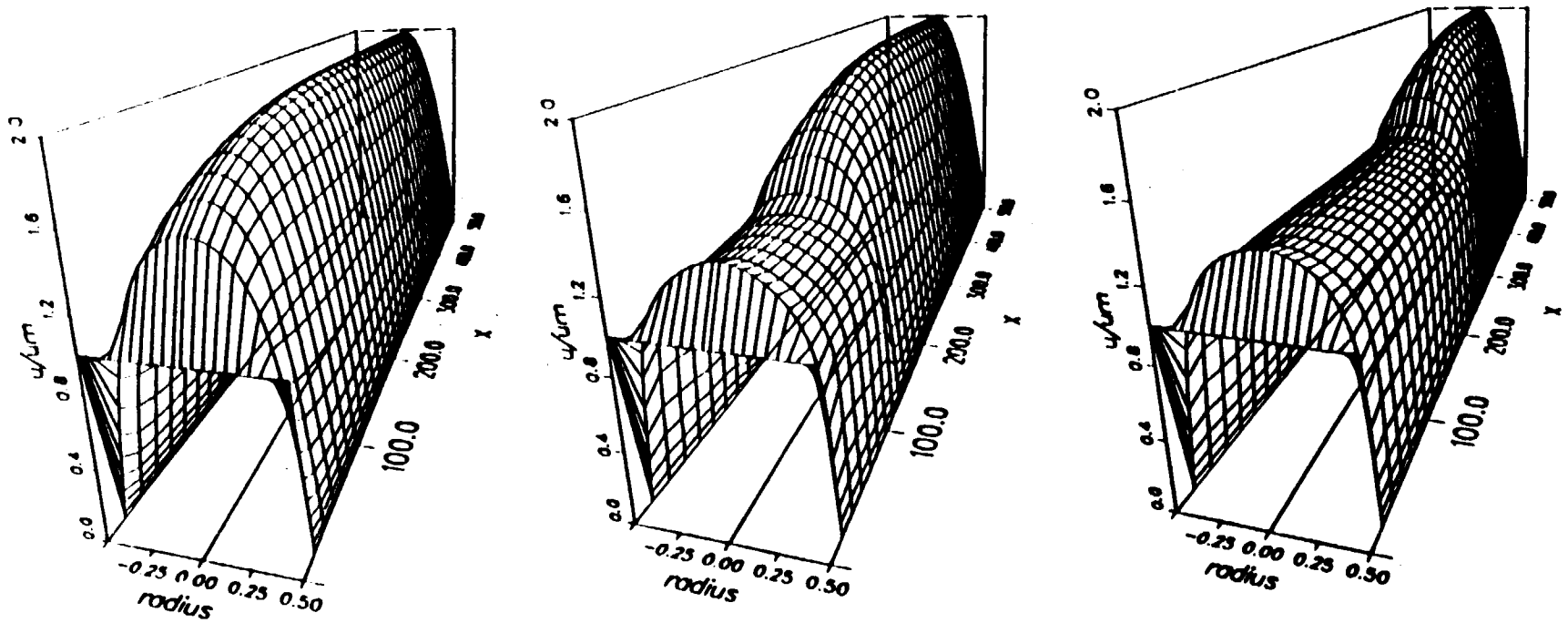

Fig. 6.5: Entrance length relaminarization at Re=3450 for different levels of turbulence intensity at the inflow.

Left: TI=0.5%; center: TI=2%; right TI=10%.

33 by 51 grid

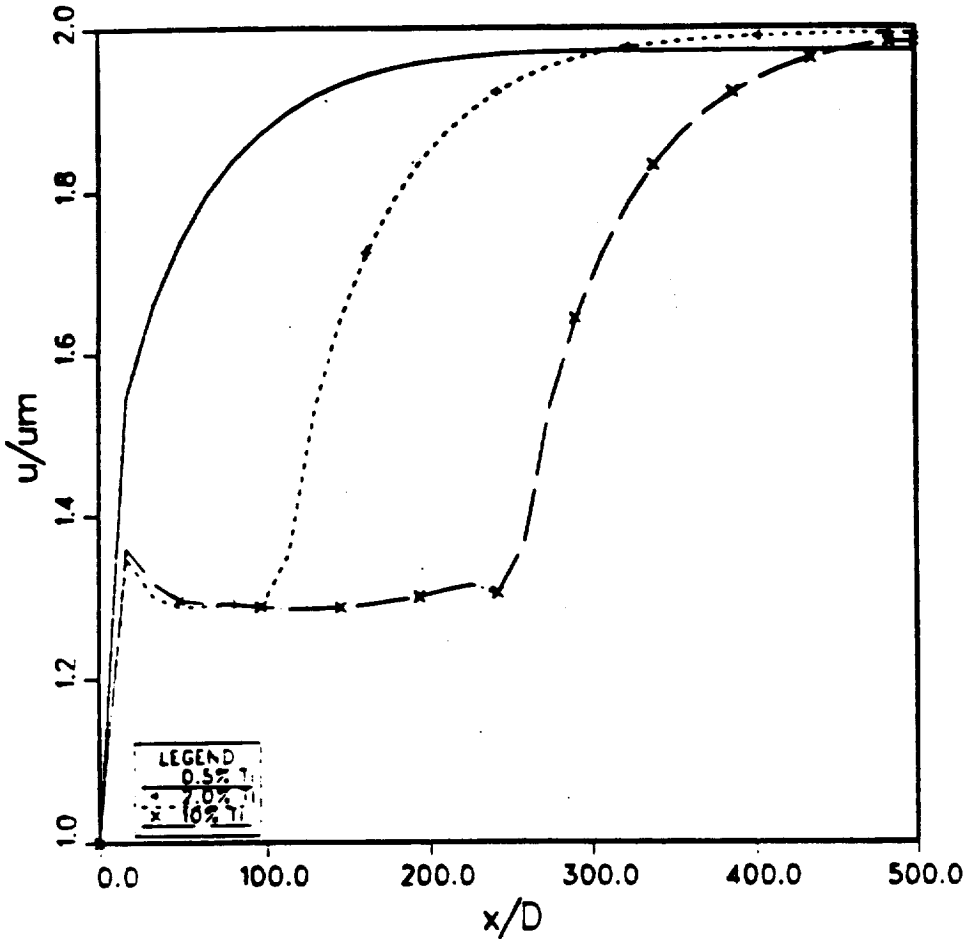

Fig. 6.6: Entrance length relaminarization at Re = 3450 for different levels of turbulence intensity at inflow: normalized centerline velocity vs. axial distance.

case, the developing region of the flow at moderate Re is strongly affected by the boundary condition at inflow.

Reynolds number dependence. As the Reynolds number is increased, the transition front moves upstream, Fig. 6.7. At higher Re numbers (e.g. >5000) and not too low turbulence intensities (e.g. >2%) the transition front can hardly be seen any more. Then, transition takes place practically instantaneously at the entrance of the tube. This is probably the reason why the existence of such a transition front is not mentioned in any of the reviewed experimental papers on turbulent pipe flow.

An interesting situation occurs around the nominal value for transition for the fully developed flow. When the Re number is decreased further, the transition front moves downstream. With very low turbulence intensity at inflow, the location of the transition front stands at an x/D of around 300 for Re = 3470. When the Re number is lowered further to 3460, the transition front hardly moves downstream any more, and immediately after the front the flow starts to relaminarize, Fig. 6.8. The final profile at this Re number looks very much like a normal laminar profile. Here, the transition front looks like a "cut" into a laminar flow. Lowering the Re number even further just reduces this "cut" until it completely disappears at Re = 3450.

Initial guess dependence. At very low inflow turbulence intensities, the predicted *location* of the transition front is also affected by the choice of the initial guess for k and ε in the computational domain. Here, the initial guess for k is under investigation. A typical initial guess for k and ε inside of the computational domain is just like the specification of k and ε at the inflow. For the results shown in Fig. 6.9, the initial choice of the turbulence intensity inside of the domain was varied while the TI at inflow was held constant. The results can also be explained with the action of "numerical disturbances" as above. Each initial guess also represents an initial error and leads to a particular level of numerical disturbance. In the near vicinity of transition, both the laminar and turbulent solutions for the equations are permissible and equally likely. In reality, such a situation would be

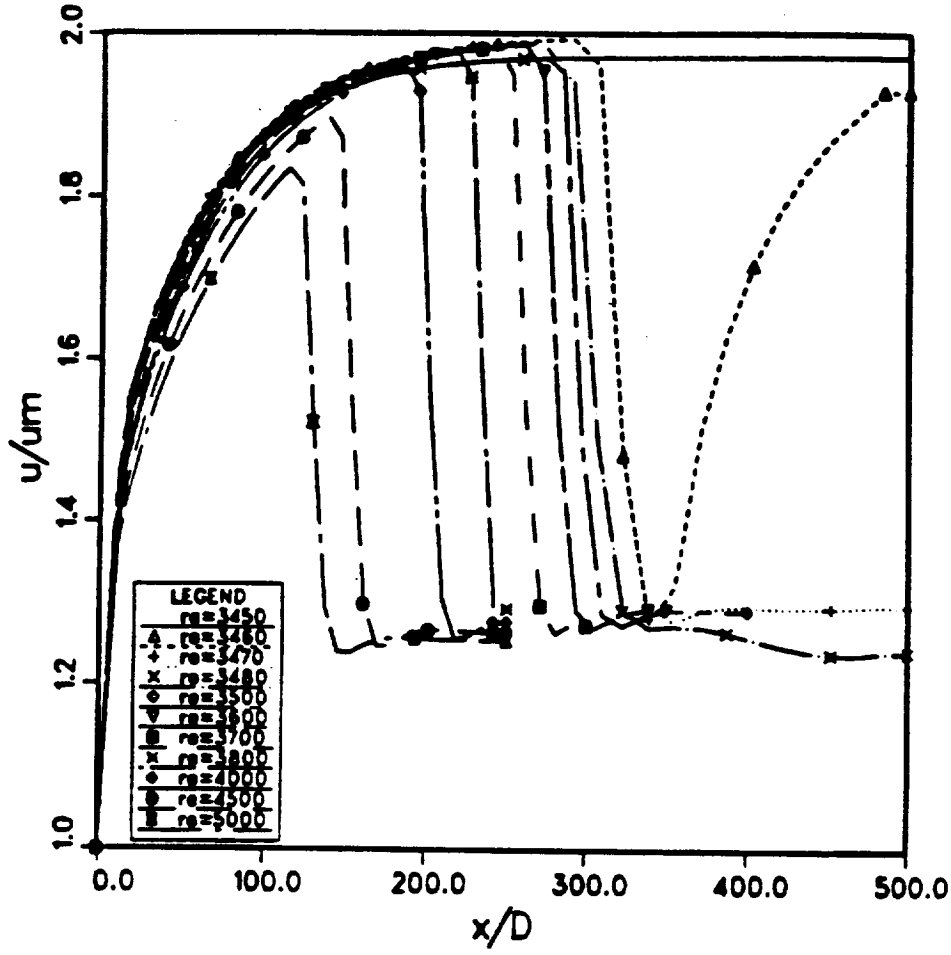

Fig. 6.7: Influence of the Reynolds number on the location of the transition front for 0.5% turbulence intensity at inflow: normalized centerline velocity vs. axial distance.

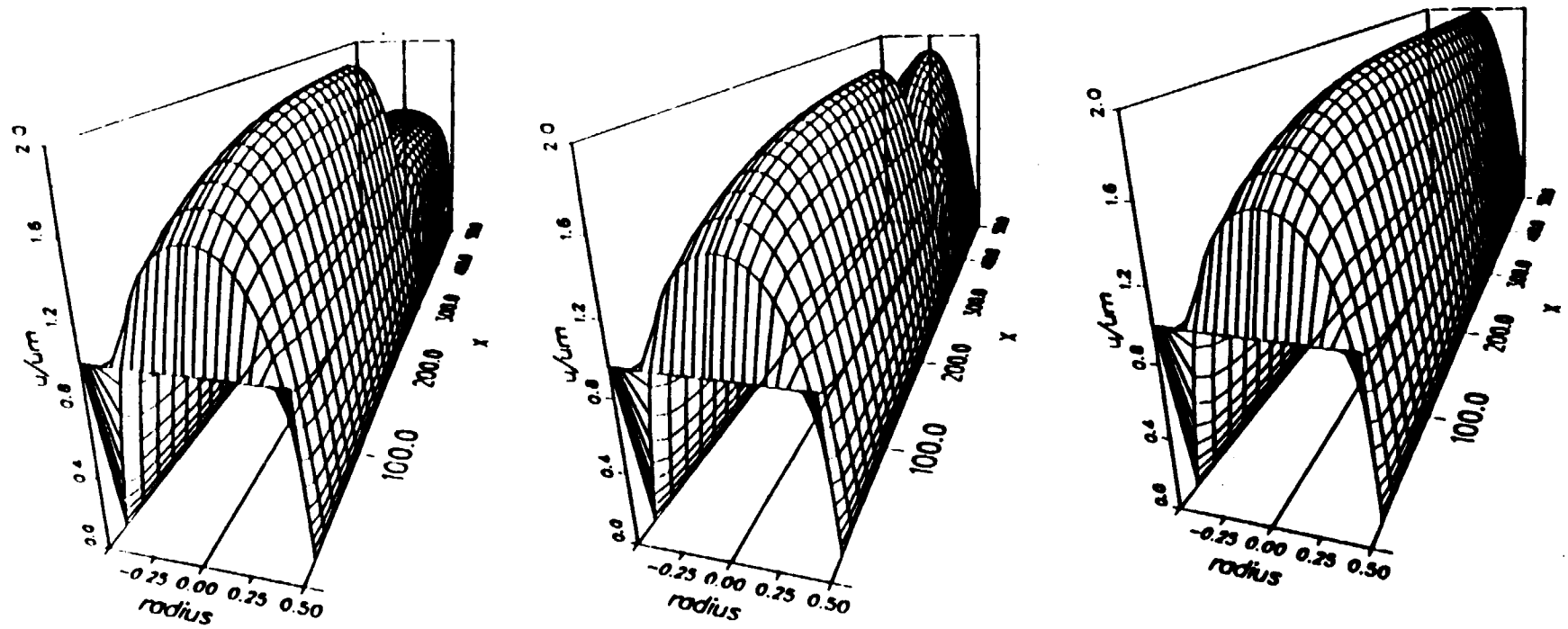

Fig. 6.8: Reynolds number and transition to laminar for 0.5% turbulence intensity at the inflow.

Left: Re=3470; center: Re=3460; right Re=3450.

Fig. 6.9: Initial guess dependence of the prediction of the transition front for low turbulence intensity at inflow (0.5%) and Re = 6000: normalized centerline velocity vs. axial distance.

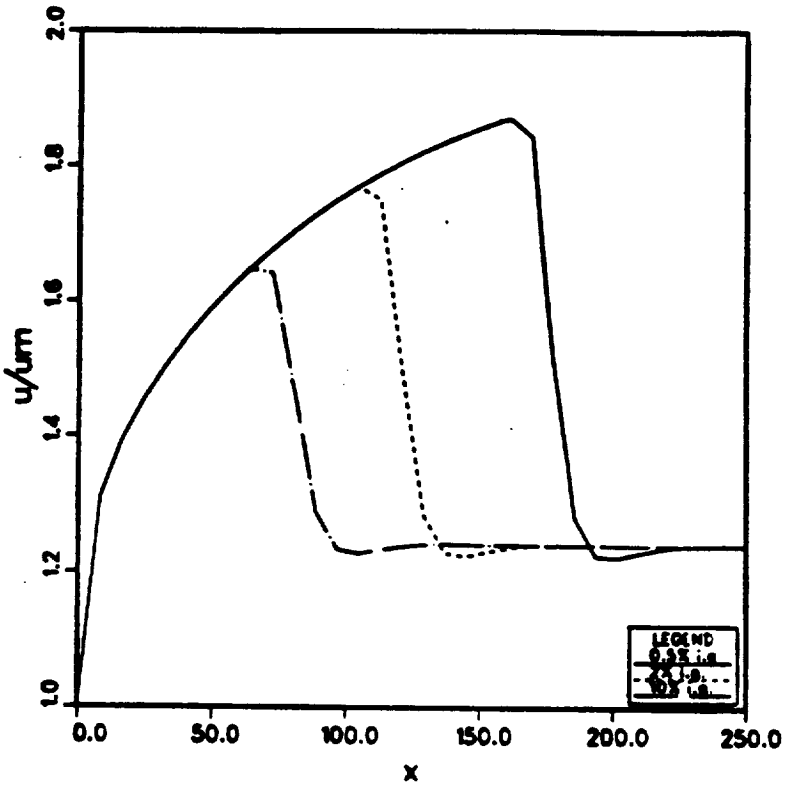

Fig. 6.10: Initial guess dependence of the prediction of the transition front for higher turbulence intensity at inflow (2%) and Re = 6000: normalized centerline velocity vs. axial distance.

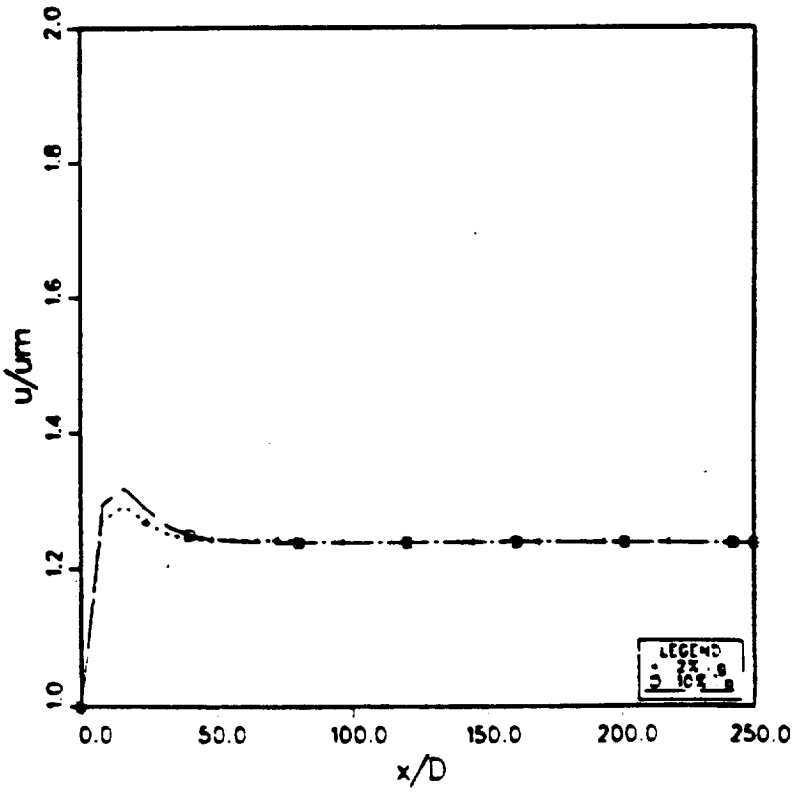

observed as intermittent. In this test we simulate a steady state situation, and the program finally must decide on one particular solution. Since both solutions are equally likely, the decision to converge in one way or the other may be influenced by small disturbances, which may very well be the ones resulting from the initial disturbance. At higher turbulence intensities, this effect is practically unnoticeable (see Fig. 6.10). It should be noted here that during the course of this research the convergence speed of the program was increased dramatically by various measures. This, however, changed the inherent numerical disturbances such that earlier results with slower convergence could not be recreated exactly with the enhanced version of the program.

Domain and grid influence. In this work it was also verified that the existence and location of the transition front is not a grid or outflow-boundary effect. It was found that a certain minimum number of radial grid points is needed to predict the front, but beyond this number, the front was predicted consistently at about the same location (Fig. 6.11).

Discussion. It is worthwhile noting that the transition front can exist at locations where the flow should be fully developed. Even though there is disagreement over the length of the turbulent entrance, it is clear that spatial transition at low TI occurs *after* this "entrance region". For the nominal, fully developed transition Re number predicted, the laminar transition length is 172.5; the transition front for Re = 3460 develops only at around $x_{tr}/D = 300$. These findings suggest that at low Re numbers and low TI the entrance length is much longer than previously assumed.

The results of this study suggest that the transition process in a finite pipe must be described by two parameters, Re and x_{tr}/D, where x_{tr}/D is the transition front cross section. Or, alternatively, the number of parameters can be reduced by adopting the notion of an external boundary layer and working with a momentum thickness Reynolds number. However, speaking of *the* transition is misleading because there is *spatial* transition from a Lagrange point of view, and there is *ordinary* transition from an Eulerian point of view very far down the pipe which depends on the Re number only.

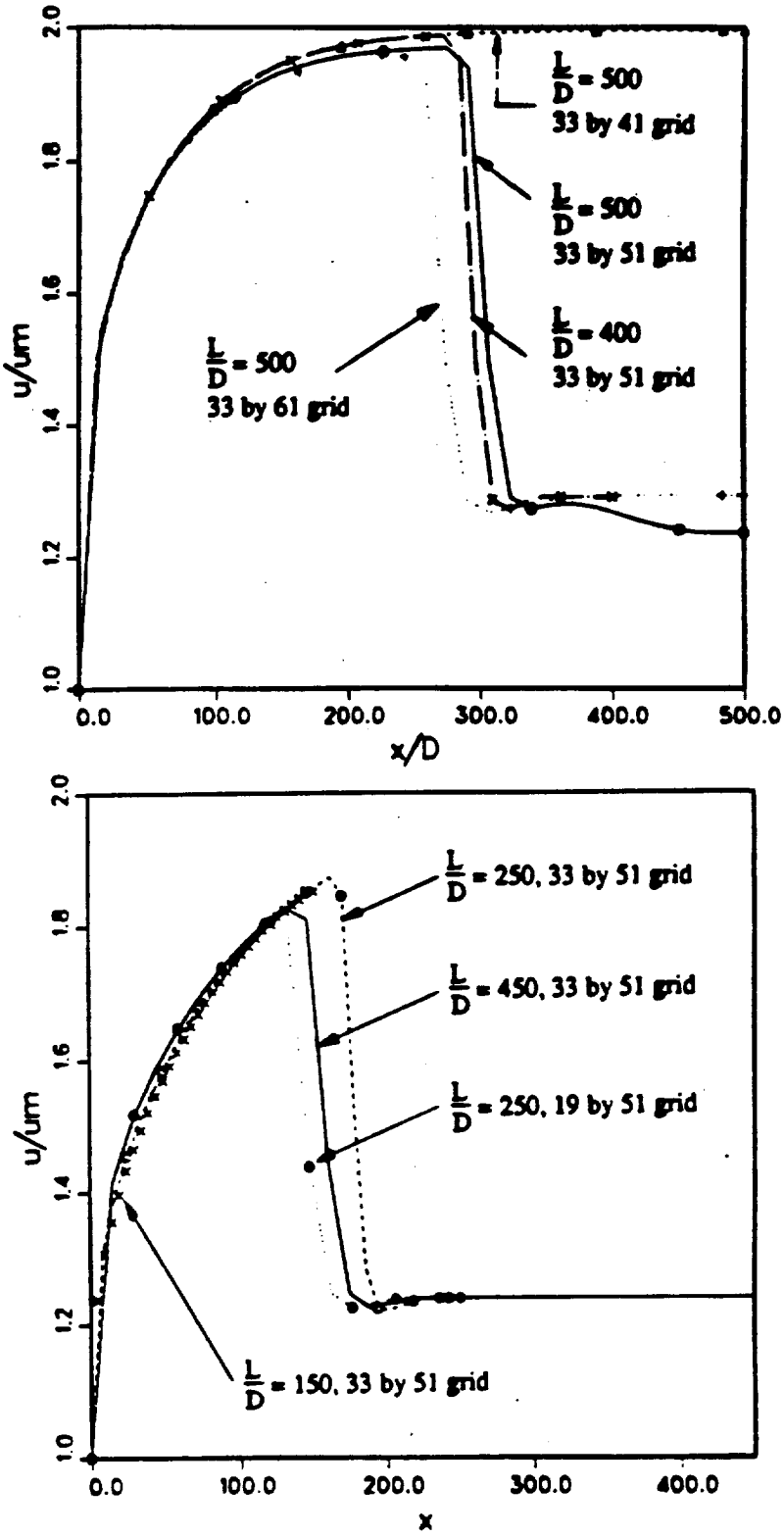

Fig. 6.11: Domain and grid influence on the predicted location of the transition front: normalized centerline velocity vs. axial distance. ***Top****: Influence of radial grid at Re = 3500.* ***Bottom****: Influence of axial grid at Re = 6000. TI = 0.5%.*

Conclusions. For developing and fully developed pipe flow, qualitatively and quantitatively correct transition predictions can be made by the Lam-Bremhorst form of the LRN k-ε turbulence model, but the transitional Re number range is too narrow. Even though the prediction for the fully developed flow is insensitive to the turbulence intensity at the inflow, the developing region is very sensitive to it with regard to transition. Since the practical applications--which we are ultimately interested in--will limit the situations to mostly developing flows, we can say that for this model, transition in the developing region can be triggered by the choice of boundary conditions for k and ε. This is very desirable in light of the findings of Seume (1988) who concluded that transition in oscillating flow is often determined by the state of the fluid before flow reversal. This fluid might have been *outside* of the computational domain at flow reversal and might be entering the domain during the computation.

6.4. On the Reproducibility of Transitional Steady Flow Results

Most of the results shown in chapter 6.2 were produced with a 33*51 grid, the same grid as used for the first computation of oscillating flow with a LRN turbulence model. It was shown that the initial guess for k and ε *does* have an effect on the prediction of the location of the transition from (Fig. 6.9) It had been found that a minimum number of radial grid points is necessary to predict spatial transition and that, generally, more radial grid points shift the transition front to lower x/D's (Figure 6.11a). However, the *existence* of a transition front seems to be independent of grid and domain effects, as long as a sufficient number of grid points are taken. A close look at Figure 6.11 shows that these conclusions were drawn at Re numbers of 3500 and 6000, both *above* the predicted "critical" Re number of 3450.

Matters are more complicated *at* the critical Re number of 3450: The findings of Figure 6.5 are quite reproducible for the exactly the same conditions (i.e. initial guess, grid, TI etc.). However, it was found that , for a TI of 2% and a finer grid of 63 by 63 grid points,

the relaminarization of Figure 6.5b could *not* be reproduced. Rather, the flow would converge to a fully turbulent situation (Figure 6.12)! To test the stability of the coarse grid solution (33 by 51, Fig. 6.5b), it was transposed on a 63 by 63 grid and served as the initial guess for a continuation of this solution with the fine grid. The results of this continuation are identical to the initial guess and the solution does not change (Figure 6.13). Vice versa, the results originally obtained from the fine grid solution (63 by 63) were transformed to a coarser grid (33 by 51) and used as initial guess for a continuation of this solution on the coarser grid. Similarly, the results were identical to their initial guess, and *no* spatial relaminarization was predicted (Figure 6.14). This leads to the conclusion that a continuation of a converged solution obtained with one grid will not change these converged results independently of the grid used in the continuation. Additional computations (no continuations) done with a 51*51 grid and a 33 by 63 grid did not predict the relaminarization of Figure 6.5b (Figure 6.15).

Table 6.1: Grid influence at "critical" Reynolds number of 3450

Re	TI	grid	continuation of other grid	relaminarization predicted?	Figure
3450	2%	33*51	-	yes	6.5b
3450	2%	33*51	63*63	no	6.14
3450	2%	51*51	-	no	6.15
3450	2%	33*63	-	no	6.15
3450	2%	63*63	-	no	6.12
3450	2%	63*63	33*51	yes	6.13

For a TI of 0.5%, the 33 by 51 and 51 by 51 grids predict fully laminar flow, whereas the 33 by 63 and 64 by 64 grid predict fully developed turbulent flow (Figure 6.16). These

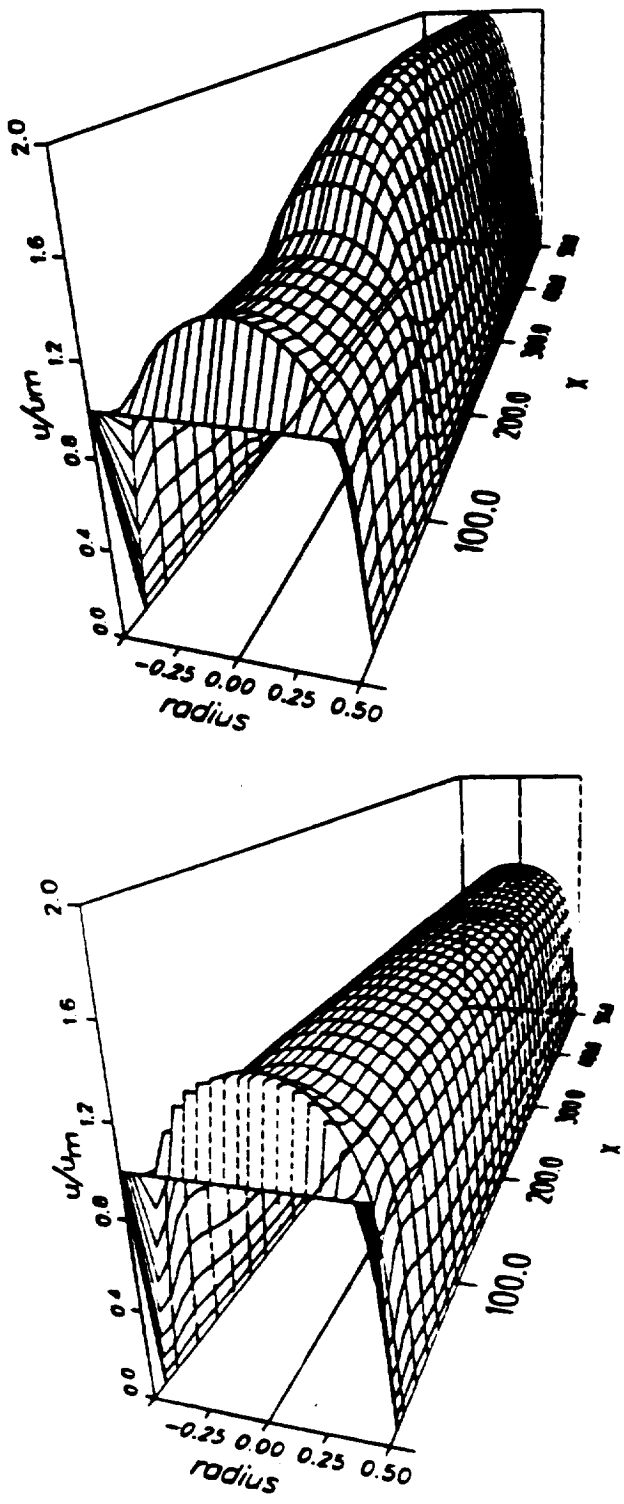

*Fig. 6.12: Predictions for Re = 3450 and TI = 2%. **Top**: Relaminarization predicted with 33 by 51 grid. **Bottom**: Fully turbulent flow prediction with 63 by 63 grid*

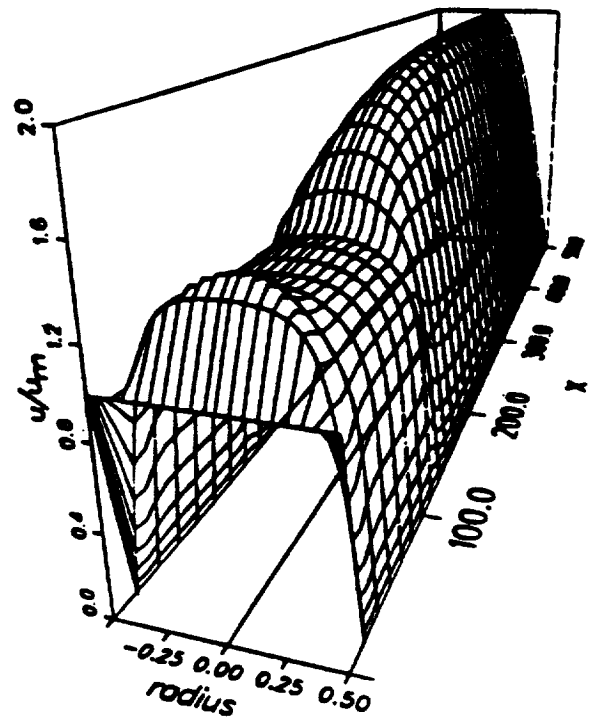

Fig. 6.13: Continuation of results of Fig. 6.12a with 63 by 63 grid.

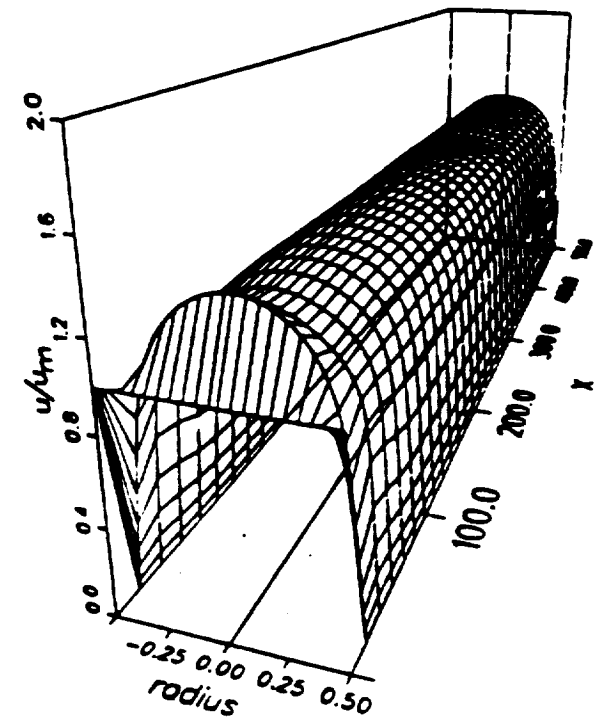

Fig. 6.14: Continuation of results of Fig. 6.12b with 33 by 51 grid.

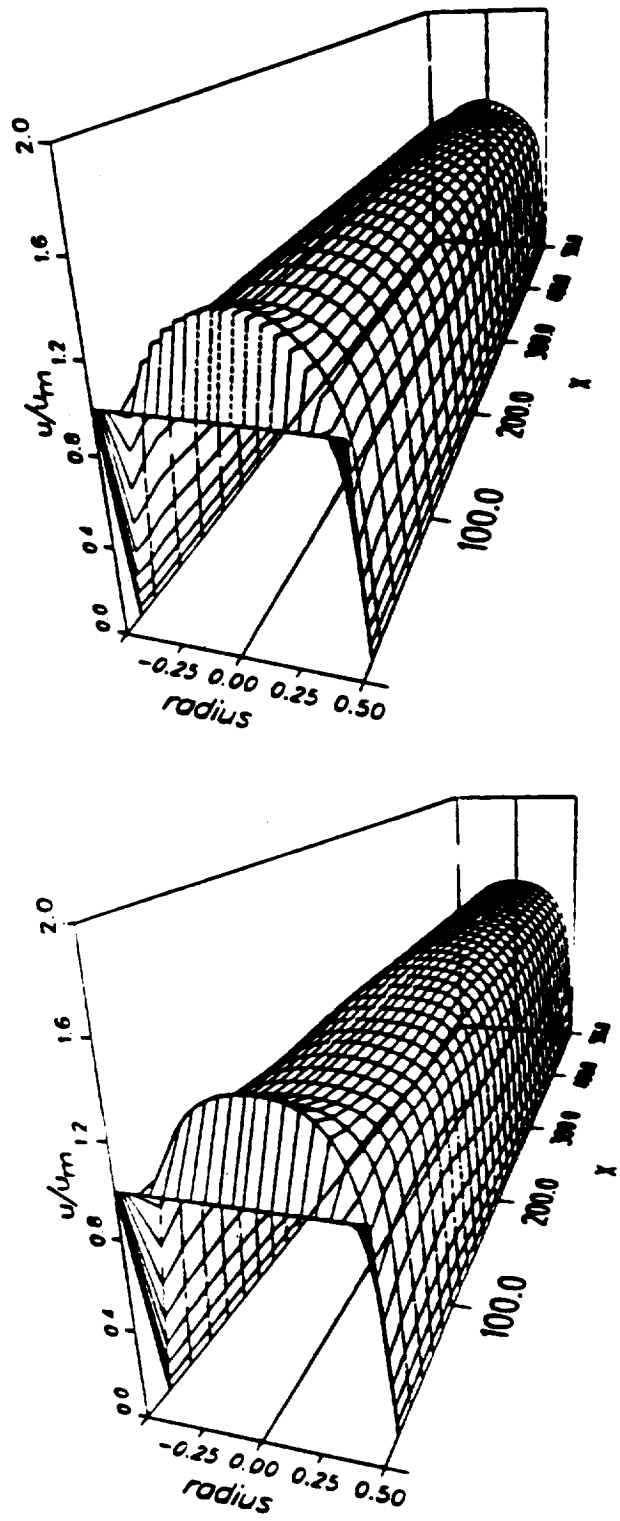

Fig. 6.15: Predictions for Re = 3450 and TI = 2%. Top: 51 by 51 grid, bottom: 33 by 63 grid.

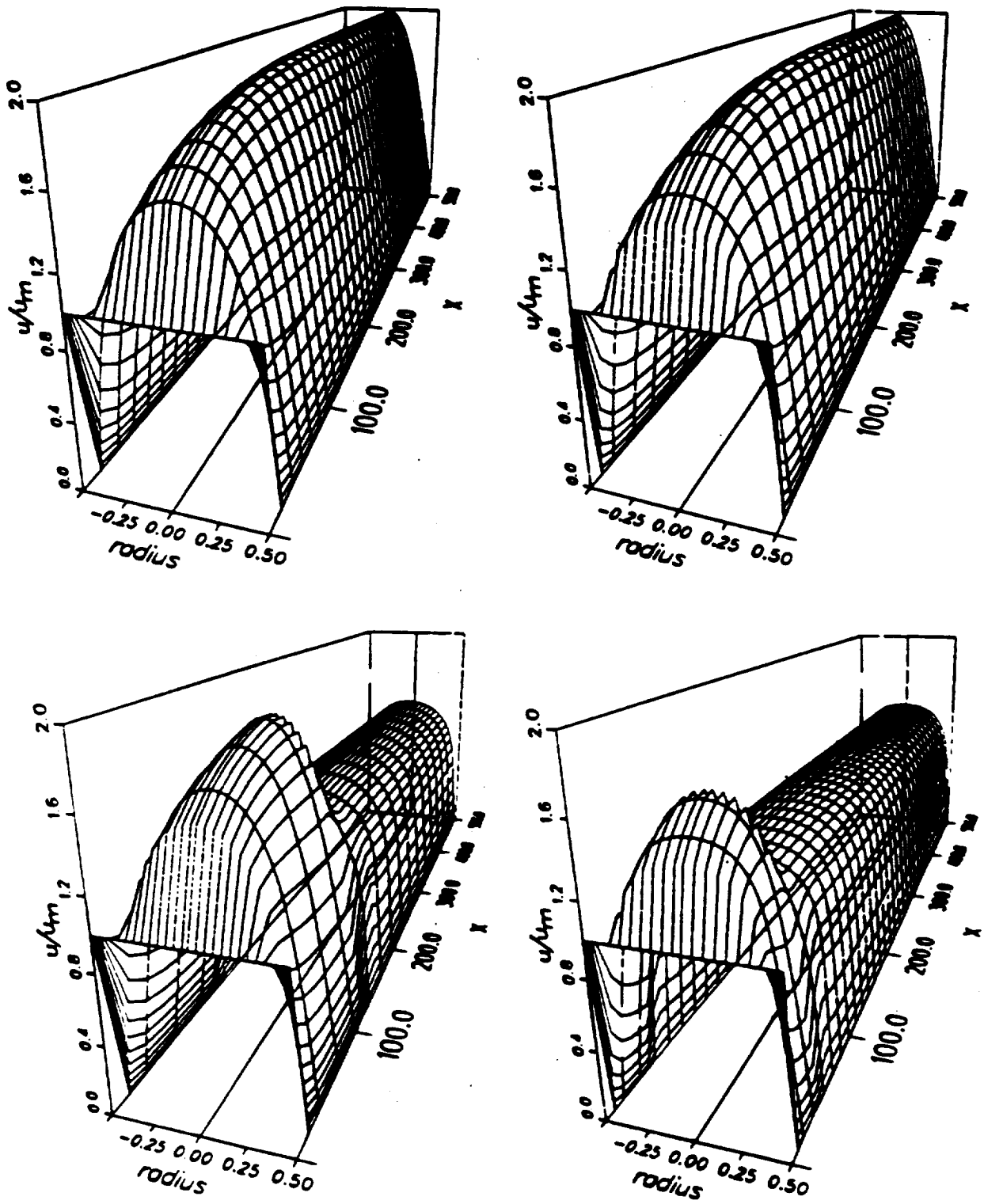

Fig. 6.16: Predictions for Re = 3450 and TI = 0.5% for various grids. Top left: 33 by 51; top right: 51 by 51; bottom left: 33 by 63; bottom right: 64 by 64.

findings clearly show that there is a severe grid influence on the predictions at the "critical" Re number of 3450.

Figure 6.17 shows another influence: both velocity profiles are computed for the exactly same conditions, except for the under-relaxation factors for k and ε. It is evident that the loci of the transition front are not identical.

The next consideration was whether qualitatively similar results as described in chapter 6.2 (e.g. at a somewhat different Re number) are predicted for a finer grid (64 by 64). A number of computations determined that the new $Re_{cr,64*64}$; it was found to be at Re = 2985 (Figure 6.18). However, at Re = 2990, the flow underwent a "normal" spatial transition at around x/D=400, whereas at Re=2885 a transition did not occur. A relaminarization of the flow as shown in Figure 6.8 for 3460 was *not* detected with this grid.

Table 6.2: Predictions at around Re = 2985

Re	TI	grid	fully developed flow prediction
2985	0.5%	33*51	laminar
2985	0.5%	64*64	laminar
2985	0.5%	50*91	laminar
2990	0.5%	33*51	laminar
2990	0.5%	64*64	turbulent
2995	0.5%	50*91	laminar

The grid independence of the new critical Re number $Re_{cr,64*64}$ was checked by again changing the grid to a finer radial grid and a slightly coarser axial grid (50 by 91 grid

points). Two computations at Re numbers of 2985 and 2995 *did not* predict transition for a TI of 0.5% (Figure 6.19).

At the new "critical" Re number, the influence of TI was studied. While for a TI of 0.5% the flow is laminar throughout, a TI of 10% causes the flow to undergo transition to turbulent without spatial relaminarization. This means that for the 64 by 64 grid the TI boundary condition *does* influence predictions for the fully developed regime. This is a clear contradiction to the statement made earlier, i.e. that the TI does not influence the fully developed regime (Figure 6.20).

It is interesting to see how a predicted solution changes if the TI is varied suddenly. For this, the converged solution of Re = 2985, TI = 0.5% (64 by 64 grid) was taken as initial guess for a computation with TI set to 10%. The result of this computation can be seen in Figures 6.21 and 6.22 as a function of the number of iterations. As one sees, the laminar portion of the flow is slowly pushed out as the iterations proceed, or--alternatively--with time, the flow in the pipe will become turbulent when all of a sudden the low turbulence intensity at the inflow is replaced by a high one. Alternatively, if the converged solution for Re = 2985, TI = 10% is taken as an initial guess for a computation where TI = 0.5%, the greatest part of the flow remains turbulent. The laminar portion of the flow near the entrance of the pipe is extended only slightly due to the sudden decrease of the disturbance level (Figures 6.21 and 6.23).

Conclusions:

1) In the transitional Re number range the results of chapter 6 are
   - qualitatively valid.
   - quantitatively valid only for the very conditions for which they were established (e.g. a 33 by 51 grid, specific under-relaxation factors, etc.).
2) Transition in the fully developed regime as well as spatial transition is influenced by numerical disturbances which in turn depend on grid, under-relaxation, initial guess for

the various variables, etc.. Therefore there is no *one* typical transition performance of the k-ε turbulence model.

3) For lower and higher Re numbers, the predictions are valid and unambiguous.
4) The performance of the turbulence model reflects the physics insofar as two solutions, namely the laminar and the turbulent one, become equally likely around transition and "compete" for dominance.
5) For about the first 100 diameters downstream from the pipe entrance the contradiction with regard of the sensitivity of fully developed flow to TI does not have severe consequences. This region *is* definitively affected by the TI as shown by all computations.

6.5. Transition Predictions of Constant Acceleration Pipe Flow

The next logical step to check the performance of the k-ε model regarding transition to turbulence is to apply it to this physical situation: A fluid in a long pipe is initially at rest. At time = 0, the fluid is accelerated at a constant rate. As the Re number increases, the flow will undergo transition at a Re number higher than in quasi-steady flow. This situation was experimentally investigated by Lefebre and White (1987). Comparison of the numerical predictions with the experiment allows the turbulence model to be tested for acceleration in a transitional situation. Although this experiment has much in common with the accelerating phase in oscillating flow, there is one major difference: Here, the flow before transition is absolutely undisturbed, and the disturbances develop only at transition. In oscillating flow, there is some level of residual turbulence before transition which will most probably trigger transition earlier than seen here. While we may expect to see some grid dependence for the situation considered in this chapter, this dependence will be significantly smaller in oscillating flow because of the residual turbulence.

The goal of this study is to determine how well the turbulence model predicts transition to turbulence in accelerated pipe flow.

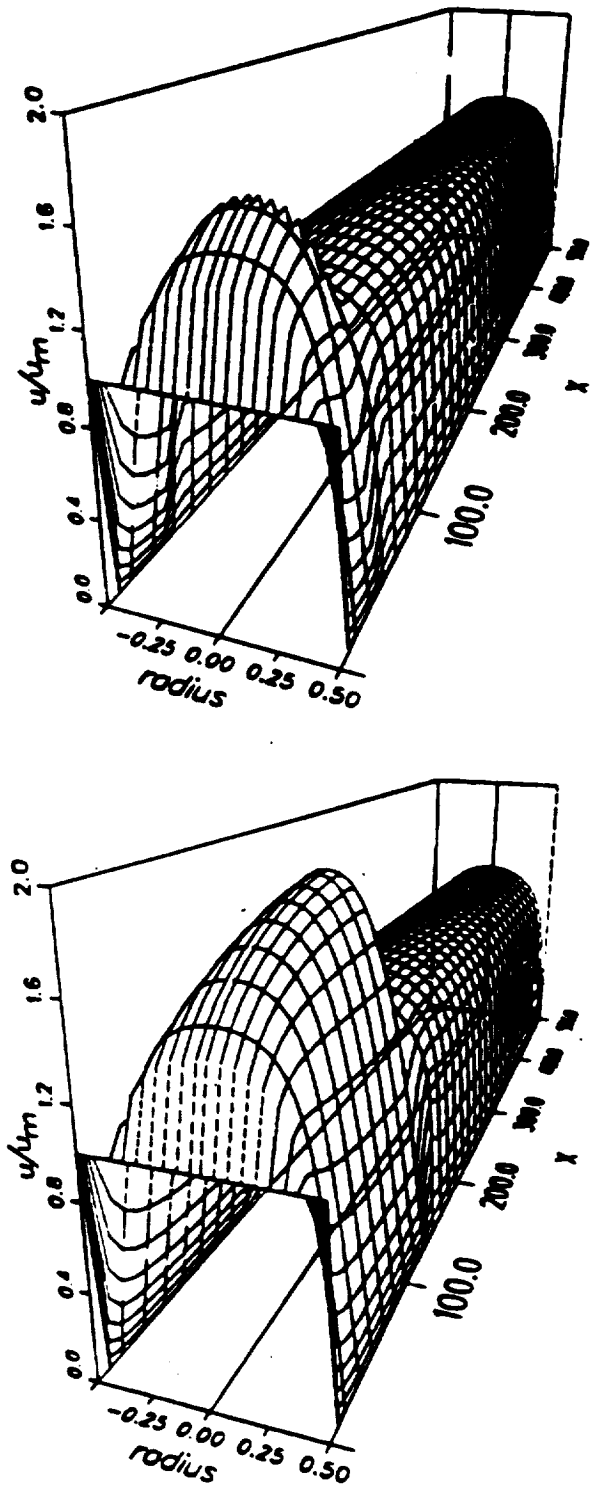

Fig. 6.17: Predictions for Re = 3450 and TI = 0.5% for various under-relaxation factors α: Top: $\alpha_k = \alpha_\varepsilon = 0.5$; bottom: $\alpha_k = \alpha_\varepsilon = 0.7$.

Fig. 6.18: Influence of the Reynolds number on the location of the transition front for 0.5% TI at inflow: normalized centerline velocity vs. axial distance.

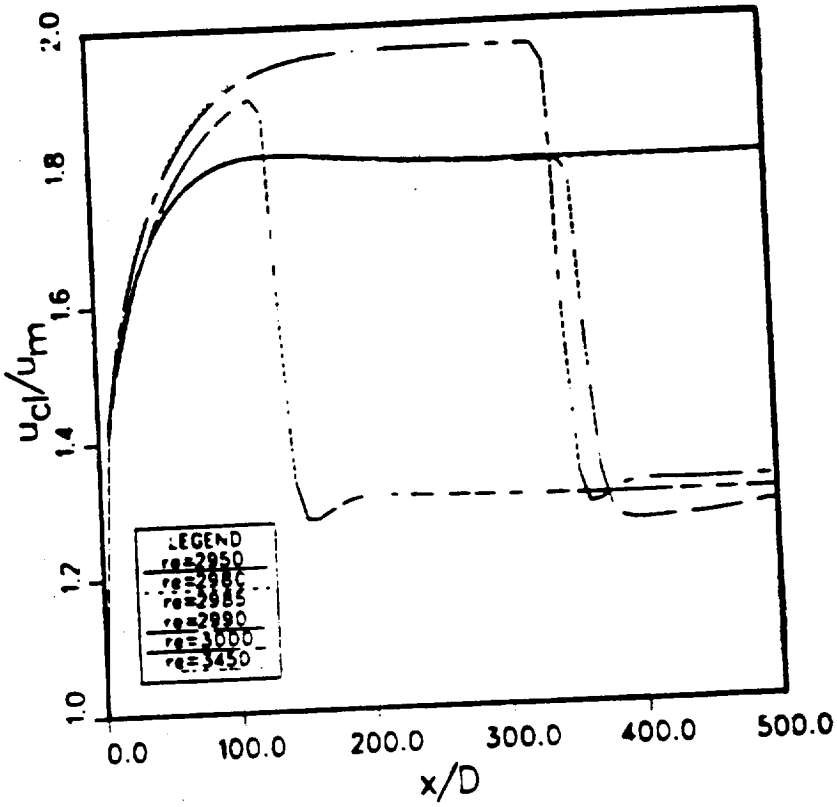

Fig.6.19: Grid dependence of the critical Re number obtained on the 64 by 64 grid.

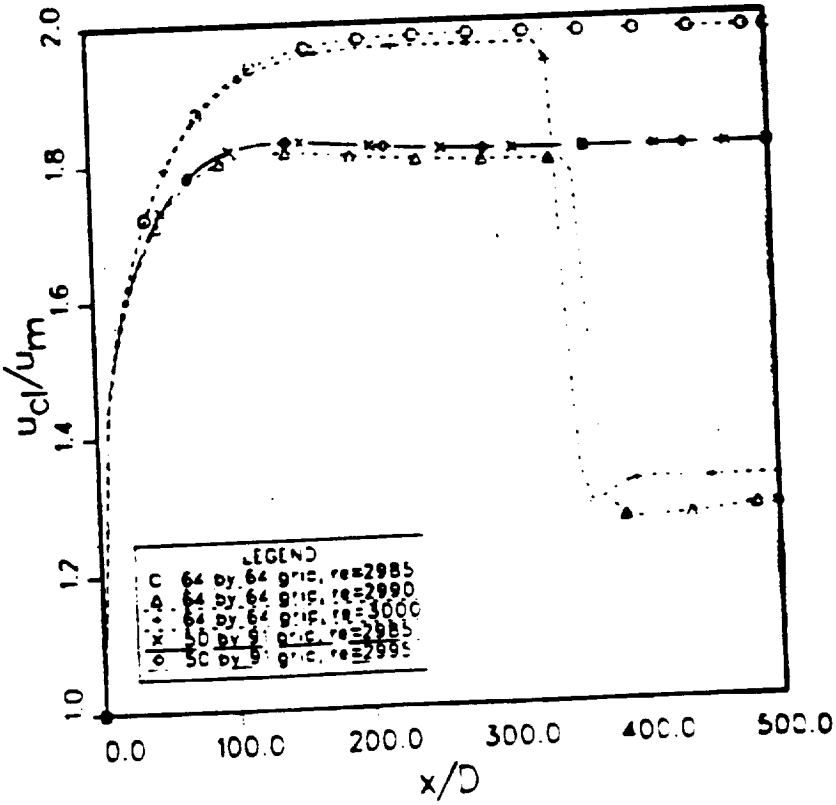

Fig. 6.20a: Predictions at Re = 2985 for different levels of TI at inflow. TI = 0.5%, 64 by 64 grid.

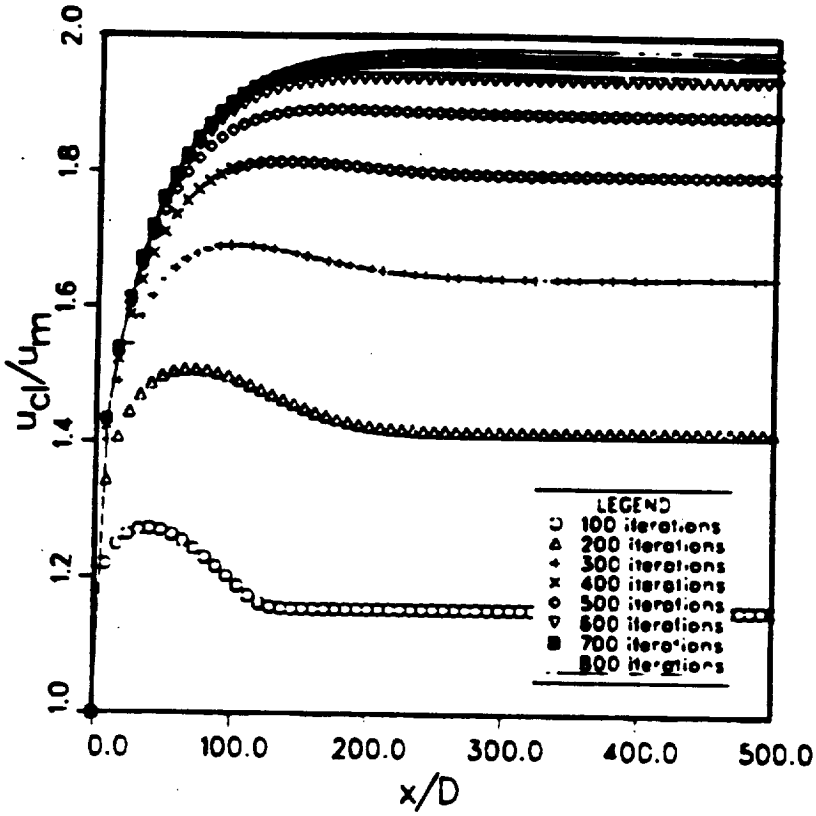

Fig. 6.20b: Predictions at Re = 2985 for different levels of TI at inflow. TI = 10.0%, 64 by 64 grid.

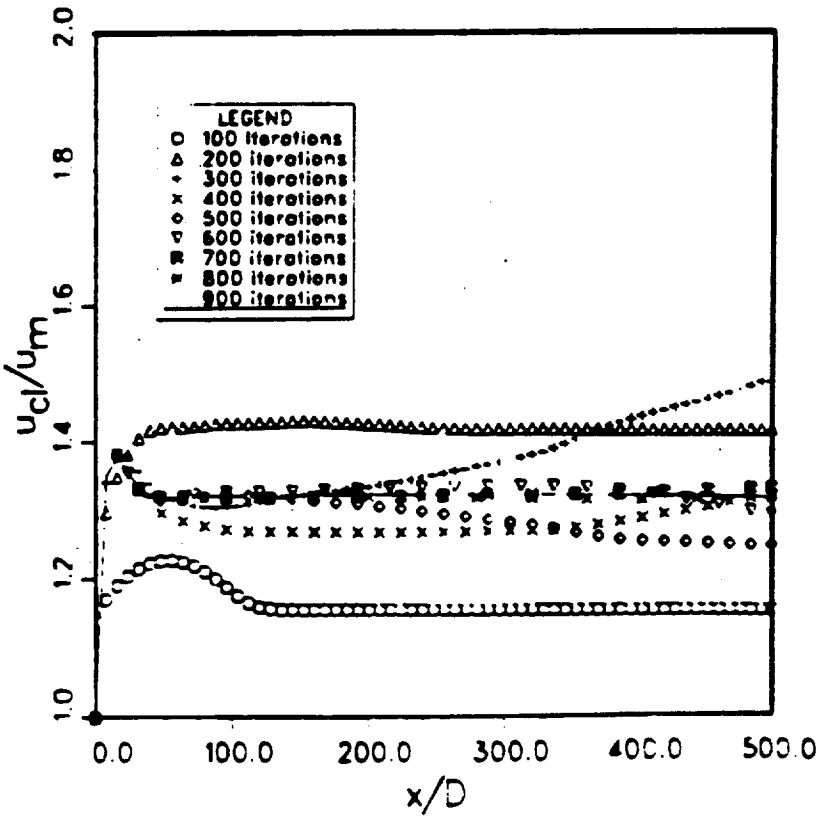

Fig.6.21a: Convergence of solution when TI is suddenly varied. a) Start from the solution for TI = 0.5%, continuation with TI = 10%.

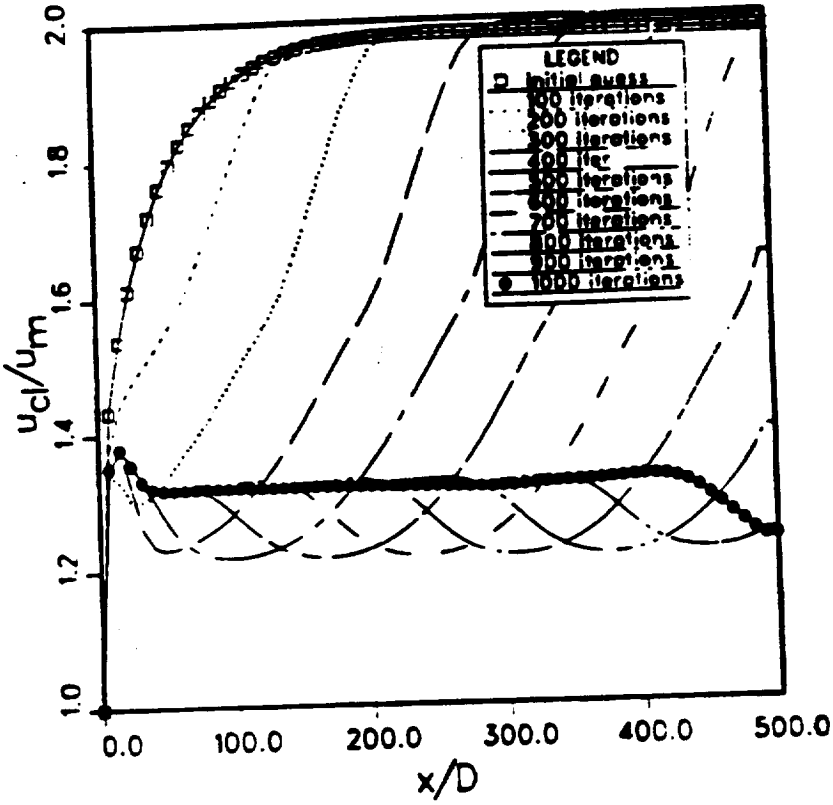

Fig.6.21b: Convergence of solution when TI is suddenly varied.b) Start from solution for TI = 10%, continuation with TI = 0.5%.

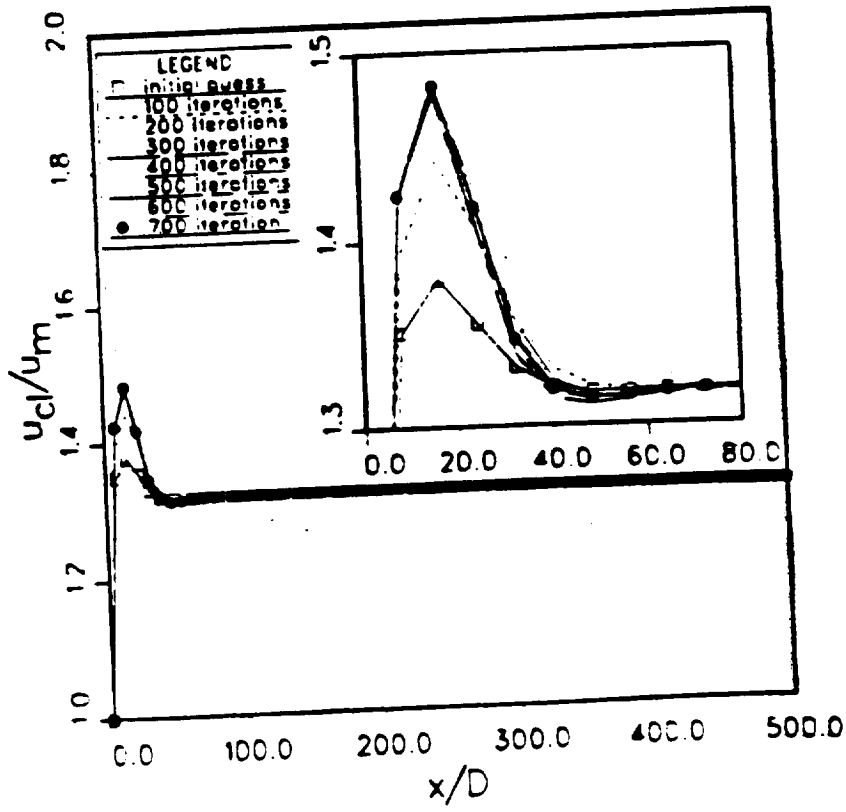

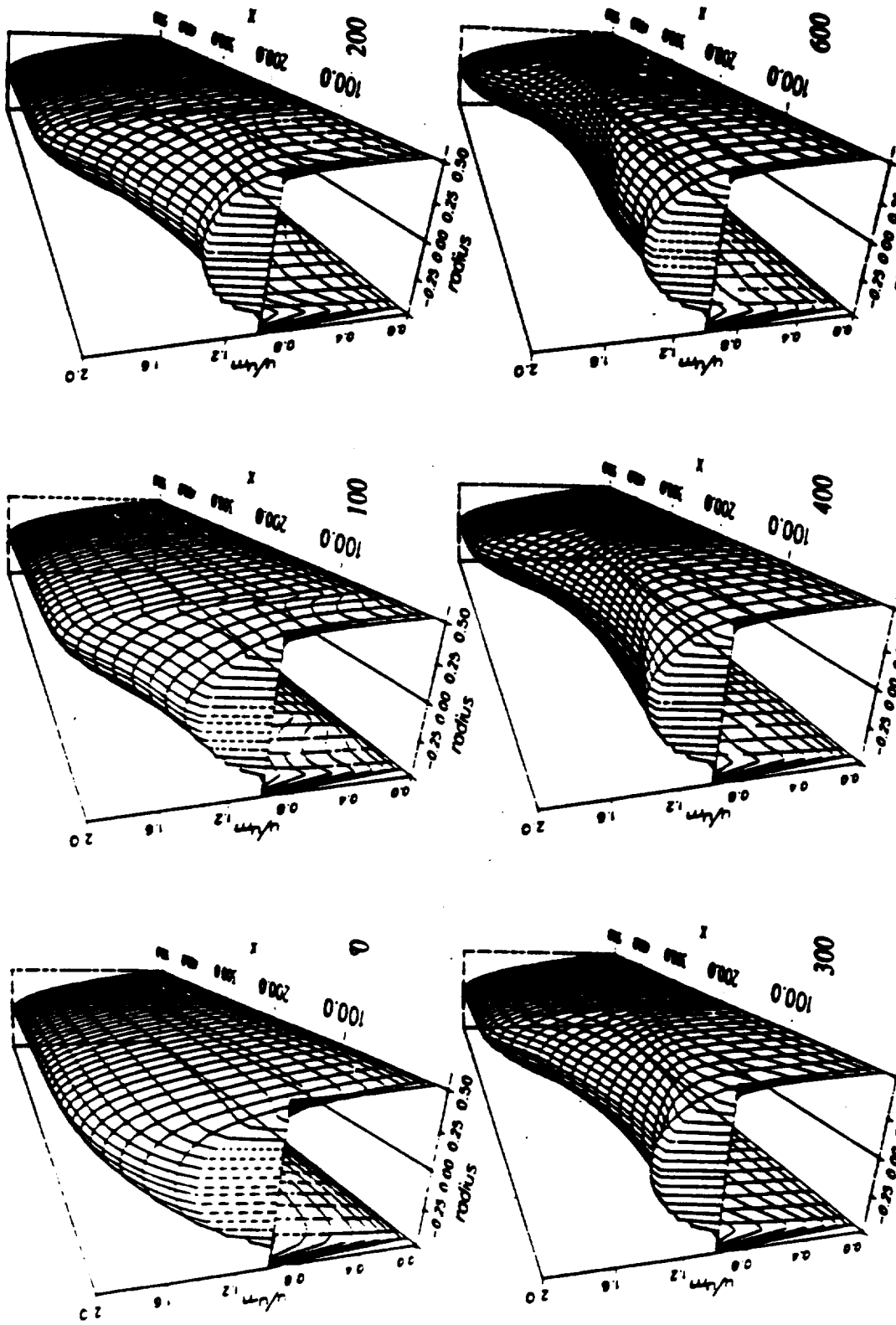

Fig. 6.22: Convergence of solution when TI is suddenly increased. Start of the calculations from the solution for TI=0.5%, continuation with TI=10.0%. Numbers indicate the number of nonlinear iterations, i.e. the computational time.

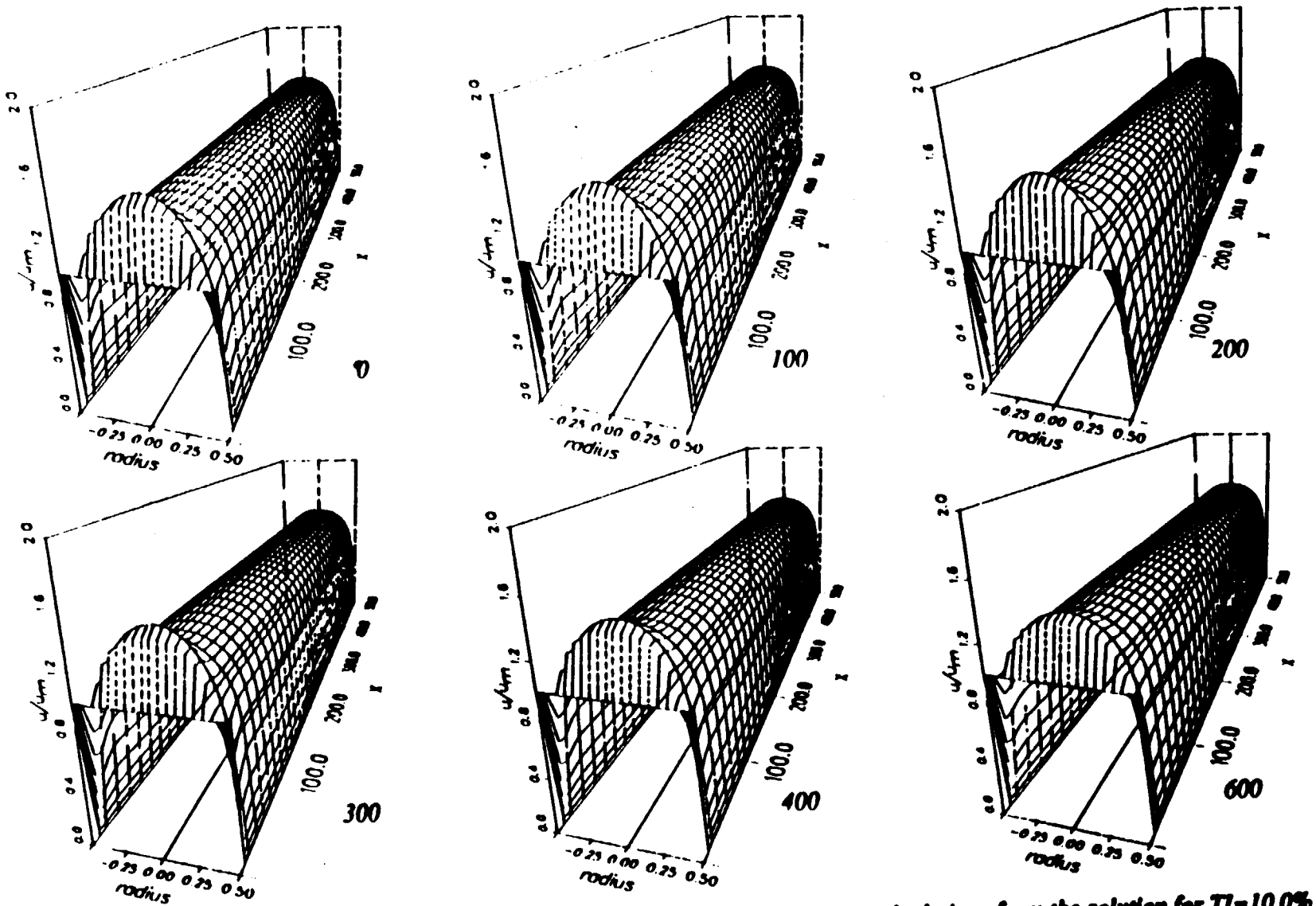

Fig. 6.23: Convergence of solution when TI is suddenly increased. Start of the calculations from the solution for TI=10.0%, continuation with TI=0.5%%. Numbers indicate the number of nonlinear iterations, i.e. the computational time.

Lefebre and White (1987) used a 30 m long test section (ID = 5 cm) with water as the working fluid. The flow was accelerated from rest to 9 or 11 m/s with accelerations between 1.85 and 11.8 m/s^2. Their LDV and surface shear stress sensor measurements showed that the flow underwent transition throughout the test section at practically the same time. An acceleration parameter was defined as

$$K_a = \frac{\mu}{\rho u_m(t)^3} \frac{du_m(t)}{dt} \tag{6.21}$$

as well as a dimensionless time

$$t = \frac{\mu t}{\rho R^2} \tag{6.22}$$

In their experiments, the transitions times t reported are from 0.00105 to 0.0032. The acceleration parameter at transition was nearly constant for the experiments at $K_{a,tr} = 1.53 \times 10^{-8}$. However, during the acceleration, this parameter changes due to its definition.

Computations have been made for the same non-dimensional situation as in the experiment. To translate the dimensionally given acceleration data of Lefebre and White, a non-dimensional acceleration was defined as

$$K_a^* = \frac{2 \rho^2 R^3}{\mu^2} \frac{du_m(t)}{dt} \tag{6.23}$$

Since dU/dt was constant for each experiment, this parameter remained constant during acceleration. Using the property data of water and the ID of the experiment, the non-dimensional acceleration could be determined for different cases I, II and III. Case I is set arbitrarily to a very low acceleration, case II corresponds to the lowest experimentally investigated level and case III to the highest investigated level of acceleration. As will be

Table 6.3: Results of accelerated pipe flow computations

	I	II	III	experiment
K_a^*	5.0e+6	5.724e+7	3.651e+8	same
$K_{a,tr}$	2.5e-6	3.58e-6	3.91e-6	1.53e-8
$Re_{D,tr}$	2.0e+4	4.0e+4	7.2e+4	not given
t_{tr}	4.0e-3	7.0e-4	2.0e-4	1.05e-3 to 3.2e-3
$\frac{\delta_{99}}{R\ t_{tr}^{0.5}}$	2.37	3.17	3.11	2.80[1]
$Re_{\delta,tr}$	1500	1680	1584	23200 ± 15%

seen later, the range of non-dimensional accelerations corresponds to the range found in the different test cases for oscillating flow. The results of the computations are listed in Table 6.3. In the computations, transition to turbulence was defined to happen at that time step when the computed turbulent viscosity at any point in the domain became at least of the order of the molecular viscosity. The findings of this study are:

1.) The turbulence model displays *qualitatively* the correct behavior: As the acceleration increases, $Re_{D,tr}$ increases.

2.) Quantitatively, transition to turbulence is predicted about one order of magnitude too early (at too high values of the acceleration parameter and at too low times corresponding to too low Re_D).

3.) The computational value of $K_{a,tr}$ is varies only slightly for the different experiments; in the experiment this value is also almost constant.

4.) The computed non-dimensional boundary layer thickness is close to the theoretical value of 2.85 cited in Lefebre and White.

5.) The predicted transitional Re number based on the 99% boundary layer thickness is about one order of magnitude too low.

[1] Correlation equation (4) given by Levebre and White (1987)

Conclusions. While the turbulence model displays qualitatively the correct results, it predicts the actual onset of transition about one order of magnitude too early. Given the fact that (i) because of expected grid dependence, only qualitative results were pursued and (ii) the transition criterion applied is somewhat arbitrary, the performance of the turbulence model is viewed as being satisfactory. However, this study is important for suggesting possible future improvement in the chosen turbulence model.

7. PREDICTIONS OF OSCILLATORY FLOW

Since turbulence models are generally highly empirical, their predictions should be compared with experiments when they are applied to a new situation. A novel situation is given when the k-ε model is applied to oscillating flow, and comparison with the data of the oscillating flow test facility of the University of Minnesota will be made. But according to which criteria will the agreement between the computed prediction and the experiment be judged ? Ideally, a direct comparison of the turbulent shear stresses seems to be desirable. However, shear stresses have not been measured and might not be measured at all.

Experimental data documenting the transition in oscillatory flow have been established by Seume (1988). This data can be taken to check the transition predictions of the turbulence models qualitatively. A quantitative comparison is not possible, since (i) the transition data itself are valid only qualitatively (cf. Seume, 1988) and (ii) the only measured fluctuation component is u', and a comparison with the quantity k of the turbulence model involves knowledge of how isotropic the turbulence is. From the data of Laufer (1954) it is evident that $k \neq 1.5\ \overline{u'^2}$ even for steady flow.

Measured velocity profiles are available for one data point (termed SPRE in this work). Quantitative agreement of the predictions with the experimental data can be checked. For engine design considerations it is important to know the local and average friction coefficient, c_f, which is proportional to $\partial u/\partial r$ at the wall. Exact prediction of the velocity gradient near the wall is difficult because of the steep gradients there. Therefore, a comparison between the computed c_f and the measured is desirable. While in principle the experimental data reveals this information, due to experimental problems it has not been possible so far to measure c_f. Computationally, c_f data is available whenever velocity profiles are computed.

Thus, the availability of experimental data allow the following comparisons to-date:

1) qualitative prediction of transition

2) quantitative agreement of velocity profiles not too close near the wall.

Nomenclature: In the following, the nomenclature and comparisons will refer to the University of Minnesota oscillating flow experiment. For a description of the experimental set-up see Seume (1988). The the x-axis starts at the "drive end" of the tube and ends at the "open end". Four out of the five cases investigated here used a pipe length L/D of 60. Consequently, an axial location x/D of 44 is closer to the open end and an x/D of 16 is closer to the drive end. The mean flow velocity will be of the type

$$u_m(t) = u_{m,max} \sin(\omega t) \tag{7.1}$$

The cycle time will be expressed in terms of crank angle. However, contrary to Seume (1988), here we define crank angles between 0° and 180° when the mean flow is *along* the positive x-axis (i.e., coming from the drive end), while crank angles between 180° and 360° refer to flow *against* the positive x-axis (i.e. coming from the open end). For the comparison with predictions, the experimental data were converted to this frame of reference.

7.1. SPRE Test Case: Moderate Reynolds Number, Moderate Valensi Number

7.1.1. Prediction of Laminar Oscillating Flow

To demonstrate the capability of the numerical scheme adapted here, laminar oscillating flow in a finite pipe was computed for Va = 80. The resulting velocity profiles in the axial center of the tube were compared with analytical results from the Uchida analysis. As can be seen from Fig. 7.1, the agreement is excellent. The computations were made with the

same 23 by 23 grid employed later for the HRN k-ε model. Also, 12 time steps per cycle were used in connection with a Crank-Nicholson time integration scheme.

7.1.2. Predictions with the High-Reynolds Number k-ε Model

For preliminary studies, 3 cycles of oscillatory flow at Re_{max} = 11 700, Va = 80 and L/D = 60 have been computed. Even though is known that the HRN form of the turbulence model (i) cannot predict transition and (ii) is not well suited for pipe flows at moderate Re numbers, a computation seemed worthwhile. First, the computational scheme could be checked with the much simpler HRN formulation, and secondly, this computation provides a useful limiting estimate which can serve as an initial guess for more detailed and exact computations.

The grid used here was a coarse grid of 23 by 23 grid points where the points in the radial direction were densely packed near the wall. Thus, the first internal grid point was placed either in the viscous sublayer or close to it throughout the cycle. The grid was fine enough for this test. The first two cycles were computed with 12 time steps per cycle, the third with 24. All computations were carried out with a fixed Crank-Nicholson time integration scheme. The three cycles come very close to the periodic steady state as can be seen from the performance of the friction factor (Fig. 7.2). A smaller time step does not have a dramatic impact on the results of the primitive variables u and v. This suggests that the time stepping procedure is well chosen. A smaller time step, however, changes the values of k, ε, μ_t more significantly than u and v.

Since the HRN model does not have the ability to predict transition, the turbulence model must be switched off "by hand" during the computations. In this study our empirical transition criterion was simply to switch off the solution of the k and ε equation whenever the Re number fell below 2300 and to switch it on otherwise. For a Re number of less than 2300, the laminar flow was anticipated, and the arrays of k, ε and μ_t were set to zero. As

can be seen in the graphs below, the sudden disappearance of μ_t at relative cycle times of 0, 0.5, 1 etc. illustrate how unrealistic the transition process is modeled this way.

It proved to be extremely difficult to keep the scheme stable at the point where Re = 0 (reversal of the mean flow direction). Even after many trial runs it remained somewhat unpredictable whether the computation would "survive" the next mean flow reversal. This pointed out the need for optimizing the initial guesses from which a computation at a given time step was started and/or for another time stepping procedure.

So far we used as initial guesses:

$$p(i,j) = 0$$

$$u(i,j) = (1\text{-}fgp)\, u_{old}(i,j) + fgp\, u_m$$

$$v(i,j) = 0$$

$$k(i,j) = \frac{3}{2} \cdot TI^2 \cdot u_m^2 \text{ for } Re > 2300$$

$$\varepsilon(i,j) = 0.05\, k^2/\nu$$

where fgp is a first guess parameter which varies continuously between zero and one (1 for large time steps and few time steps per cycle, 0 for small time steps and many time steps per cycle).

Also, reliable criteria for nonlinear convergence were determined. Define σ_{max} as the maximum absolute scaled value of the error in the mass conservation for any one control volume. Then:

$$\sigma_{max} < \frac{relax(u)*relax(v)*relax(p)}{ll*ml}$$

$$d\sigma_{max} < 0$$

$$\frac{\text{change in overall kinetic energy in domain}}{\text{relax(k)*relax(}\varepsilon\text{)*relax(}\mu_t\text{)}} < 1\%$$

was required for at least 3 consecutive iterations.

The boundary conditions for the turbulent kinetic energy and the turbulent dissipation rate were 6% turbulence intensity and $\zeta = 0.05$ in eq. (6.2). A velocity boundary condition of sinusoidally-varying slug flow into the domain was assumed.

In the following, the results of the computations are presented. A comparison with the measured data of Simon, Seume and Friedman (1989) is given later together with the results of the low Reynolds number turbulence model.

Results. The results of the computations are shown in Figs. 7.2 and 7.5 Figure 7.2 shows the computed friction factor as a function of the crank angle and compares it with the friction factor correlations for steady situations at the respective Re number.

Discussion. Compared to the laminar flow computation hardly any flow reversal is predicted. This is good news for the boundary condition treatment of the outflow boundary: Since at an outflow boundary *outflow* is assumed, complete upwinding is used there to eliminate the need to know the boundary conditions there. However, if there were to be *inflow* at an outflow boundary, information about the outflow boundary would be needed a priori. And this information is not normally available.

As can be seen from Fig.7.5, the gross characteristics of the flow can be obtained from a HRN computation. But the near wall velocity and thus the friction factor predictions do not follow the experimental data well . This should not be a surprise, because the validity of the universal law of the wall, on which the HRN relies, is very questionable for the situation investigated.

Fig. 7.1: Prediction of laminar oscillatory flow, Va = 80. Velocities correspond to a maximum pressure gradient which would yield a velocity of 1000 in steady flow ----- : Uchida analysis, dot symbols : numerical computation.

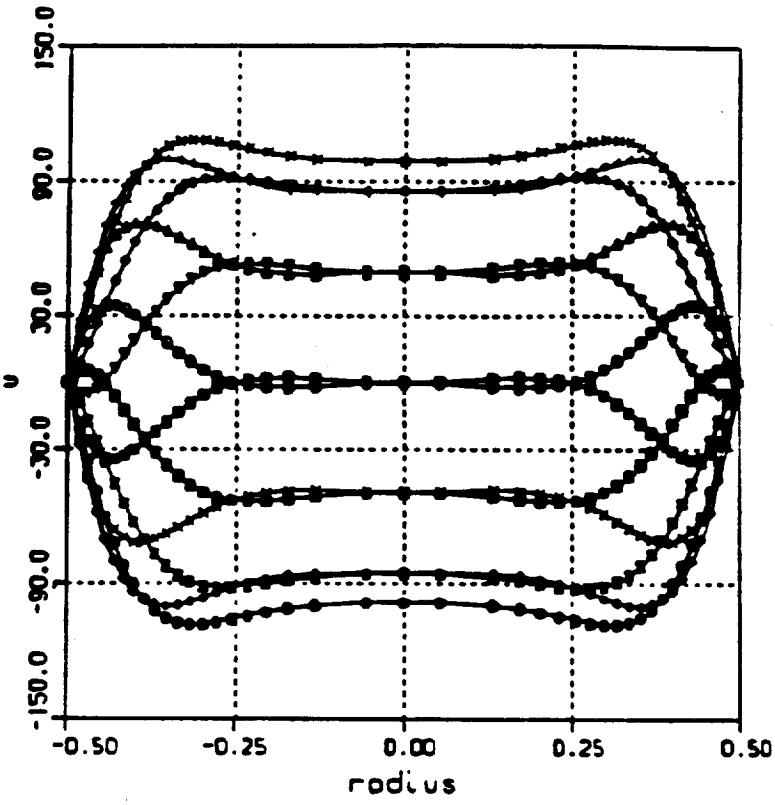

Fig. 7.2: Comparison of the friction coefficient prediction by the high-Reynolds number model with friction coefficient from turbulent and laminar steady state correlations.

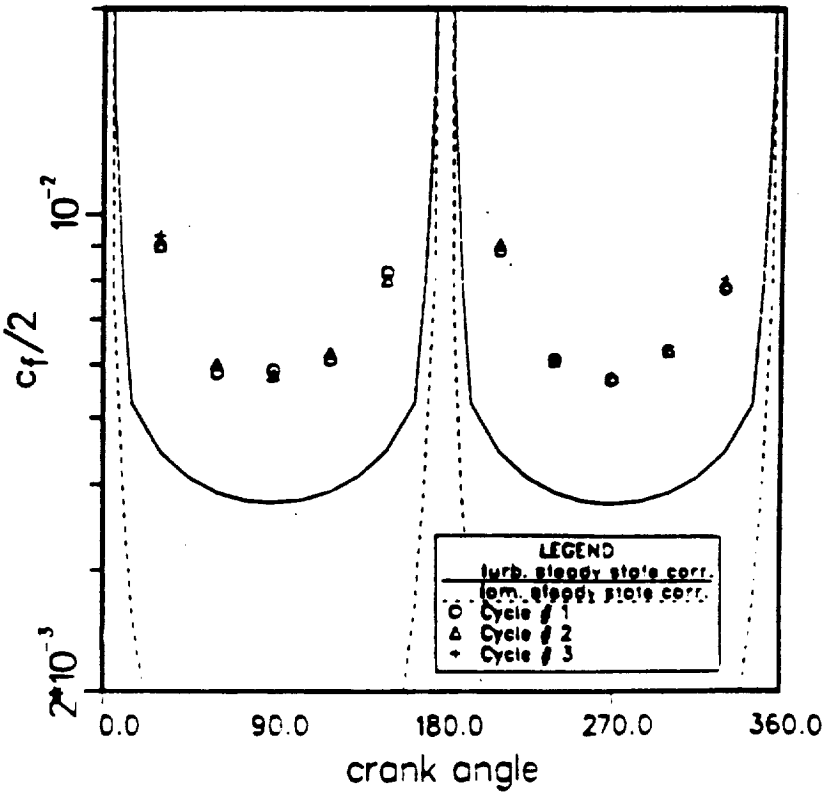

7.1.3. Prediction with the Low Reynolds Number k-ε Model

7.1.3.1. Development of Computations

For the SPRE test case (Re_{max} = 11 700, Va = 80 and L/D = 60), a fluid flow computation was made using the Lam Bremhorst form of the low Re number k-ε turbulence model. For the first cycle computed with the LRN model, the computations at each time step were started from the results obtained with the HRN model described above. Except in the case where the number of time steps per cycle was 120, the computations of the later cycles were started from the corresponding results of the previous cycle.

At first, four additional cycles were computed, cycles # 4, 5, 6 and 7, each with 24 time steps per cycle. In cycle #7 the periodic steady state was reached and the results practically did not change any more. As inflow boundary conditions a TI of 5% for the kinetic energy and a ζ of $1/(TI\ Re^{0.875})$ [cf. eq. (6.20)] for the dissipation rate were used.

Later on, two more cycles (#8 and #9) were computed using measured velocity fluctuation data at the open end as the actual inflow boundary condition for k. This was done to eliminate the uncertainty associated with the assumed boundary condition in cycles #4 to #7.

Finally, the grid independence of the results obtained was verified. 3/2 cycles were computed with 120 time steps per cycle and a grid of 33 by 51 grid points, and 3/2 cycles with 24 time steps and a larger grid of 64 by 91 grid points. The computation with 120 time steps per cycle was started at 0° crank angle with the results from cycle #9. The subsequent computations were started with the converged result of the previous time step. For the large grid computation, the results of cycle #9 were transposed to the finer grid, and the computations were started from the corresponding results of cycle #9. As will be shown later, the results of both tests were practically identical to cycle #9. The prediction of transition was not altered by the use of a finer grid nor by the use of more time steps. This is an important finding since in Chapter 6 some grid dependence of the transition prediction

was found. The different behavior of the LRN model might be explained by the fact that in oscillating flow, due to history effects, the flow before transition is never totally undisturbed as assumed in the quasi-steady transition tests. From this we conclude that quantitatively trustful results may be, in principle, obtainable for oscillating flow from the turbulence model used.

7.1.3.2. A New Time Integration Scheme

For the computation of the fourth cycle, the same time integration scheme as for the HRN model was used: a fixed Crank-Nicholson scheme. However, it was found that convergence frequently was not reached after as many as 200 nonlinear iterations. Then, if a solution of the next step was tried (even though the previous step was not fully converged), this solution nearly always diverged. Sufficient and dynamic under-relaxation and very many nonlinear iterations were the key to convergence at each time step.

As initial guess, the values of the previous cycle were used at each time step of the fifth cycle. Initially it was assumed that only a few iterations would be necessary at each time step to reach convergence. But this hope did not come true. Again, many iterations needed to be done to prevent the subsequent time steps from diverging.

A thorough review of the time integration scheme used so far revealed the underlying problem. In the LRN model computation 33*51 grid points were used, most of them placed very close to the wall. As the numerical grid becomes finer and finer, the Crank-Nicholson formulation may become physically unstable. The fine grid near the wall practically assures that the the Crank-Nicholson scheme would become unstable unless many more time steps are taken. One possible solution would be to use a scheme between the fully implicit and the Crank-Nicholson scheme which is stable. This, however, would imply that the time integration scheme for the total domain would be based on the most unfavorable conditions for a Crank-Nicholson scheme in it, namely on the conditions near the wall. Near the wall, the effect of mass inertia is relatively small, whereas in the center

that effect is significant. Wherever inertia plays an important role, time history effects become important which are - in an always changing situation - better represented by the Crank-Nicholson scheme. Therefore, it is not as important to have a Crank-Nicholson scheme for the near wall region as it is for the center. This consideration bore out a time integration scheme which picks a time integration factor for each control volume and for each interface individually, based on the local conditions. For the situation under investigation here, the time integration factor varied from almost 1.0 near the wall to around 0.95 in the center. Surely, for time integration factors that close to 1.0, a simple fully implicit method would have provided almost the identical results. This scheme proved to be stable at all times and was used for all cycles from #5 on.

7.1.3.3. Results

Comparison with measured u'_{rms} data. Assuming isotropic turbulence, the computed turbulent kinetic energy can be transformed to the rms axial velocity fluctuations:

$$u'_{rms} = \sqrt{2/3\ k} \tag{7.2}$$

Figure 7.3 shows a comparison of the measured velocity fluctuations with the computations at an axial location of x/D = 44 and 3 radial locations, centerline, intermediate and near the wall. The three computational curves plotted show the influence of the grid size in time and space. The measured TI at the inflow is used in either case. However, even with a flat TI of 5% (cycle #7) the computed curve looks alike and is not shown. The significant rise of u'_{rms} at circa 230° coincides in the experiment and the computations closer to the wall. However, the computations do not forecast a rise in the center. Also, the predicted decrease in turbulent fluctuations occurs over a much longer period than measured. It is believed that here the computation and the experiment show two completely different mechanisms of transition and relaminarization. The sudden decrease of u'_{rms} at 300° during the decelerating phase at a relatively high Re number indicates that the measured fluctuations between 230° and 300° correspond to a "turbulent slug" being sucked

in from the open end (cf. Seume, 1988). Without this slug, the flow at this location would remain laminar-like. On the other hand, the computations do *not* "see" that slug and rather describe an ordinary transition to turbulence at a too low, but computationally high enough Re number. This hypothesis is supported by Chapter 6.4., where it was found that in accelerated flow the turbulence model predicts transition at too low Re numbers. The computational transition predicts boundary layer instabilities and happens first near the walls. The high fluctuations closer to the wall will be transported to the center, but will reach the centerline only further downstream. Therefore, no rise of u'_{rms} is shown at the centerline in the computations at this axial location. This explanation is supported by the computed fluctuations rising at about 90°. Here the axial location is further downstream of the inflow and the numerically predicted fluctuations spread over the entire cross section. In this case, experiment and computation "see" the same thing, i.e. ordinary transition to turbulence. Again, the turbulence model predicts transition at a too low Re number, given the rapid acceleration. The third rise in u'_{rms} just after flow reversal at 180° is predicted very faithfully by the computation. It is believed that this rise is due to fluid that has become turbulent just after passing the probe location at x/D=44. Just after flow reversal, the fluctuations have not died down yet and revisit the probe location.

In the following, we try to shed light on the question why the turbulence model does not predict the experimentally observed turbulent slug, even though the correct inflow boundary condition is used for the turbulent kinetic energy. Fig. 7.4a shows the measured u'_{rms} at the inflow, the theoretical mean flow for this flow situation and the ratio of the two quantities $u'_{rms}/u_m(t)$ which is equivalent to the TI at the inflow. The u'_{rms} values were actually measured at the open end, but it is assumed that the inflow conditions are the same for both ends of the tube. The given curves can be repeated for crank angeles 180° to 360°. Figure 7.4b shows axial profile of k at the centerline at different crank angles during the period of inflow from the open end. The values of k at x/D=60 correspond to the measured u'_{rms} values of Fig.7.4a. It can be seen that the k values vary sharply between x/D=60 and x/D=58. At x/D=50, virtually all information about the inflow boundary condition is lost

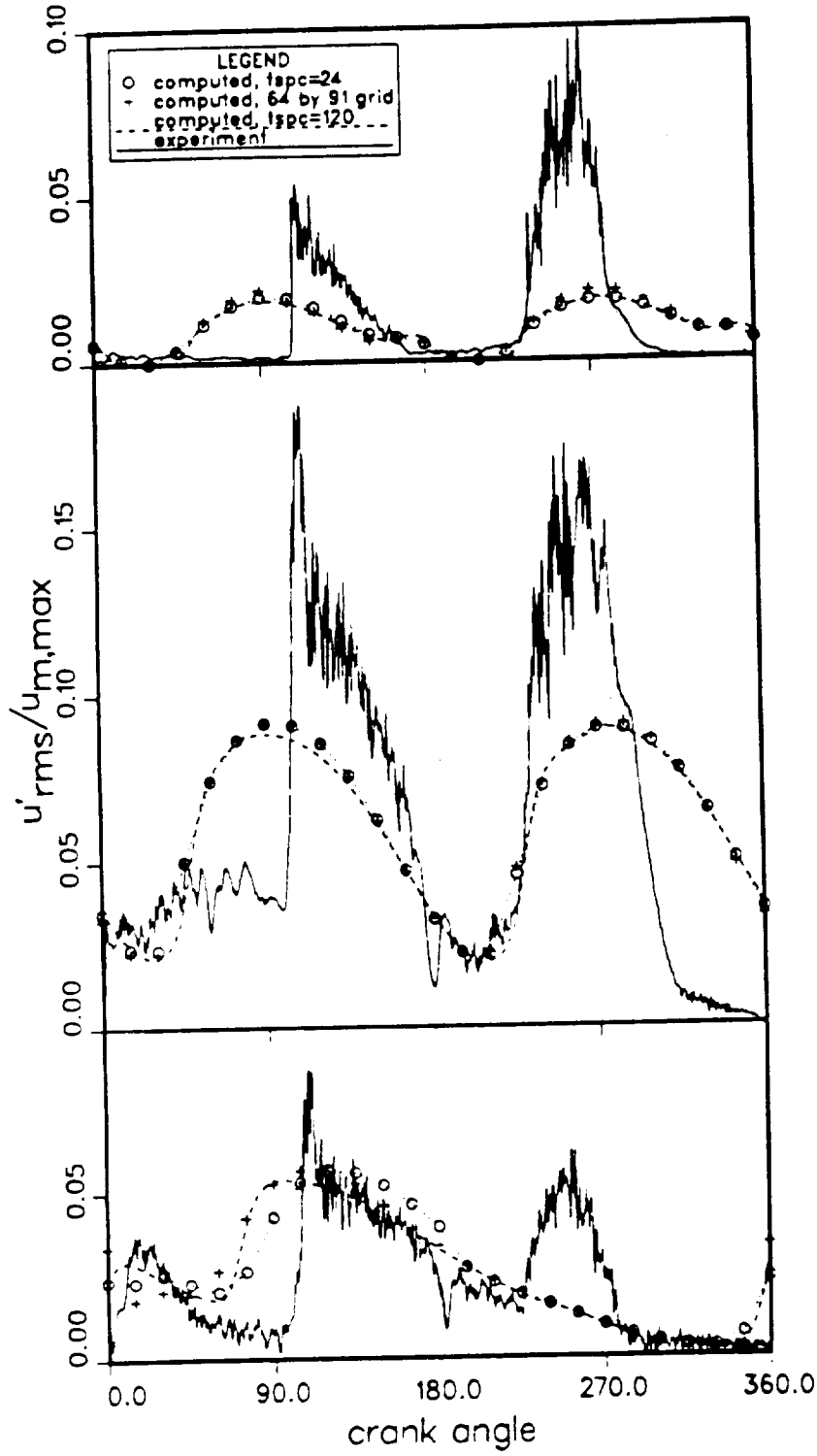

Fig. 7.3: Comparison of computed velocity fluctuations with experiment at x D=44 (near open end). Top: r D=0.48; center: 0.433; bottom: centerline.

Fig. 7.4a: Measured velocity fluctuations at the inflow cross section and theoretical u_m (right); associated turbulence intensity (left).

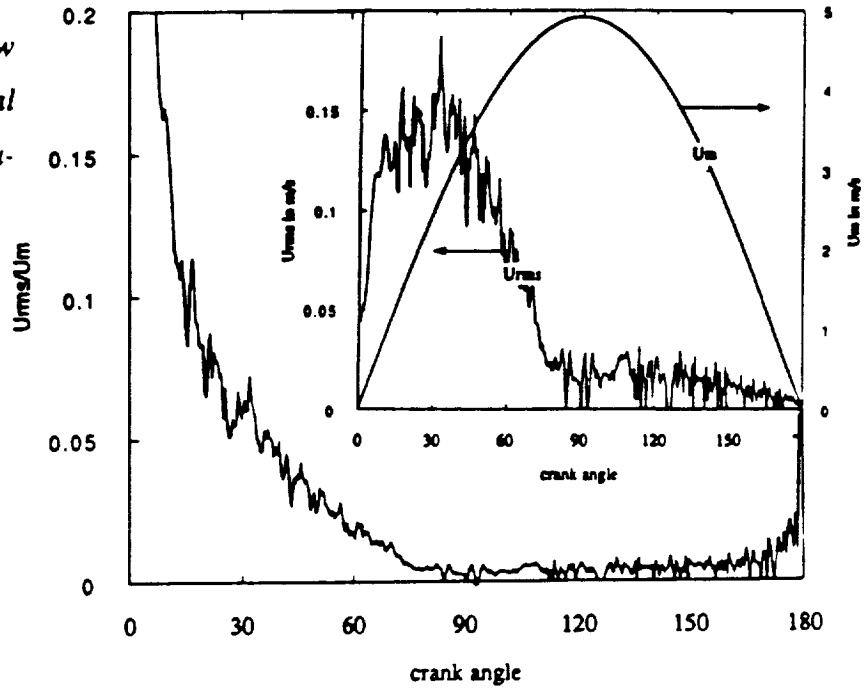

Fig. 7.4b: Axial profiles of the turbulent kinetic energy at the centerline.

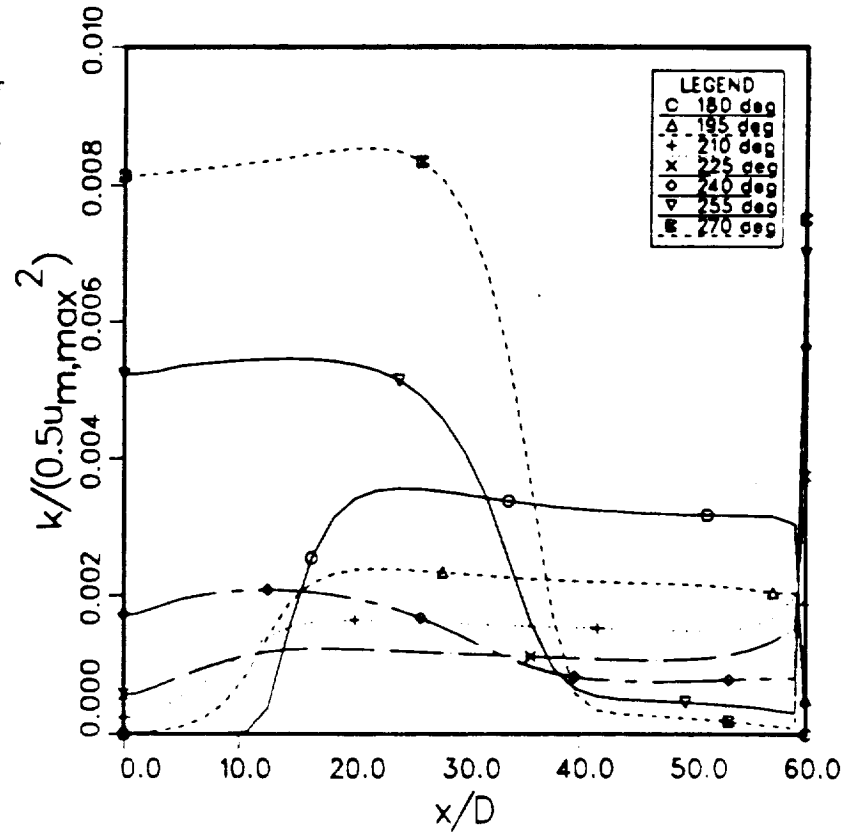

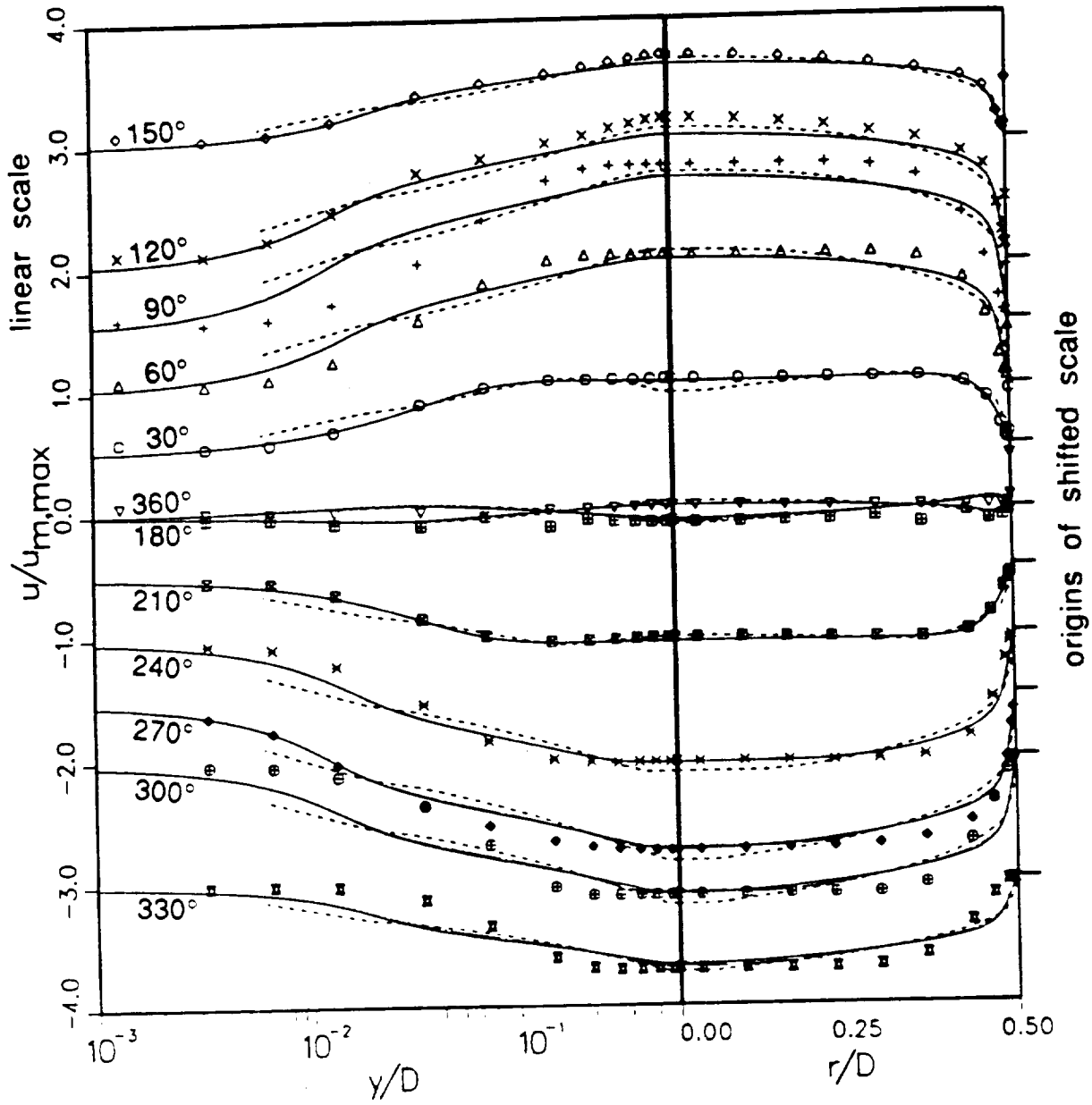

Fig. 7.5: Comparison of computed velocity profiles with measured data. x/D = 44. Data point SPRE: Re_{max}=11700, Va=80, L/D=60. symbols indicate measurments of Simon, Seume and Friedman; - - - - - - - computed with high-Re number model, dots indicate measured values;. ——— LRN, 24 time steps per cycle, 33 by 51 grid, no experimental TI; - · - · - LRN, 120 time steps per cycle, 33 by 51 grid, experimental TI; ····· LRN, 24 time steps per cycle, 64 by 91 grid, experimental TI. Crank angles below 180° indicate a mean flow from the "piston end" of the experimental rig, crank angles between 180° and 360° indicate a mean flow from the open end. Vertical line indicates the centerline. To the right of the centerline, the velocity is plotted vs the radius linearly; to the left, it is plotted against the logarithmic wall distance. The individual profiles are vertically shifted.

or dissipated. We suspect that inflow boundary condition for ε provides unrealistically high values. High values of ε lead to a rapid dissipation of k just after the inflow and imply that in the computations no "turbulent slugs" could travel any significant distance downstream from the inlet. This suggests that further work is required to realistically specify ε at the inflow and that $\zeta(Re)$ of eq. (6.20) should be modified.

Comparison with measured velocity profiles. Figure 7.5 shows a comparison of the computed and measured velocity profiles at an axial location x/D = 44. It can be seen that the HRN and the LRN models give similar results in the center of the tube, but differ considerably towards the wall. In general, the HRN model predicts too high velocities near the wall. The results of three LRN computations are shown:

(i) *no* experimental TI, 24 time steps per cycle, 33 by 51 grid

(ii) experimental TI, 120 time steps per cycle, 33 by 51 grid

(iii) experimental TI, 24 time steps per cycle, 64 by 91 grid

The three LRN computations are practically indistinguishable. This verifies the grid independence and shows that the measured TI does not influence the predictions at this axial location. Table 7.1 tries to evaluate and to classify the results shown in Fig.7.5.

Table 7.1: *Evaluation of Figure 7.5*

Agreement with experiment			Agreement with experiment		
Crank Angle	HRN	LRN	Crank Angle	HRN	LRN
30°	satisf.	good	210°	satisf.	good
60°	fair	satisf.	240°	fair	satisf.
90°	fair	satisf.	270°	fair	satisf.
120°	fair	satisf.	300°	poor	fair
150°	satisf.	good	330°	fair	fair
180°	good	good	360°	good	good

Scale: good - satisfactory - fair - poor

From this evaluation, a number of questions arise:

1) Why is there good agreement for the LRN case at 150° and only fair at 330° ?
2) Why is there satisfactory agreement for the LRN case at 120° and fair at 300° ?
3) Why is there only little improvement at 60°, 90°, 300° and 330° from the HRN to the LRN model ?

The following discussion shall assess these questions. From Fig. 7.5 and from Table 7.1 it is evident that the results do not show symmetric deviations from the experimental results, i.e. the deviations at 150° differ significantly from the ones at 330° etc. For the data pair 60°/240° the predicted data is generally "too turbulent". However, this trend is more pronounced at 60°. The centerline velocities are underpredicted at 60° and on target at 240°. Near the wall, the absolute value of the velocity is overpredicted. An explanation for the deviation at 60° could be that the strong acceleration keeps the flow longer laminar than the turbulence model can predict. This is in line with the test of the model for constant acceleration flows (see Chapter 6.4). From Fig. 7.3 it becomes clear that the better agreement at 240° comes from separated turbulent eddies being sucked in from the nozzle at the beginning of the second half of the cycle. The action of these eddies would increase the turbulent kinetic energy and counter the effect of the acceleration. Therefore, the measured data at 240° are "more turbulent" than those at 60°. This explanation also holds for the data pair 90°/270°. However, it appears that at 90° there is a very strong overprediction of the absolute values of the velocities between $y/D=7x10^{-3}$ and 10^{-1}, whereas at 270° the prediction follows the experiment much better. Yet, at 270° all experimental data lie below or on the predicted curve. This indicates that the mass balance was not satisfied in the experiment. If the experimental data of 270° is shifted to give the same mass flow as in the computation, a similar trend as in the case of 240° can be seen. For 120° and 150° crank angle, similar deviation patterns are found. First, all experimental data are above or on the predicted curve, again indicating experimental differences in maintaining the mass flow rate. Near the wall, the prediction is right on target, whereas in the center, the predicted data is too low. The data at 300° and on 330° shows an overprediction of the absolute value

of the velocity near the wall, followed by an underprediction towards the center and the correct values at the centerline. The experimental data clearly looks laminar-like. Based on the measured boundary conditions for u'_{rms} and on Fig. 7.3 that is due to the action of the nozzle before the flow enters the tube. There, fluid from the quiescent outside is sucked in and accelerated. The flow into the tube is relatively little disturbed and may well develop like a laminar flow initially. As seen in Chapter 6.2, at an axial distance of 16 diameters from the inlet, the flow will be laminar-like at moderate Re numbers unless the TI is very high. In the equivalent cases of 120° and 150°, the axial distance from the inflow is x/D = 44. By then, a spatial transition is very likely to have happened which could explain the different behavior between 120° and 300° or 150° and 330°.

It is remarkable that the near wall velocities are generally well predicted. It is the near wall velocities which determine the computed c_f value. Therefore the c_f predictions can be regarded with confidence.

Given the remaining uncertainties of the experimental results, the general agreement of the LRN predictions with the experiment is considered to be good.

Law of the wall. As can be seen in Fig. 7.6, the predictions support the hypothesis that the universal law of the wall is *not* a good representation for the velocity profile near the wall or even throughout the cross section. This does not come as a surprise since the universal law of the wall has already been shown for steady flows to be not applicable at low Re numbers.

However, it can be seen that, except at flow reversal, there exists a laminar sublayer up to a y^+ of about 7. Beyond this value, a logarithmic relationship between u^+ and y^+ may be formed, but the slopes are neither identical to the universal value nor constant at all.

Tu and Ramaprian (1981) argue for pulsatile flow that the velocity does not scale with the wall shear stress at the same instance of time. Since the wall shear stress and the mean velocity have a phase difference could one scale the velocity with the shear stress of the

corresponding phase angle? To answer this question conclusively for oscillating flow, a phase relationship between u and τ_0 should be established, similarly like in laminar flow.

Friction coefficient. The friction coefficient for fully developed flow derived from the turbulent steady state correlation does not agree well for the accelerated part of the cycle with the computed friction factor, which predicts lower values (Fig.7.7). The agreement get rather close in the decelerated phase. The predictions of the HRN and LRN models are significantly different. Given the superiority of the velocity predictions obtained with the HRN model, it can be claimed that the HRN model does not give realistic values for c_f.

Entrance length effects. Entrance length effects are important for about one third of the length of the tube during most of the cycle (Fig. 7.8). The fact that $c_{f,x}$ initially decreases below the fully developed limit can be explained by the laminar-like flow development downstream of the inlet. This effect is relatively pronounced because of the low (experimentally determined) TI. It seems appropriate that a locally averaged friction factor for this case takes account for the entrance length effects.

Other quantities. Fig. 7.9 shows the computed pressure distribution throughout the cycle. Figures 7.10, to 7.12 show the time variation of the turbulent kinetic energy, the dissipation rate and the turbulent viscosity at x/D = 44. Figure 7.13 is a vector plot of the the velocity. Figures 7.14, 7.15 and 7.16 show the variation of k, ε and μ_τ at different crank angles.

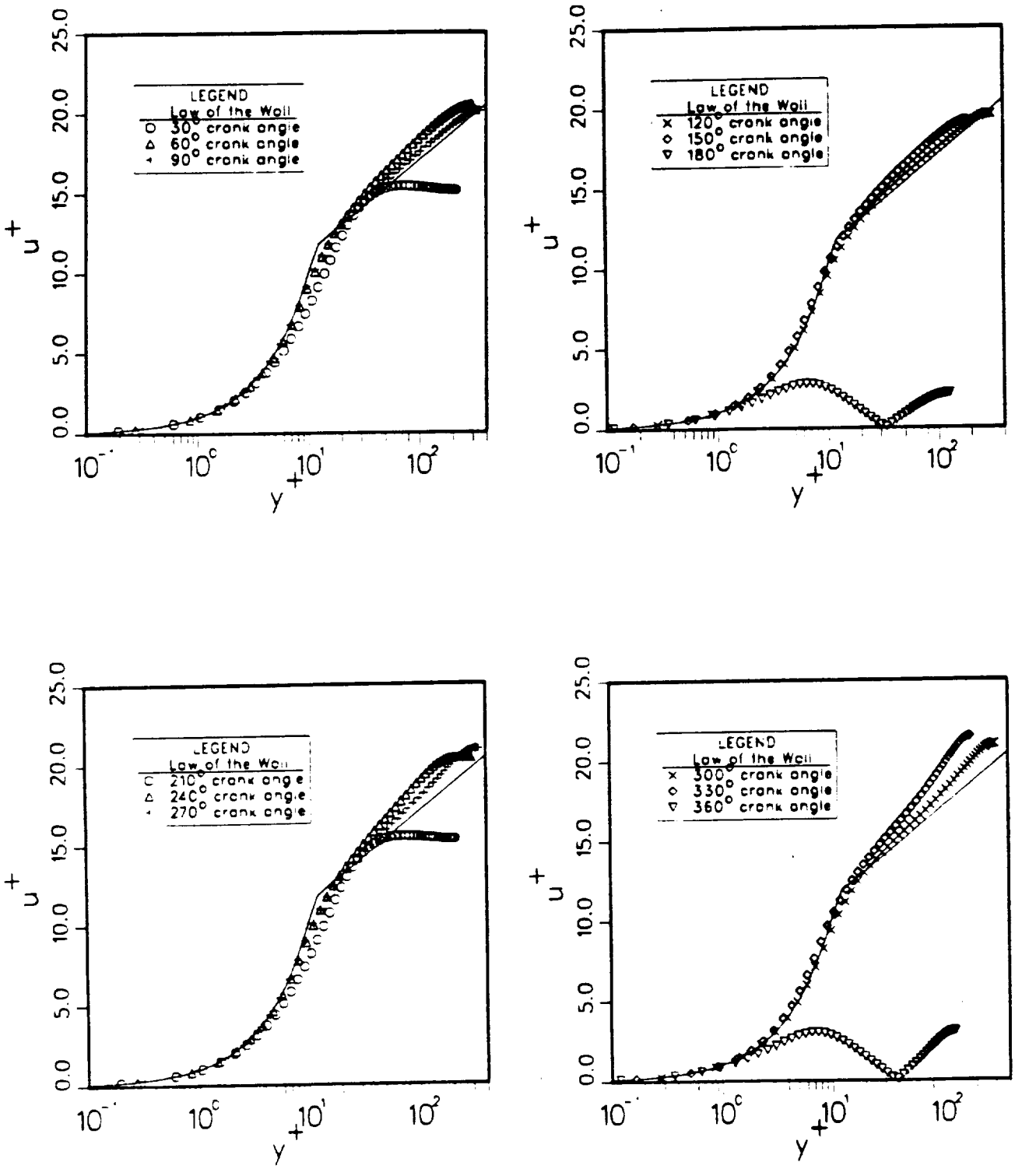

Fig. 7.6: Comparison of near wall prediction of the low-Re number model with the universal law of the wall. x/D=44. Data point ***SPRE****: Re_{max}=11700, Va=80, L/D=60.*

Fig. 7.7: Comparison of friction coefficient prediction at the outflow cross section: Low-Reynolds number model vs. friction coefficient from turbulent and laminar steady state correlation.

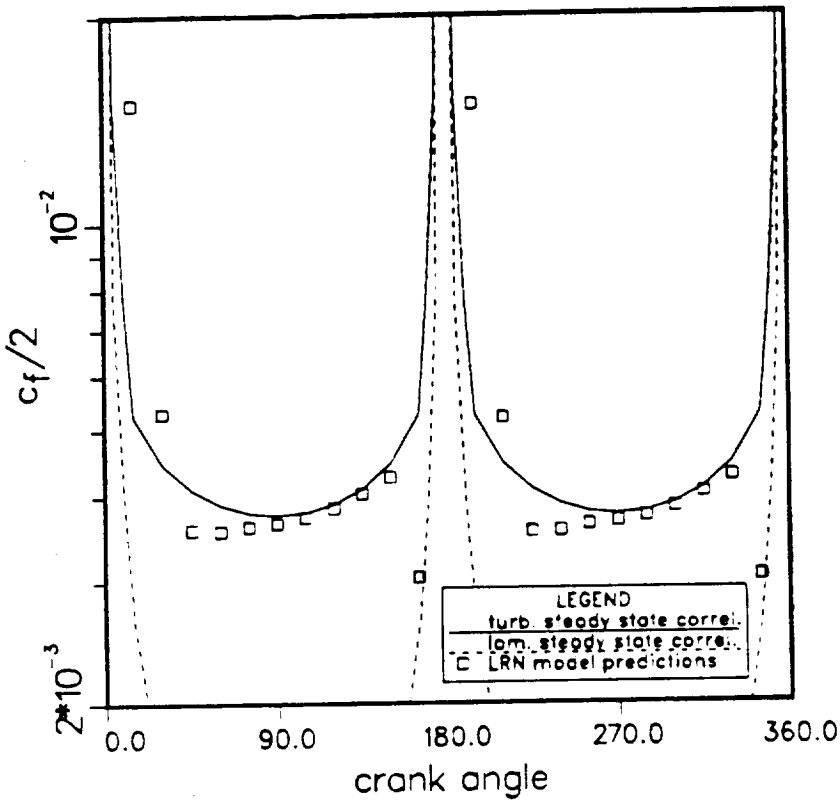

Fig. 7.8: Ratio of local to fully developed friction coefficient at various crank angles.

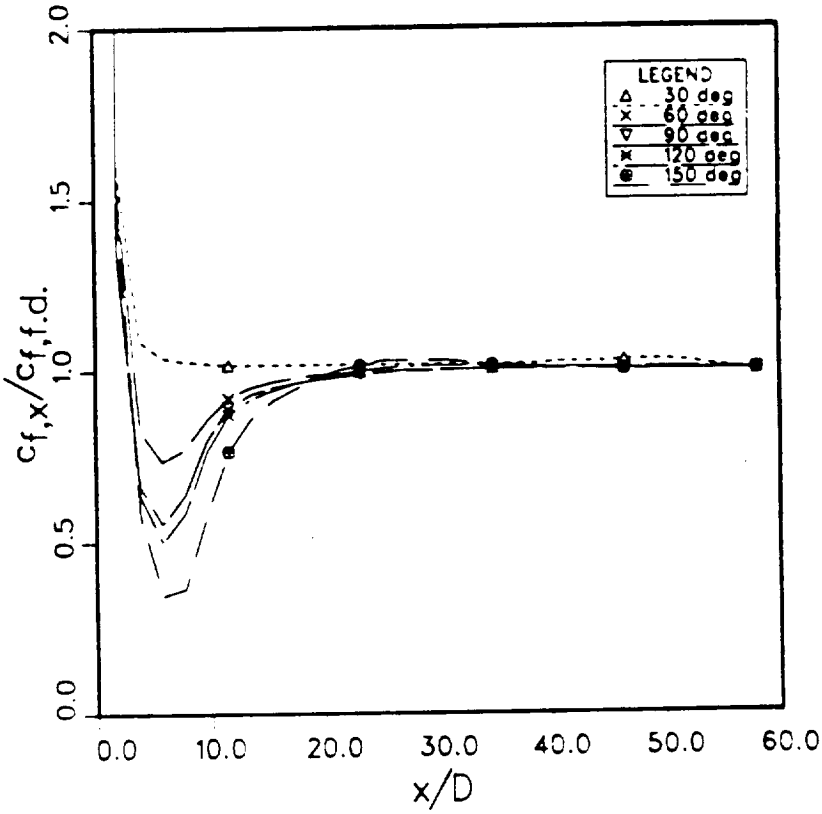

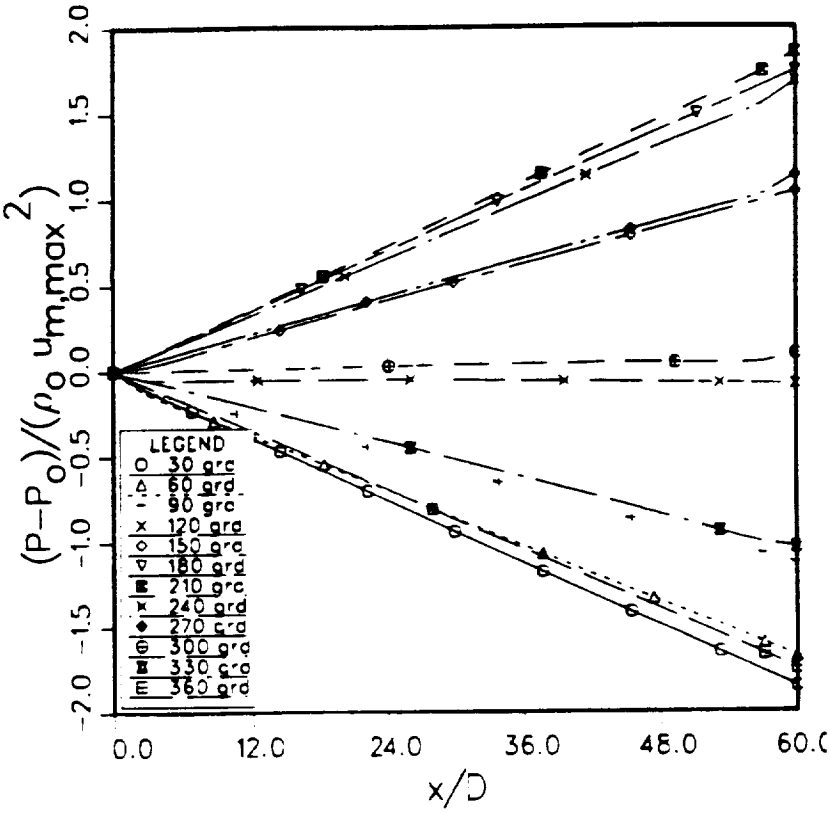

Fig. 7.9: Predicted axial pressure distribution. Re_{max}= 11700, Va = 80, L/D = 60.

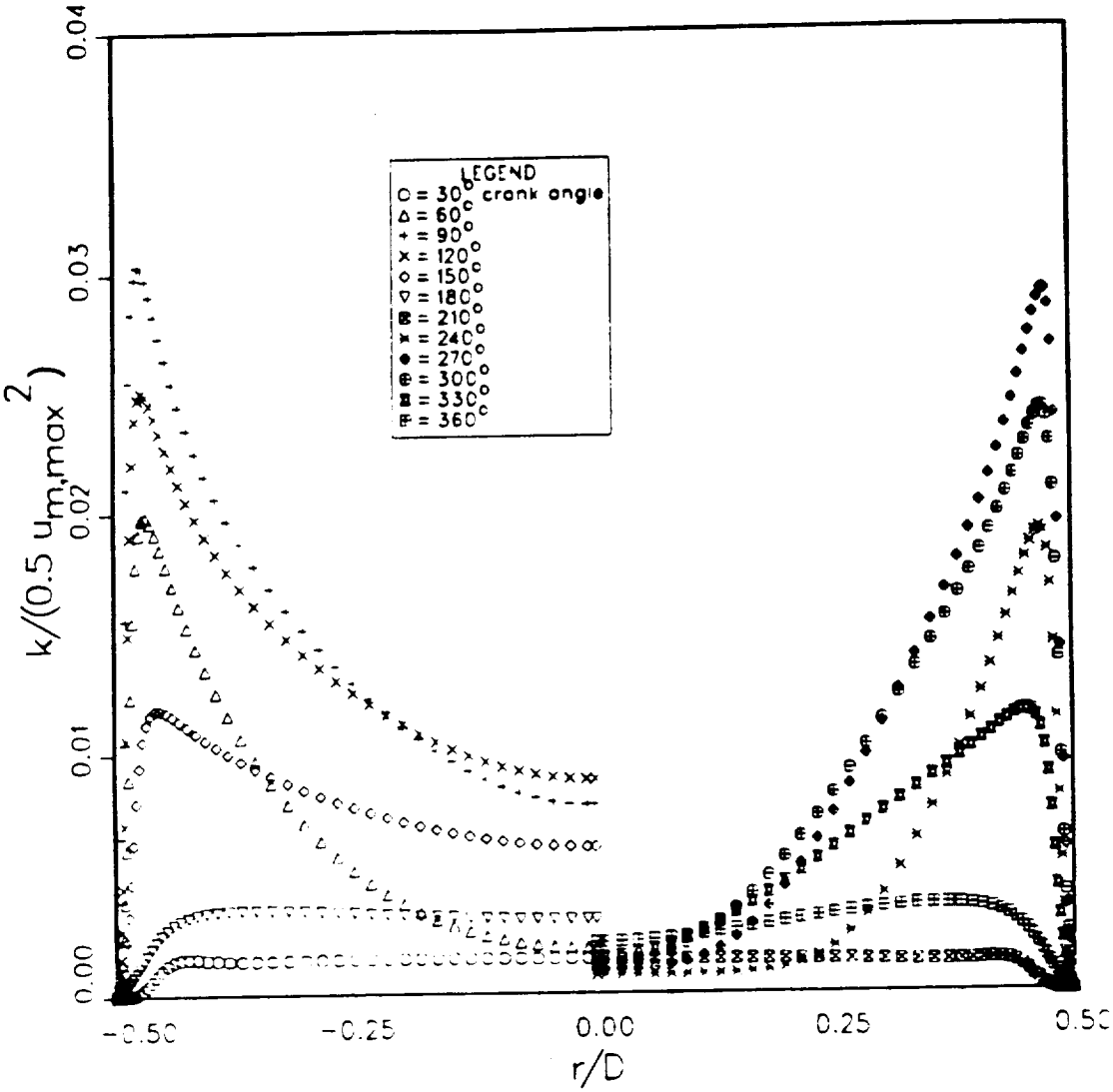

Fig. 7.10: LRN predicted turbulent kinetic energy profiles at x/D = 44. Data point ***SPRE:*** *Re_{max} = 11700, Va = 80, L/D = 60. The half profiles do not come together at the centerline because the x/D location is not in the axial center of the tube*

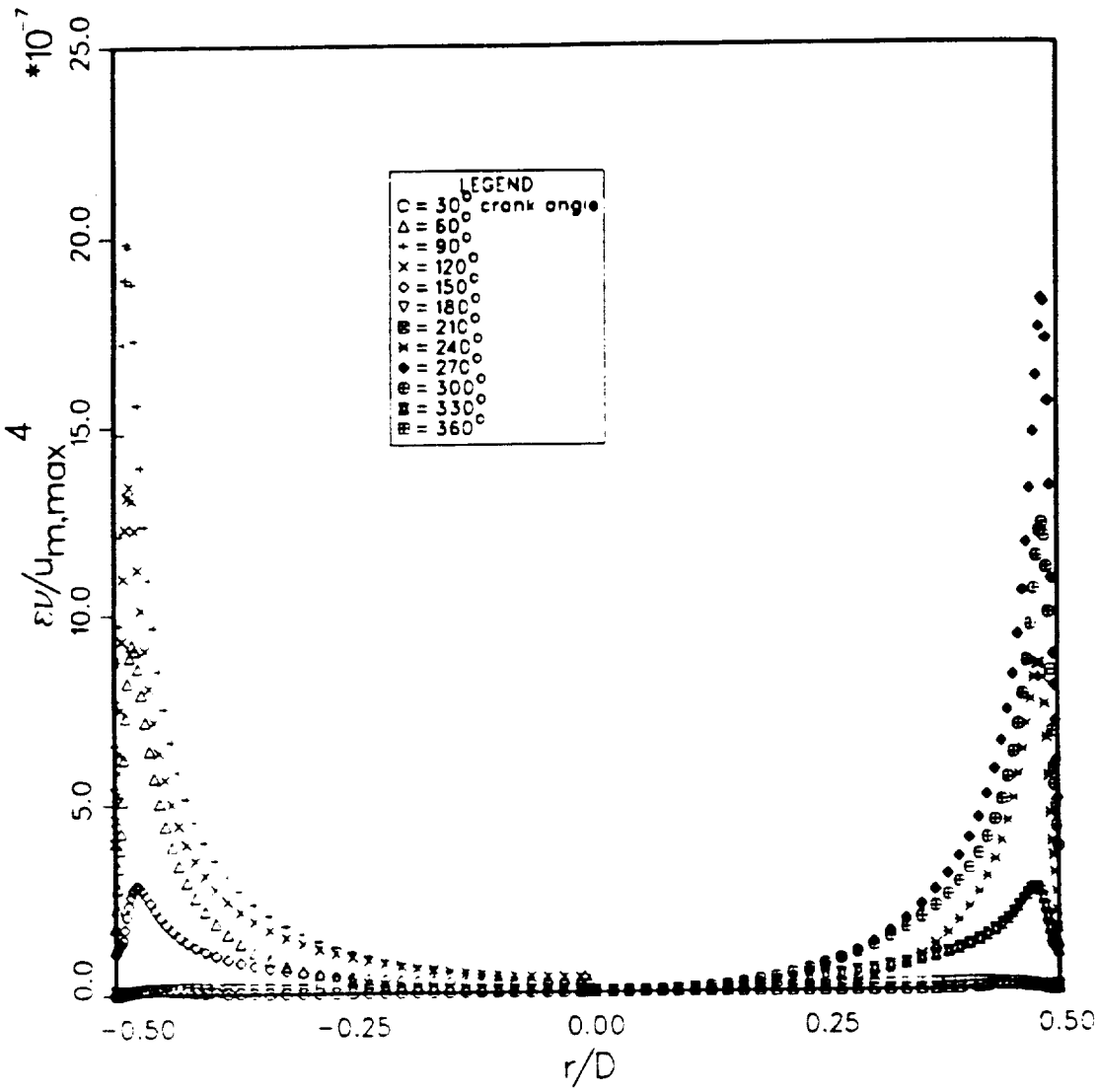

Fig. 7.11: *LRN predicted turbulent dissipation rate profiles at x/D = 44. Data point* ***SPRE:*** *Re_{max} = 11700, Va = 80, L/D = 60.The half profiles do not come together at the centerline because the x/D location is not in the axial center of the tube.*

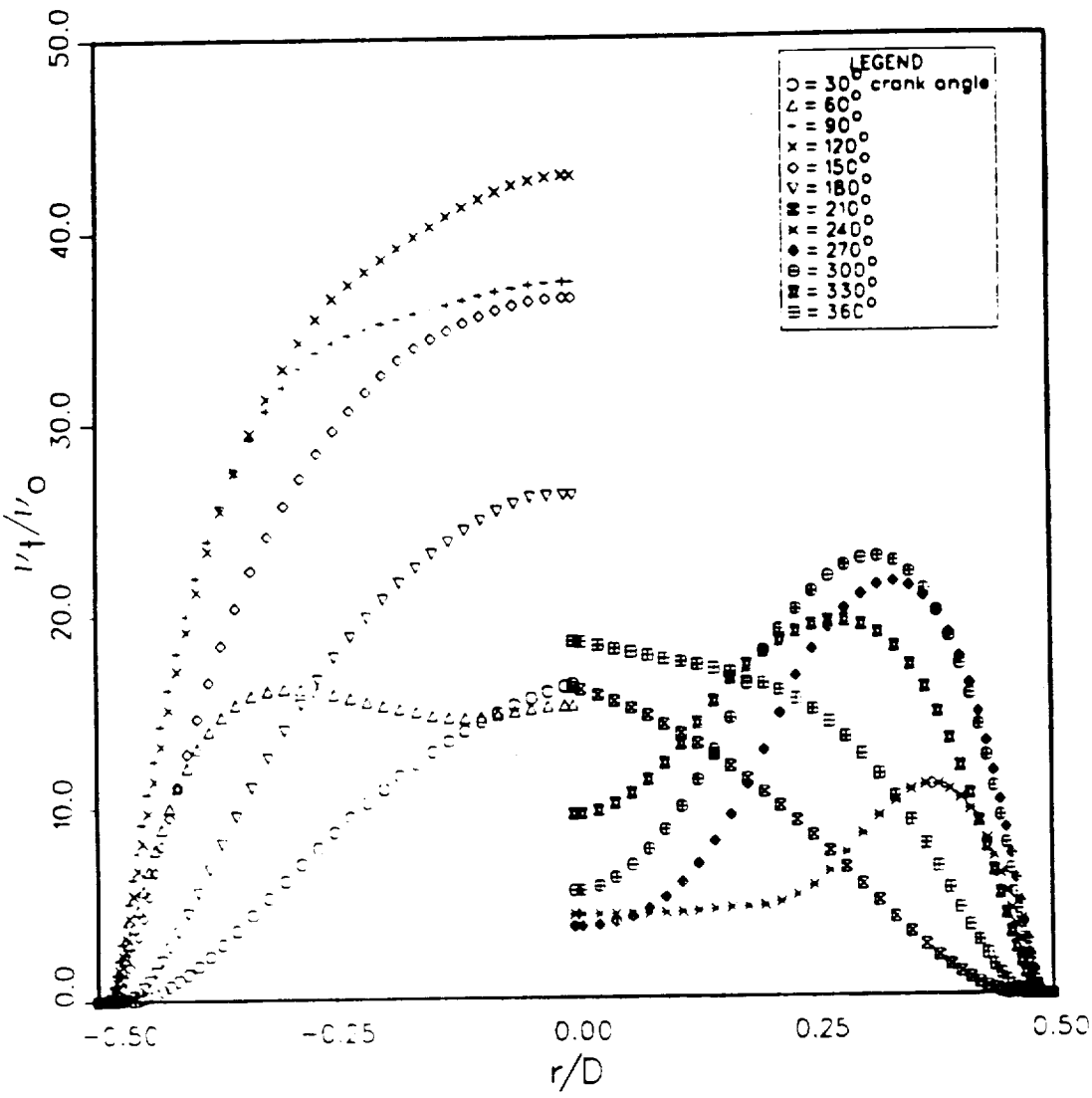

***Fig. 7.12**: LRN predicted turbulent viscosity profiles at x/D = 44. Data point SPRE: Re_{max} = 11700, Va = 80, L/D = 60. The half profiles do not come together at the centerline because the x/D location is not in the axial center of the tube.*

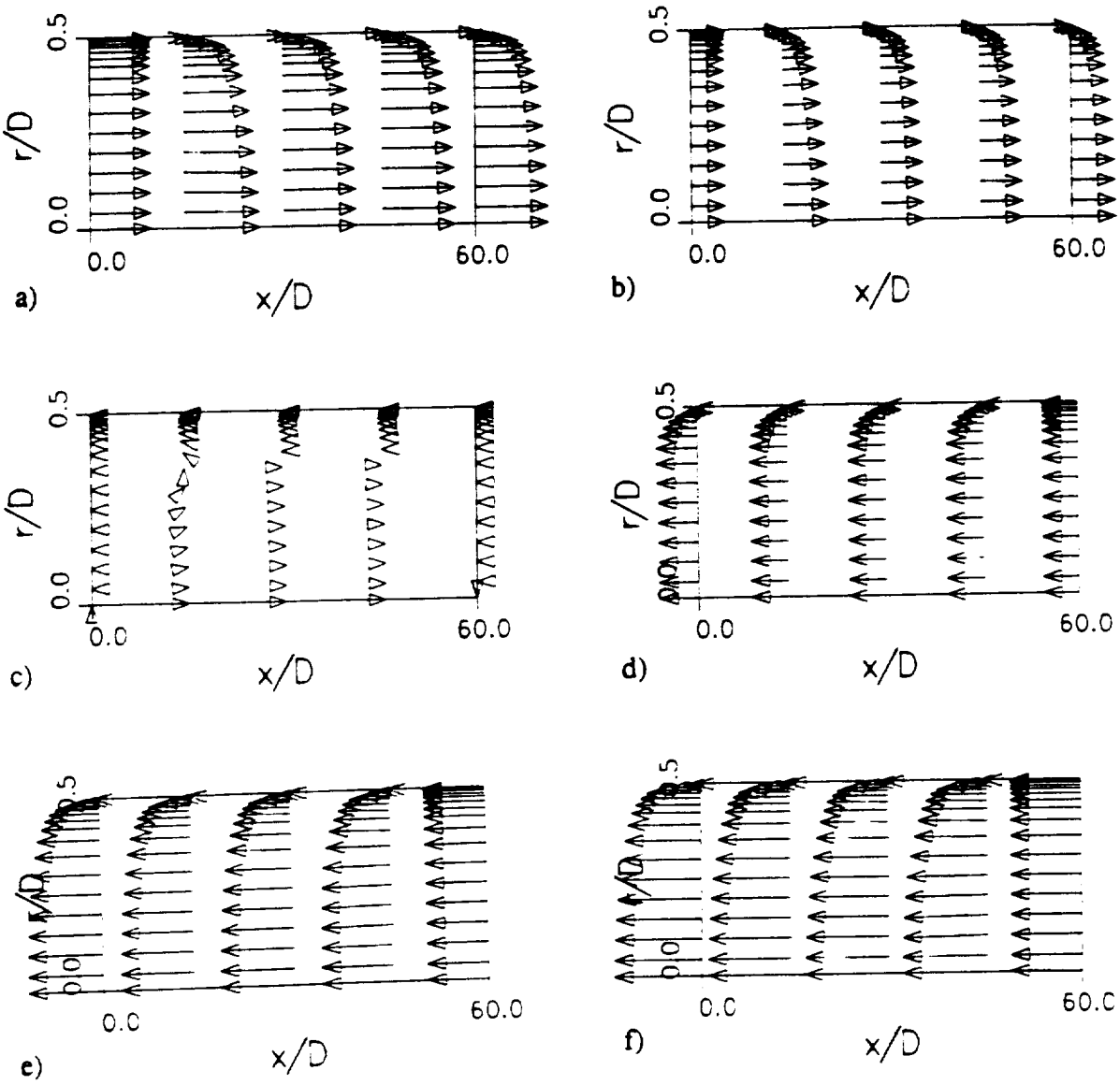

Fig. 7.13: Normalized velocity vectors. Data point **SPRE**: Re_{max} = 11700, *Va = 80, L/D = 60. Crank angles: a) 120°, b) 150°, c) 180°, d) 210°, e) 240°, f) 270°.*

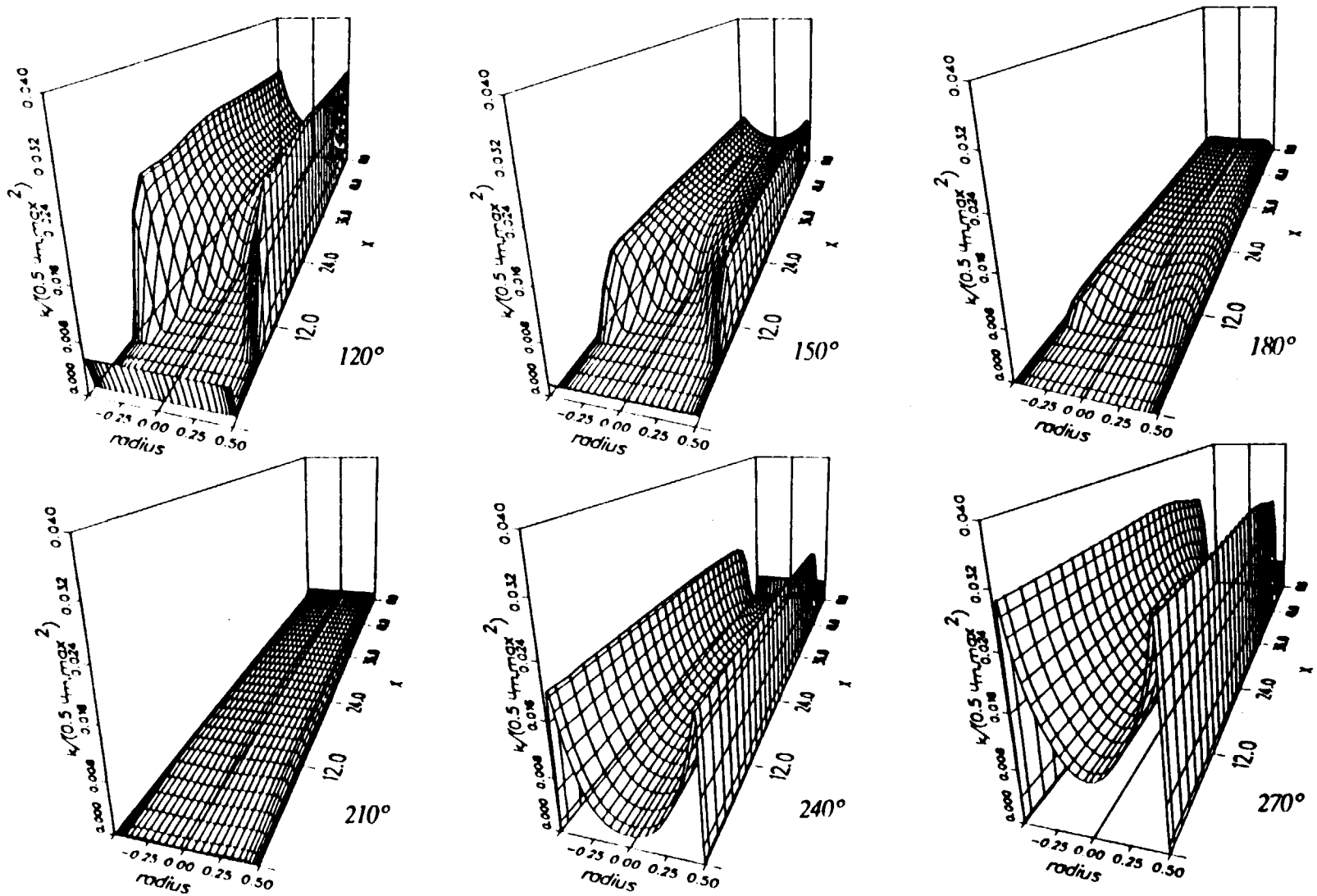

Fig. 7.14: Normalized turbulent kinetic energy $k/(0.5\ u^2_{m,max})$ *at various crank angles. Data point* ***SPRE****:* $Re_{max}=1.17x10^4$*, Va=80, L/D=60. Mean flow direction: 120°, 150° into plane; 180° flow reversal; 210°, 240°, 270° out of plane.*

Fig. 7.15: Normalized turbulent dissipation rate $\varepsilon_{ref}/u_{m,max}^4$ at various crank angles. Data point SPRE: Re_{max}=1.17x10⁴, Va=80, L/D=60. Mean flow direction: 120°, 150° into plane; 180° flow reversal; 210°, 240°, 270° out of plane.

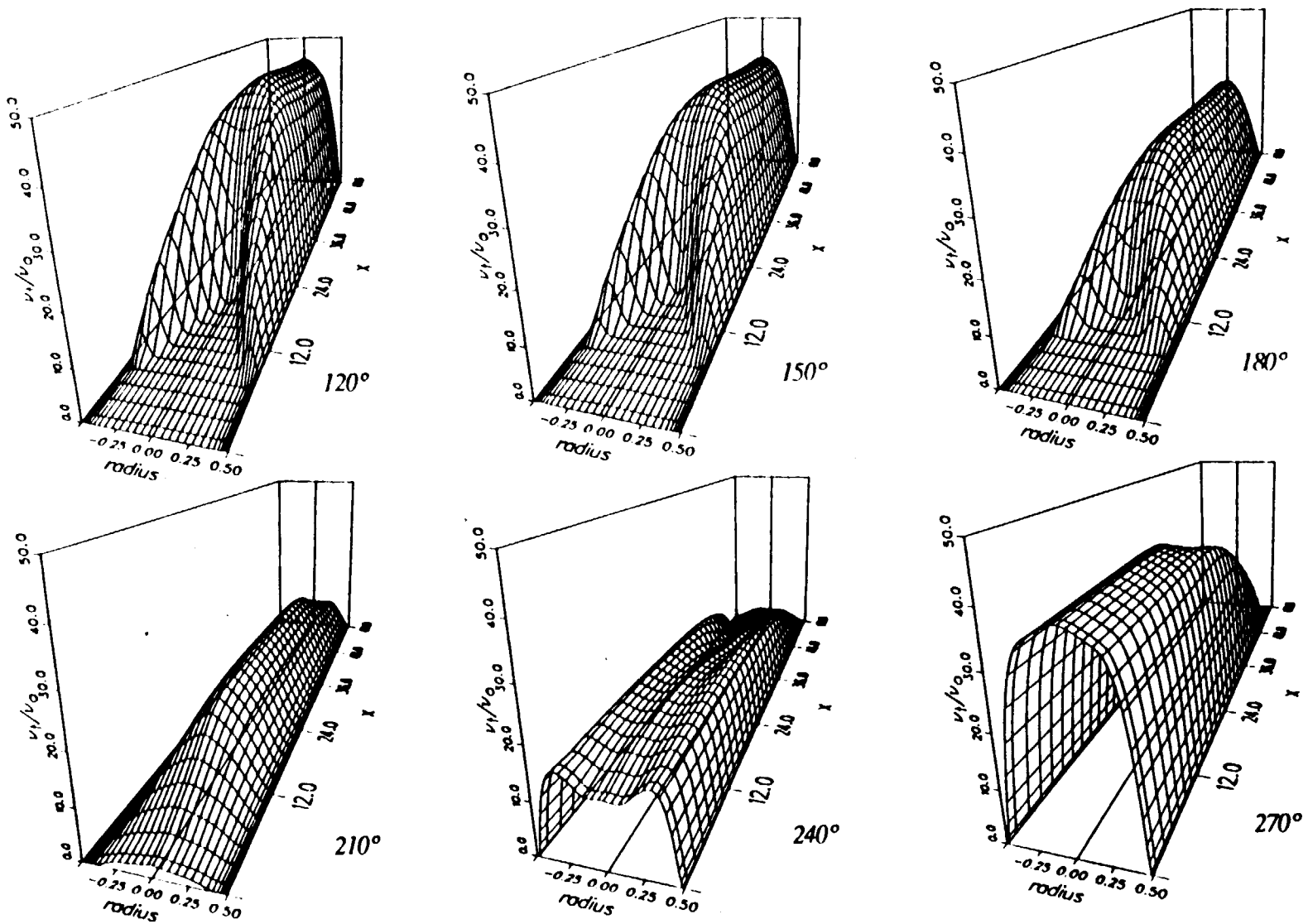

*Fig. 7.16: Normalized turbulent viscosity ν_t/ν_{ref} at various crank angles. Data point **SPRE**: $Re_{max}=1.17x10^5$, Va=80, l/D=60. Mean flow direction: 120°, 150° into plane; 180° flow reversal; 210°, 240°, 270° out of plane.*

7.2. Other Test Cases Computed

There were four more test cases computed, case e, d, m, p. The lettering of the cases corresponds to the names of Seume's experiments. According to Seume's findings, case e lies in the "fully turbulent" region, a region where the maximum Re number is high enough to cause instabilities to significantly perturb the flow, but where the frequency is too high to allow the fluctuations to die down as the flow reverses directions and accelerates. In this case, the ability of the turbulence model to predict transition is secondary. Case p is the corresponding case on the laminar side. According to the experiments by Seume (1988) and Ohmi et al. (1982) and Iguchi et al. (1983), the flow in case p always remains

Table 7.2: Test cases investigated

Case	Re_{max}	Va	Str	L/D	A_R	Ma_{max}	$K_{a,max}^*$
SPRE	1.17e4	80	0.0274	60	1.22	0.015	9.36e5
d	1.32e5	81.2	0.0025	60	13.6	0.17	1.07e7
e	1.87e5	230.3	0.0049	60	6.8	0.23	4.31e7
m	2.39e4	230.3	0.0386	68.5	0.8	0.03	5.50e6
p	8.43e3	231.1	0.0548	60	0.3	0.01	1.95e6

laminar. Here, the ability of the turbulence model to accurately represent transition is the primary factor for accurate predictions. Case d and m are in the transitional regime where the flow is laminar-like during parts of the cycle, and turbulent-like during the rest. In particular, with case d we can test the influence of increasing the Re number from the SPRE case while keeping the frequency constant; with case m we can test the influence of increasing the Valency number while maintaining the order of magnitude of Re number. The maximum non-dimensional acceleration occurring in each of the test cases falls approximately in the range of accelerations investigated in Chapter 6.4.

Comparison with experiment. No measured velocity profiles are available for either of these cases. However, since the profiles in the SPRE case can be predicted fairly well, we presume that also in the cases considered here the predicted profiles will be realistic provided that we can model transition correctly. For case p the laminar computation can give some basis for comparing velocity profiles. Available from experiment are the rms fluctuations at different locations for cases e, d and p. Even though case m is cited in Seume (1988), the data files could not be found any more. Figure 7.17 shows a *qualitative* comparison of the measured rms velocity fluctuations with the computed data at x/D=16 (near the drive end). While the agreement is a very close between experiment and computation in cases e and d, it is decidedly worse for case p.

In case e and d, the computed fluctuations in the center show a more structured, wave-like behavior than their experimental counterparts. In case e, the experimental near wall profile shows a clear phase lag as compared to the computations. As discussed in Chapter 3.3.6., the relaxation time of turbulence seems to play a role in this case. The computational fluctuations are in phase with the mean flow field because the present turbulence model requires an immediate turbulent stress response to a large scale shear. The measured phase lag in the near wall fluctuations will most likely lead to a phase lag in the friction coefficient which is larger than predicted. In case d, where the frequency is only about one third of that in case e, no such phase lag can be detected in the measurements. In case p, the assumption of a specific value of TI at the inflow influences the result significantly. For a short pipe this outcome can be expected in light of the findings of Chapter 6. Based on the measured TI in the SPRE case, it is believed that the 0.5% TI for case p is closer to the experimental conditions. The computations show a clearer up-and-down trend than the experiment. Also, disregarding the pitfalls of a quantitative comparison for a moment, the level of the fluctuations predicted seems to be higher than seen experimentally. However, especially for the case of 0.5% TI, the level of fluctuations remains very low throughout, even near the wall.

Cross stream transport of turbulence. The effect of cross stream transport of turbulence is manifested by a phase shift between the near wall fluctuations and the centerline fluctuations and can be seen from Figure 7.18. The three cases shown (e, m and p) have the same frequency but different Re_{max}. The computed shift is greatest for case p and small for e. In case e, practically during the entire cycle time, turbulence is generated near the wall and transported toward the center. In case p, fluctuations will be transported towards the center during the decelerating phase, and toward the wall in the accelerating phase. Case m lies in between those two extremes.

Friction coefficient for fully developed flow. Figure 7.19 shows the computed friction coefficients and compared them with the laminar and turbulent steady state correlations. It becomes clear that for cases d and e the turbulent steady state friction coefficient is an excellent representation, whereas the results for case m are similar like for the SPRE case where the c_f values depart markedly from the steady state correlation in the accelerating phase. For case p, the steady state correlation is very bad. This, however, has long been known from analyses, experiments and computations of laminar oscillatory flows. This finding supports the Shemer's (1985) hypothesis that a similarity parameter like the Va number which describes the influence of the unsteadiness of the flow on the various flow parameters like c_f should be built using some kind of *effective* viscosity instead of the molecular value. It is the effective viscosity that connects the motions of the boundary layer with the core in the tube. If the effective viscosity is high throughout the cycle (case d and e), then the influence of the unsteadiness on the flow parameters is small, even though the ordinarily used Va number suggests a strong influence. Note that for cases SPRE and m the average effective viscosity is higher in the decelerating phase where the steady state correlation agrees much better. Fig 7.19d shows, in addition to the laminar and turbulent steady state correlations, the results of a computation of case p in which the turbulence model was turned off completely. It can be seen that a variation in the specification of TI influences the near-outflow c_f predictions only marginally. During the accelerating phase, the "turbulent" computations follow exactly the "laminar" values. In the

decelerating phase, the "turbulent" computed friction coefficients are clearly higher than the corresponding "laminar" values.

Entrance length effects. Effects of the hydrodynamical entrance length are negligible for cases e, d and m (Fig.7.20). Given the proximity of the Re_{max} numbers of cases SPRE and m, it is striking that the entrance length effects are quite different. However, the TI used in case m is a flat 5% throughout the cycle which is much higher than what is used in the SPRE case. As known from Chapter 6, a higher TI causes the flow to develop sooner as a turbulent flow which explains this apparent discrepancy. Case p with 5% TI looks much like case SPRE. However, with 0.5% TI, the behavior at 150° crank angle deviates considerably from a steady state entrance length behavior. Generally, for case p, entrance length effects do play a role for the given pipe length.

Other quantities. Figures 7.21 to 7.36 show 3-D plots for the axial velocity, turbulent kinetic energy, turbulent dissipation rate and turbulent viscosity for the various cases. It may be noted here that for case p the velocity distributions obtained with the turbulence model switched on look very much like the laminar profiles.

Fig. 7.17a: Comparison of computed velocity fluctuations with experiment. Data point e: $Re_{max}=1.87x10^5$, Va=230, x/D=16 (near drive end), L/D=60.

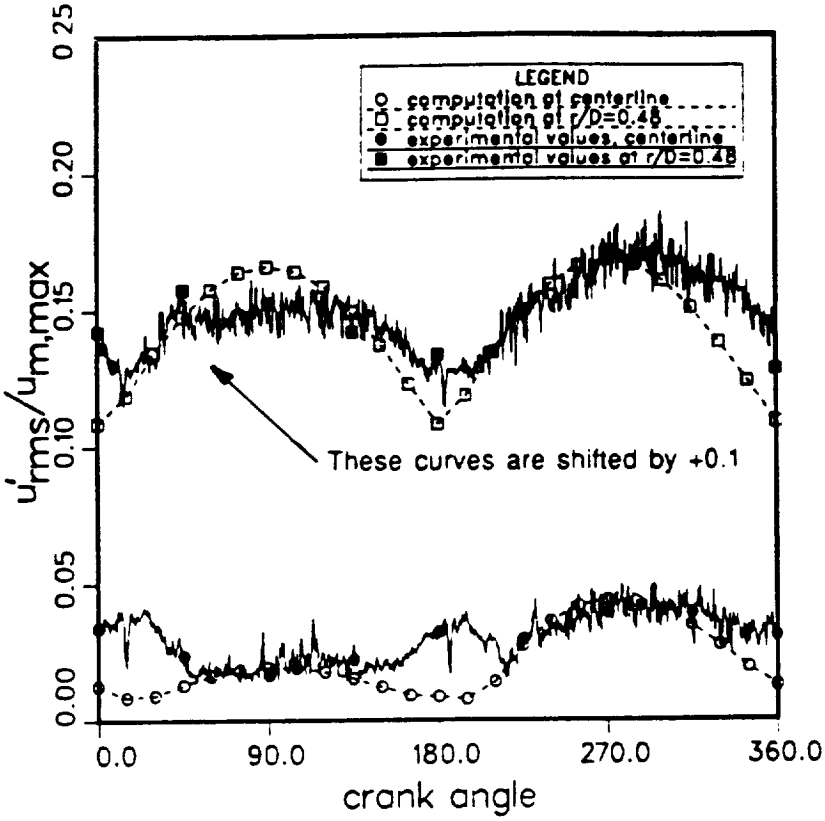

Fig.7.17b: Comparison of computed velocity fluctuations with experiment. Data point d: $Re_{max}=1.32x10^5$, Va = 81, x/D=16 (near drive end), L/D=60.

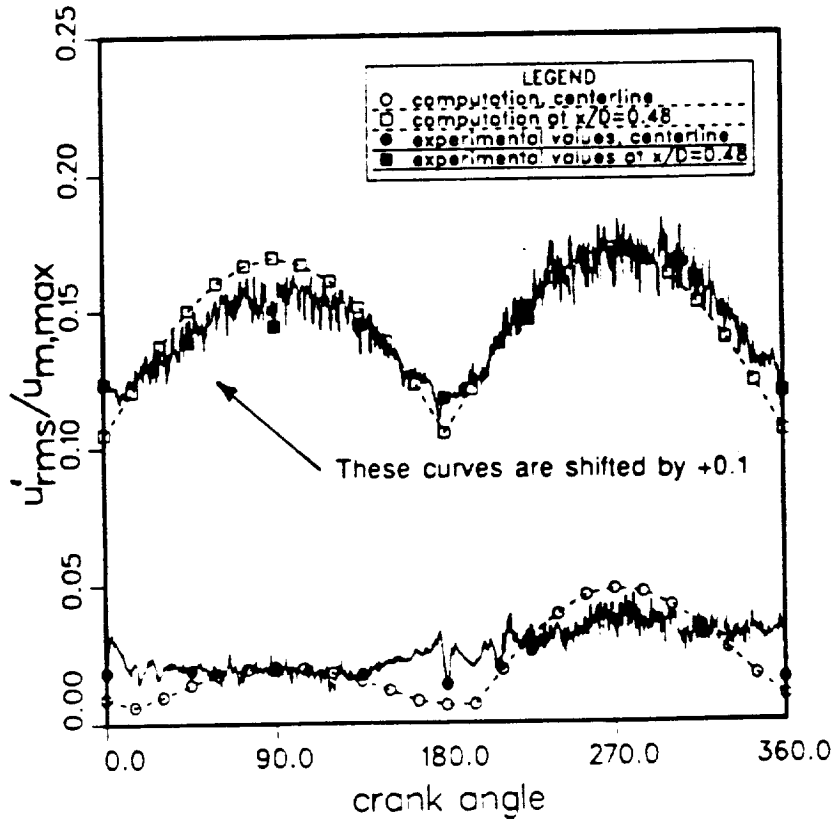

Fig. 7.17c: Comparison of computed velocity fluctuations with experiment. Data point p: $Re_{max}=8.43x10^3$, Va=231, x/D=16 (near drive end), L/D=60.

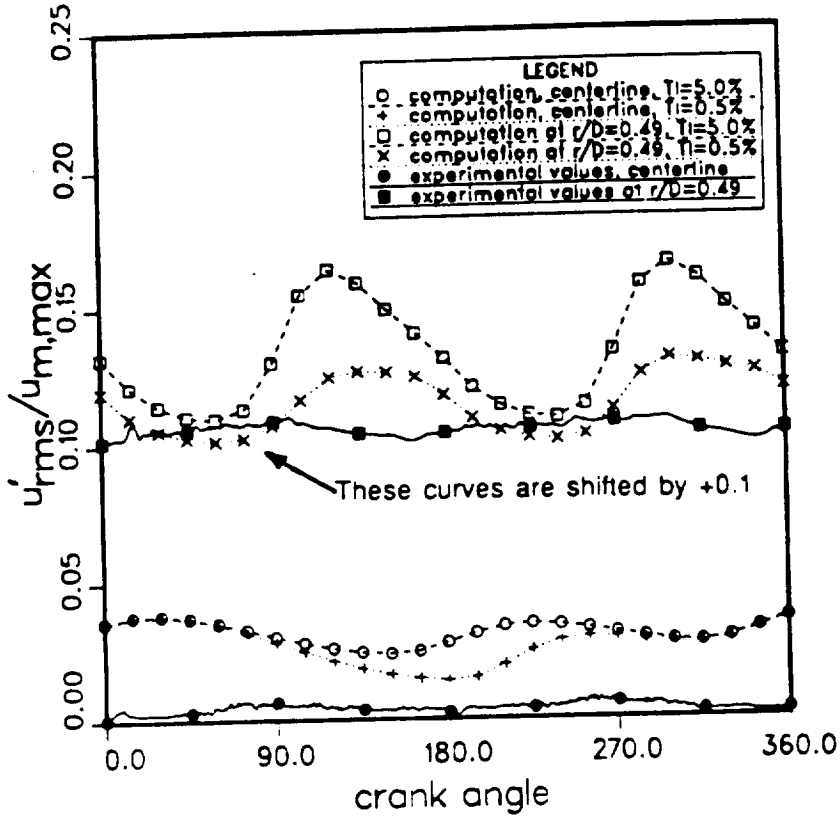

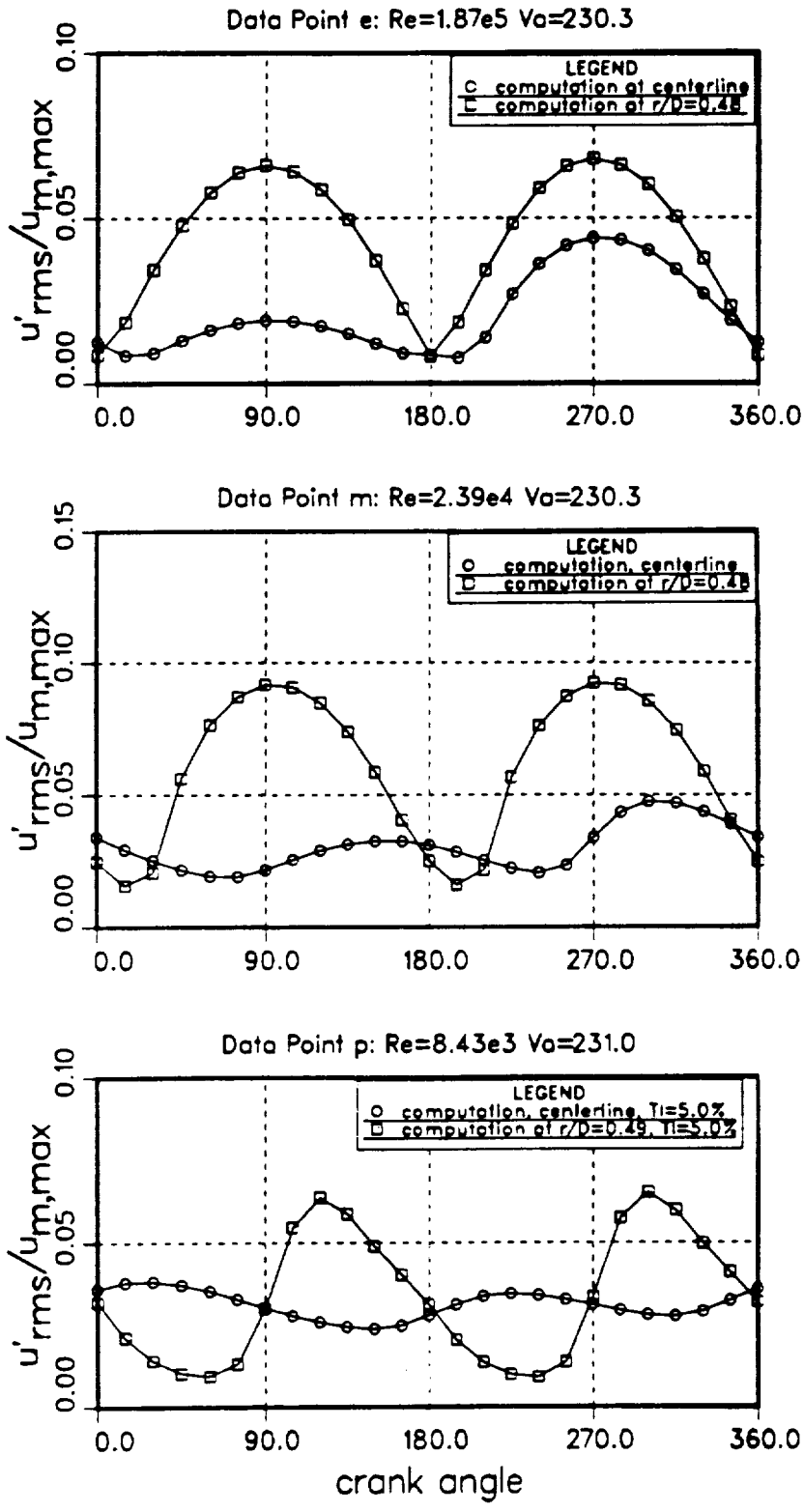

Fig. 7.18: Radial transport of turbulence for three different data points with the same Va number but different Re_{max} number.

Fig. 7.19a: Comparison of computed fully developed friction coefficient with steady state correlations. Data point e: $Re_{max}=1.87x10^5$, Va=230, L/D=60.

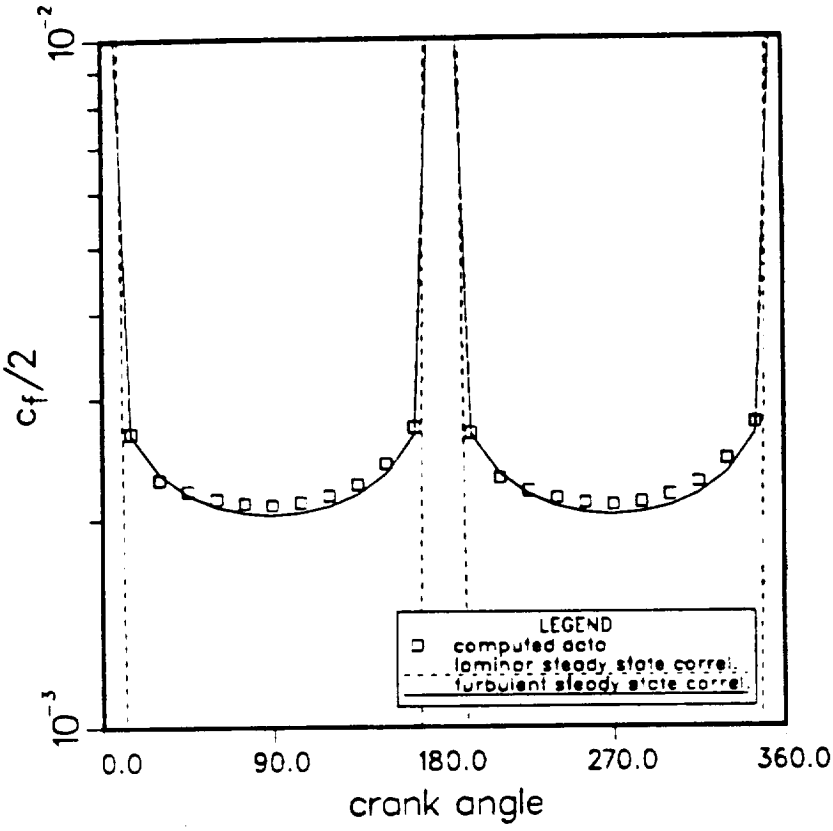

Fig. 7.19b: Comparison of computed fully developed friction coefficient with steady state correlations. Data point d: $Re_{max}=1.32x10^5$, Va = 81, L/D=60.

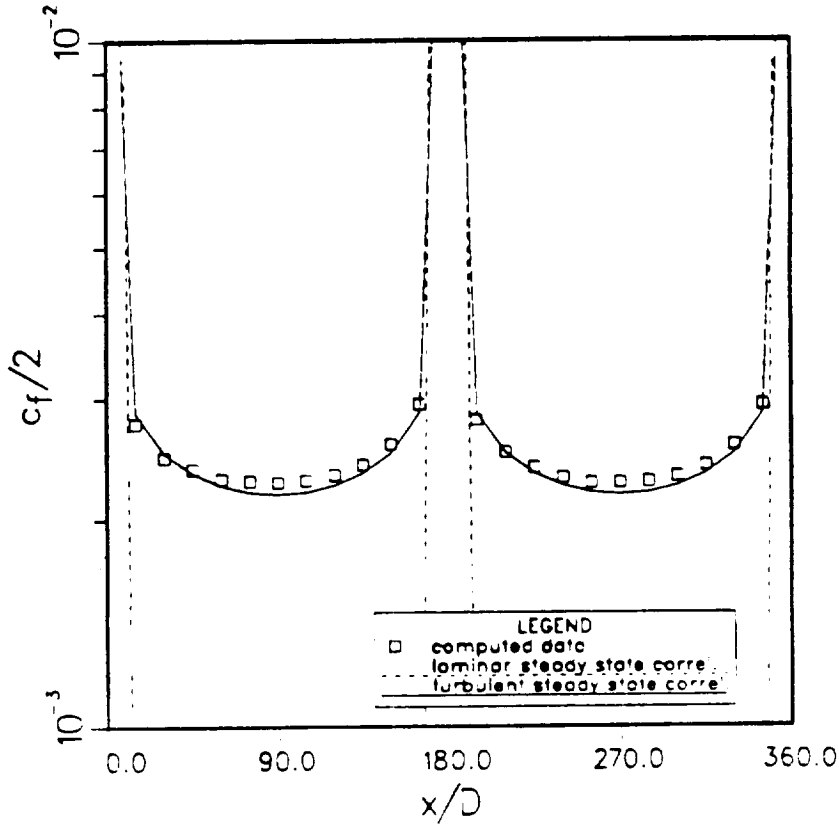

Fig. 7.19c: Comparison of computed fully developed friction coefficient: with steady state correlations. Data point m: $Re_{max}=2.39x10^4$, Va =230, L/D=68.5.

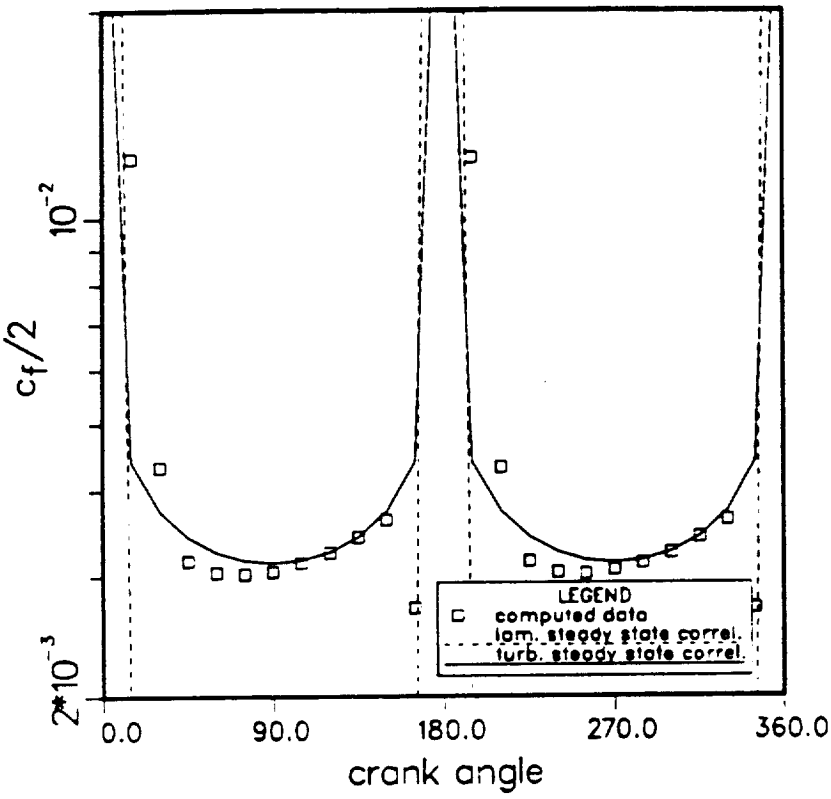

Fig. 7.19d: Comparison of computed fully developed friction coefficient with steady state correlations. Data point p: $Re_{max}=8.43x10^3$, Va=231, L/D=60.

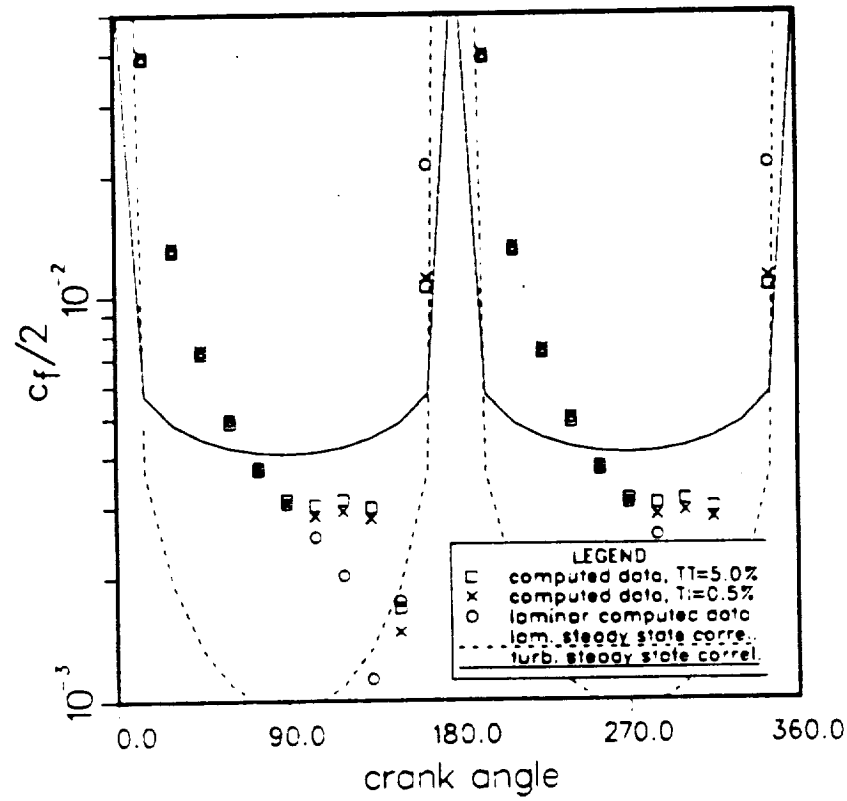

Fig. 7.20a: Ratio of local to fully developed friction coefficient at various crank angles. Data point e: $Re_{max}=1.87x10^5$, Va=230, L/D=60.

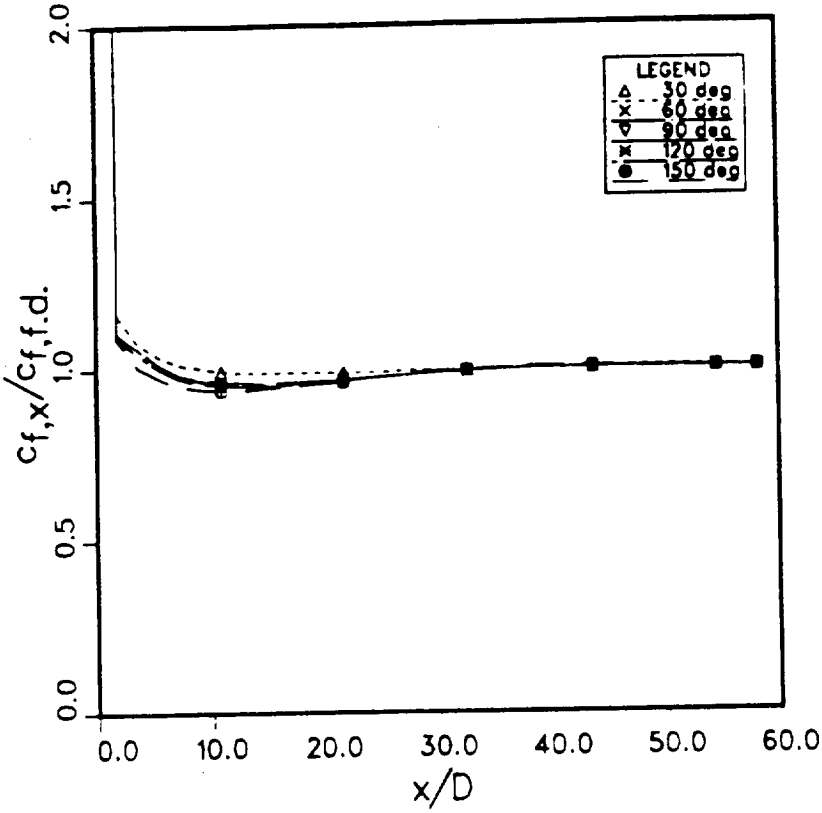

Fig. 7.20b: Ratio of local to fully developed friction coefficient at various crank angles. Data point d: Re_{max} = 1.32x10^5, Va=81, L/D=60.

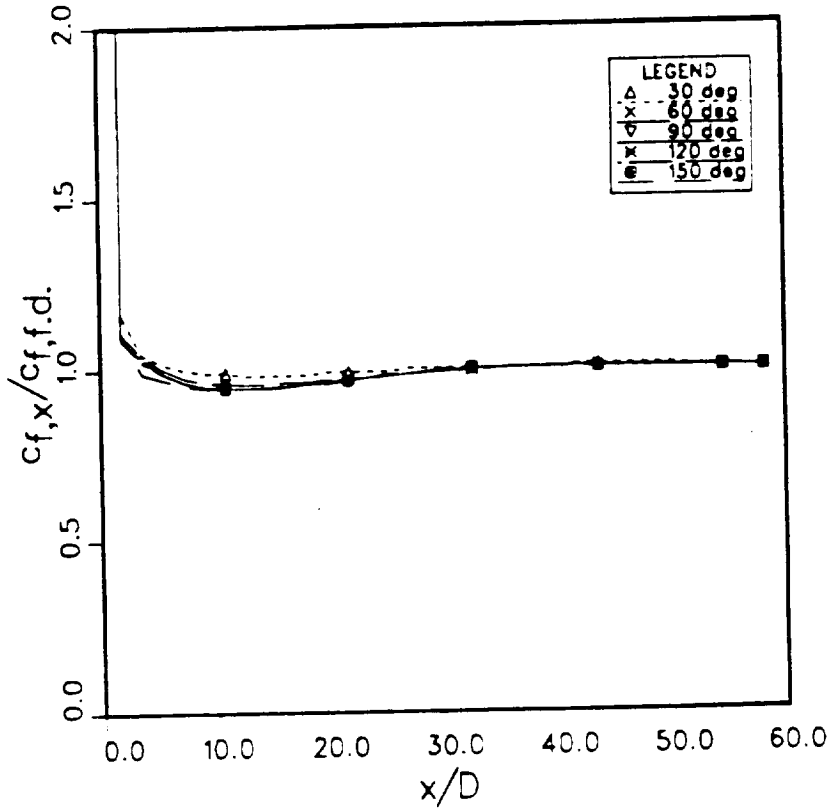

Fig. 7.20c: Ratio of local to fully developed friction coefficient at various crank angles. Data point m: $Re_{max}=2.39x10^4$, Va=230, L/D=68.5.

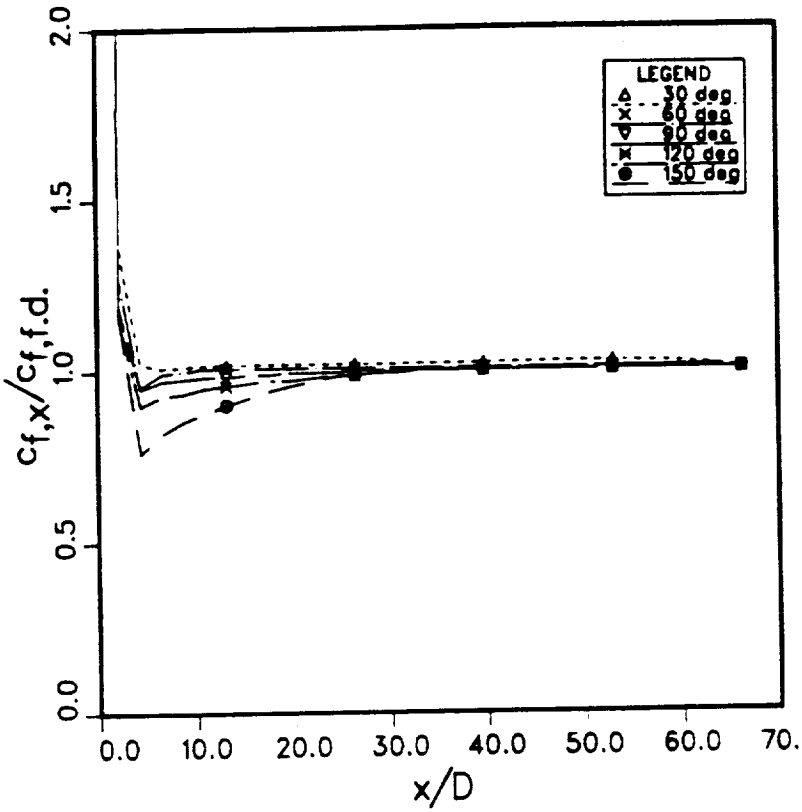

Fig. 7.20d: Ratio of local to fully developed friction coefficient at various crank angles. Data point p: $Re_{max}=8.43x10^3$, Va=231, L/D=60, Tl=5.0%.

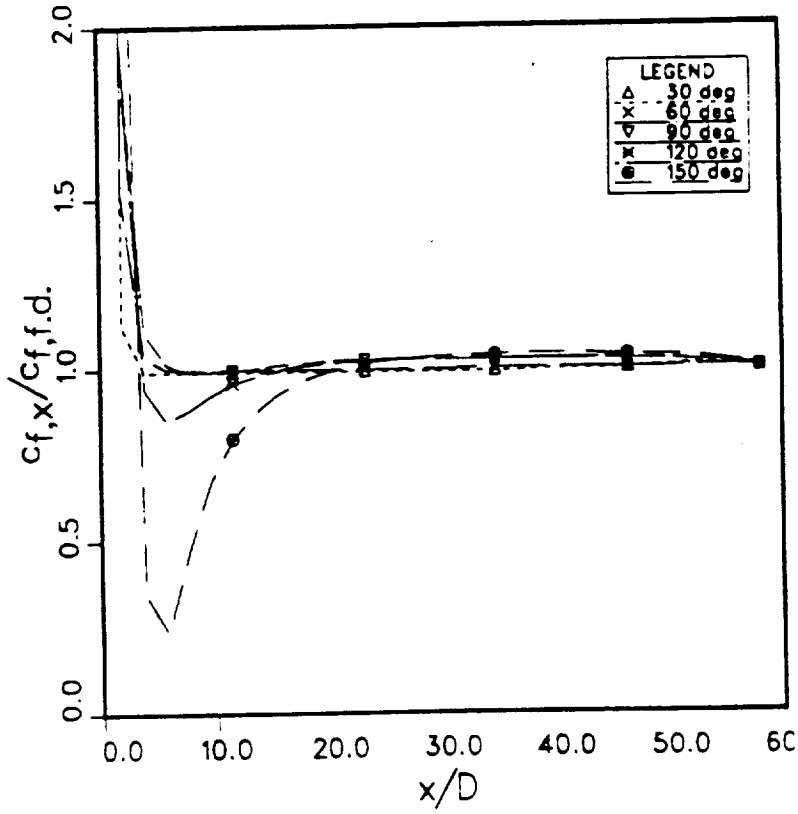

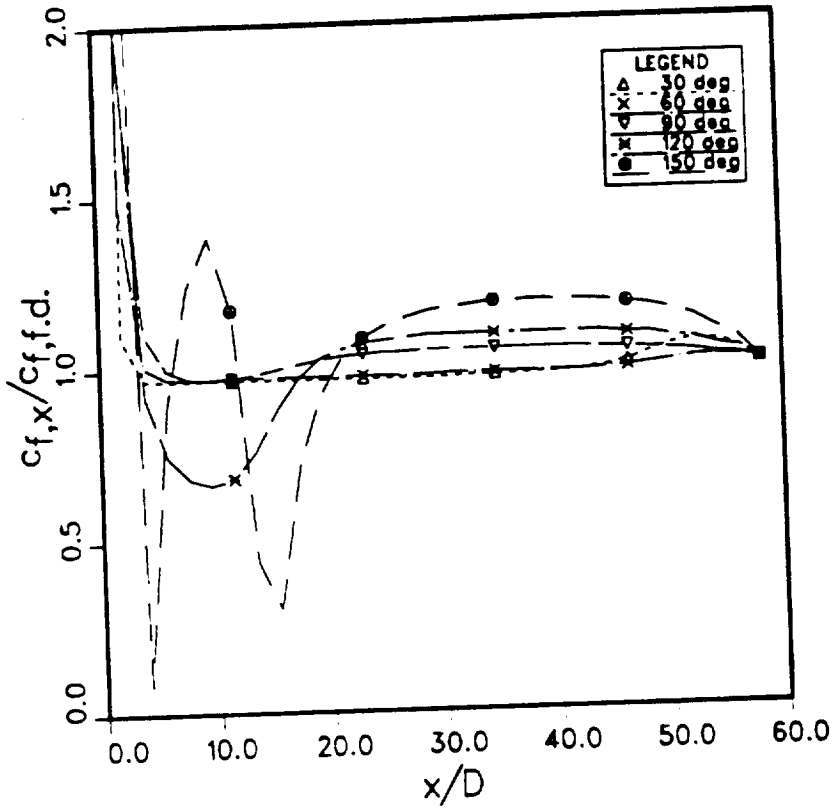

Fig. 7.20e: *Ratio of local to fully developed friction coefficient at various crank angles. Data point* ***p****:* $Re_{max}=8.43x10^3$, *Va=231, L/D=60, TI=0.5%.*

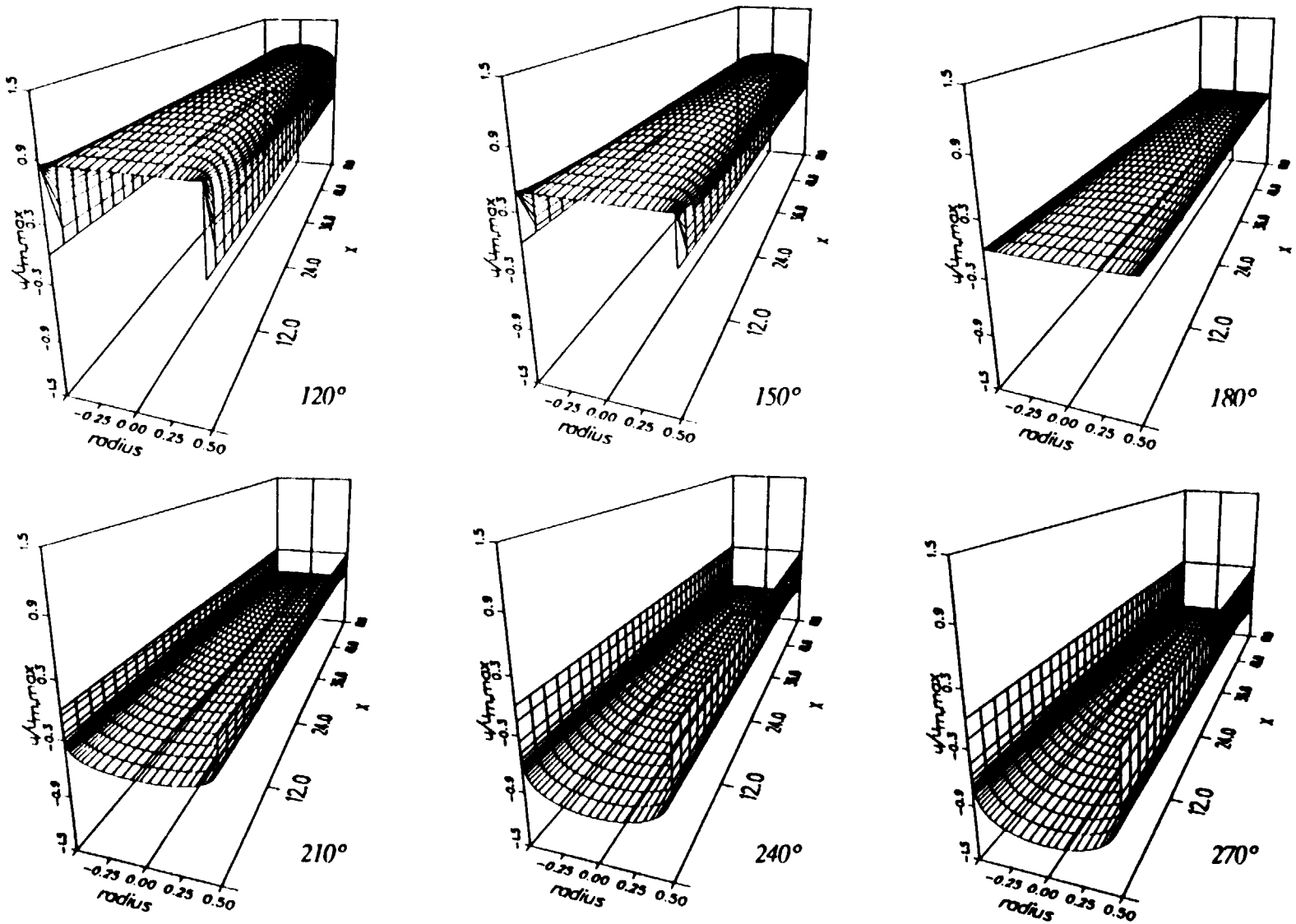

Fig. 7.21: Normalized velocity $u/u_{m,max}$ at various crank angles. Data point e: $Re_{max}=1.87x10^5$, Va=230, L/D=60. Mean flow direction: 120°, 150° into plane; 180° flow reversal; 210°, 240°, 270° out of plane.

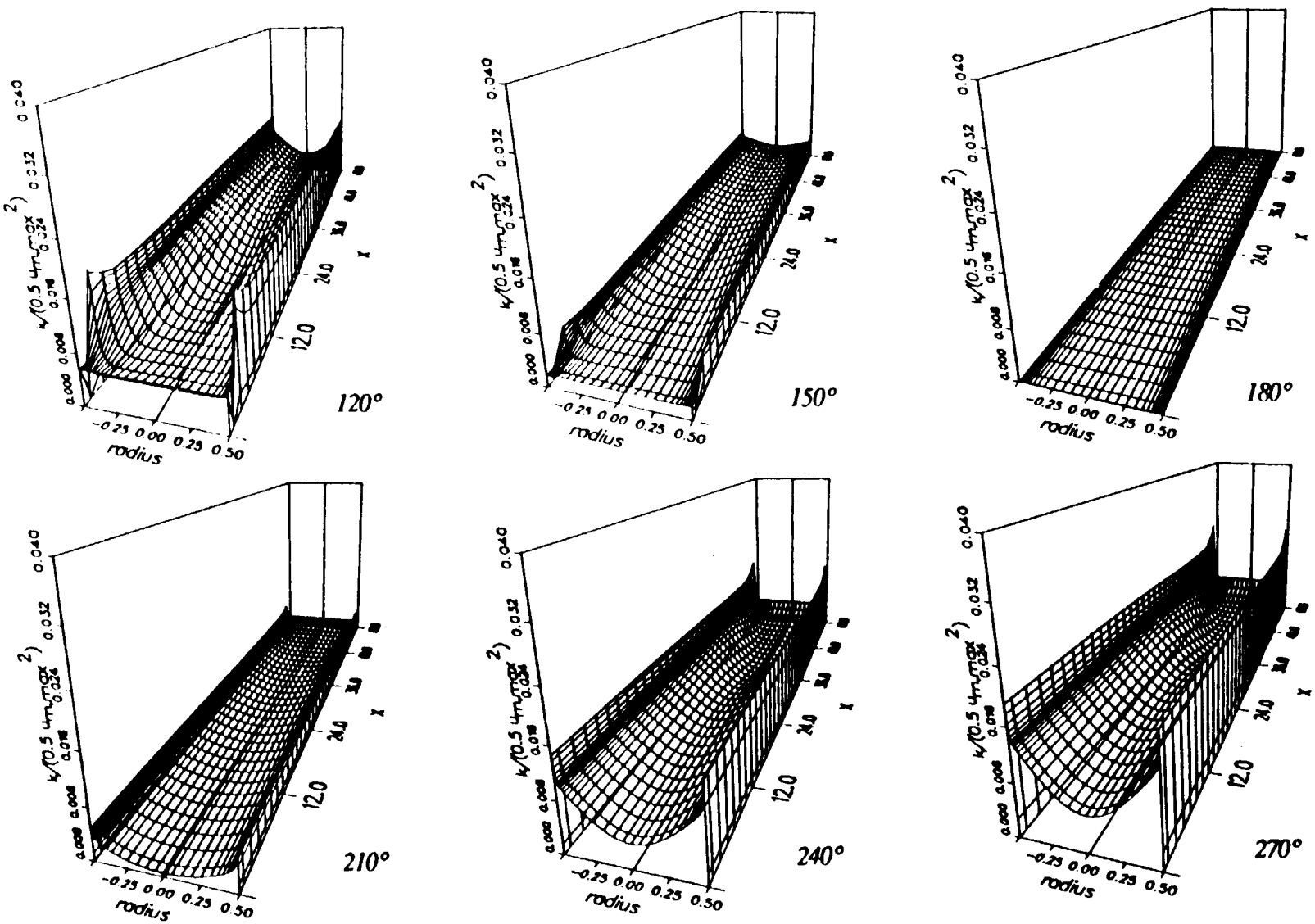

Fig. 7.22: Normalized turbulent kinetic energy $k/(0.5\ u^2_{m,max})$ *at various crank angles. Data point e:* $Re_{max}=1.87x10^5$, *Va=230, LJD=60. Mean flow direction: 120°, 150° into plane; 180° flow reversal; 210°, 240°, 270° out of plane.*

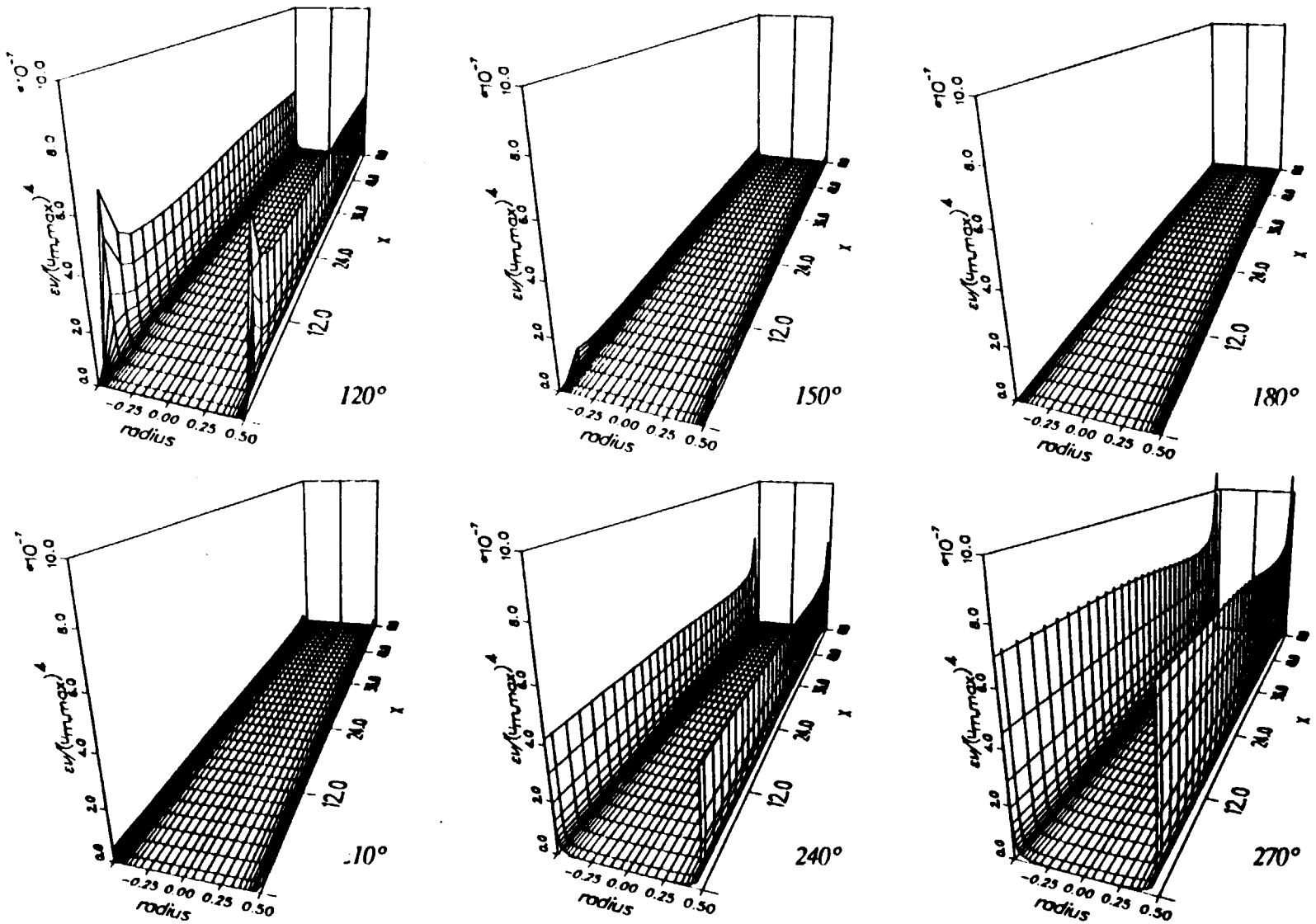

Fig. 7.23: Normalized turbulent dissipation rate $\varepsilon\nu_{ref}/u^4_{m,max}$ at various crank angles. Data point e: $Re_{max}=1.87x10^5$, Va=230, L/D=60. Mean flow direction: 120°, 150° into plane; 180° flow reversal; 210°, 240°, 270° out of plane.

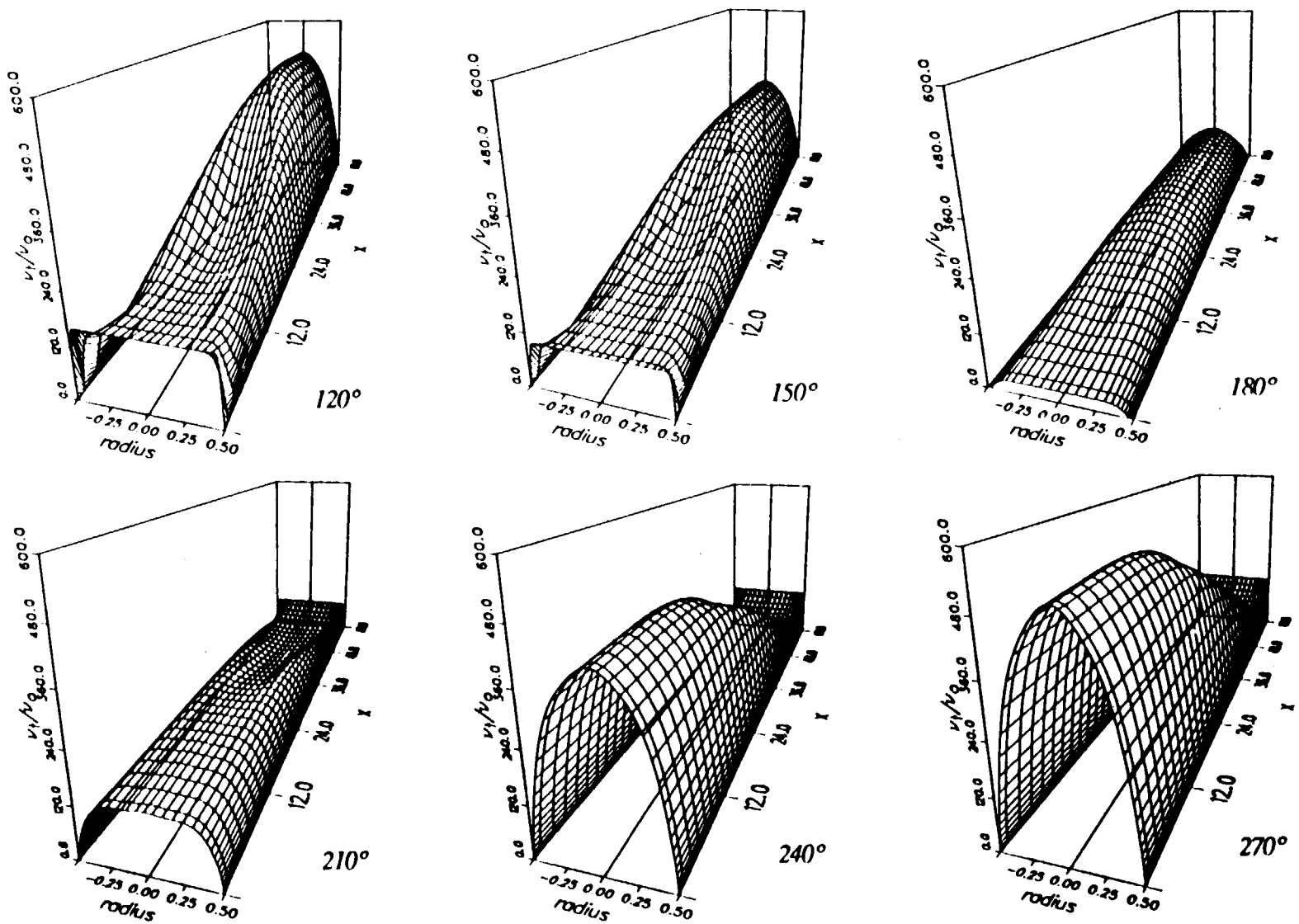

Fig. 7.24: Normalized turbulent viscosity ν_t/ν_{ref} at various crank angles. Data point e: $Re_{max}=1.87x10^5$, Va=230, L/D=60. Mean flow direction: 120°, 150° into plane; 180° flow reversal; 210°, 240°, 270° out of plane.

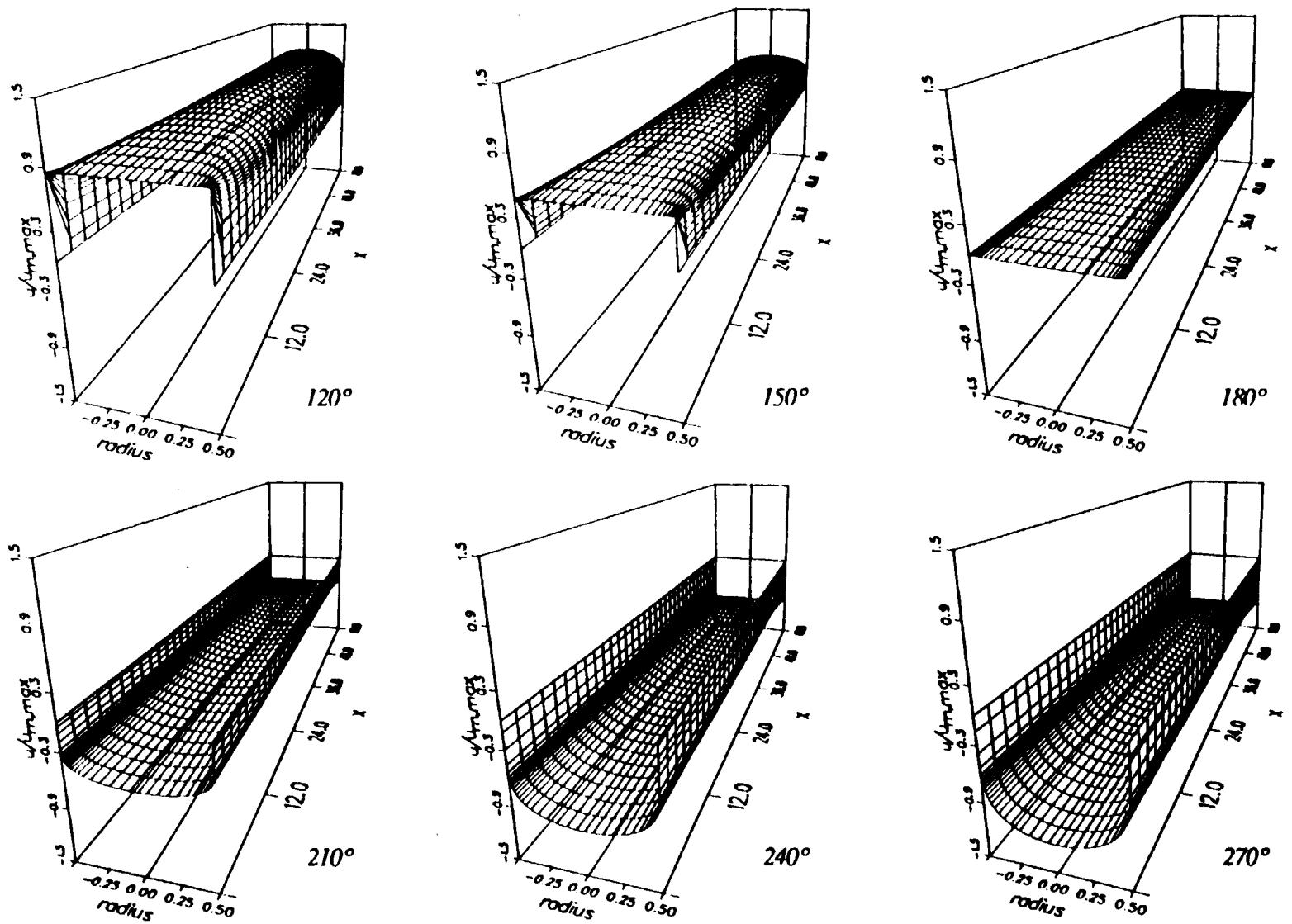

Fig. 7.25: Normalized velocity $u/u_{m,max}$ at various crank angles. Data point d: $Re_{max}=1.32x10^5$, Va=81, L/D=60. Mean flow direction: 120°, 150° into plane; 180° flow reversal; 210°, 240°, 270° out of plane.

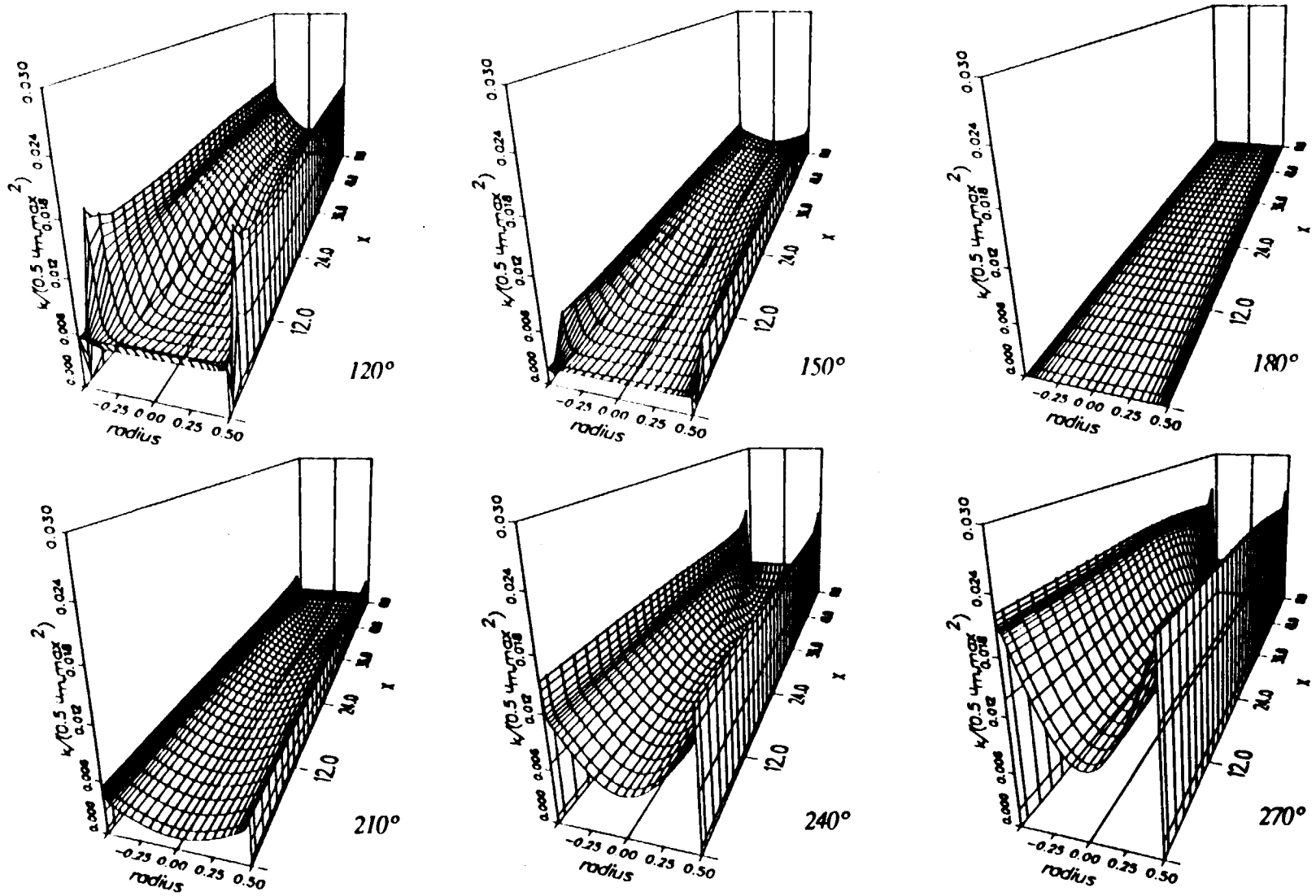

Fig. 7.26: Normalized turbulent kinetic energy $k/(0.5\ u^2_{m,max})$ *at various crank angles. Data point d:* $Re_{max}=1.32x10^5$, *Va=81, L/D=60. Mean flow direction: 120°, 150° into plane; 180° flow reversal; 210°, 240°, 270° out of plane.*

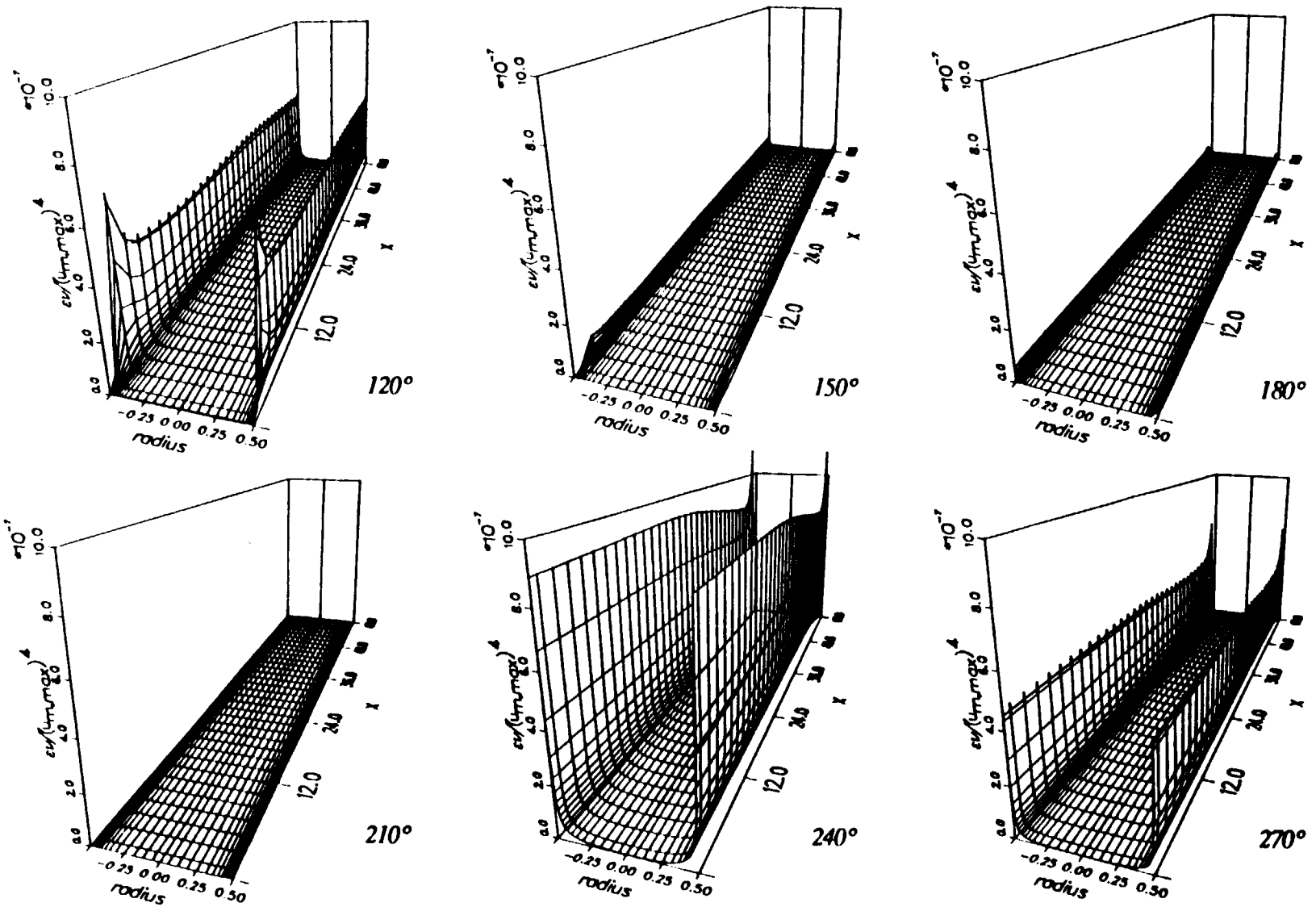

Fig. 7.27: Normalized turbulent dissipation rate $\varepsilon\nu_{ref}/u^4_{m,max}$ at various crank angles. Data point d: Re_{max}=1.32x10^5, Va=81, L/D=60. Mean flow direction: 120°, 150° into plane; 180° flow reversal; 210°, 240°, 270° out of plane.

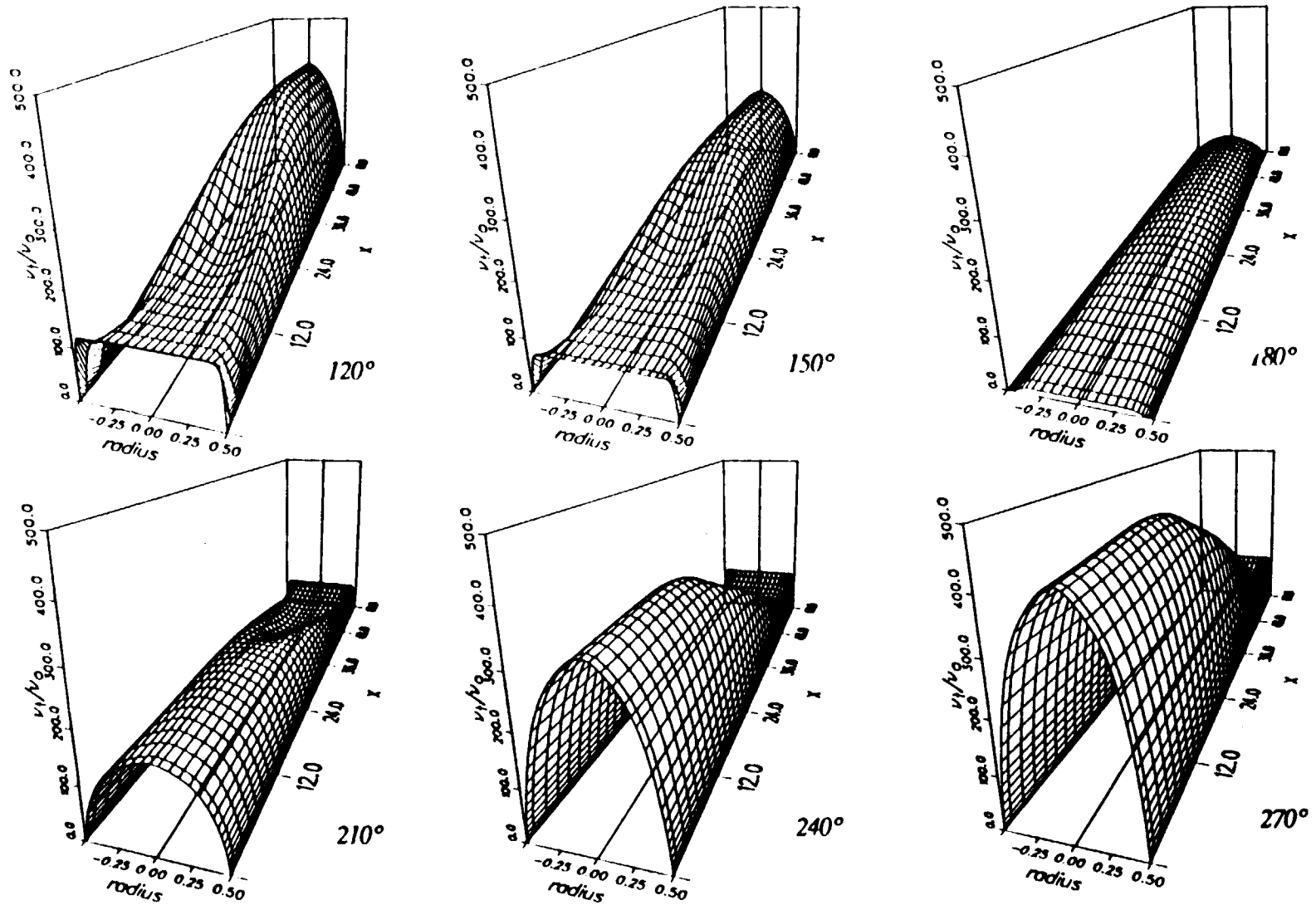

Fig. 7.28: Normalized turbulent viscosity ν_t/ν_{ref} at various crank angles. Data point d: $Re_{max}=1.32x10^5$, Va=81, L/D=60. Mean flow direction: 120°, 150° into plane; 180° flow reversal; 210°, 240°, 270° out of plane.

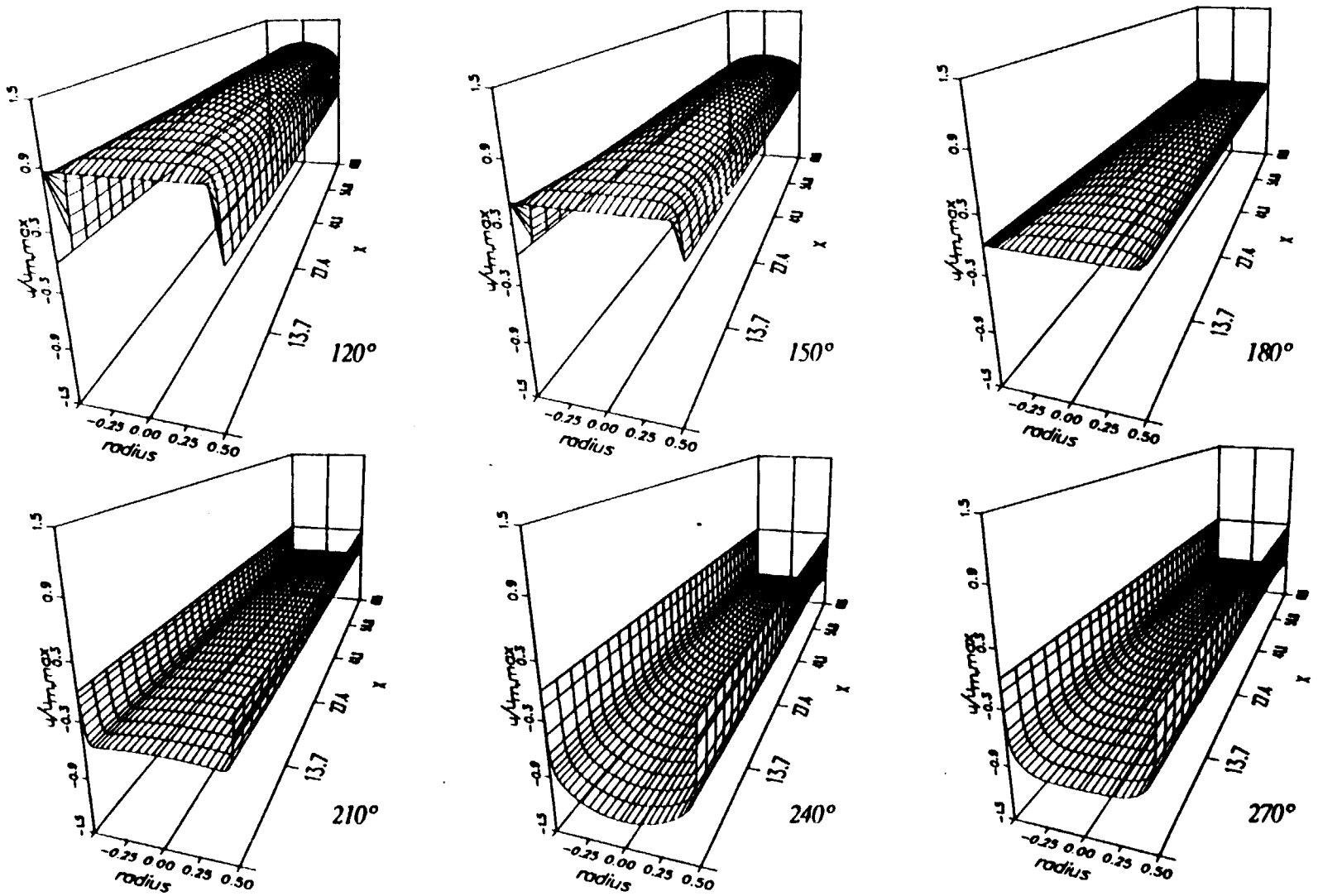

Fig. 7.29: Normalized velocity $u/u_{m,max}$ *at various crank angles. Data point m:* $Re_{max}=2.39x10^4$, *Va=230, L/D=68.5. Mean flow direction: 120°, 150° into plane; 180° flow reversal; 210°, 240°, 270° out of plane.*

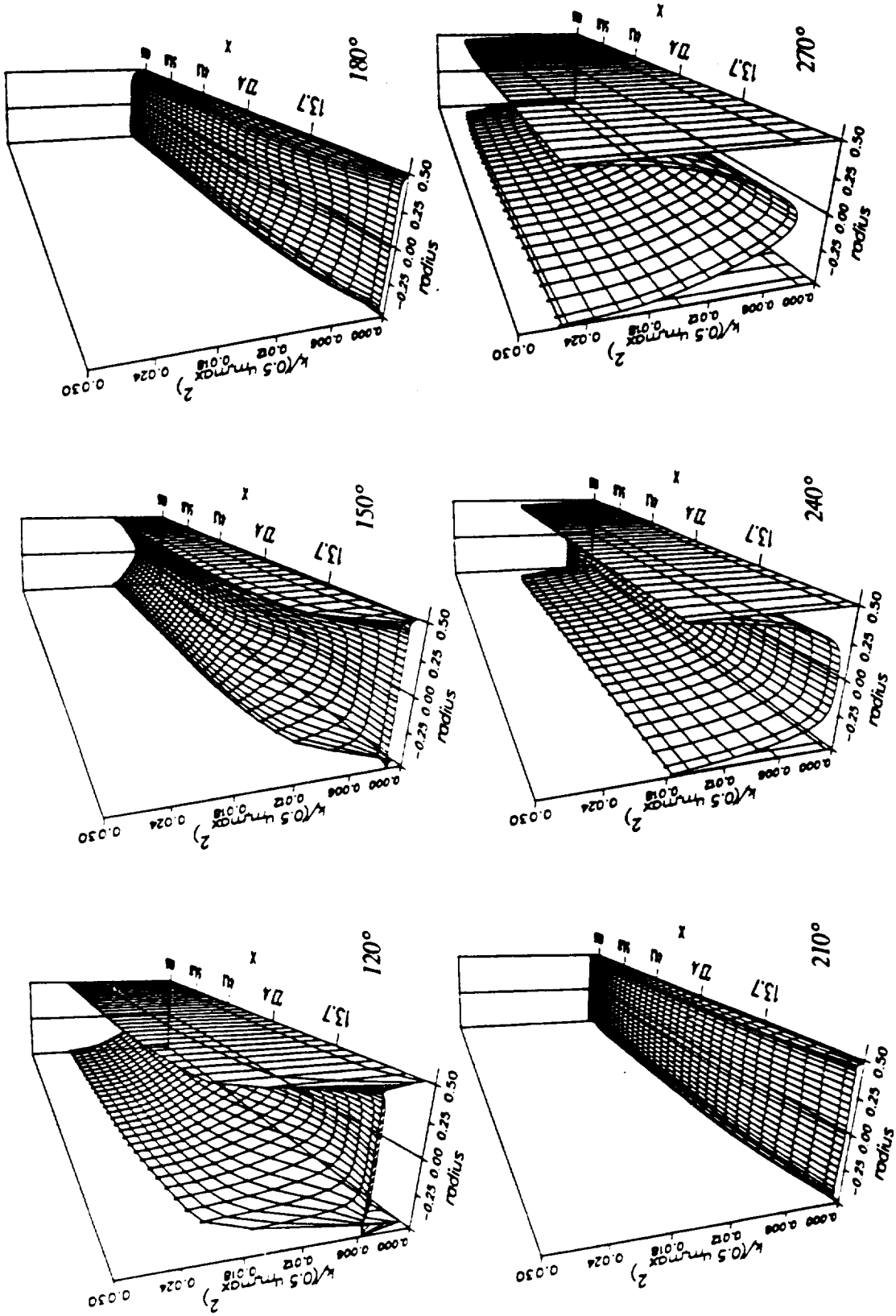

Fig. 7.30: Normalized turbulent kinetic energy $k/(0.5\ u^2_{m,max})$ *at various crank angles. Data point* **m**: $Re_{max}=2.39x10^4$, $Va=230$, $L/D=68.5$. *Mean flow direction: 120°, 150° into plane; 180° flow reversal; 210°, 240°, 270° out of plane.*

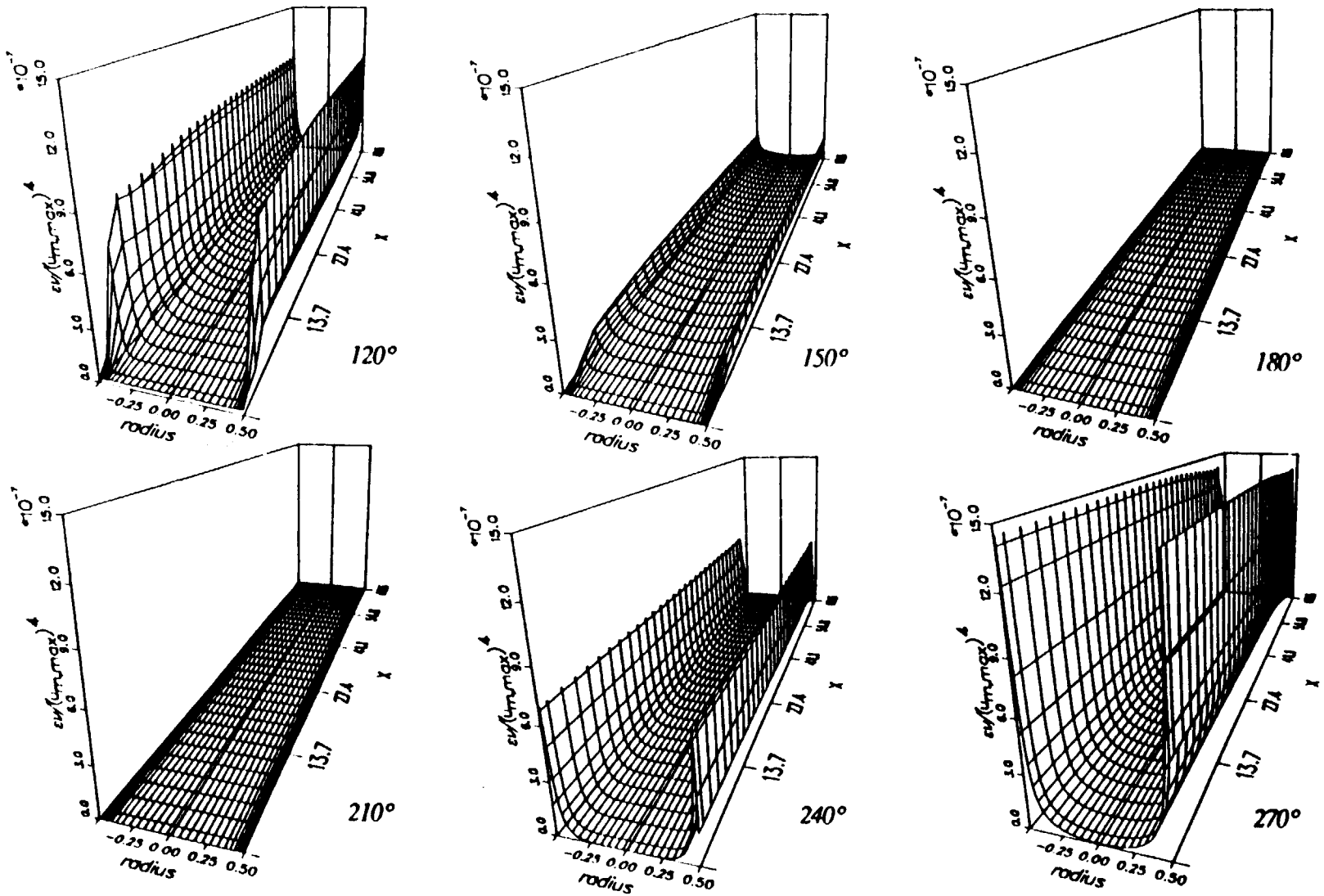

Fig. 7.31: Normalized turbulent dissipation rate $\varepsilon\nu_{ref}/u^4_{m,max}$ at various crank angles. Data point m: $Re_{max}=2.39x10^4$, Va=230, L/D=68.5. Mean flow direction: 120°, 150° into plane; 180° flow reversal; 210°, 240°, 270° out of plane.

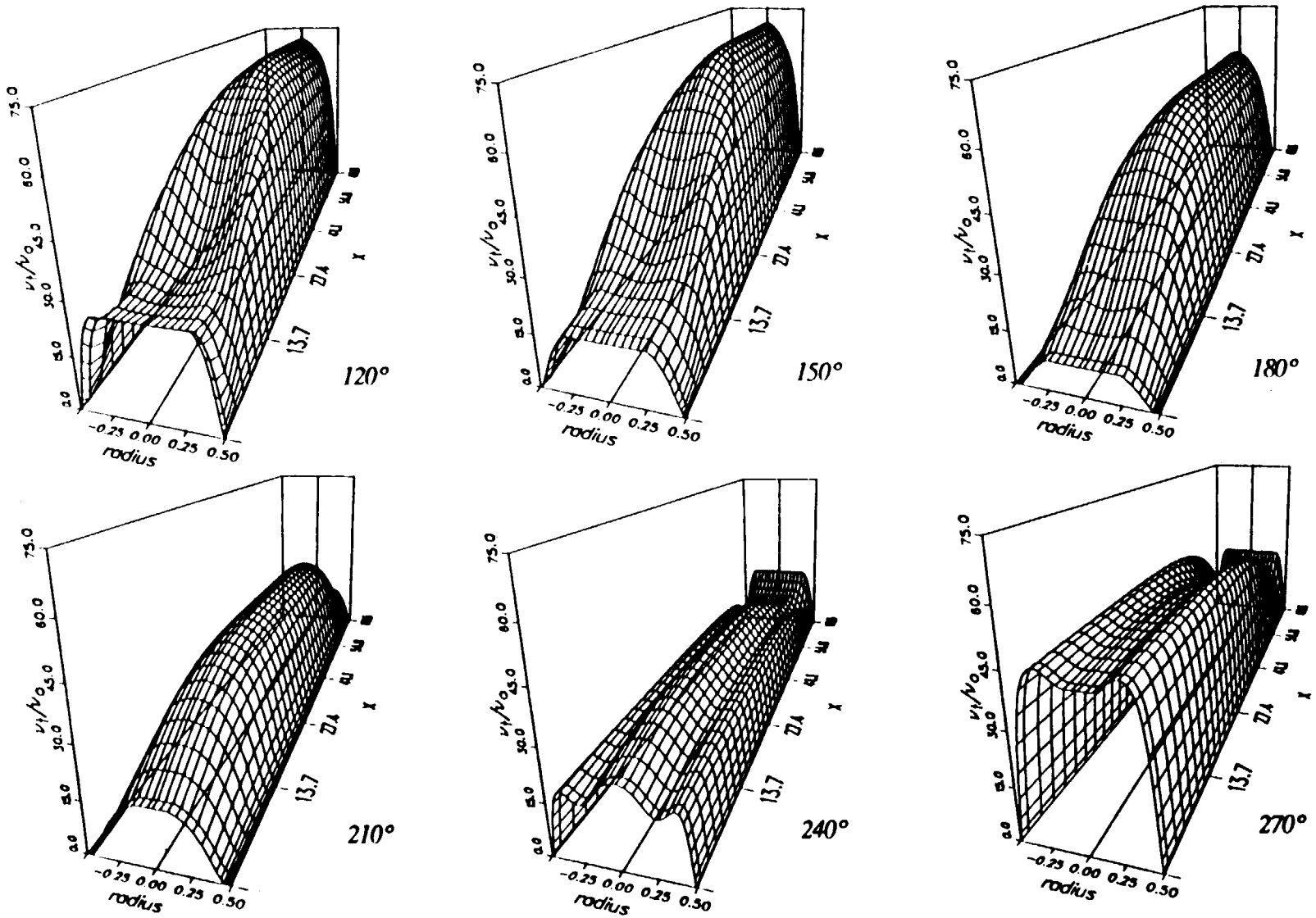

Fig. 7.32: Normalized turbulent viscosity ν_t/ν_{ref} at various crank angles. Data point m: $Re_{max}=2.39x10^4$, Va=230, L/D=68.5. Mean flow direction: 120°, 150° into plane; 180° flow reversal; 210°, 240°, 270° out of plane.

Fig. 7.33a: Turbulent computation, TI=5.0%. Normalized velocity $u/u_{m,max}$ at various crank angles. Data point p: $Re_{max}=8.43x10^3$, Va=231, L/D=60. Mean flow direction: 120°, 150° into plane; 180° flow reversal; 210°, 240°, 270° out of plane.

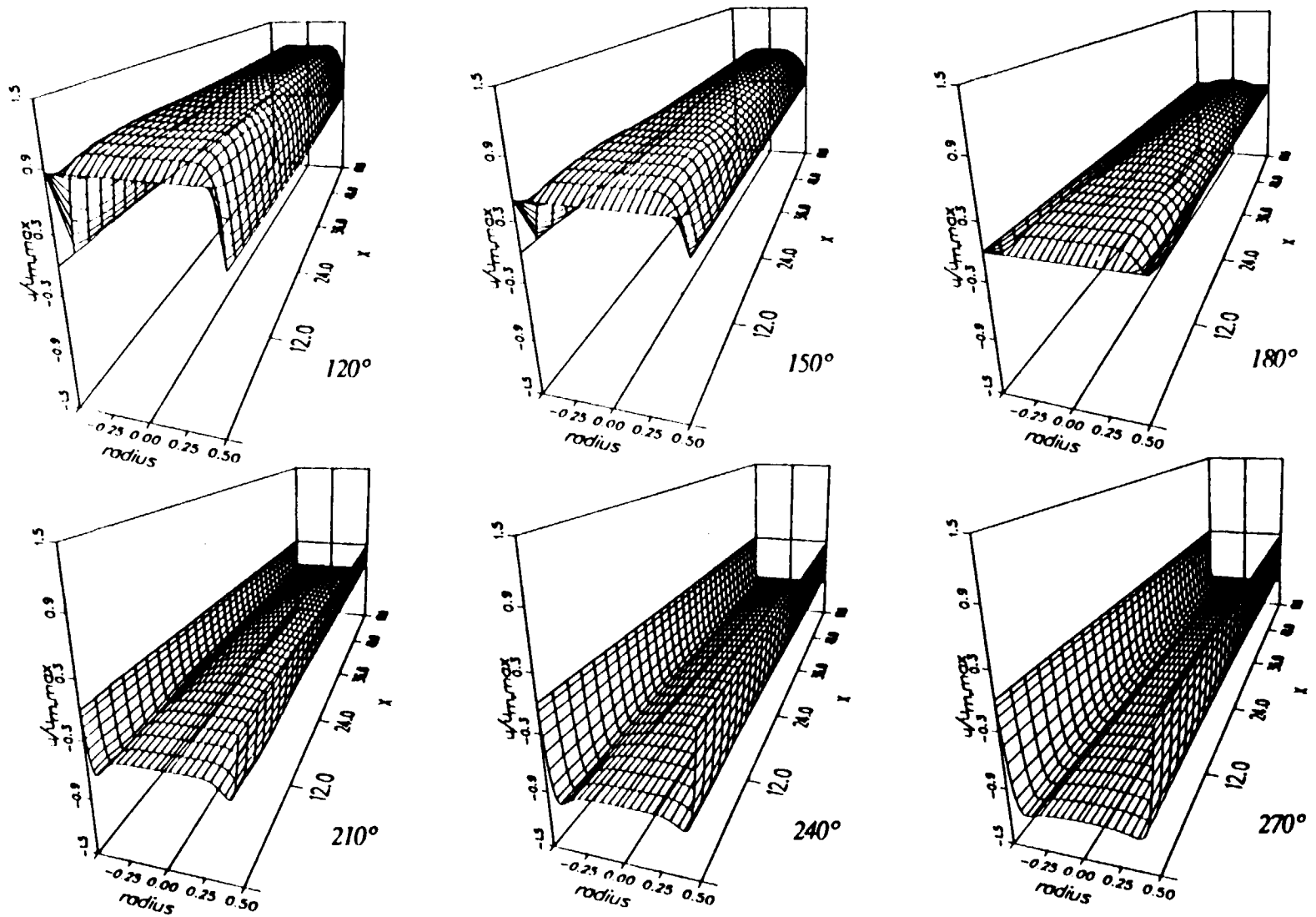

Fig. 7.33b: Turbulent computation, TI=0.5%. Normalized velocity $u/u_{m,max}$ at various crank angles. Data point p: $Re_{max}=8.43x10^3$, Va=231, L/D=60. Mean flow direction: 120°, 150° into plane; 180° flow reversal; 210°, 240°, 270° out of plane.

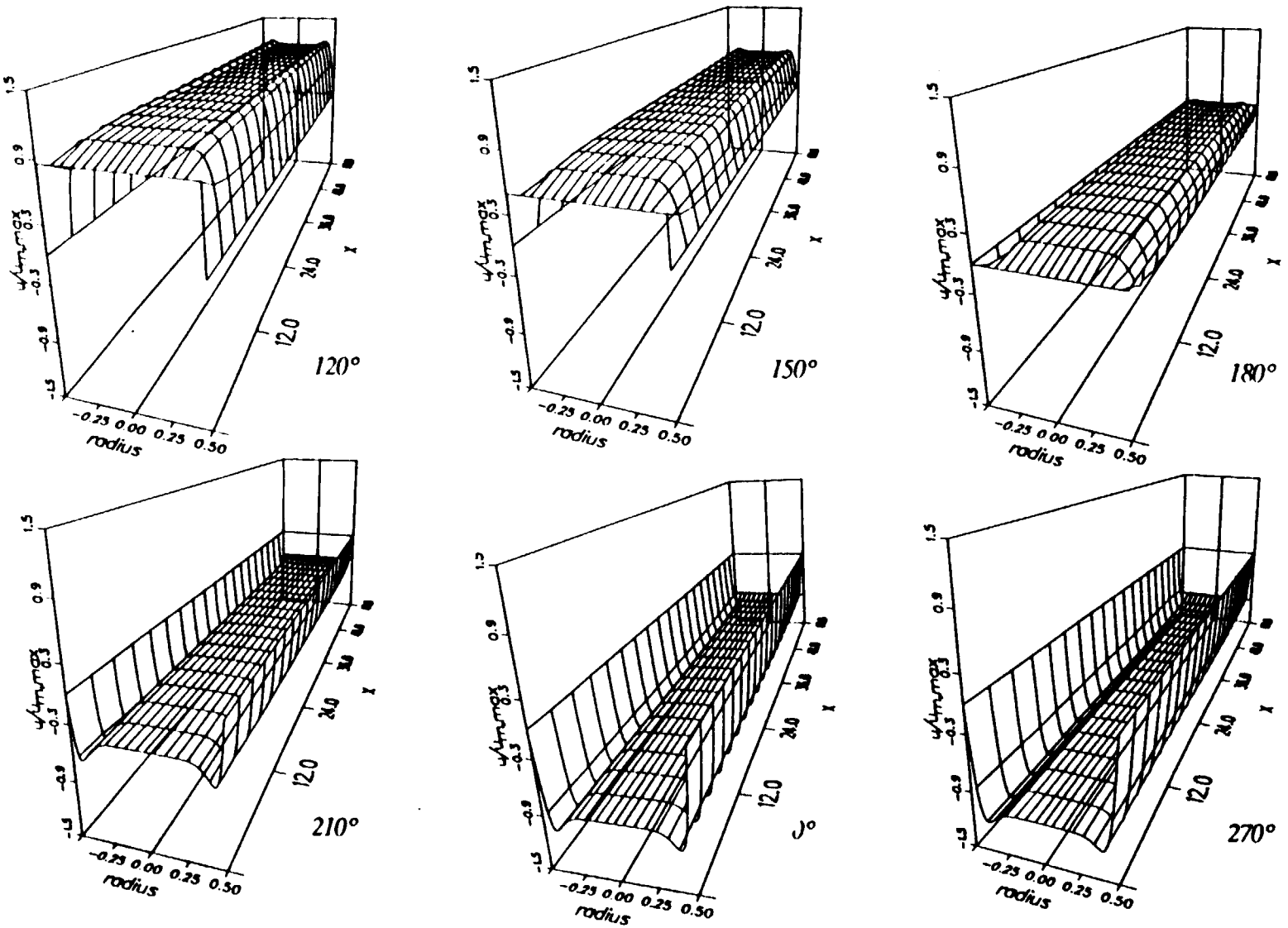

Fig. 7.33c: Laminar computation. Normalized velocity $u/u_{m,max}$ *at various crank angles. Data point p:* $Re_{max}=8.43x10^3$, *Va=231, L/D=60. Mean flow direction: 120°, 150° into plane; 180° flow reversal; 210°, 240°, 270° out of plane.*

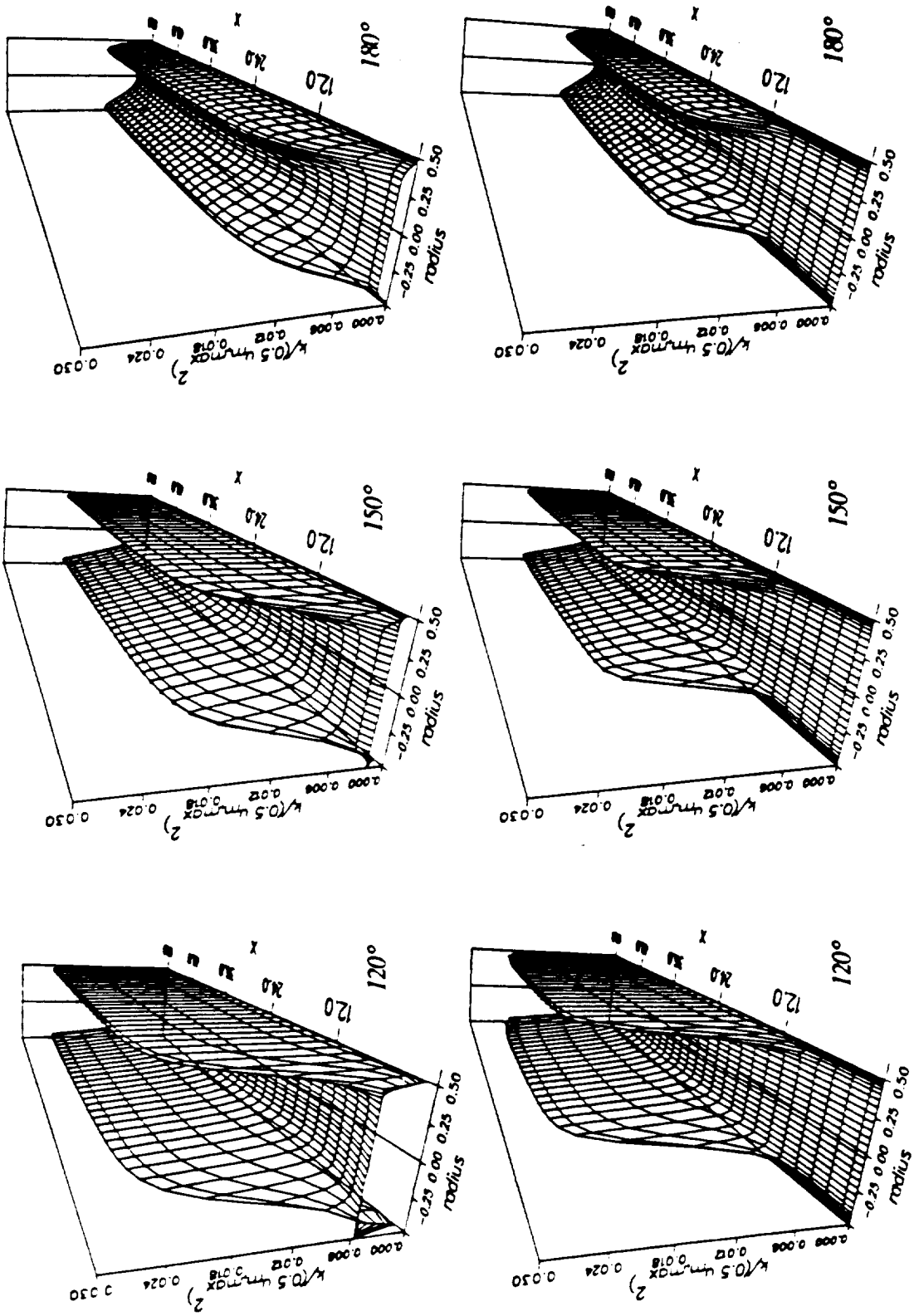

Fig. 7.34: Normalized turbulent kinetic energy $k/(0.5\ u^2_{m,max})$ at various crank angles. Data point P: $Re_{max}=8.43x10^3$, Va=231, L/D=60. Top row: TI=5.0%; bottom row: TI=0.5%. Mean flow direction: 120°, 150° into plane; 180° flow reversal.

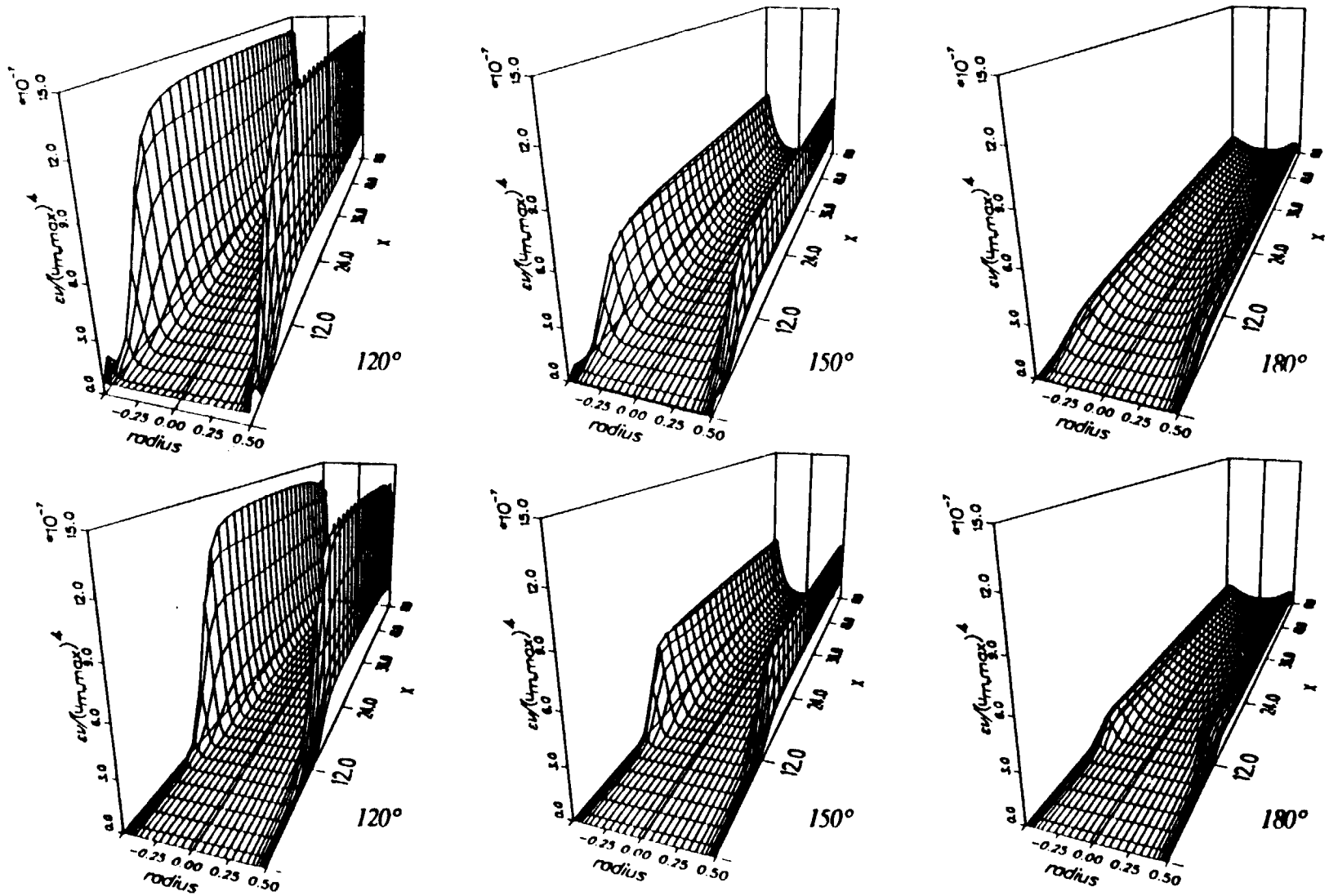

Fig. 7.35: Normalized turbulent dissipation rate $\varepsilon\nu_{ref}/u^4_{m,max}$ at various crank angles. Data point p: $Re_{max}=8.43x10^3$, Va=231, L/D=60. Top row: TI=5.0%; bottom row: TI=0.5%. Mean flow direction: 120°, 150° into plane; 180° flow reversal.

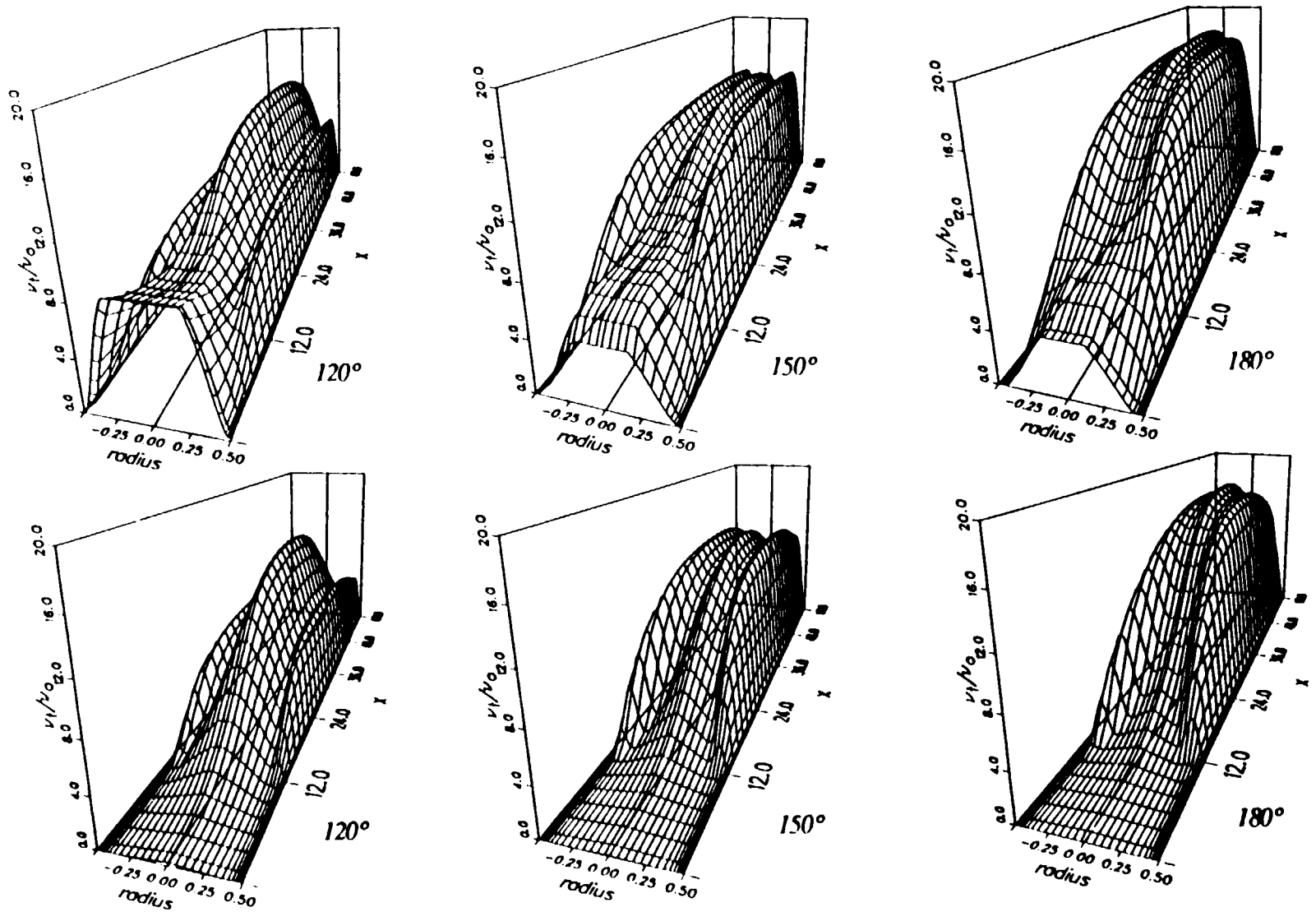

Fig. 7.36: Normalized turbulent viscosity ν_t/ν_{ref} at various crank angles. Data point p: $Re_{max}=8.43x10^3$, Va=231, L/D=60. Top row: TI=5.0%; bottom row: TI=0.5%. Mean flow direction: 120°, 150° into plane; 180° flow reversal.

7.3. Conclusions

1.) Starting from the results of the computations with the HRN turbulence model, the periodic steady state for case SPRE was successfully computed with the LRN turbulence model. In this model, no empirical transition criterion whatsoever was used.

2.) The predictions obtained are grid independent.

3.) Transition triggered by turbulent slugs (as seen in the SPRE case and described by Seume, 1988) is not predicted at the axial location investigated. In the SPRE case, ordinary transition is faithfully predicted but at somewhat too low Re numbers. The transition predictions for the high Re_{max} cases e and d compare very favorably with the experiment. The always lamiar case p is computed very laminar-like.

4.) Based on the transition performance observed here, it is *not* necessary to take measures to broaden the predicted transitional Re number range (cf. Chapter 6.3.).

4.) For case SPRE, the computed velocity profiles at $x/D \approx 44$ agree rather well with the experimental data and show clear improvements over the HRN computation.

5.) The universal law of the wall does not hold for oscillating flow. However, a viscous sublayer following $u^+=y^+$ does exist at least up to $y^+=7$.

6.) The friction coefficient predictions show that for the two cases where Re_{max} was greater than 10^5, the steady state correlation is appropriate, at least up to Va=230. For the two cases where $10^4 < Re_{max} < 10^5$, the steady state correlation can be used for the decelerating periods of the cycle. Here, the friction coefficients of the accelerating parts of the cycle have yet to be correlated. Below $Re_{max} = 10^4$ the steady state correlation definitely does not hold throughout the cycle, at least for Va=200.

7.) Entrance length effects are not important for the high Re_{max} cases, but are significant for all other cases.

8.) To judge the impact of the unsteadiness on the flow parameters, an *effective* Va number should be used, $Va_{eff} \equiv \omega R^2/\nu_{eff}$.

9.) In contrast to the findings of Rodi and Scheurer (1986) for the flat plate boundary layer, here the LRN k-ε model does not seem to have particular problems with adverse pressure-gradients and decelerations. Rather, the problems come with strong acceleration.

10.) The shortcomings of the LRN computations are threefold:

- In accelerated flow, the turbulence model predicts transition at too low Re numbers.
- The inflow boundary condition for ε does not reflect reality and does not allow turbulent slugs to exist long enough compared with the experiment.
- The observed phase shift between the mean flow and the fluctuations at high Re and Va numbers is not predicted by the turbulence model.

PART III: HEAT TRANSFER AND IRREVERSIBILITY ANALYSIS

8. HEAT TRANSFER IN STEADY PIPE FLOW

In order to validate the part of the computer program responsible for the heat transfer problem, laminar and turbulent steady pipe flow was computed for constant heat flux and constant wall temperature boundary conditions. The criteria for the validation were the following questions:

1.) How well does the code predict Nusselt numbers for fully developed flow?

2.) Is the thermal entrance region realistically predicted?

The Nusselt number correlations used to compare the predictions against were[1]:

	constant heat rate	constant wall temperature
laminar flow	$Nu = 4.364$	$Nu = 3.658$
turbulent flow	$Nu = 0.22\ Re^{0.8}\ Pr^{0.5}$	$Nu = 0.021\ Re^{0.8}\ Pr^{0.5}$

Figure 8.1 shows the computed local Nusselt numbers for a thermally and hydrodynamically developing pipe flow (L/D=150). The laminar computations were obtained with a 21 by 25 coarse grid, the turbulent computations with a 33 by 51 grid. The computed Nusselt numbers for the laminar case approach the theoretical values exactly. The computed values for the turbulent case are a little too high (136 vs. 121 for constant wall temperature, 138 vs. 126 for constant heat flux) but are within an error margin small enough to be acceptable. Also, the constant heat rate problem yields a higher Nu number

[1]W. M. Kays and M.E. Crawford in Convective Heat and Mass Transfer, MacGraw-Hill Book Co., New York, 1980.

than the constant wall temperature problem. Yet, the fact that both numbers are over-predicted seems to indicate that the turbulence model employed slightly over-predicts the wall heat transfer. The entrance region is resolved realistically. For the laminar flow, the computed Nu number decreases monotonically to the asymptotic limit of fully developed flow. In case of turbulent flow, the predicted local Nu number decreases at first below the fully developed flow limit because of a short laminar-like development of the flow. As soon as the flow undergoes a spatial transition to turbulence (cf. Fig. 5.2 for the local frictions coefficient), the Nu number increases to the fully developed flow value.

Figure 8.2 shows three-dimensional views of the temperature development in the pipe for two different dimensionless temperatures. In Fig. 8.2a the non-dimensional temperature is simply T/T_o, whereas in Fig 8.2b it is $(T_w - T)/(T_w - T_{bulk})$. Those plots are supposed to be a reference against which one can compare the development of the temperature profiles in oscillating flow.

For the 1.5" pipe of the University of Minnesota oscillating flow experiment and air, the following relationship between the Ec number and the Re_{max} number can be established:

$$Ec = 5.2 \cdot 10^{-13} \frac{Re_{max}^2}{\Delta\theta}$$

where $\Delta\theta$ is defined as $(T_w - T_{in})/T_{in}$. Here, the representative temperature difference $(\Delta T)_{ref}$ entering the Eckert number is taken as $T_w - T_o$, and $T_o = T_{in}$. Clearly, when $\Delta\theta$ approaches a very small value, the Eckert number becomes large and viscous effects play a significant role in the energy equation considered. In the given study, the temperature at the inflow was constant at a value of 300, and in the constant wall temperature case, T_w was set to 360. This choice ensured that viscous heating was negligible. This is in line with Seume and Simon (1986) who stated that viscous heating does not play a role in Stirling engine heat exchangers. Despite that, the viscous dissipation function was always included in the calculations.

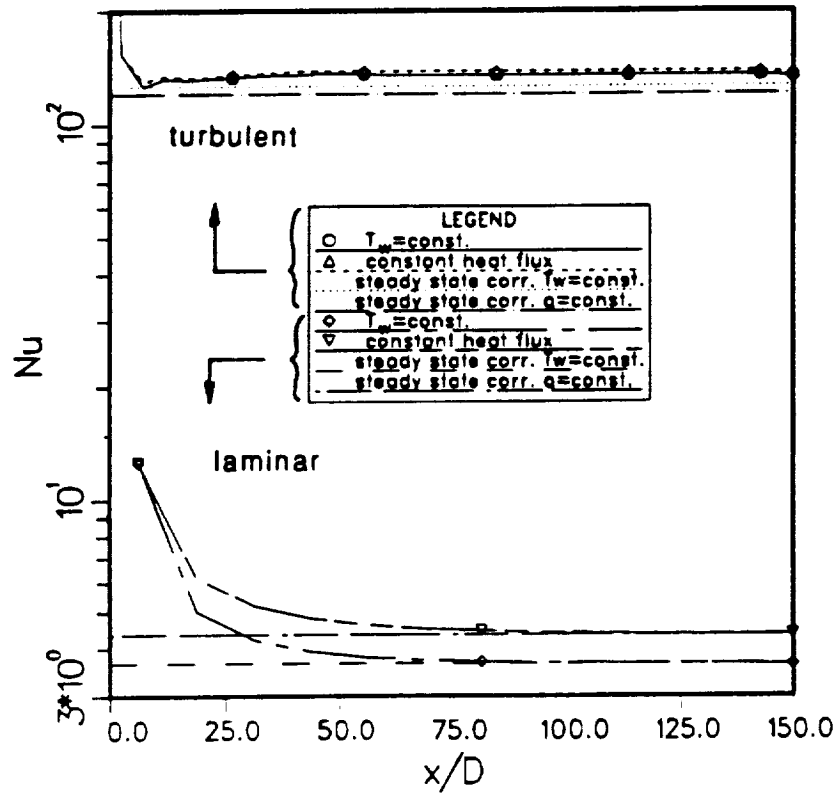

Fig. 8.1: Computed local Nu numbers and steady state correlations for fully developed flow.

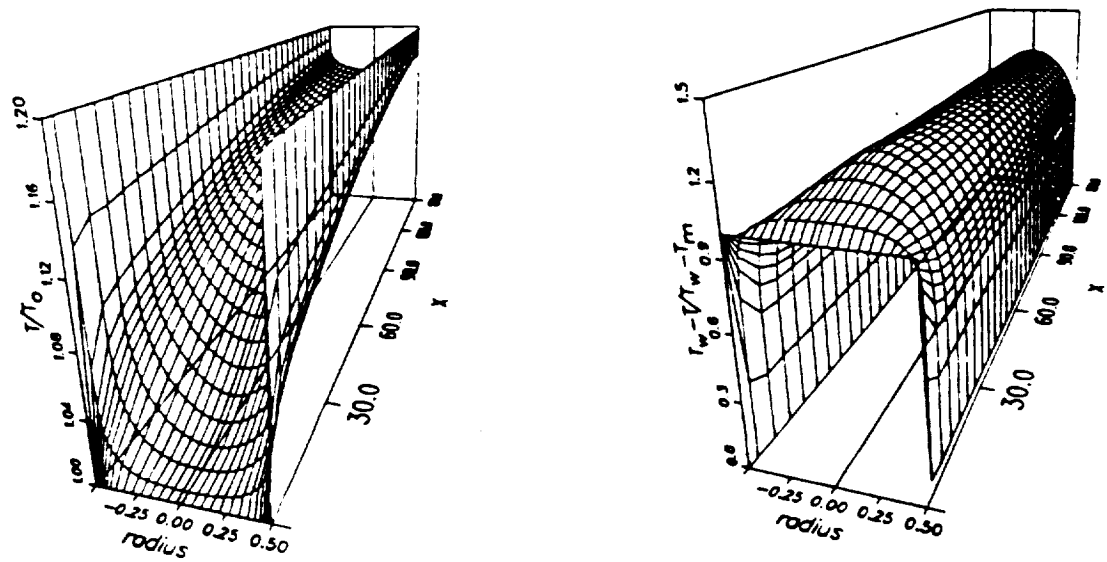

Fig. 8.2: Dimensionless temperatures T/T_0 *and* $(T_w - T)/(T_w - T_{in})$ *for Re=50000, Pr=1.0 and* T_w*=constant.*

9. PREDICTIONS OF HEAT TRANSFER IN TURBULENT OSCILLATING FLOW

Given the assumptions outlined in Chapter 2, the properties are all considered as being constant in this study. Therefore the heat transfer problem is decoupled from the fluid flow problem and linear. Having obtained realistic solutions for the fluid flow problem, we can then expect realistic solutions for the heat transfer problem, too. The computations shown in this chapter will possess all weaknesses of the turbulence model discussed above. Those shortcomings will not be discussed here.

For a practical application, the calculation of Nusselt numbers for the test cases considered is probably the most important task. The most precious question to be answered by this study is whether the steady state Nu number correlations are applicable in case of turbulent flow. Also of interest is the question whether entrance length effects play a more significant role in heat transfer than in the fluid flow part. We will restrict our attention to a Dirichlet boundary condition at the wall and inflow, and Neumann boundary condition at the centerline and outflow. The alternative case of a Neumann boundary condition at the wall could easily be obtained, too. However, in case of turbulent flow and Pr=1, the difference in boundary conditions leads to an only insignificant difference of resulting Nu numbers. To maintain similarity with the University of Minnesota oscillating flow test rig, the temperature at the inflow cross section was assumed to be the same for inflow from the drive and from the open end.

9.1. Nusselt Number Calculations near the Outflow

Figure 9.1 shows the computed Nu numbers near the outflow cross section. As is the case for the friction coefficients, cases SPRE and m as well as cases e and d correspond to each other. Case p stands out alone. In all cases, the magnitude of the Nu number

throughout the cycle is much closer to the turbulent steady state correlation than for the laminar correlation.

Cases SPRE and m, where Re_{max} is moderate, display a definite phase shift of about the same magnitude (≈20° crank angle). In the accelerating phase, the Nu number is less then the turbulent steady state correlation. This is expected since the accelerated flow is "more laminar-like", and less cross stream eddy transport takes place. It may be noted here that the corresponding friction factors at 15° and 30° crank angle are *larger* than the turbulent steady state correlation, whereas the corresponding Nu number are *smaller*. For the friction factor this can be explained by the velocity gradients alone, which are very steep near the wall because of the acceleration. This is so even if there is no eddy transport. The Nu number not influenced by this velocity gradient, but determined by the eddy transport. On the other hand, the Nu number in the deceleration phase is enhanced by the *increased* eddy transport.

The Nu numbers for cases e and d follow very nicely the turbulent steady state correlation. Apparently, the eddy activity here is high enough to lock the boundary layer to the core of the flow, similarly as in steady flow.

The Nu number pattern for case p shows the flow like laminar oscillating flow during the acceleration phase and deviates from that towards a more turbulent Nu number in the decelerating phase. The peak of the Nu numbers is offset by circa +80° compared to the steady correlation peak.

9.2. Local Nusselt Numbers

Figure 9.2 shows the local Nusselt numbers as computed. For cases e and d, where Re_{max} is relatively high, the thermal entry length is short and the Nusselt number of the thermally and hydrodynamically fully developed flow gives a good representation for the entire tube. For cases SPRE and m, the thermal entry length affects a significant portion of the tube. In the SPRE case, where the experimentally determined, low TI boundary

condition is used, the initially flow develops laminar-like, and the Nu number is less than the fully developed value for about one third of the pipe length. In case m, a flat 5% TI at the inflow was assumed which causes the hydrodynamical entry length to be shorter than in the SPRE case. Here, about one fourth of the length is permanently a thermal entry length. The latter two cases show a similar behavior of the local Nu number at 30° crank angle: the local Nu number here is significantly higher than the fully developed Nu number practically throughout the tube. This can be explained as a history effect of the flow. What is the near outflow cross section during one half of the cycle is the near inflow cross-section during the other. Near the inflow, the respective inflow boundary conditions are strongly felt, whereas away from it the flow is more determined by local conditions. Shortly before flow reversal the level of turbulence is very low near the entrance. Then, after flow reversal, the level of turbulence at the former near-entrance cross section builds up only slowly. In contrast, in the center of the tube or at the near-outflow cross section the level of turbulence is still relatively high before flow reversal . Therefore, just after flow reversal, the level of turbulence there is higher than at the now outflow cross-section. Consequently, the Nu number is lowest at the outflow cross section. In case m, due to the high frequency, this history effect is still slightly present at 60° crank angle. Case p (5% TI) is different from the previous two cases in that this history effect affects most of the cycle. Only the curves from 120° on are practically free of this effect. Hence, the fully developed Nu number value is not a good spatial mean.

9.3. Temperature Solutions

Underlying the Nusselt number results above are temperature solutions. In Figures 9.3 to 9.5 the temperature solutions are shown in two different ways: The temperature is normalized simply by division by a reference temperature T_o. For the SPRE case, a normalization like in steady pipe flow is used, $\theta = (T_w - T)/(T_w - T_{bulk})$. The shown plots look similar like plots for steady state. but the normalization brakes down for flow reversal. Only cases SPRE, e and p are shown.

9.4. Conclusions

1.) For Re_{max} numbers above 10^5, the turbulent steady state Nu number correlation approximates well the computed instantaneous Nu number for the fully developed flow, at least up to Va=230.

2.) For $10^4 < Re_{max} < 10^5$, the fully developed instantaneous Nu number can be related to the steady state correlation by a simple phase lag relation (to be developed).

3.) Below $Re_{max} \approx 10^4$, the instantaneous fully developed Nu number differs in phase and magnitude from the turbulent steady state correlation.

4.) Thermal entry length effects are negligible for Re_{max} numbers above 10^5.

5.) Below a Re_{max} of 10^5, the thermal entry length becomes appreciable and history effects begin to play a role.

Fig. 9.1a: Comparison of computed fully developed Nu number with steady state correlations. Data point ***SPRE****: $Re_{max}=1.17x10^4$, Va=80, L/D=60.*

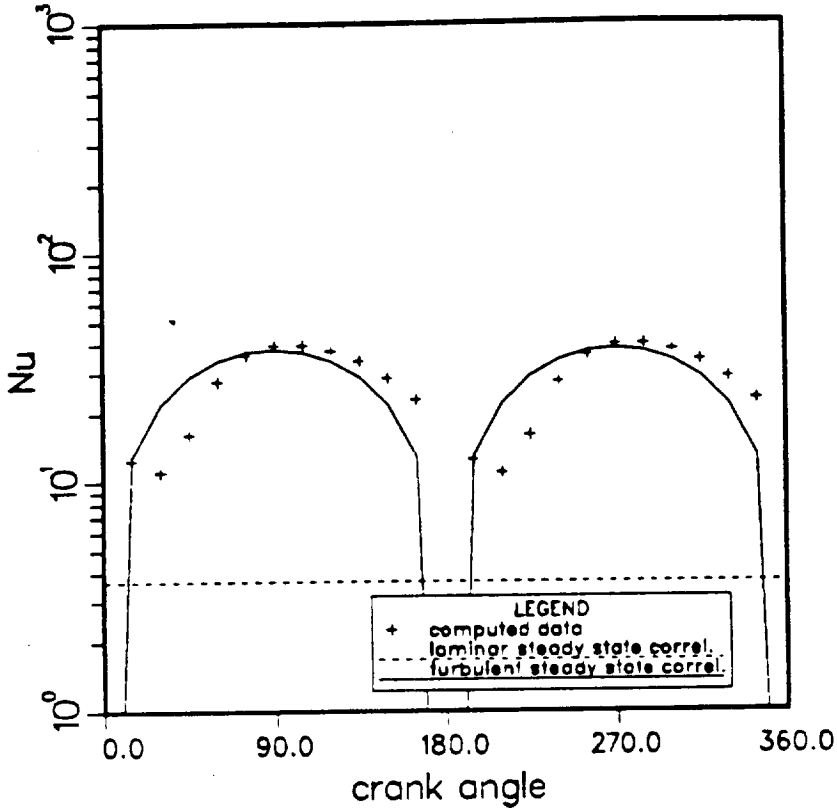

Fig. 9.1b: Comparison of computed fully developed Nu number with steady state correlations. Data point ***m****: $Re_{max}=2.39x10^4$, Va=230, L/D=68.5.*

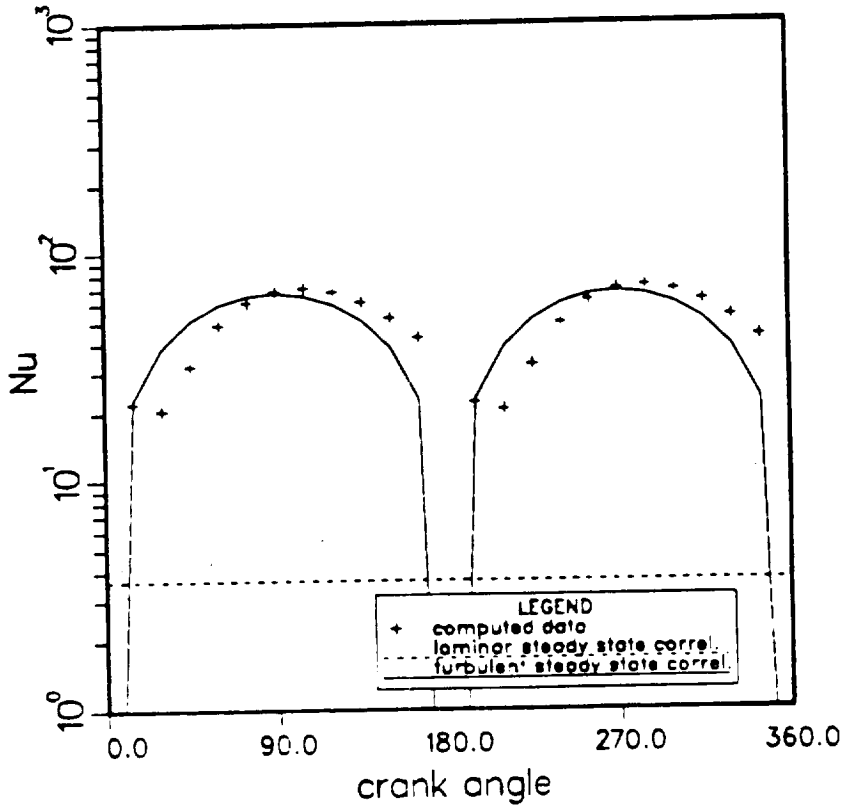

Fig. 9.1c: Comparison of computed fully developed Nu number with steady state correlations. Data point e: $Re_{max}=1.87x10^5$, Va=230, L/D=60.

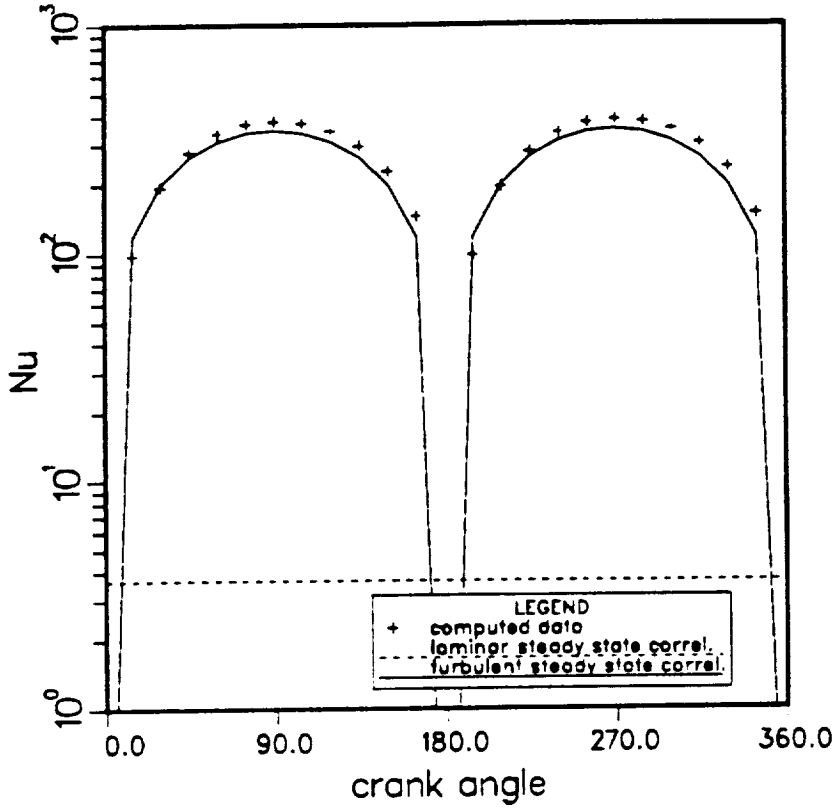

Fig. 9.1d: Comparison of computed fully developed Nu number with steady state correlations. Data point d: $Re_{max}=1.32x10^5$, Va=81, L/D=60

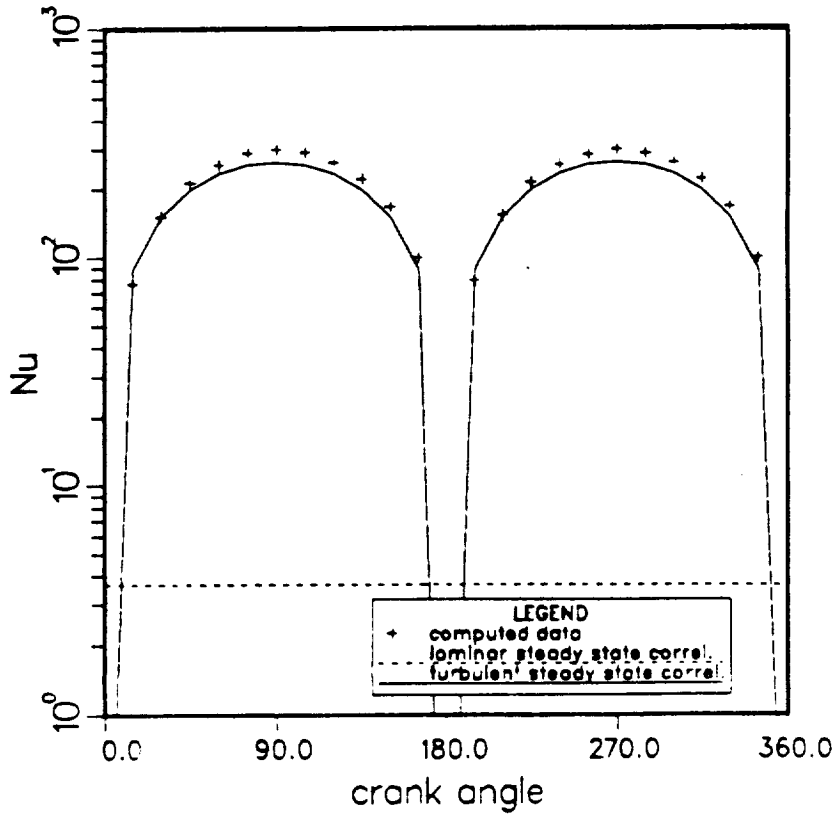

Fig. 9.1e: Comparison of computed fully developed Nu number with steady state correlations. Data point p: $Re_{max}=8.43x10^3$, Va=231, L/D=60, TI=5.0%.

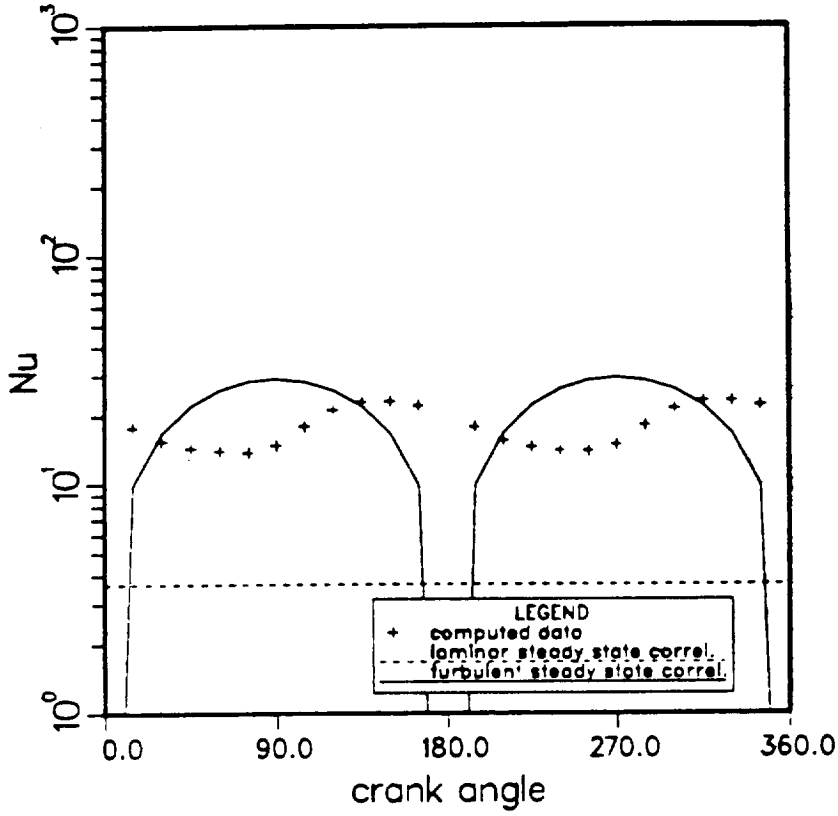

Fig. 9.1f: Comparison of computed fully developed Nu number with steady state correlations. Data point p: $Re_{max}=8.43x10^3$, Va=231, L/D=60, TI=0.5%.

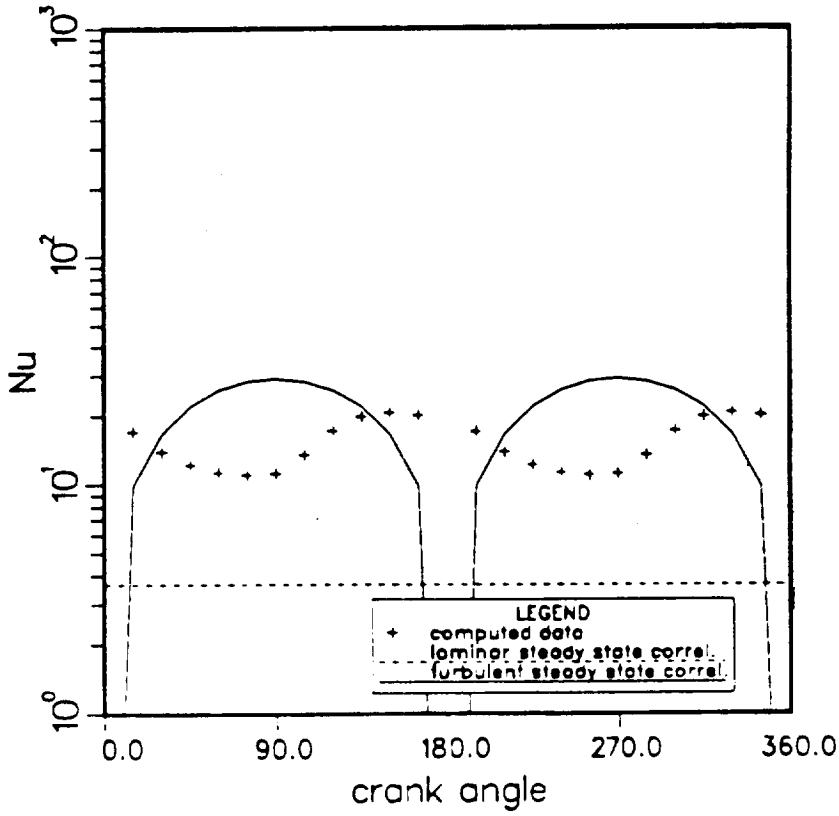

Fig. 9.2a: Ratio of local to fully developed Nu number at various crank angles. Data point ***SPRE****: Re_{max}= 1.17x10^4, Va=80, L/D=60.*

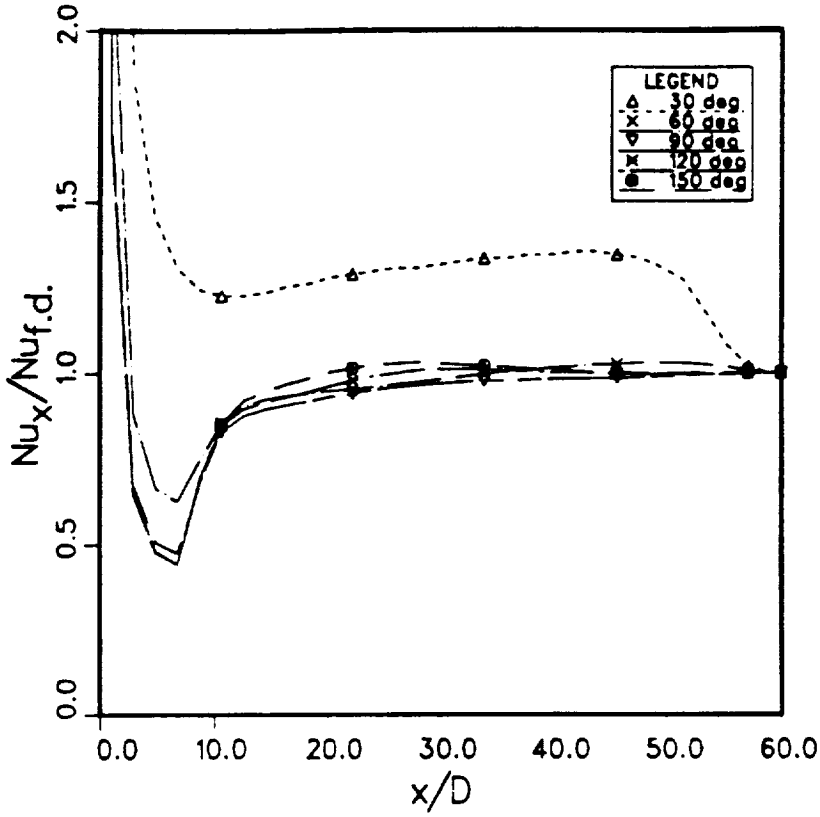

Fig. 9.2b: Ratio of local to fully developed Nu number at various crank angles. Data point ***m****: Re_{max}=2.39x10^4, Va=230, L/D=68.5.*

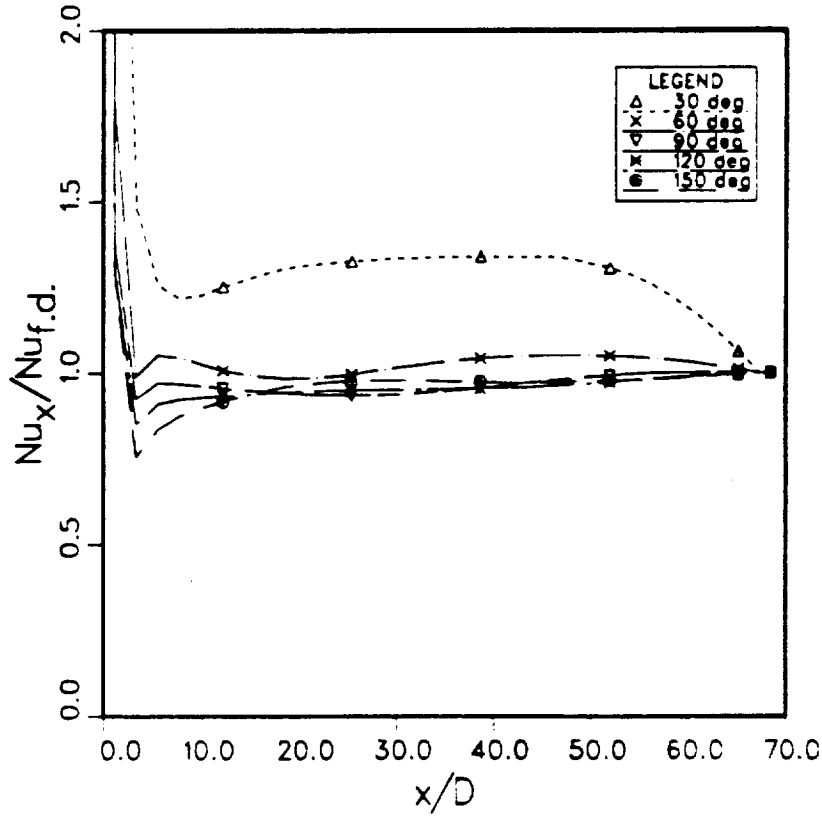

Fig. 9.2c: Ratio of local to fully developed Nu number at various crank angles. Data point e: $Re_{max}=1.87x10^5$, Va=230, L/D=60.

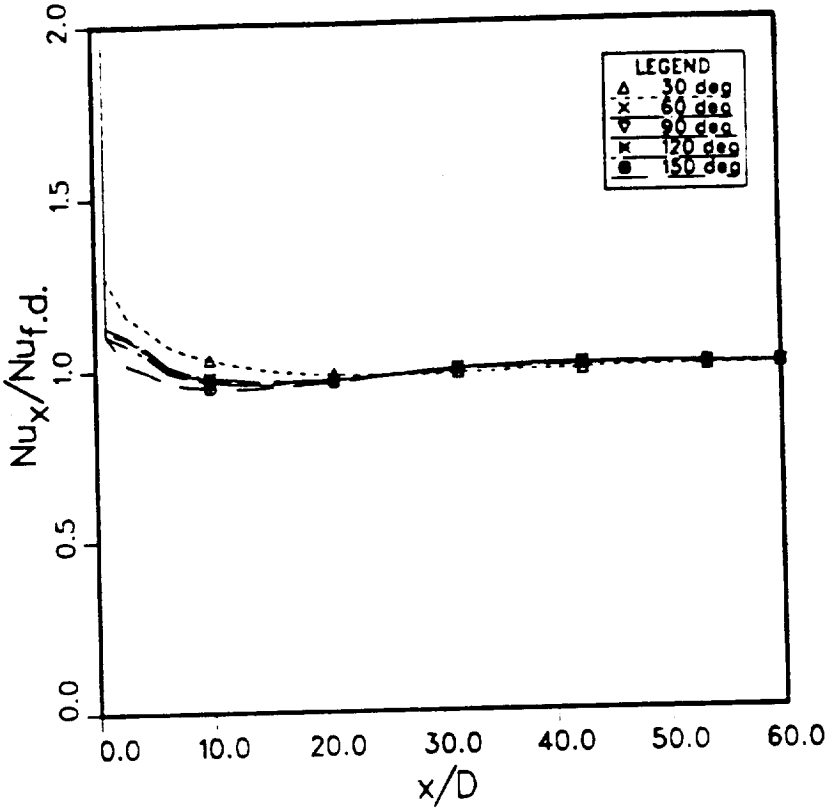

Fig. 9.2d: Ratio of local to fully developed Nu number at various crank angles. Data point d: $Re_{max}=1.32x10^5$, Va=81, L/D=60.

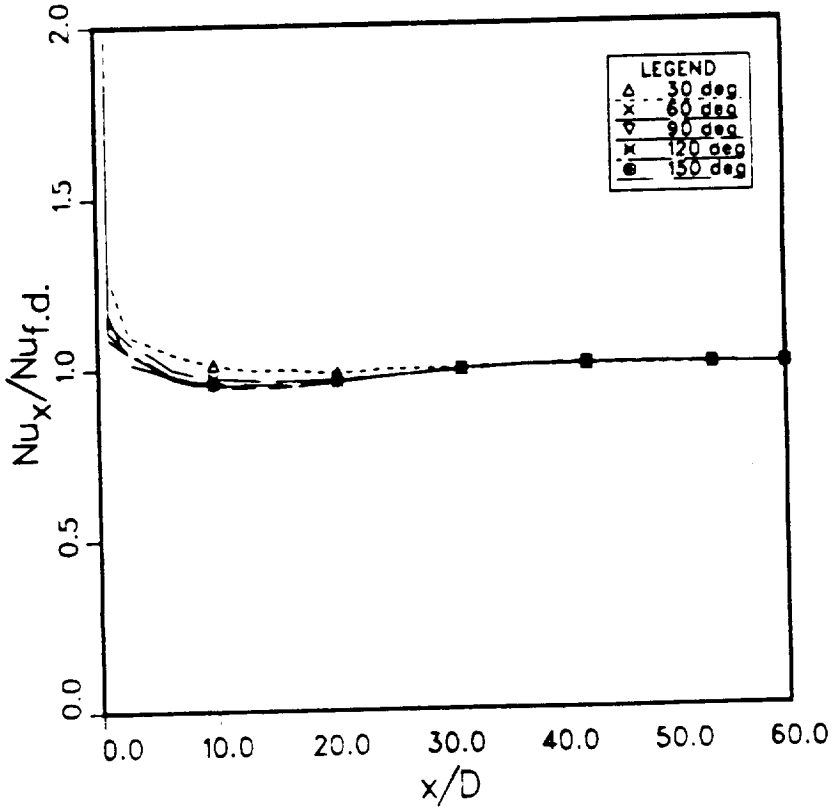

Fig. 9.2e: Ratio of local to fully developed Nu number at various crank angles. Data point p: $Re_{max}=8.43x10^3$, Va=231, L/D=60, TI=5.0%.

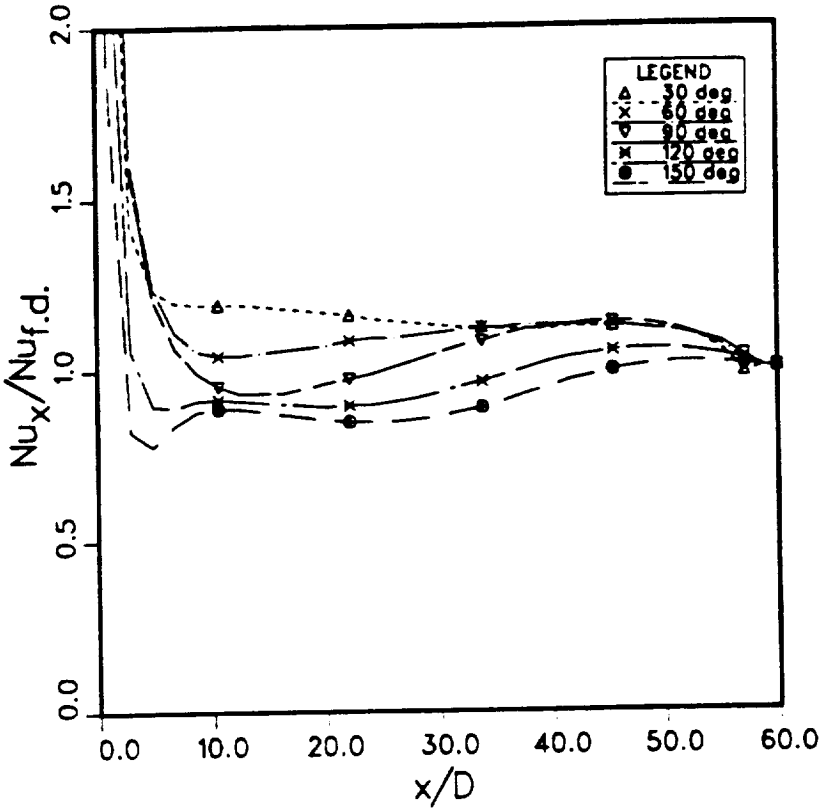

Fig. 9.2f: Ratio of local to fully developed Nu number at various crank angles. Data point p: $Re_{max}=8.43x10^3$, Va=231, L/D=60, TI=0.5%.

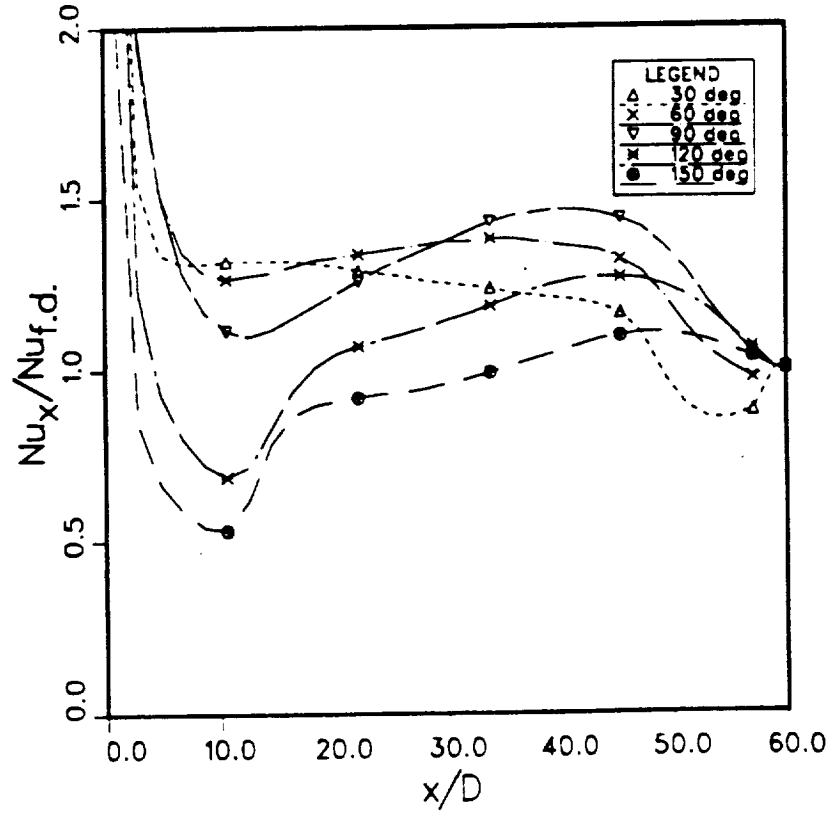

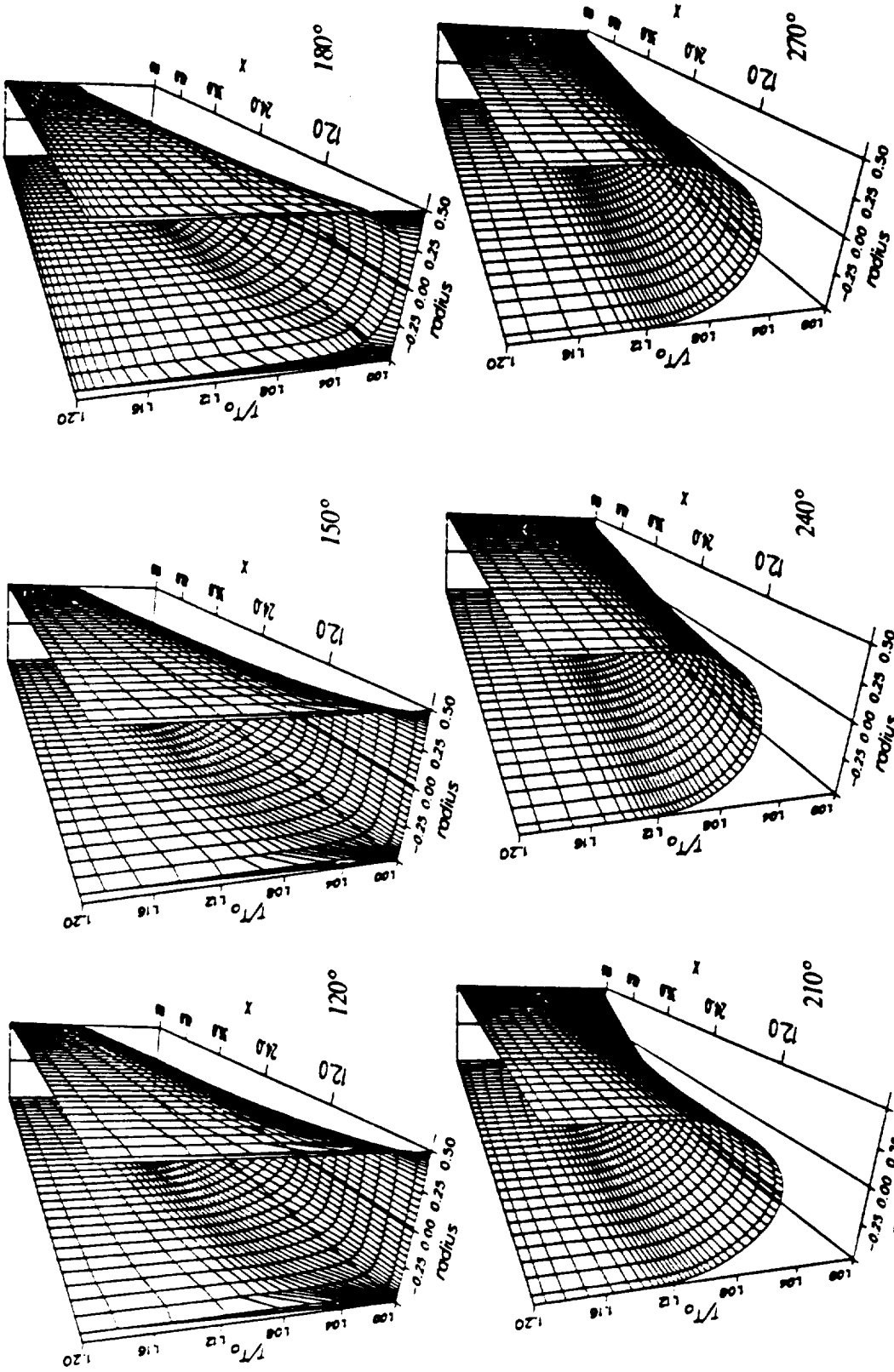

Fig. 9.3: Normalized temperature T/T_o at various crank angles. Data point e: $Re_{max}=1.87x10^5$, Va=230, L/D=60, Pr=1.0, $E_C \rightarrow 0$, $T_w/T_o=1.2$. Mean flow direction: 120°, 150° into plane; 180° flow reversal; 210°, 240°, 270° out of plane.

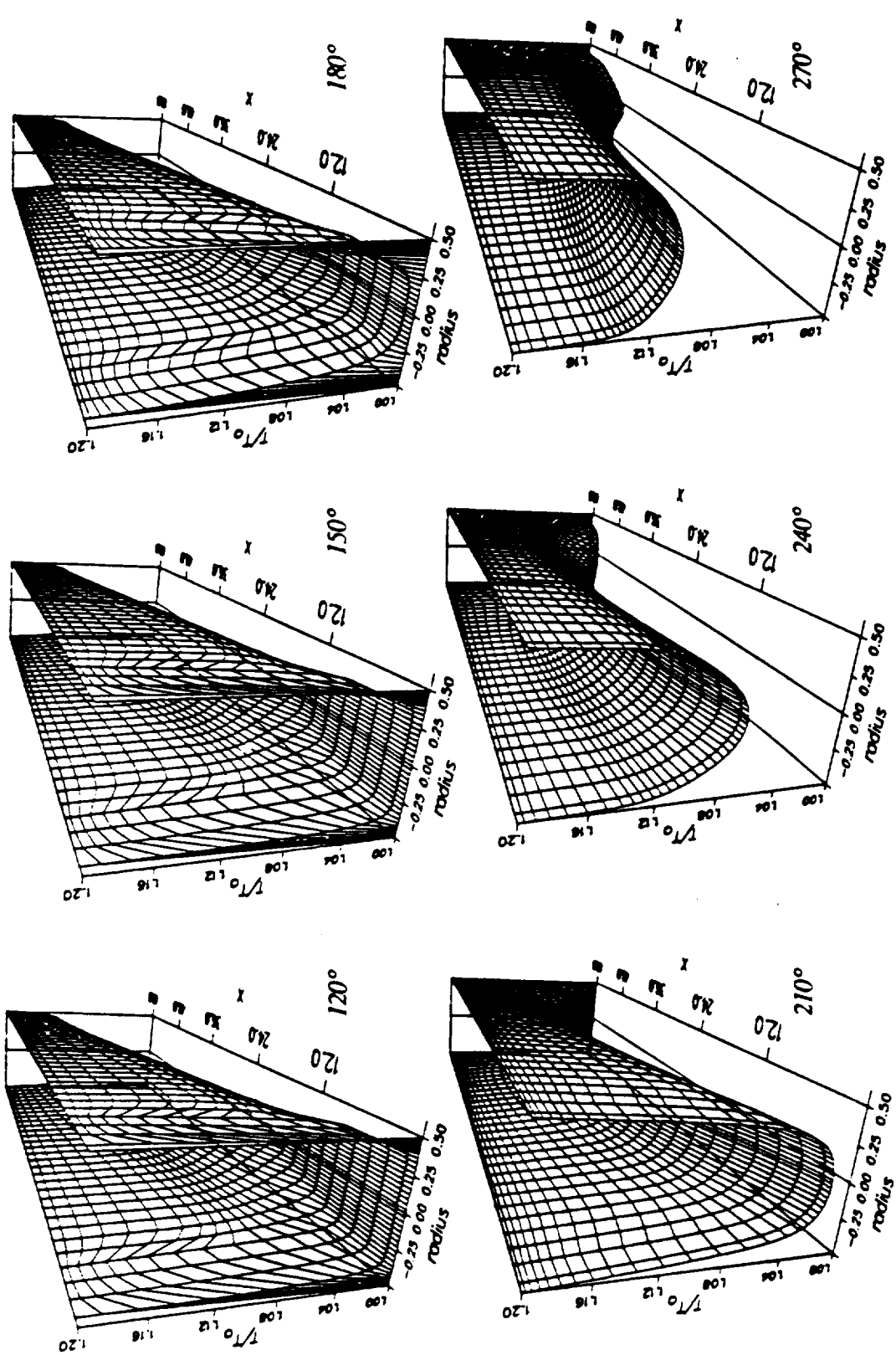

Fig. 9.4a: Normalized temperature T/T_o at various crank angles. Data point SPRE: Re_{max}=1.17x10⁴, Va=80, L/D=60, Pr=1.0, Ec→0, T_w/T_o=1.2. Mean flow direction: 120°, 150° into plane; 180° flow reversal; 210°, 240°, 270° out of plane.

Fig. 9.4b: Normalized temperature ($T_w - T)/(T_w - T_{in}$) at various crank angles. Data point SPRE: Re_{max}=1.17x10^4, Va=80, L/D=60, Pr=1.0, Ec→0, T_w/T_o=1.2. Mean flow direction: 120°, 150° into plane; 180° flow reversal; 210°, 240°, 270° out of plane.

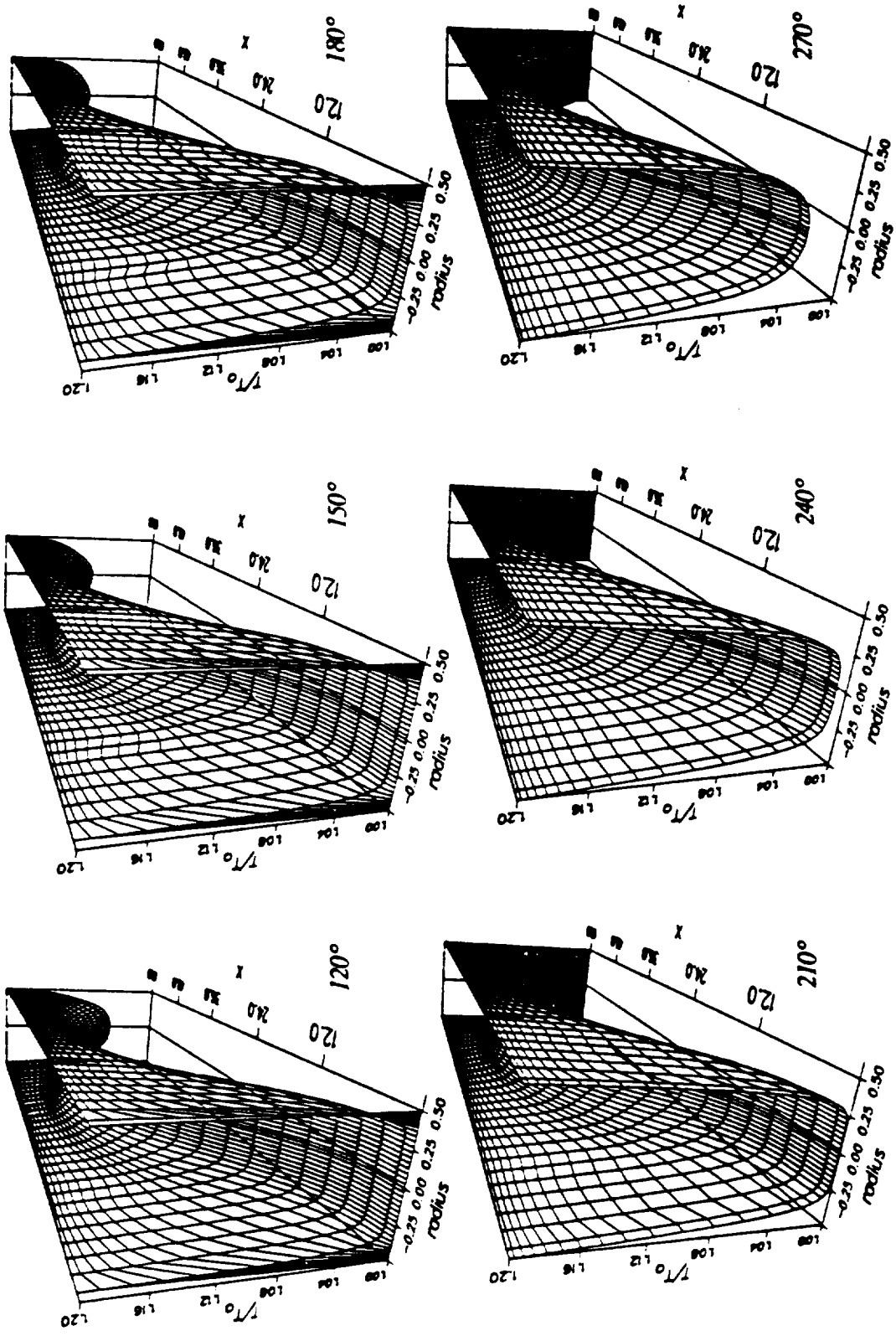

Fig. 9.5: Normalized temperature T/T_o at various crank angles. Data point p: Re_{max}=8.43x10^3, Va=231, L/D=60, Pr=1.0, Ec→0, T_w/T_o=1.2, TI=0.5. Mean flow direction: 120°, 150° into plane; 180° flow reversal; 210°, 240°, 270° out of plane.

10. ENTROPY GENERATION IN STEADY PIPE FLOW

10.1. Derivation of the Entropy Generation Term

As outlined in Chapter 2, the benefit of the differential equation for the entropy lies in its entropy generation term. In heat exchanger design, techniques to reduce friction and to enhance heat transfer are usually in conflict with each other. Applying the second law of thermodynamics puts both irreversible processes on the same physical scale and allows to properly evaluate their impact on the overall performance.

The differential equation for entropy can be written as[1] (Bejan, 1982)

$$\rho \frac{Ds}{Dt} = -\mathrm{div}\left(\frac{\vec{q}}{T}\right) + \dot{S}'''_{gen} \tag{10.1}$$

the energy equation is

$$\rho \frac{Dh}{Dt} = -\mathrm{div}(\vec{q}) + \frac{Dp}{Dt} + \mu\Phi \tag{10.2}$$

and the continuity equation is

$$\frac{D\rho}{Dt} + \rho\, \mathrm{div}(\vec{u}) = 0 \tag{10.3}$$

The first term on the right hand side of eq. (10.1) can be rewritten as

---

[1] In the following, the quantity $\frac{D...}{Dt}$ denotes the substantial derivative.

$$\mathrm{div}\left(\frac{\vec{q}}{T}\right) = -\frac{1}{T}\,\mathrm{div}(\vec{q}) + \frac{\vec{q}}{T^2} \bullet \mathrm{grad}(T) \tag{10.4}$$

Replacing $\mathrm{div}(\vec{q})$ with the energy equation, the equation for the entropy becomes

$$\rho\,\frac{Ds}{Dt} = \frac{\vec{q}}{T^2} \bullet \mathrm{grad}(T) + \frac{1}{T}\left(\rho\frac{Dh}{Dt} - \frac{Dp}{Dt} - \mu\Phi\right) + \dot{S}'''_{gen} \tag{10.5}$$

Using Gibbs' equation $T\,ds = dh - (1/\rho)dp$ and Fourier's law, eq. (10.5) transforms to

$$\dot{S}'''_{gen} = \frac{k}{T^2}\,[\mathrm{grad}(T)]^2 + \frac{\mu}{T}\,\Phi \tag{10.6}$$

For turbulent flow, the ensemble averaged equations are

$$\rho\,\frac{D\bar{s}}{Dt} = -\,\mathrm{div}\left(\frac{\vec{q}}{T}\right) + \dot{S}'''_{gen} - \rho\,\mathrm{div}(\overline{\vec{u}'\,s'}) \tag{10.7}$$

$$\rho\,\frac{D\bar{h}}{Dt} = -\mathrm{div}(\vec{q}) + \frac{D\bar{p}}{Dt} + \mu\bar{\Phi} + \rho\varepsilon - \rho\,\mathrm{div}(\overline{\vec{u}'\,h'}) + \mathrm{div}(\overline{\vec{u}'\,p'}) \tag{10.8}$$

It is

$$\mathrm{div}(\overline{\vec{u}'\,s'}) = \overline{s'\,\mathrm{div}(\vec{u}')} + \overline{\vec{u}' \bullet \mathrm{grad}(s')} \tag{10.9}$$

and similarly for h' and p'. For constant density flows, the first term on the right hand side drops out.

Combining equations (10.7) and (10.8), using (10.9) and applying Gibbs' equation for the fluctuation terms, the entropy generation term for turbulent flow takes the final form

$$\dot{S}'''_{gen} = \frac{k}{\bar{T}^2}\,[\mathrm{grad}(\bar{T})]^2 + \frac{\mu}{\bar{T}}\,\bar{\Phi} + \frac{\rho}{\bar{T}}\,\varepsilon \tag{10.10}$$

The individual terms in eq. (10.10) reflect the irreversibilities due to heat conduction, mean flow across a finite pressure gradient and fluctuations across finite pressure gradients. All terms of eq. (10.10) are positive which is in accordance with the second law. It is noteworthy that the heat transfer term in eq. (10.10) is governed by the molecular , not the effective conductivity.

Using the non-dimensional variables as introduced in Chapter 2 and defining

$$T \equiv \frac{\bar{T}}{T_o} \tag{10.11}$$

$$\varepsilon \equiv \frac{\rho\, R^2}{\mu_{ref}\, u^2_{m,max}}\,\varepsilon \tag{10.12}$$

$$\dot{S}'''_{gen} \equiv \frac{T_o\, D^2}{\mu_{ref}\, u^2_{m,max}}\,\dot{S}'''_{gen} \tag{10.13}$$

the non-dimensional equation for the entropy generation rate becomes:

$$\dot{S}'''_{gen} \equiv \frac{4}{\mathrm{Pr}\,\mathrm{Ec}\,(T_w - T_{in})}\,\frac{k}{T^2}\,[grad(T)]^2 + 4\,\frac{\mu}{T}\,\bar{\Phi} + 4\,\frac{\rho}{T}\,\varepsilon \tag{10.14}$$

where the factor 4 on the left hand side is due to the use of D as length scale for the rate of generated entropy. Here, the case Ec = 0 represents a singularity, and it is not clear a priory how small Ec must be in order to justify an omission of the two last terms.

To estimate how much entropy is generated in a numerical control volume, the generated entropy of eq. (10.13) will be multiplied with the dimensionless volume of the control volume,

$$\dot{S}'''_{gen,num} \equiv \dot{S}'''_{gen} \frac{\Delta V_{CV}}{0.5\ R^2 L} \tag{10.15}$$

Note: The entropy production depends on the absolute temperature at which the irreversible processes occur. Therefore, all results shown are only valid for the absolute temperatures picked, or, more exactly, for the ratio of the absolute temperatures.

10.2. Results for Steady Turbulent Flow

Figure 10.1a shows the total non-dimensional entropy generation rate for a steady turbulent pipe flow at Re = 50 000, assuming $T_{in} = 300$ and $T_w = 360$ (like in the heat transfer problem). Most of the entropy production occurs near the wall and near the entrance cross section where the gradients are especially steep.

Figure 10.1b shows the ratio of thermal entropy production (first term on RHS of eq. (10.10)) to total entropy generation. Figure 10.1c shows the ratio of frictional entropy production to total entropy production, and Figure 10.1d shows the ratio of turbulent entropy production to total entropy generation. Near the wall, where the most entropy is produced, the thermal production is dominant. Frictional production is negligible. Turbulent entropy production is significant towards the center of the tube and near the entrance. However, of all three contributors, thermal entropy production is largest.

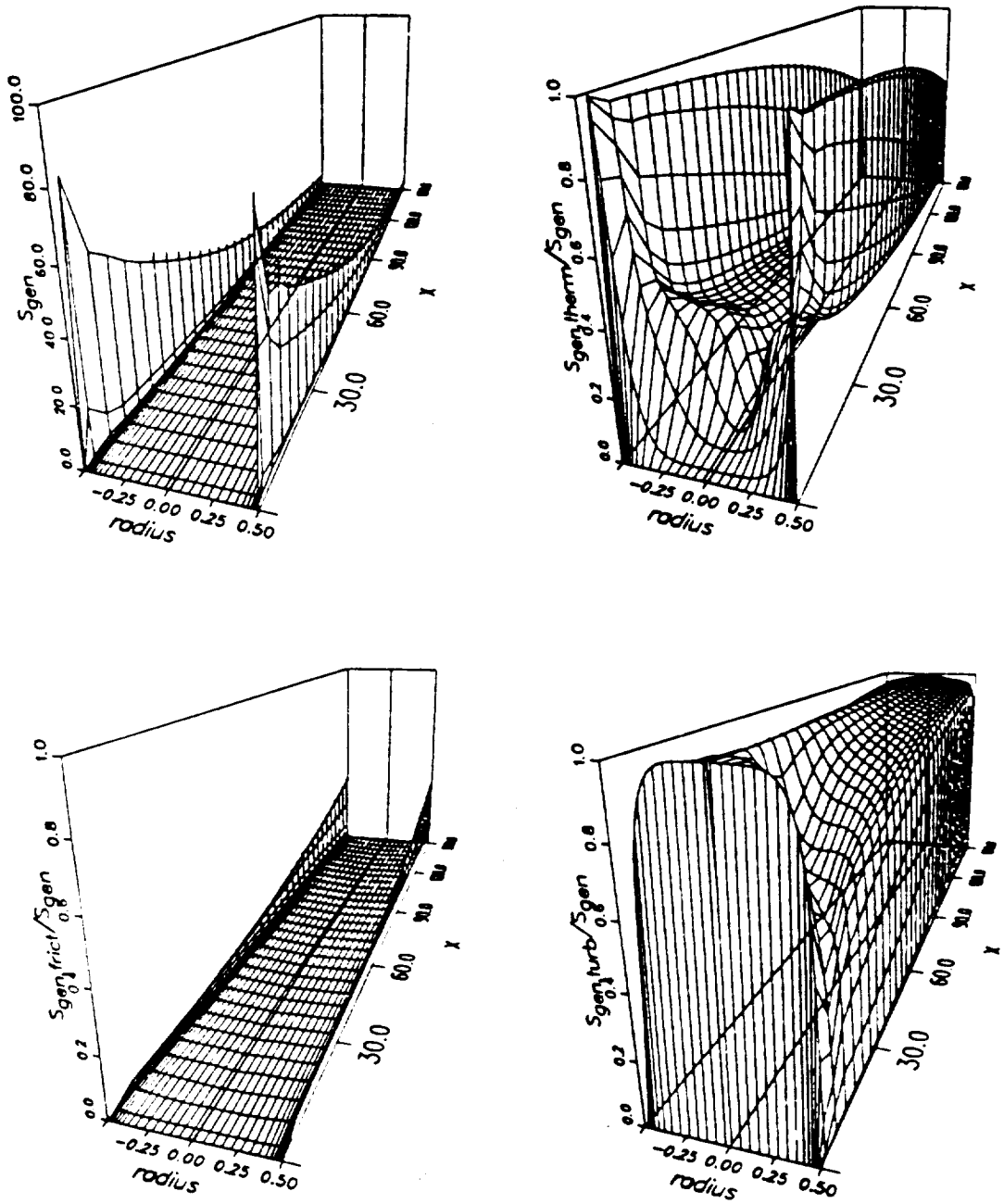

Fig. 10.1: Entropy production rate for Re=50000, Pr=1.0, T_w/T_o=1.2, $T_{in}=T_o$.
***Top left:** Normalized total entropy generation rate; **top right:** thermal fraction of total generated entropy; **bottom left:** frictional fraction; **bottom right:** turbulent fraction.*

11. ENTROPY GENERATION IN TURBULENT OSCILLATING FLOW

For the different test cases, it is of interest for the designer of a heat exchanger to have the following two questions answered:

1.) Where does the significant portion of the irreversibility take place?

2.) Which process contributes most to the irreversibilities, heat transfer, friction of the mean flow or turbulent dissipation?

As outlined in Chapter 10, the non-dimensional entropy depends on the absolute temperature chosen to non-dimensionalize it. Since there is no compelling reason to choose a particular temperature, its selection is somewhat arbitrary. This is a well known problem in exergy analyses, too. However, from exergy considerations it can be argued that the ambient temperature (if any clear defined T_∞ exists) is the preferred choice. Hence, the results shown here are only exemplary for one typical case where $T_0=T_\infty$ and $T_w/T_\infty=1.2$.

Results and Discussion. Figures 11.1 to 11.3 show the total normalized entropy generation in the domain at different crank angels for cases e, SPRE and p. In each case, nearly all of the entropy is generated very close to the wall. The peak generation is very close to the entrance cross section.

Figures 11.4 to 11.6 show the portion of entropy generation due to heat conduction for cases e, SPRE and p. It becomes clear that, overall, conduction is the main contributor to irreversibilities. This can be explained by the fact that the thermal irreversibilities depend on the gradient of T, whose radial component is zero at the centerline. The turbulent dissipation, in contrast, influences irreversibilities directly and is nonzero at the centerline.

Irreversibility contributions of turbulent dissipation do become more significant towards the center and in the inflow region (Figs 11.7 to 11.9). Especially in case e, turbulent

dissipation seems to be the main contributor(in %) for much of the domain. However, since also in this case by far the most overall entropy production takes place in a very thin layer near the wall, thermal entropy production is the largest contributor to irreversibilities.

Conclusions. No generally valid conclusions can be drawn. For the cases considered here, thermal entropy production was largest. However, this constellation can change if the temperatures involved change, or if the Re_{max} number is increased significantly. The above posed questions must be answered individually from case to case. This points at the need for reliable computer programs with whom each case can be simulated separately.

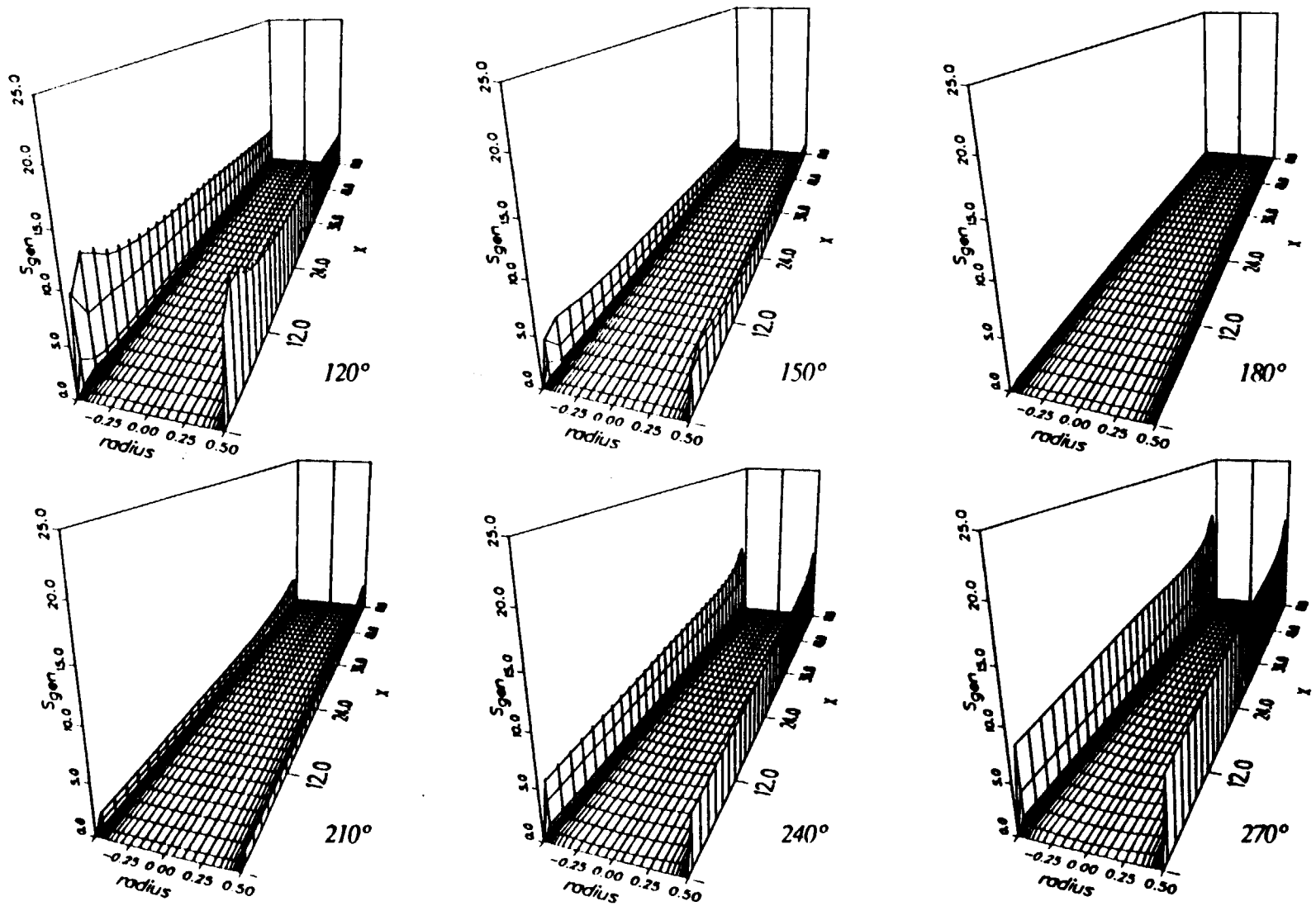

Fig. 11.1: Total normalized entropy generation rate at various crank angles. Data point e: $Re_{max}=1.87x10^5$, Va=230, L/D=60, Pr=1.0, Ec→0, $T_w/T_o=1.2$. Mean flow direction: 120°, 150° into plane; 180° flow reversal; 210°, 240°, 270° out of plane.

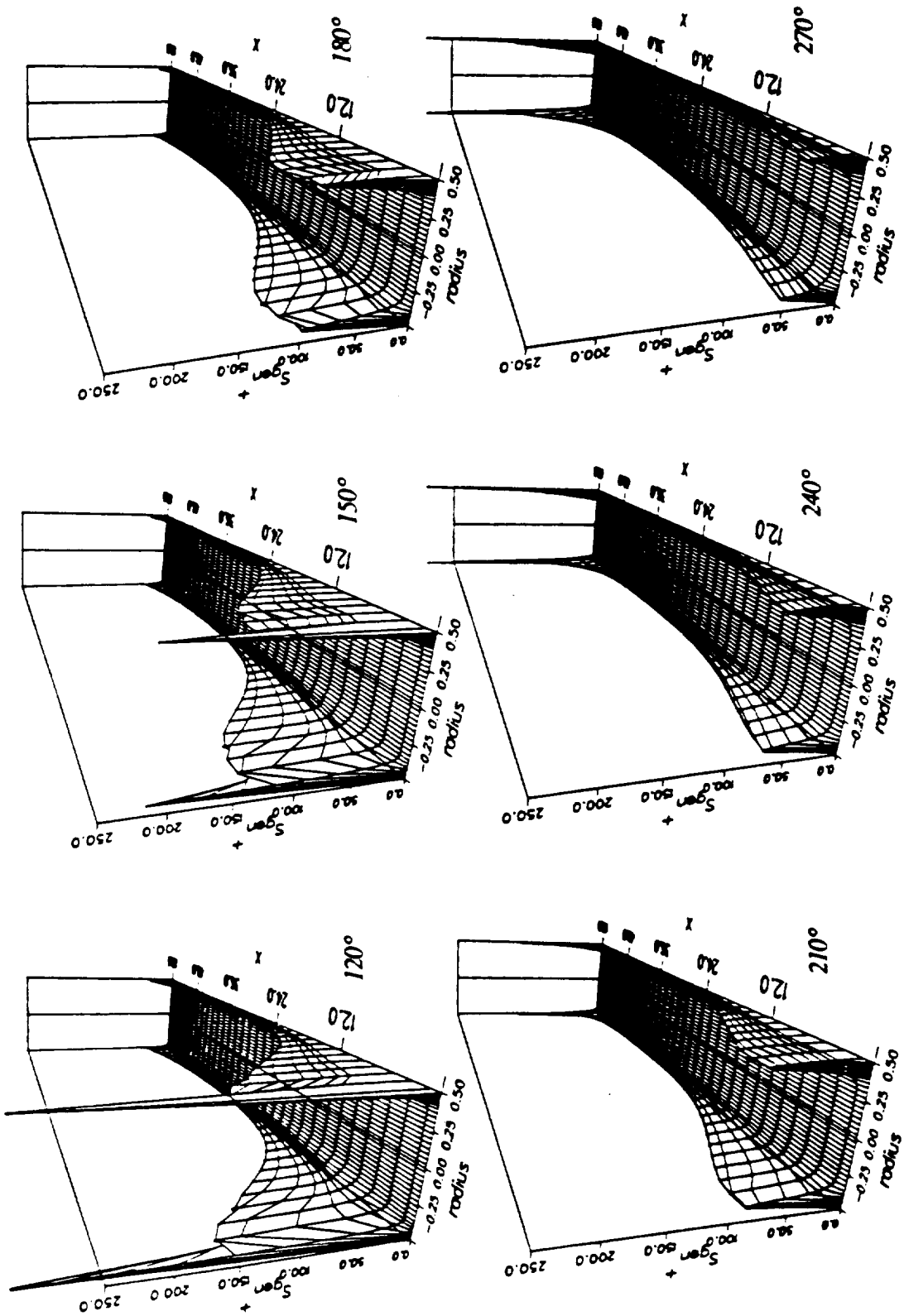

Fig. 11.2: Total normalized entropy generation rate at various crank angles. Data point SPRE: Re_{max}=1.17x10⁴, Va=80, L/D=60, Pr=1.0, Ec→0, T_w/T_o=1.2. Mean flow direction: 120°, 150° into plane; 180° flow reversal; 210°, 240°, 270° out of plane.

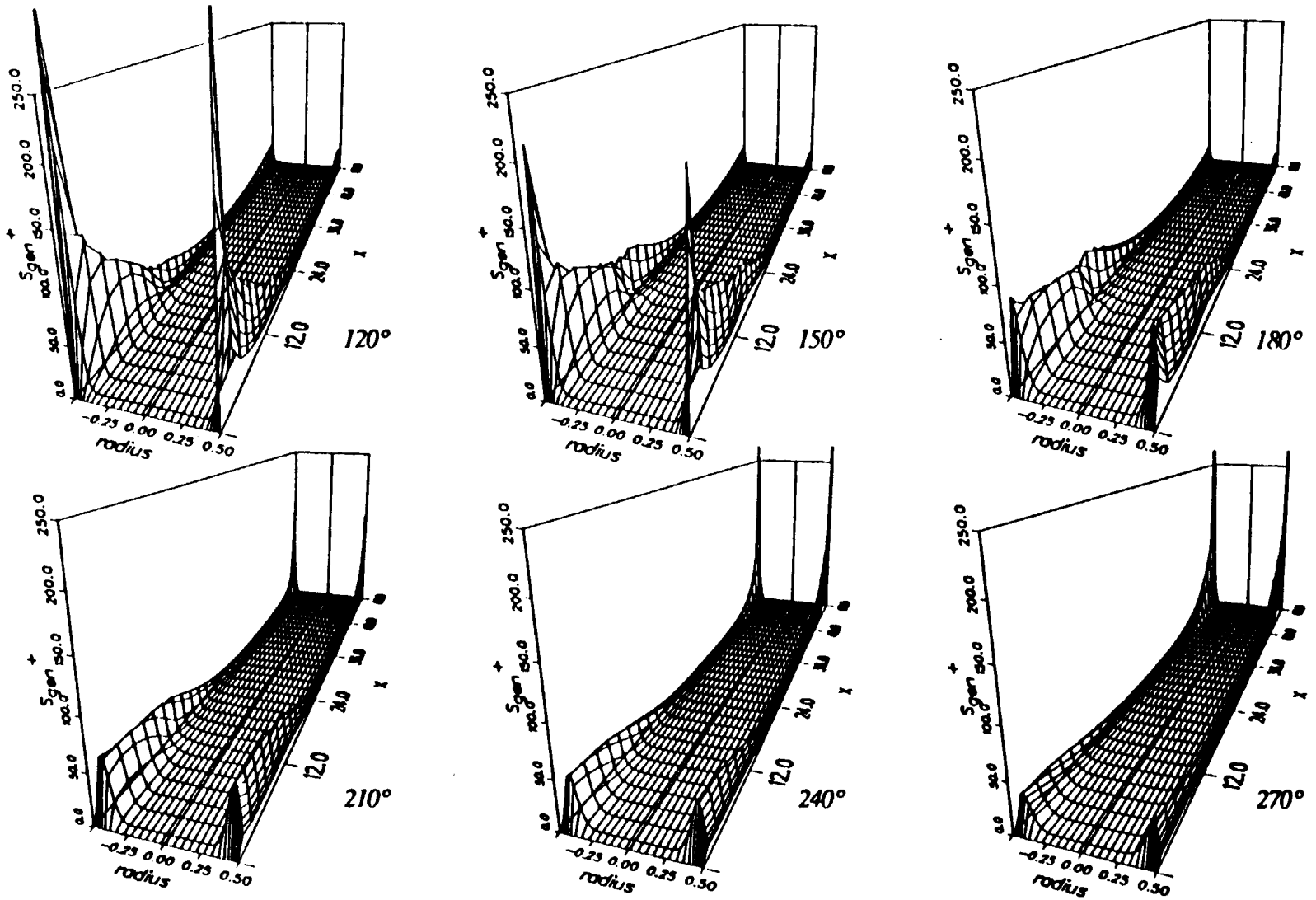

Fig. 11.3: Total normalized entropy generation rate at various crank angles. Data point p: $Re_{max}=8.43x10^3$, Va=230, L/D=60, Pr=1.0, Ec→0, $T_w/T_o=1.2$. Mean flow direction: 120°, 150° into plane; 180° flow reversal; 210°, 240°, 270° out of plane.

Fig. 11.4: Thermal fraction of entropy generation rate at various crank angles. Data point e: Re_{max}=1.87x10^5, Va=230, L/D=60, Pr=1.0, Ec→0, T_w/T_o=1.2. Mean flow direction: 120°, 150° into plane; 180° flow reversal; 210°, 240°, 270° out of plane.

Fig. 11.5: Thermal fraction of entropy generation rate at various crank angles. Data point SPRE: Re_{max}=1.17x10⁴, Va=80, L/D=60, Pr=1.0, Ec→0, T_w/T_o=1.2. Mean flow direction: 120°, 150° into plane; 180° flow reversal; 210°, 240°, 270° out of plane.

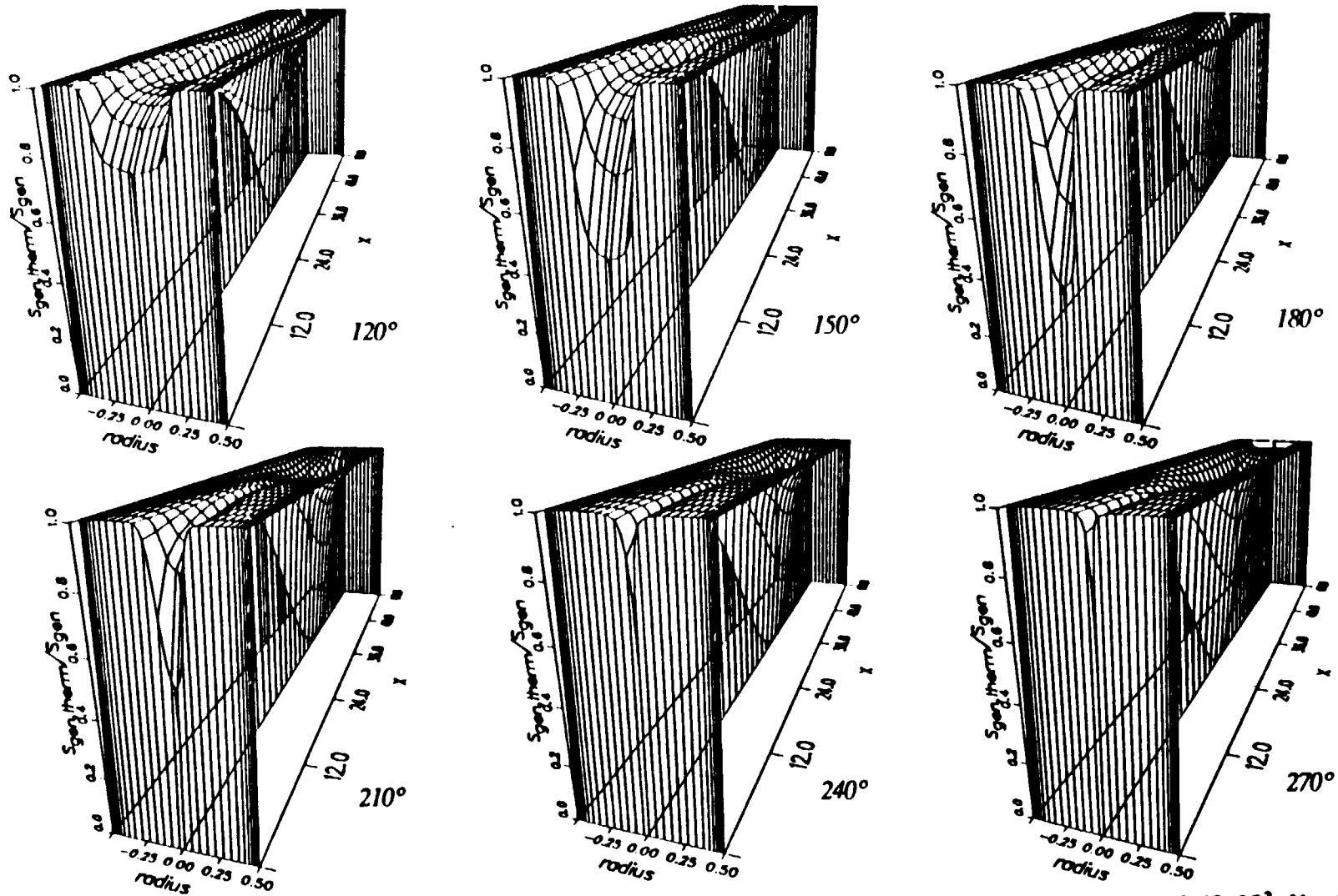

Fig. 11.6: Thermal fraction of entropy generation rate at various crank angles. Data point p: $Re_{max}=8.43x10^3$, Va=231, L/D=60, Pr=1.0, Ec→0, $T_w/T_o=1.2$. Mean flow direction: 120°, 150° into plane; 180° flow reversal; 210°, 240°, 270° out of plane.

Fig. 11.7: Turbulent fraction of entropy generation rate at various crank angles. Data point e: $Re_{max}=1.87x10^5$, Va=230, L/D=60, Pr=1.0, Ec→0, $T_w/T_o=1.2$. Mean flow direction: 120°, 150° into plane; 180° flow reversal; 210°, 240°, 270° out of plane.

Fig. 11.8: Turbulent fraction of entropy generation rate at various crank angles. Data point SPRE: Re_{max}=1.17x10⁴, Va=80, L/D=60, Pr=1.0, Ec→0, T_w/T_o=1.2. Mean flow direction: 120°, 150° into plane; 180° flow reversal; 210°, 240°, 270° out of plane.

Fig. 11.9: Turbulent fraction of entropy generation rate at various crank angles. Data point p: Re_{max}=8.43x10^3, Va=231, L/D=60, Pr=1.0, Ec→0, T_w/T_o=1.2. Mean flow direction: 120°, 150° into plane; 180° flow reversal; 210°, 240°, 270° out of plane.

PART IV: CLOSURE

12. OVERALL ASSESSMENT

12.1. Summary and Major Conclusions

1.) A literature review shows that presently no detailed numerical study into fully developed and developing turbulent oscillating flow and heat transfer is available.

2.) A control-volume based numerical algorithm suitable for solving the governing equations exactly and efficiently is developed.

3.) The k-ε model in the Lam-Bremhorst form is identified as a suitable model for oscillating flow predictions. It is shown that the model has the capability to predict transition to turbulence in quasi-steady and accelerated pipe flow at least qualitatively correct.

4.) The oscillating flow predictions generally compare well with the experiment. This validates the choice of the k-ε model for this study.

5.) With regard of the oscillating flow predictions, the major flaws of the k-ε model are:
- The ε inflow boundary condition is questionable.
- Transition in accelerated pipe flow is predicted too early.
- The present eddy-viscosity concept implies an infinite stress-response time to shear.

6.) A modification to the ε-equations is proposed in order to capture better the acceleration/deceleration effects on transition and relaminarization.

7.) A complex valued turbulence viscosity is proposed.

8.) The universal law of the wall does not hold for oscillating flow. A viscous sublayer following $u^+=y^+$ does exist at least up to a y^+ of 7.

9.) For Re_{max} numbers above 10^5, the steady state correlations for the fully developed friction coefficient and Nu number apply well. For lower Re_{max} numbers, the departures become larger with decreasing Re_{max} and increasing Va.

10.) To estimate the influence of unsteadiness, an effective Valensi number should be used, built upon the effective, not the laminar, viscosity.

11.) An irreversibility analysis demonstrates that for the conditions chosen, heat conduction is the biggest contributor towards entropy production.

12.2. Contributions of This Research

To the best knowledge of the author of this work, the new and unique features contained herein are:

1.) The development of the locally adaptive time integration scheme for a *nonlinear* convection-diffusion situation.

2.) The application and documentation of the predictions of the Lam-Bremhorst form k-ε model for quasi-steady and accelerated fully developed and developing pipe flow.

3.) The oscillatory flow and heat transfer predictions.

4.) The proposed modification to the ε-equation.

12.3. Suggestions for Further Research

Four major points emerged for further investigation:

1.) The inflow boundary condition for ε should be theoretically or, if possible, experimentally investigated in order to enable the prediction of "traveling turbulent slugs" downstream of the inflow.

2.) The concept of a complex valued turbulent viscosity should be pursued to capture the phase lag of the small scale motion with respect to the large scale motion in strongly unsteady flows.

3.) The proposed modification to the ε-equation should be tested and scaled in order to yield better predictions for accelerated/decelerated flows.

4.) The data generated herein should be reduced to yield correlations for the friction factor and Nu number which are needed in Stirling engine performance codes.

REFERENCES

Akao, F., Iguchi, M., Ohmi, M. (1986): "Velocity Distribution in Laminar Phases for Oscillatory Rectangular Duct Flows with Occurance of Turbulent Transition", Bull JSME, v 29, n 245, pp 2447-2454, August.

Atabek, B.H. (1961): "Unsteady and Oscillatory Flows in the Entrance Regions of Co-axial Tubes, Tubes and Channels", Ph.D. thesis, Univ. of Minnesota, Minneapolis, MN.

Batchelor, G.K., Townsend, A.A. (1948): "Decay of Isotropic Turbulence in the Initial Period", Proc. Roy. Soc. A, v 193, pp 539-558.

Bejan, A. (1982): **Entropy Production Through Fluid Flow and Heat Transfer**, McGraw-Hill, NY.

Binder, G., Tardu, S., Blackwelder, R.F., Kueny, J.L. (1985): "Large Amplitude Periodic Oscillations in the Wall Region of a Turbulent Channel Flow", 5th Symposium on Turbulent Shear Flows, August 7-9, 1985, Cornell University, Ithaca, NY.

Blondeaux, P., Colombini, M. (1985): "Pulsatile Turbulent Pipe Flow", 5th Symposium on Turbulent Shear Flows, August 7-9, 1985, Cornell University, Ithaca, NY.

Bowlus, D.A., Brighton, J.A. (1968): "Incompressible Turbulent Pipe Flow in the Inlet Region of a Pipe", J Basic Eng, pp 431-433, September.

Bradshaw, P., Cebeci, T., Whitelaw, J.H. (1980): **Engineering Calculation Methods for Turbulent Flows**, Academic Press, London.

Bulatowa, T.G., Grigor'ev, M. M., Kuz'min, V.V. (1986): "Oscillatory Turbulent Flow in a Cylindrical Channel", J Eng Phys, v 50, n 6, pp 632-636, June.

Carr, L.W. (1981): "A Review of Unsteady Boundary Layer Experiments", **IUTAM Symposium on Unsteady Turbulent Shear Flows** (ed. by R. Michel, J. Cousteix and R. Houdeville), pp 3-34, Springer Verlag.

Cayzac, R., Fauchas, J., Clarion, C. (1985): "Stability of Unsteady Parallel Flows by the Method of Energy", in: Kozlov, V.V. (ed): **Laminar-Turbulent Transition**, 2nd IUTATM Symp. on lam.-turb. transition, Novosibirsk, 1984, Berlin, Springer Verlag.

Cebeci, T., Smith, A.M.O. (1974): **Analysis of Turbulent Boundary Layers**, Academic Press, New York.

Cebeci, T. (1986): "Unsteady Boundary Layers with an Inteligent Numerical Scheme", J Fluid Mech , v 163, pp 129-140, February.

Chambre, P.L., Schrock, V.E. (1978): "Reversal of Laminar Flow in a Pipe", Nuclear Engineering and Design, v 47, pp 239-250.

Champagne, F.H., Harris, V.G., Corrsin, S. (1970): "Experiments on Nearly Homogeneous Turbulent Shear Flow", J Fluid Mech, v 41, pp 81-141.

Chan, K.W., Baird, M.H. (1974): "Wall Friction in Oscillating Liquid Collumns", Chemical Engineering Science, v 29, pp 2093-2099.

Chandran, K.B., Swanson, W.M., Ghista, D.N., Vayo, H.W. (1974): "Oscillatory Flow in Thin-Walled Curved Elastic Tubes", Annals of Biomedical Engineering, v 2, pp 392-412.

Charreyon, P.O. (1984): "Convective Heat Transfer Enhancement in Unsteady Channel Flow - A Review", in P.H. Roethe (ed.): **Forum on Unsteady Flows**, ASME FED-Vol 15, presented at the winter annual meeting of the ASME, New Orleans, LA, Dec 9-13, 1984.

Chen, N.C.J., Griffin, F.P. (1983): "Effects of Pressure-Drop Correlations on Stirling Engine Predicted Performance", 18th IECEC, Proceedings (IECEC paper 83-9114), pp 708-713, New York, American Institute of Chemical Engineers.

Chien, K.Y. (1982): "Predictions of Channel and Boundary Layer Flows with a Low-Reynolds Number Turbulence Model", AIAA Journal, v 20, pp 33-38, January.

Cook, W.J., Murphy, J.D., Owen, F.K. (1985): "An Experimental and Computational Study of Turbulent Boundary Layers in Oscillating Flows", 5th Symposium on Turbulent Shear Flows, August 7-9, 1985, Cornell University, Ithaca, NY.

Cousteix, J., Desopper, A., Houdeville, R. (1979): "Stucture and Development of a Turbulent Boundary Layer in an Oscillatory External Flow", **Turbulent Shear Flows I**, Springer Verlag, pp. 154-171.

Cousteix, J., Houdeville, R., Javelle, J. (1982): "Response of a Flat Plate Turbulent Boundary Layer to a Pulsation of the External Flow", in S. Carmi et al. (ed.): **Three Dimensional Turbulent Shear Flows**, presented at the 1982 AIAA/ASME joint Fluids, Plasma, Thermophysics and Heat Transfer Conference, St. Louis, MO, June 7-11, 1982, ASME, NY.

Cousteix, J., Houdeville, R. (1985): "Turbulence and Skin Friction Evaluations in an Oscillating Boundary Layer", 5th Symposium on Turbulent Shear Flows, August 7-9, 1985, Cornell University, Ithaca, NY.

Cousteix, J. (1986): "Three-dimensional and Unsteady Boundary Layer Computations", Ann Rev Fluid Mech, v 18, publ. by Annual Reviews Inc. Palo Alto, CA, pp 173-196.

Davis, S.H. (1976): "The Stability of Time-Period Flows", in VanDyke, W. Vincenti and J.V. Weheuser (eds): Annual Review of Fluid Mech, v 8, pp 57-74.

Deissler, R.G. (1950): "Analytical and Experimental Investigation of Adiabatic Turbulent Flow in Smooth Tubes", NACA Techn. Note 2138.

Deissler, R.G. (1955): "Turbulent Heat Transfer and Friction in the Entrance Region of Smooth Passages, Trans. ASME, v 77.

Dijkstra, K. (1984): "Non-Stationary Heat Transfer in Heat Exchangers", 19th IECEC, Proceedings (IECEC paper 84-9176), pp 2033-2036, Am. Nuc. Soc..

Disselhorst, J.H.M., Wijngaarden, L. van (1980): "Flow in the Exit of Open Pipes During Acoustic Resonance, J Fluid Mech, v 99, part 2, pp 293-319.

Drake, D.G. (1965): "On the Flow in a Channel Due to a Periodic Pressure Gradient", Q J Mech Appl Math, v 18, part 1, pp 1-10.

Duck, P.W. (1985): "Pulsatile Flow Through Constricted and Dilated Channels II", Q J Mech Appl Math, v 38, part 4, November.

Dutoga, D., Michard, P. (1981): "A Program for Calculating Boundary Layers Along Compressor and Turbine Blades", **Numerical Methods in Heat Transfer** (ed. by R.W. Lewis, K. Morgan and O.C. Zienkiewicz), John Wiley & Sons, New York.

Edwards, M.F., Wilkinson, W.L. (1971): "Review of Potential Aplications of Pulsating Flow in Pipes, Transactions of the Institute of Chemical Engineers, v 49, n 2, pp 85-94.

Gaver, D.P. (1986): "Experimental Investigation of Oscillating Flows in a Tapered Channel", J Fluid Mech, v 172, November, pp 47-61.

Gedeon, D. (1986): "Mean-Parameter Modelling of Oscillatory Flow, ASME J Heat Transf, v 108, pp 513-518, August .

Gerrard, J.H. (1971): "An Experimental Investigation of Pulsating Turbulent Water Flow in a Tube", J Fluid Mech, v 46, part 1, pp 43-64.

Gosman, A.D., Johns, R.J.R., Watkins, A.P. (1980): "Development of Prediction Methods", in **Symposium on Combustion Modeling in Reciprocating Engines**, General Motors Research Laboratories, 1978.

Grassmann, P., Tuma, M. (1979): "Kritische Reynolds-Zahlen bei Oszillierenden und Pulsierenden Rohrströhmungen", Wärme-und Stoffübertragung, v 12, p 203.

Hanjalic, K., Launder, B.E. (1972): "A Reynolds Stress Model of Turbulence and Its Application to Thin Shear Flows", J Fluid Mech, v 52, part 4.

Hanjalic, K., Launder, B.E. (1980): "Sensitizing the Dissipation Equation to Irrotational Strains", J Fluids Eng, v 102, March, pp 34-40.

Harlow, F.H., Nakayama, P.I. (1967): "Turbulent Transport Equations", Phys Fluids, v 10, p 2323.

Hassid, S., Poreh, M. (1978): "A Turbulent Energy Dissipation Model for Flows with Drag Reduction", J Fluids Eng, v 100, pp 107-112.

Henkes, R.A.W.M., Hoogendoorn, C.J. (1989): "Comparison of Turbulence Models for the Natural Convection Boundary Layer Along a Heated Vertical Plate", Int J Heat Mass Transfer, v 32, n 1, pp 157-169.

Hino, M., Sawamoro, M, Takasu, S. (1976): "Experiments on Transition to Turbulence in an Oscillatory Pipe Flow", J Fluid Mech, v 75, part 2, pp 193-207.

Hino, M., Kashiwayanagi, M., Nakayama, A., Hara, T. (1983): "Experiments on the Turbulence Statistics and the Structure of a Reciprocating Oscillaory Flow", J Fluid Mech, v 131, pp 363-400.

Hoffmann, G.H. (1975): "Improved Form of the Low-Reynolds Number k-ε Model", Phys Fluids, v 18, pp 309-312.

Iguchi, M., Ohmi, M. (1983a): "Turbulent Accelerating and Decelerating Pipe Flows in Quasi Steady Motion", Technol Rep Osaka Univ, v 33, n 1684-1702 , pp 97-106, March.

Iguchi, M., Ohmi, M., Maegawa, K. (1982): "Analysis of Free Oscillating Flow in a U-Shaped Tube", Bull JSME, v 25, n 207, pp 1398-1405, September.

Iguchi, M., Ohmi, M. (1983b): "Unsteady Frictional Losses in Decelerating Turbulent Pipe Flows", Technol Rep Osaka Univ, v 33, n 1703-1740, pp 349-358, October.

Iguchi, M., Ohmi, M., Akao, F. (1985a): "Time Dependent Wall Shear Stress In a Duct with Arbitrary Cross Section", Bull JSME, v 28, n 244, October.

Iguchi, M., Ohmi, M., Tanaka, S. (1985b): "Experimental Study of Turbulence in a Pulsatile Flow", Bull JSME, v 28, n 246, pp 2915-2922, December.

Iguchi, M., Ohmi, M., Nishizawa, K. (1986a): "Relaminarization of Pulsatile Turbulent Flow in a Rectangular Duct", Bull JSME, v 29 , n 247, pp 59-66, January.

Iguchi, M., Ohmi. M., Kimura, H. (1986b): "Propagation of Turbulent Slugs in a Pulsating Pipe Flow", Nippon Kikai Gakkai Ronbunshu B Hen, v 52, n 478, pp 2390-2397, June (in Japanese).

Ikeo, S., Uzawa, K. (1986): "Oscillatory Flow through a Convergent Tube", Bull JSME, v 29, n 254 pp 2501-2507, August,.

Jones, J.D. (1985): "Flow Losses in Stirling Engine Heat Exchangers", 20th IECEC, Proceedings (IECEC paper 85- 9437), v 3, pp 366-371, SAE, Warrendale, PA.

Jones, W.P., Launder, B.E. (1972): "The Prediction of Laminarization with a Two-Equation Model of Turbulence", Int J Heat Mass Trans, v 15, pp 301-314.

Jones, W.P., Launder, B.E. (1973): "The Calculation of Low-Reynolds Number Phenomena with a Two-Equation Model of Turbulence", Int J Heat Mass Trans, vol 16, pp 1119-1130.

Kays W.M., Crawford, M.E. (1980): **Convective Heat and Mass Transfer**, McGraw-Hill, NY.

Kebede, W., Launder, B.E., Younis, B.A. (1985): "Large Amplitude Periodic Flow: A Second-Moment Closure Study", 5th Symposium on Turbulent Shear Flows, Aug. 7-9, 1985, Cornell University, Ithaca, NY.

Kelkar, K.M. (1988): "Numerical Study of Stability of Fluid Flow", Ph.D. Thesis, Mechanical Engineering Department, University of Minnesota, Minneapolis, MN.

Kerczek, C. von, Davis, S.H. (1972): "The Stability of Oscillatory Stokes Layers", Studies in Applied Mathematics, v LI, n 3.

Kirmse, R.E. (1979): "Investigation of Pulsating Turbulent Pipe Flow", Trans ASME, J Fluids Eng, v 101, pp 436-442.

Kita, Y., Adachi, Y., Hirose, K. (1980): "Periodically Oscillating Turbulent Flow in a Pipe", Bull JSME, v 23, n 179, May.

Knight, D.W. (1978): "Review of Oscillatory Boundary Layer Flows", Journal of the Hydraulics Division, Proceedings of the American Society of Civil Engineering, v 104, n HY6, June.

Kudva, A.K., Sesonske, A. (1972): "Structure of Turbulent Velocity and Temperature Fields in Ethylene Glycol Pipe Flow at Low Reynolds Numbers", Int J Heat Mass Trans, v 15, pp.127-145.

Lam, C.K., Bremhorst, K. (1981): "A Modified Form of the k-ε Model for Predicting Wall Turbulence", J Fluids Eng, v 103, pp 456-460.

Laufer, J. (1953): "The Structure of Turbulence in Fully Developed Pipe Flow", NACA Rep. 1174.

Launder, B.E., Sharma, B. (1974): "Application of the Energy-Dissipation Model of Turbulence to the Calculation of Flow Near a Spinning Disc", Letters in Heat Transfer, v 1, pp 131-138.

Launder, B.E., Reece, G.J., Rodi, W. (1975): "Progress in Development of Reynolds-Stress Turbulence Model", J Fluid Mech, v 68, pp 537-566.

Lefebre, P.J., White, F.M. (1987): "Correlation of Transition to Turbulence in a Constant-Acceleration Pipe Flow", in W.W. Bower (ed.): **Forum on Turbulent Flows - 1987**, presented at the 1987 ASME applied mechanics, bioengineering and fluids engineering conference, Cincinatti, OH, June 14-17, 1987.

Lu, S., Nunge, R.J., Erian, F.F., Mohajery, M. (1973): Proceedings of the 2nd Symposium on Turbulence in Liquids, Univ. of Missouri-Rolla, pp 375-392.

Mansuor, N.N., Kim, J., Moin, P. (1989): "Near-Wall k-ε Turbulence Modeling", AIAA Journal, v 27, n 8, pp 1068-1073.

Mao, Z.X., Hanratty, T.J. (1985): "Studies on the Wall Shear Stress in a Turbulent Pulsating Pipe Flow", 5th Symposium on Turbulent Shear Flows, Aug. 7-9, 1985, Cornell University, Ithaca, NY.

Mao, Z.X., Hanratty, T.J. (1986): "Studies on the Wall Shear Stress in a Turbulent Pulsating Pipe Flow", J Fluid Mech, v 170, pp 545-564, September.

Martinuzzi, R., Pollard, A. (1989): "Comparative Study of Turbulence Models in Predicting Turbulent Pipe Flow-Part 1: Algebraic Stress and k-ε Models", AIAA Journal, v 27, n 1, pp 29-36, January.

Merkli, P., Thomann, H. (1975): "Transition to Turbulence in Oscillating Pipe Flow", J Fluid Mech, v 68, part 3, pp 567-575.

Mizushina, T., Maruyama, T., Shiozaki, Y. (1973): "Pulsating Turbulent Pipe Flow in a Tube", J Chem Eng Jpn, v 6, pp 487-494.

Naot, D., Shavit, A., Wolfstein, M. (1970): "Interactions Between Components of the Turbulent Velocity Correction Tensor", Israel Journal of Technology, v 68, p 259.

Nikuradse, J. (1932): "Untersuchungen über die Geschwindigkeitsverteilung in turbulenten Strömungen", Forsch Arb Ing Wes, Heft 356.

Ohmi, M., Iguchi, M., Tateo, U., Minami, H. (1980a): "Flow Pattern and Frictional Losses in Pulsating Pipe Flow. Part I: Effect of Pulsating Frequency on the Turbulent Flow Pattern", Bull JSME, v 23, n 186, December.

Ohmi, M., Iguchi, M. (1980b): "Flow Pattern and Frictional Losses in Pulsating Pipe Flow. Part II: Effect of Pulsating Frequency on the Turbulent Frictional Losses", Bull JSME, v 23, n 186, December.

Ohmi, M., Manabu, I. (1980c): "Flow Pattern and Frictional Losses in Pulsating Pipe Flow. Part III: General Reperesentation of Turbulent Flow Pattern", Bull JSME, v 23, n 186, December.

Ohmi, M., Iguchi, M. (1981a): "Flow Pattern and Frictional Losses in Pulsating Pipe Flow. Part IV: General Reperesentation of Turbulent Frictional Losses", Bull JSME, v 24, n 187, January.

Ohmi, M., Iguchi, M., Usui, T. (1981b): "Flow Pattern and Frictional Losses in Pulsating Pipe Flow. Part V: Wall Shear Stress and Flow Pattern in Laminar Flow", Bull JSME, v 24, n 187, January.

Ohmi, M., Iguchi, M. (1981c): "Flow Pattern and Frictional Losses in Pulsating Pipe Flow. Part VI: Frictional Losses in a Laminar Flow", Bull JSME, v 24, n 196, October.

Ohmi, M., Iguchi, M. (1981d): "Flow Pattern and Frictional Losses in Pulsating Pipe Flow. Part VII: Wall Shear Stress in a Turbulent Flow", Bull JSME, v 24, n 196, October.

Ohmi, M., Iguchi, M., Urahata, I. (1982): "Flow Patterns and Frictional Losses in an Oscillating Pipe Flow", Bull JSME, v 25, n 202, pp 536-543, April.

Ohmi, M., Koyomen, S., Iguchi, M. (1983): "Experimental Study of the Eddy Viscosity Distribution in Pulsating Pipe Flow", Technol Rep Osaka Univ, v 33, n 1703-1740, pp 359-356, October.

Ohmi, M., Iguchi, M., Urahata, I. (1986a): "Experimental Study of Velocity Distribution and Inlet Length in the Inlet Region of Laminar Oscillatory Pipe Flow", Nippon Kikai Gakkai Ronbunshu B Hen, v 52, n 479, pp 2518-2525, July (in Japanese).

Ohmi, M., Iguchi, M., Urahata, I. (1986b): "Turbulent Slug and Velocity Field in the Inlet Region for a Pulsatile Pipe Flow", Nippon Kikai Gakkai Ronbunshu B Hen, v 52, n 479, pp 2526-2534, July (in Japanese).

Park, J., Baird, M. (1970): "Transition Phenomena in an Oscillating Manometer", Canadian Journal of Chemical Engineering, v 48, pp 491-495.

Patankar, S.V. (1980): **Numerical Heat Transfer and Fluid Flow**, Hemisphere Publ. Co., Washington.

Patankar, S.V. (1988): "Recent Developments in Computational Heat Transfer", J Heat Transfer, v 110, November.

Patel, V.C., Rodi, W., Scheurer, G.(1985): " Turbulence Models for Near Wall and Low-Reynolds Number Flows: a Review", AIAA J, v 23, pp 1308-1319.

Peacock, J.A., Stairmand, J.W. (1983): "Film Gauge Calibration in Oscillatory Pipe Flow", J Phys E: Sci Instrum, v 16, pp 571-576.

Ragallo, R.S., Moin, P.(1984): "Numerical Rimulation of Turbulent Flows", Ann. Rev. Fluid Mech, v 16, pp 99-137.

Ramaprian, B.R., Tu, S.W. (1983): "Fully Developed Turbulent Pipe Flow. Part 2: The Detailled Structure of the Flow", J Fluid Mech, v 137, pp 59-81.

Recktenwald, G.W. (1989): "A Study of Heat Transfer Between the Walls and Gas Inside the Cylinder of a Reciprocating Cylinder", Ph.D. Thesis, Mechanical Engineering Department, University of Minnesota, Minneapolis, MN.

Reddy, U., McLaughlin, J.B., Nunge, R.J. (1985): "Numerical Study of Pulsed Turbulent Pipe Flow", Fluid Eng Trans ASME, v 107, n 2, pp 205-211, June.

Reynolds, W.C. (1976): "Computation of Turbulent Flows", Ann Rev Fluid Mech, v 8, pp 183-208.

Reynolds, W.C., Hussain, A.K.M.F. (1972): "The Mechanics of an Organized Turbulent Wave in Turbulent Shear Flow - part 3: Theoretical Models and Comparison with Experiments", J Fluid Mech, v 54, part 2, pp 263-288.

Richardson, E.G., Tyler, E. (1929): "The Transverse Velocity Gradient near the Mouths of Pipes in which an Alternating Continous Flow of Air is Established, Proc Phys Soc, London, v 42, part 1.

Rodi, W. (1984): **Turbulence Models and Their Application in Hydraulics: A State of the Art Review**, 2nd ed., Int. Assoc. for Hydraul. Res., Delft.

Rodi, W., Scheurer, G. (1986): "Scutinizing the k-ε Turbulence Model Under Adverse Pressure Gradient Conditions", J Fluid Eng Trans ASME, v 108, n 2, pp. 174-179, June.

Schlichting, H. (1982): **Grenzschichttheorie**, 8th German ed., Braun, Karlsruhe.

Schmidt, R.C., Patankar, S.V. (1987): "Two-Equation Low-Reynolds Number Turbulence Modeling of Transitional Boundary Layer Flow Characteristic of Gas Turbine Blades", NASA Contractor Report 4145.

Sergeev, S. (1966): "Fluid Oscillations at Moderate Reynolds Numbers", Fluid Dynamics, v 1, n 1, pp. 121-122.

Seume, J.R., Simon, T.W. (1986a): "A Survey of Oscillating Flow in Stirling Engine Heat Exchangers", Yearly Report for NASA Lewis Research Center.

Seume, J.R., Simon, T.W. (1986b): "Oscillating Flow in Stirling Engine Heat Exchangers", 21th IECEC, Proceedings (IECEC paper 86-9118), ACS.

Seume, J.R., Simon, T.W. (1987): "Flow Oscillation Effects in Tubes and Porous Material: Unresolved Issues", Symposium on Fluid Flow and Heat Transfer in Reciprocating Machinery, ASME Winter annual meeting, Dec. 14-16, 1987, Boston, MA.

Seume, J.R. (1988): "An Experimental Investigation of Transition in Oscillating Pipe Flow", Ph.D. Thesis, Mechanical Engineering Department, University of Minnesota, Minneapolis, MN.

Sexl, T. (1930): "Über den von E.G. Richardson Entdeckten 'Annulareffekt'", Zeitschrift für Physik, v 61, pp 349-362.

Shadid, J. (1989): "Experimental and Computational Study of the Stability of Natural Convection in an Inclined Enclosure," Ph.D. Thesis, Mechanical Engineering Department, University of Minnesota, Minneapolis, MN.

Shemer, L., Wygananski, I. (1985a): "On the Impedance of the Pipe in Laminar and Turbulent Pulsating Flows", Exp Fluids, v 3, n 4, pp 185-189.

Shemer, L., Wygananski, I., Kit, E. (1985b): "Pulsating Flow in a Pipe", J Fluid Mech, v 153, pp 313-337, April.

Shizgal, A.S., Goldsmith, H.L., Mason, S.G. (1965): "The Flow of Suspensions through Tubes. IV: Oscillatory Flow of Rigid Spheres", Canadian Journal of Chemical Engineering, v 43, n 3, pp 97-101.

Simon, T.W., Seume, J.R., Friedman, G. (1989): private communication.

Sobey, I.J. (1985): "Observation of Waves during Oscillatory Channel Flow", J Fluid Mech, v 151, February.

Stettler, J.C., Hussain, A.K.M.F. (1986): "On Transition of the Pulsatile Pipe Flow", J Fluid Mech, v 170, pp 169-197, September.

Sudou, K., Sumida, M., Takami, T., Toshihiro, Y. (1985): "Study of Oscillatory Flow in Curved Pipes (2nd Report, Axial Velocity Profiles)", Bull JSME, v 28, n 245, pp 2644-2651, November.

Sumida, M., Sudou, K., Takami, T. (1984): "Pulsating Flow in Curved Pipes (2nd Report, Expeiments)", Bull JSME, v 27, n 234, pp 2714-2721, December.

Sumida, M., Sudou, K. (1985): "Oscillatory Flow in Curved Pipes of Rectangular Cross Section (1st Report, Numerical Analysis of Laminar Flow in Square Sect. Pipes)", Bull JSME, v 28, n 243, pp 1899-1905, September.

Sumida, M., Sudou, K. (1986a): "Oscillatory Flow in Curved Pipes of Rectangular Cross Section (2nd Report, Effect of Aspect Ratio of a Pipe)", Nippon Kikai Gakkai Ronbunshu B Hen, v 52, n 480, pp 2881-2887, August (in Japanese).

Sumida, M., Sudou, K. (1986b): "Pulsating Flow in Curved Pipes (3rd Report, Axial Velocity Profile)", Bull JSME, v 29, n 256, pp 3334-3340, October.

Takami, T., Sudou, K., Sumida, M. (1984): "Pulsating Flow in Curved Pipes (1st Report, Numerical and Approximate Analyses)", Bull JSME, v 27, n 234, pp 2706-2713, December.

Taylor, D.R., Aghili, H. (1984): "An Investigation of Oscillatory Flow in Tubes", 19th IECEC, Proceedings (IECEC paper 84-9176)", pp 2033-2036, Am. Nuc. Soc..

Telionis, D.P. (1975): "Calculation of the Time Dependent Boundary Layers", **Unsteady Aerodynamics**, v 1, ed. by R.B. Kinney, pp. 155-190.

Telionis, T.P. (1981): **Unsteady Viscous Flows**, Springer Verlag, New York.

Thomas, L.C. (1974): "Adaption of the Surface Renewal Approach to Momentum and Heat Transfer for Turbulent Pulsatile Flow", J Heat Transfer, paper no. 74-HT-MM.

To, W.M., Humphrey, J.A.C. (1986): "Numerical Simulation of Buoyant Turbulent Flow-1. Free Convection Along a Heated Flat Plate", Int J Heat Mass Transf, v 29, pp 573-592.

Tozzi, J.T., Kerczek, C.H. von (1986): "Stability of Oscillatory Hagen-Poiseulle Flow", J Appl Mech Trans ASME, v 53, n 1, pp 187-192, March.

Trikha, A.K. (1975): "An Efficient Method for Simulating Frequency-Dependent Friction in Transient Liquid Flow", ASME J Fluid Eng, pp 97-105, March.

Truckenbrodt, E. (1980): **Fluidmechanik**, 2nd ed., v 1, Springer, Heidelberg.

Tu, S.W., Ramaprian, B.R. (1983): "Fully Developed Periodic Turbulent Pipe Flow. Part 1: Main Experimental Results and Comparisons with Predictions". J Fluid Mech, v 137, pp 31-58.

Uchida, S. (1956): "The Pulsating Viscous Flow Superposed on the Steady Laminar Motion of Incompressible Fluid in a Circular Pipe", Zeitschrift für angewandte Mathematik und Physik, v 7, pp 403-422.

Van Doormaal, J.P., Raithby, G.D. (1984): "Enhancements of the SIMPLE Method for Predicting Incompressible Fluid Flows", Numerical Heat Transfer, v 7, pp 147-164.

Valensi, J. (1947): "Oscillation d'un Liquide Pesant et Visqueux dans un Tube en U de Faible Diamètre", Comptes Rendus de la Academie des Sciences de Paris, v 224, pp 446, 532, 893 and 1695.

Vasilev, O.F., Kvon, V.I. (1971): "Friction Forces of Unsteady Flows in Open Channels and Pipes", Proceedings of the 14th conference, v 1, subject B, Int Assoc for Hydr Research.

Vosse, F.N. van de, Segal, A., Steenhoven, A.A. van, Janssen, S. (1986): "Finite Element Approximation of the Unsteady Two-dimensional Navier-Stokes equations", Int J Numer Methods Fluids, v 6, n 7, pp 427-443, July.

Wang, J.S., Tullis, J.D. (1974): "Turbulent flow in the Entrance Region of a Rough Pipe", J Fluids Eng, pp 62-68, March.

Wilcox, D.C., Rubesin, W.M. (1980): "Progress in Turbulence Modeling for Complex Flow Fields Including Effects of Compressibility", NASA tech. paper 1517.

Wommersley, J.R. (1955): "Method for the Calculation of Velocity, Rate of Flow and Viscous Drag in Ateries when the Pressure Gradient is Known", Journal of Physiology, v 127, pp 553-563.

Yakhot, V., Orzsag, S.A. (1986): "Renormalization Group Analysis of Turbulence I. Basic theory", J Sci Comp, v 1, n 1.

Yamane, R., Oshima, S., Sudou, K., Sumida, M., Okamoto, N., Kizaki, M. (1985): "Study of Oscillatory Flow in a Curved Channel", Bull JSME, v 28, n 237, March.

Yoshiki, H., Tsumura, S., Endoh, T., Takama, N. (1986): "Study on Some Periodically Oscillating Flows in a Circular Pipe (Experimental Velocity Distribution)", Nippon Kikai Gakkai Ronbunshu B Hen, v 52, n 483, pp 3650-3654, November.

Younis, B.A. (1978): "Calculation of Fully-Developed Oscillating Turbulent Flow in a Pipe", M.Sc. thesis , Imperial College, London.

APPENDIX

A. Vector Quantities in Axisymmetric Coordinates

Note: In this appendix, the following conventions apply:

Tensors are given in the form: $\begin{bmatrix} rr & r\varphi & rx \\ \varphi r & \varphi\varphi & \varphi x \\ xr & x\varphi & xx \end{bmatrix}$

2-D Vectors are given in the form: $\begin{bmatrix} x \\ r \end{bmatrix}$

Stress tensor:

$$\tau = \begin{bmatrix} -p + \mu\left[2\frac{\partial v}{\partial r} - \frac{2}{3}\mathrm{div}(\vec{u})\right] & 0 & \mu\left[\frac{\partial u}{\partial r} + \frac{\partial v}{\partial x}\right] \\ 0 & \mu\left[2\frac{v}{r} - \frac{2}{3}\mathrm{div}(\vec{u})\right] & 0 \\ \mu\left[\frac{\partial u}{\partial r} + \frac{\partial v}{\partial x}\right] & 0 & \mu\left[2\frac{\partial u}{\partial x} - \frac{2}{3}\mathrm{div}(\vec{u})\right] \end{bmatrix}$$

Kinematic vector quantities in axisymmetric coordinates:

$$\text{grad}(\vec{u}) = \begin{bmatrix} \frac{\partial v}{\partial r} & 0 & \frac{\partial v}{\partial x} \\ 0 & \frac{v}{r} & 0 \\ \frac{\partial u}{\partial r} & 0 & \frac{\partial u}{\partial x} \end{bmatrix}$$

$$\text{def}(\vec{u}) = \frac{1}{2}\begin{bmatrix} 2\frac{\partial v}{\partial r} & 0 & \frac{\partial v}{\partial x} + \frac{\partial u}{\partial r} \\ 0 & 2\frac{v}{r} & 0 \\ \frac{\partial u}{\partial r} + \frac{\partial x}{\partial x} & 0 & 2\frac{\partial u}{\partial x} \end{bmatrix}$$

$$\vec{u} \bullet \text{grad}(\vec{u}) = \begin{bmatrix} u\frac{\partial u}{\partial x} + v\frac{\partial u}{\partial r} \\ u\frac{\partial v}{\partial x} + v\frac{\partial v}{\partial r} \end{bmatrix}$$

$$\text{div}(\mu\ \text{grad}(\vec{u})) = \begin{bmatrix} \frac{\partial}{\partial x}(\mu\frac{\partial u}{\partial x}) + \frac{1}{r}\frac{\partial}{\partial r}(\mu r\frac{\partial u}{\partial r}) \\ \frac{\partial}{\partial x}(\mu\frac{\partial v}{\partial x}) + \frac{1}{r}\frac{\partial}{\partial r}(\mu r\frac{\partial v}{\partial r}) - \frac{\mu v}{r^2} \end{bmatrix}$$

$$\operatorname{div}\left[\mu\ \operatorname{grad}(\vec{u})\right]^{T}\Big] = \begin{bmatrix} \frac{\partial}{\partial x}\left(\mu \frac{\partial u}{\partial x}\right) + \frac{1}{r}\frac{\partial}{\partial r}\left(\mu r \frac{\partial v}{\partial x}\right) \\ \frac{\partial}{\partial x}\left(\mu \frac{\partial u}{\partial r}\right) + \frac{1}{r}\frac{\partial}{\partial r}\left(\mu r \frac{\partial v}{\partial r}\right) - \frac{\mu v}{r^2} \end{bmatrix}$$

Viscous dissipation function Φ and generation term G for turbulent kinetic energy:

$$\Phi = G = 2\left(\frac{\partial u}{\partial x}\right)^2 + 2\left(\frac{\partial v}{\partial r}\right)^2 + 2\left(\frac{v}{r}\right)^2 + \left(\frac{\partial u}{\partial r} + \frac{\partial v}{\partial x}\right)^2$$

B. System of Differential Equations Solved

$$\frac{\partial u}{\partial x} + \frac{1}{r}\frac{\partial}{\partial r}(rv) = 0$$

$$\rho\frac{\partial u}{\partial t} + \rho u\frac{\partial u}{\partial x} + \rho v\frac{\partial u}{\partial r} = -\frac{\partial P}{\partial x} + \frac{\partial}{\partial x}\left(\mu_{eff}\frac{\partial u}{\partial x}\right) + \frac{1}{r}\frac{\partial}{\partial r}\left(r\,\mu_{eff}\frac{\partial u}{\partial r}\right) + \frac{\partial}{\partial x}\left(\mu_{eff}\frac{\partial u}{\partial x}\right) + \frac{1}{r}\frac{\partial}{\partial r}\left(r\,\mu_{eff}\frac{\partial v}{\partial x}\right)$$

$$\rho\frac{\partial v}{\partial t} + \rho u\frac{\partial v}{\partial x} + \rho v\frac{\partial v}{\partial r} = -\frac{\partial P}{\partial r} + \frac{\partial}{\partial x}\left(\mu_{eff}\frac{\partial v}{\partial x}\right) + \frac{1}{r}\frac{\partial}{\partial r}\left(r\,\mu_{eff}\frac{\partial v}{\partial r}\right) + \frac{\partial}{\partial x}\left(\mu_{eff}\frac{\partial u}{\partial r}\right) + \frac{1}{r}\frac{\partial}{\partial r}\left(r\,\mu_{eff}\frac{\partial v}{\partial r}\right) - 2\mu_{eff}\frac{v}{r^2}$$

$$P = p + \frac{2}{3}\left\{\mu_{eff}\left(\frac{\partial u}{\partial x} + \frac{\partial v}{\partial r} + \frac{v}{r}\right) + \rho k\right\}$$

$$\rho\frac{\partial T}{\partial t} + \rho u\frac{\partial T}{\partial x} + \rho v\frac{\partial T}{\partial r} = \frac{\partial}{\partial x}\left(\left(\frac{k}{c_p} + \frac{\mu_t}{\sigma_T}\right)\frac{\partial T}{\partial x}\right) + \frac{1}{r}\frac{\partial}{\partial r}\left(\left(\frac{k}{c_p} + \frac{\mu_t}{\sigma_T}\right)\frac{\partial T}{\partial r}\right) + \frac{1}{c_p}\left(\frac{\partial p}{\partial t} + u\frac{\partial p}{\partial x} + v\frac{\partial p}{\partial r}\right) + \frac{\mu}{c_p}\Phi + \frac{\rho}{c_p}\varepsilon$$

$$\rho\frac{\partial k}{\partial t} + \rho u\frac{\partial k}{\partial x} + \rho v\frac{\partial k}{\partial r} = \frac{\partial}{\partial x}\left(\frac{\mu_t}{\sigma_k}\frac{\partial k}{\partial x}\right) + \frac{1}{r}\frac{\partial}{\partial r}\left(\frac{\mu_t}{\sigma_k}\frac{\partial k}{\partial r}\right) + \rho G - \rho\varepsilon$$

$$\rho\frac{\partial \varepsilon}{\partial t} + \rho u\frac{\partial \varepsilon}{\partial x} + \rho v\frac{\partial \varepsilon}{\partial r} = \frac{\partial}{\partial x}\left(\frac{\mu_t}{\sigma_\varepsilon}\frac{\partial \varepsilon}{\partial x}\right) + \frac{1}{r}\frac{\partial}{\partial r}\left(\frac{\mu_t}{\sigma_\varepsilon}\frac{\partial \varepsilon}{\partial r}\right) + c_1 f_1 \rho G\frac{\varepsilon}{k} - c_2 f_2 \rho\frac{\varepsilon^2}{k}$$

C. Grid Generation

The grid generation can be divided into the two parts of dividing the radial and axial directions into small stretches from which the control volumes will be built. The width of a control volume will be denoted as YV(J) for the radial direction and XU(I) for the axial direction. There are M1 grid lines dividing the radial direction and L1 for the axial direction. J is the numbering of the grid points for the radial direction, I for the axial direction. The axial grid lines were equidistant in all computations.

The objectives for the radial grid were:

- very dense near the wall
- neighboring control volumes should not vary too much in width
- sufficient number of grid points also in the center region should be maintained

Let us define χ radial grid coordinate

$$\chi \equiv \frac{J - 2}{M1 - 2}$$

and χ_1 be an intermediate location where we switch from one grid form to another. There are many approaches thinkable. However, in axisymmetric coordinates, the following customary approach does *not* work well:

$$\frac{YV(J)}{YL} = \begin{cases} a\chi + b & \chi < \chi_1 \\ c\chi^d + e & \chi > \chi_1 \end{cases}$$

The reason for this is that in axisymmetric coordinates, not enough grid lines can be placed in the region near the wall--which should be resolved finely--since the quantity χ get close to 1.0. even with a high exponent d. On the contrary, near the centerline, χ

approaches zero, and the resulting variation in the width of neighboring control volumes is tremendous.

A remedy is to specify the following grid:

$$F(\chi) = \frac{YV(J)}{YL} = \begin{cases} \alpha\chi & \chi < \chi_1 \\ a\,e^{b\chi} + c & \chi > \chi_1 \end{cases}$$

Which gives a linear grid between the centerline and χ_1 and an exponential grid between χ_1 and the wall. The parameters b and χ_1 must be specified, the others are fixed.

At the wall, $\chi = 1 \Rightarrow$. $F(\chi) = 1$. Therefore:

$$c = 1 - a\,e^{b}$$

At χ_1, we require that the grid function is continuous and differentiable. Thus

$$a = \frac{1}{e^{b} + e^{b\chi_1}\,[b\chi_1 - 1]}$$

and $$\alpha = a\,b\,e^{(b\chi_1)}$$

For $b \rightarrow -\infty \Rightarrow$ very dense near the wall;

for $b \rightarrow +\infty \Rightarrow$ very dense near χ_1.

This form was used for the grid generation of the LRN computations. For the computations with the 33 by 51 grid, $\chi_1 =$ 0.4 and $b = -5$ were customarily used. For the computations with the 35 by 64 grid, $\chi_1 =$ 0.2 and $b = -6$ were used. Figure C.1 shows a typically used grid.

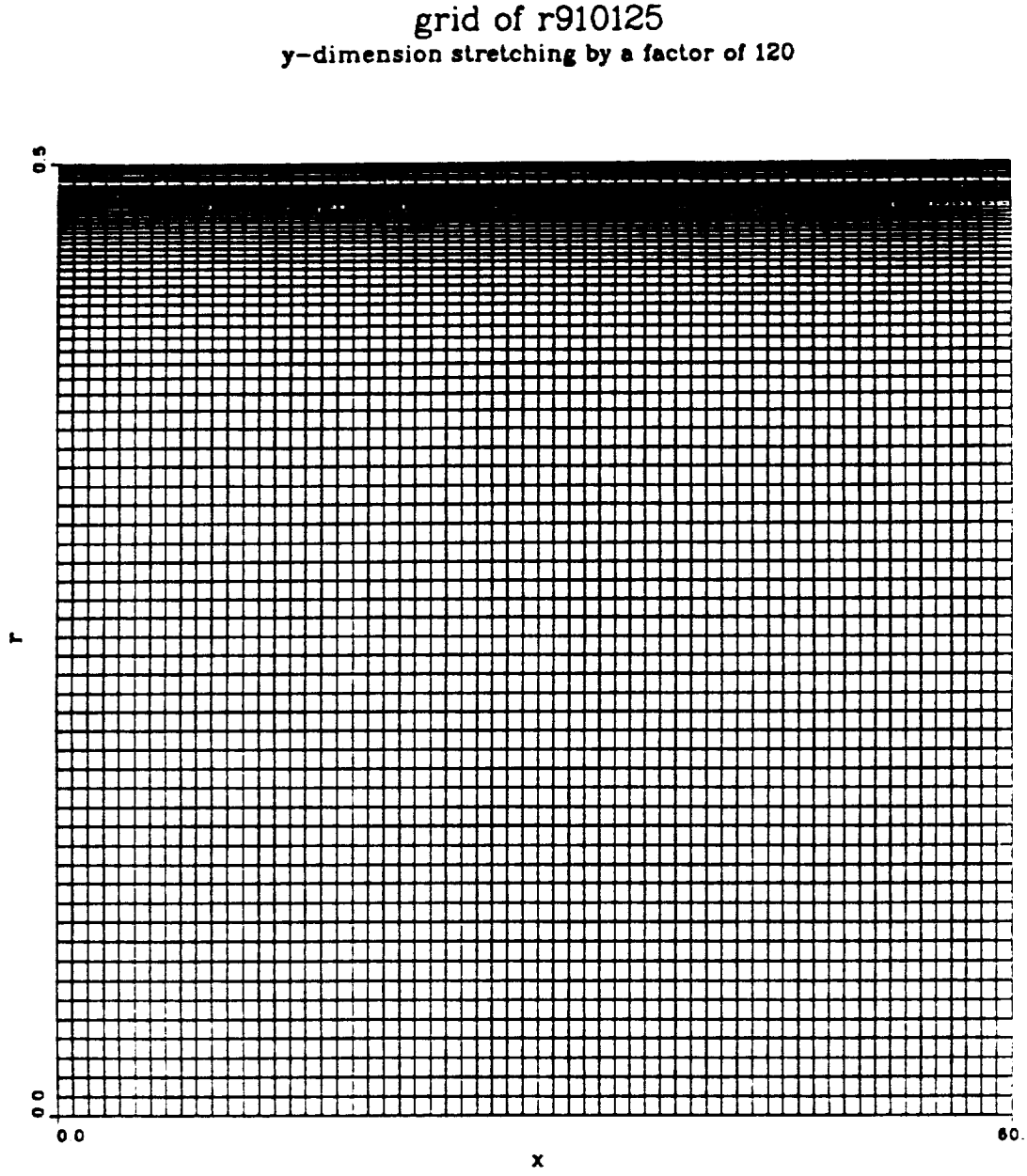

Figure C.1: *A typical grid, 64 by 91 grid points. Note that the radial dimension is stretched by a factor of 120.*

REPORT DOCUMENTATION PAGE

Form Approved
OMB No. 0704-0188

1. AGENCY USE ONLY (*Leave blank*)	2. REPORT DATE	3. REPORT TYPE AND DATES COVERED
	August 1991	Final Contractor Report

4. TITLE AND SUBTITLE
Numerical Prediction of Turbulent Oscillating Flow and Associated Heat Transfer

5. FUNDING NUMBERS
WU-590-13-11
G-NAG3-1024

6. AUTHOR(S)
W.J. Koehler, S.V. Patankar, and W.E. Ibele

7. PERFORMING ORGANIZATION NAME(S) AND ADDRESS(ES)
University of Minnesota
Department of Mechanical Engineering
Minneapolis, Minnesota 55455

8. PERFORMING ORGANIZATION REPORT NUMBER
None

9. SPONSORING/MONITORING AGENCY NAMES(S) AND ADDRESS(ES)
National Aeronautics and Space Administration
Lewis Research Center
Cleveland, Ohio 44135-3191

10. SPONSORING/MONITORING AGENCY REPORT NUMBER
NASA CR-187177

11. SUPPLEMENTARY NOTES
Project Manager, Roy C. Tew, Power Technology Division, NASA Lewis Research Center, (216) 433-8471.

12a. DISTRIBUTION/AVAILABILITY STATEMENT
Unclassified - Unlimited
Subject Category 34

12b. DISTRIBUTION CODE

13. ABSTRACT (*Maximum 200 words*)

A crucial point for further development of Stirling engines is the optimization of its heat exchangers which operate under oscillatory flow conditions. It has been found that the most important thermodynamic uncertainties in the Stirling engine designs for space power are in the heat transfer between gas and metal in all engine components and in the pressure drop across the heat exchanger components. So far, performance codes cannot predict the power output of a Stirling engine reasonably enough if used for a wide variety of engines. Thus, there is a strong need for better performance codes. However, a performance code is usually not concerned with the details of the flow. This information must be provided externally. While for laminar oscillating flow analytical relationships exist, there has been hardly any information about transitional and turbulent oscillating flow which could be introduced into the performance codes. In 1986 a survey by Seume and Simon revealed that most Stirling engine heat exchangers operate in the transitional and turbulent regime. Consequently, research has since focused on the unresolved issue of transitional and turbulent oscillating flow and heat transfer. Since 1988, the University of Minnesota oscillating flow test facility has obtained experimental data about transitional and turbulent oscillating flow. However, since the experiments in this field are extremely difficult, lengthy and expensive, it is advantageous to numerically simulate the flow and heat transfer accurately from first principles. This report summarizes work done at the University of Minnesota on development of such a numerical simulation.

14. SUBJECT TERMS
Oscillating flow; Heat transfer; Stirling engines

15. NUMBER OF PAGES
246

16. PRICE CODE
A11

17. SECURITY CLASSIFICATION OF REPORT	18. SECURITY CLASSIFICATION OF THIS PAGE	19. SECURITY CLASSIFICATION OF ABSTRACT	20. LIMITATION OF ABSTRACT
Unclassified	Unclassified	Unclassified	